

Thermal conductivity of low-dimensional materials: Recent progress, prospects, and challenges

Cite as: Appl. Phys. Rev. **12**, 041325 (2025); doi: [10.1063/5.0274620](https://doi.org/10.1063/5.0274620)

Submitted: 7 April 2025 · Accepted: 19 November 2025 ·

Published Online: 11 December 2025



Ali Sheraz,¹ Oleg Korotchenkov,^{1,2} Mohammad Ali Nasiri,¹ Marco Antonio López de la Torre,³ and Andrés Cantarero^{1,a)}

AFFILIATIONS

¹Institut de Ciència Molecular, Universitat de València, P.O. Box 22085 Valencia, Spain

²Faculty of Physics, Taras Shevchenko National University of Kyiv, Kyiv 01601, Ukraine

³Departamento de Física Aplicada, Facultad de Ciencias Ambientales y Bioquímica, Universidad de Castilla-La Mancha, Avda. Carlos III s/n, 45071 Toledo, Spain

^{a)}Author to whom correspondence should be addressed: Andres.Cantarero@uv.es

ABSTRACT

The performance and reliability of thermoelectric materials and devices based on low-dimensional materials are strongly influenced by heat dissipation and thermal stability, which are directly linked to the thermal conductivity of the materials. Therefore, accurate determination of the thermal properties remains a critical aspect of material development efforts, which requires the continuous advancement and refinement of the measurement techniques. In recent years, substantial progress has been achieved in theoretical and experimental approaches for the characterization of thermal conductivity in low-dimensional materials. This article reviews these advances, focusing on recent developments in the measurement of thermal conductivity in thin films, two-dimensional materials, and other nanostructures. The fundamental concepts underlying a range of experimental and theoretical techniques are presented together with their theoretical framework, underscoring the critical role of selecting a measurement approach appropriate to the sample thickness, thermal conductivity regime, and material characteristics. Special attention is paid to the thermal conductivity of emerging materials relevant for thermal management, including carbon-based materials, black phosphorus, MXenes, and boron nitride. Furthermore, the advantages and limitations of the different measurement techniques are discussed, in relation to the type and structure of the material under study. Finally, the review summarizes the key findings and outlines future research opportunities, highlighting promising directions across different classes of low-dimensional materials.

Published under an exclusive license by AIP Publishing. <https://doi.org/10.1063/5.0274620>

TABLE OF CONTENTS

I. INTRODUCTION.....	3	2. In-plane and cross-plane thermal conductivity	25
II. FUNDAMENTALS OF HEAT TRANSFER	4	B. Laser flash analysis	29
A. Heat equations.....	4	C. Time-domain thermoreflectance.....	30
B. Harmonic heat transfer.....	6	D. Frequency-domain thermoreflectance	32
C. Coupled thermoelastic effects	8	IV. THERMAL CONDUCTIVITY IN ULTRA-THIN	
D. Nanoscale heat transfer	10	MATERIALS	35
E. Non-reciprocal heat transport.....	13	A. Raman thermometry technique	36
F. Simulating heat transfer	16	B. Bolometric technique	42
G. Interface thermal conductance	18	C. Time- and frequency-domain thermoreflectance ..	44
H. Strategies for measuring thermal conductivity....	21	D. Suspended thermal micro bridge method.....	46
III. THERMAL CONDUCTIVITY IN THIN FILMS	22	E. 3ω technique	49
A. 3ω technique.....	22	V. THERMAL CONDUCTIVITY IN	
1. Principles of the 3ω technique.....	22	NANOSTRUCTURES.....	49
		A. Self-heating DC and 3ω technique	50

B. Electron beam self-heating technique.....	53
C. Suspended thermal micro bridge method.....	55
D. Scanning thermal microscopy.....	56
E. Bolometric technique	60
F. Photothermal radiometry	60
G. Laser flash analysis	62
VI. MEASURING THERMAL BOUNDARY	
CONDUCTANCE	63
A. 3ω technique.....	63
B. Time- and frequency-domain thermoreflectance ..	65
C. Theoretical simulations.....	68
VII. CONCLUSIONS AND OUTLOOK.....	69

NOMENCLATURE**Physical parameters**

A	Cross-sectional area
$2b$	Metallic bridge or thermometer width
C	Specific heat
d	Crystal lattice spacings, thickness
d_1	Grain size of a thin film
E_F	Fermi energy
$Ei(x)$	Exponential integral
ET-Raman	Energy transport state-resolved Raman
f_i	Frequency of the i -th vibration mode
FET-Raman	Frequency domain ET-Raman
f_0	Equilibrium Bose–Einstein distribution function
g	Density of states
GR	Graphene
G_{th}	Thermal conductance
h	Planck constant
\hbar	Reduced Planck constant
h_K	Thermal boundary conductance
I	Electrical current
$I_{S(AS)}$	Stokes (anti-Stokes) Raman intensity
I_0	Amplitude of a periodic uniform heat source, AC or DC amplitude
$I_0(x)$	Bessel function of the first kind
k	Phonon wave vector
k_B	Boltzmann constant
Kn	Knudsen number
$K_0(x)$	Bessel function of the second kind
l	Length
L_z	Linear spacing between interfaces, propagation distance, metallic bridge, or thermometer length
M	Atomic mass
MR	Atomic mass ratio
n	Phonon distribution function
NA	Numerical aperture of the objective
p	Surface specularity
P	Dissipated/absorbed power
q	Heat flux vector
Q	Heat flux
\dot{q}	Thermal energy generation rate
q_i	Heat flux across interface
q_j	Heat flux normal to interface
q_{rad}	Radiation heat losses

R	Hole radius, electrical resistance
R_b	Equivalent thermal resistance of suspension beams
$R_{contact}$	Thermal contact resistance
R_i	Thermal resistance at i -th sample point
R_K	Thermal boundary resistance
R_{sf}	Thermal resistance due to a boundary layer between a film and a substrate
R_T	Resistance of the metallic line (resistance thermometer)
R_{th}	Thermal resistance
R_{tot}	Total thermal resistance
r_0	Laser spot radius
R_0	Heater resistance, DC component of the resistance time
t	Time
T	Temperature
t_e	Excitation pulse duration
t_r	Thermal relaxation duration
T_{amb}	Ambient temperature
U	Lattice energy
u_i	Atomic displacement components
V	Electric voltage
$V_{in(out)}$	In-phase (out-of-phase) voltage
$V_{3\omega}$	Third-harmonic voltage
Y	Young's modulus
Z	Acoustic impedance, dimensionless thermal transfer function
Δn	Change in the free carrier density
ΔT_{AC}	Periodic temperature oscillation
ΔT_{DC}	Time-independent temperature rise
ΔV_b	Voltage due to bolometric effect
ΔV_{PC}	Voltage due to photoelectric effect

Greek symbols

α	Thermal diffusivity
β_R	Temperature coefficient of the resistance
β_{TR}	Thermoreflectance coefficient
δ	Thermal penetration depth
ℓ	Thermal diffusion length
η	Thermal rectification factor
γ	Euler constant
κ	Thermal conductivity
κ_a	Apparent thermal conductivity
κ_i	Intrinsic thermal conductivity of a film
Λ	Phonon mean free path
λ	Wavelength
μ	Carrier mobility
ω	Angular frequency
ω_0	Phonon angular frequency
ω_1	Raman frequency
ω_i	Frequency of the incident laser light
ϕ	Phase shift
Φ_{ijk}	Third order force constants
Φ_{ij}	Harmonic force constants
ρ	Mass density
σ	Electrical conductivity
σ_{SB}	Stefan–Boltzmann constant

τ	Delay between temperature gradient and the heat flux (intrinsic relaxation time)
τ	Phonon lifetime
τ_D	Thermal-diffusion time
τ_d	Optical delay time
τ_s	Phonon relaxation time
Θ	Dimensionless frequency
Θ_D	Debye temperature
v	Phonon velocity
v_g	Phonon group velocity
ϑ	Complex temperature function
ζ	Interface transmission coefficient

Subscripts and superscripts

β	Wavenumber of the thermal oscillation
ν	Phonon branch number
\parallel	in plane
\perp	cross plane
f	film
P	polarization
s	substrate

Abbreviations

2DEG	Two-dimensional electron gas
AFM	Atomic force microscopy
AGF	Atomistic Green's function
AMM	Acoustic mismatch model
BTE	Boltzmann transport equation
CCD	Charge-coupled device
CNT	Carbon nanotube
CVD	Chemical vapor deposition
CW	Continuous wave
DFT	Density functional theory
DMM	Diffuse mismatch model
DOS	Density of states
DWCNT	Double-walled carbon nanotube
EMD	Equilibrium molecular dynamics
EOM	Electro-optic modulator
EPRT	Modified phonon radiative heat transfer
FDTR	Frequency domain thermoreflectance
FEM	Finite element modeling
FIB	Focused ion beam
GNR	Graphene nanoribbon
hBN	Hexagonal boron nitride
HRTEM	High-resolution transmission electron microscopy
ICMA	Interface conductance modal analysis
IR	Infrared
LFA	Laser flash analysis
LO	Longitudinal optical
MD	Molecular dynamics
MEMS	Microelectromechanical system
MFP	Mean free path
MODFET	Modulation-doped field effect transistor
MR	Mass ration
MTM	Maximum transmission model
MWCNT	Multi-walled carbon nanotube

NEGF	Non-equilibrium Green's function
NEMD	Nonequilibrium molecular dynamics
NM	Nanomesh
NW	Nanowire
PA	Photoacoustic
PBO	Poly(p-phenylene-2,6-benzobisoxazole)
PC	Polycarbonate
PLTR	Pulsed laser-assisted thermal relaxation
PMMA	Poly(methyl methacrylate)
PT	Photothermal
QD	Quantum dot
rGO	Reduced graphene oxide
RT	Resistance thermometer
SDTR	Spatial-domain thermoreflectance
SEM	Scanning electron microscopy
SL	Superlattice
SPM	Scanning probe microscopy
SThM	Scanning thermal microscopy
STM	Scanning tunneling microscopy
STO	Strontium titanate
SWCNT	Single-walled carbon nanotube
TATB	1,3,5-Triamino-2,4,6-trinitrobenzene
TBC	Thermal boundary conductance
TBR	Thermal boundary resistance
TDTR	Time domain thermoreflectance
TIM	Thermal interface material
TMD	Transition-metal dichalcogenide
TMO	Transition-metal oxide
TO	Transversal optical
TTR	Transient thermoreflectance
VLS	Vapor-liquid-solid

I. INTRODUCTION

Thermal conductivity is a key material property^{1–3} of high relevance, applicable in a wide range of fields, ranging from the thermal management of high-power electronic devices to thermal insulation in construction materials.^{4–6}

As device architectures continue to shrink to the nanoscale, new or refined techniques are required to accurately measure thermal conductivity. Non-contact methods, which require only a small surface area for heating and probing, have become dominant in the thermal characterization of nanomaterials.^{7–9} They usually utilize laser heating sources and are typically divided into three types, including time-domain techniques, frequency-domain techniques, and spectroscopy.⁷ Meanwhile, conventional thermal measurement methods that employ a contact heating source or probing sensor, such as the 3ω method^{10,11} have proven to be robust techniques capable of measuring the thermal properties of both bulk and thin-film materials.

The optothermal methods in the time and frequency domains have the advantage over the 3ω method of being non-contact techniques. They, however, can be expensive and difficult to implement, as they generally require the detection of the phase shift of a signal that needs to be separated from the electronic phase shifts of the instrument along with additional knowledge of the heat capacity of the material.⁸

A significant body of literature offers a compelling opportunity to examine the physical mechanisms limiting the thermal conductivity of

macroscopic materials. However, a thorough understanding of heat conduction in many forms of nanoscale materials, including bulk nanostructured materials, thin films, superlattices, nanowires, and nanotubes, is not available, partly because of the interface and interphase effects in multiphase systems. Despite intensive research and numerous insightful reviews that address experimental and theoretical advances in the field,^{12–18} comparative assessments that describe the applicability of different experimental techniques for the study of the various classes of low-dimensional materials remain quite limited. For instance, analyzing the reviews and progress articles by Sett *et al.*,¹⁹ Zhang and Chen,²⁰ Dames,²¹ and others, advanced experimental methods, such as Raman thermometry,²² electron-beam self-heating,^{23,24} T-type method,²⁵ and the 3ω technique, apply to cases of nanowires and thin films.^{19–21} Since the classic analyses of Ruoff and Lorents,²⁶ Berber *et al.*,²⁷ Kim *et al.*,²⁸ Pop *et al.*,²⁹ Balandin *et al.*,³⁰ and others, the development of measurement and computational techniques has allowed to handle the difficult problem of measuring thermal conductivities of graphene and carbon nanotubes (CNTs).^{13,31–34} Even though enormous interest in this field has led to rapid progress in experimental measurements, nanoscale heat conduction measurements remain extremely challenging, and the measured values may lack accuracy due to numerous unforeseen factors.³⁵ A major challenge in interpreting the measured values of κ lies in the need for computational methods to uncover the fundamental mechanisms governing heat transport.

This review fills a critical gap in the current literature on thermal conductivity measurements in low-dimensional systems. Despite significant progress in both experimental and theoretical research, there remains a lack of a unified and comprehensive overview that highlights the rich variety and applicability of the available experimental techniques and the corresponding theoretical and simulation approaches. By systematically analyzing and comparing these methodologies, this review provides an integrated framework for understanding their applicability, limitations, and reliability in evaluating heat transport at the nanoscale.

The review begins with a background on the classical laws of heat transfer, the basics of nanoscale heat transfer, and periodic heat transfer, which is a necessary part of frequency domain measurements. One major influence on the measurement of κ in low-dimensional systems is the thermal boundary conductance, which is also briefly outlined in Sec. II. Particular attention will be devoted to the emerging concepts of non-reciprocal and ballistic heat transport, which are essential for understanding energy flow in low-dimensional materials. These phenomena not only challenge the conventional diffusive description of thermal conduction but also open new opportunities for engineering directional heat control and thermal rectification in nanoscale devices. In Secs. III and VI, a detailed description of the methods used to measure κ in low-dimensional materials is extensively discussed. Recognizing that previously published reviews in this area have looked at closely related problems, we believe that reconciling these various contributions with a detailed analysis of the applicability of measurement techniques to particular examples of thin films (Sec. III), ultrathin materials (Sec. IV), nanostructures (Sec. V), and measuring thermal boundary conductance (Sec. VI) can only help to clarify the state of the literature. Over the past few years, many applications have been posited in emerging thermal materials such as nanostructured carbon materials (e.g., CNTs and graphene), black phosphorous,

MXenes, hexagonal boron nitride, and we follow the analysis of their beneficial impact on thermal properties, which we believe to be emerging areas that may lead to breakthroughs soon. We conclude with a summary and outlook in Sec. VII, including the prospects for useful thermal materials and some interesting physical questions related to measurement techniques.

II. FUNDAMENTALS OF HEAT TRANSFER

A. Heat equations

In classical and isotropic material, thermal conduction is fundamentally described by Fourier's law, as illustrated in Fig. 1. This law states that the heat flux through a material is directly proportional to the temperature gradient ΔT across its boundaries and the cross-sectional area perpendicular to the direction of the heat flow, under steady-state conditions. Accordingly, Fourier's law can be expressed as³⁶

$$\mathbf{q}(\mathbf{r}) = -\kappa \nabla T, \quad (1)$$

where \mathbf{q} (W m^{-2}) is the heat flux vector, κ ($\text{W m}^{-1}\text{K}^{-1}$) is the thermal conductivity tensor, and ∇T is the temperature gradient vector. Heat flux, or heat flux density, represents the heat flow rate per unit area.

It is important to distinguish between thermal conductivity and thermal conductance, much like the distinction between electrical resistivity and electrical resistance. Thermal conductivity is an intrinsic property of the material, independent of the sample's size or shape. In contrast, thermal conductance G_{th} (W K^{-1}) depends on both material properties and geometry. For a sample of length l and cross-sectional area A , the conductance is given by

$$G_{th} = \kappa \frac{A}{l}. \quad (2)$$

The time-dependent temperature distribution $T(x, y, z)$ is governed by the heat diffusion equation, which in Cartesian coordinates³⁷ is given by

$$\frac{\partial}{\partial x} \left(\kappa \frac{\partial T}{\partial x} \right) + \frac{\partial}{\partial y} \left(\kappa \frac{\partial T}{\partial y} \right) + \frac{\partial}{\partial z} \left(\kappa \frac{\partial T}{\partial z} \right) + \dot{q} = \rho C \frac{\partial T}{\partial t}. \quad (3)$$

If the thermal conductivity κ does not depend on the coordinates,

$$\frac{\partial^2 T}{\partial x^2} + \frac{\partial^2 T}{\partial y^2} + \frac{\partial^2 T}{\partial z^2} + \frac{\dot{q}}{\kappa} = \frac{1}{\alpha} \frac{\partial T}{\partial t}, \quad (4)$$

where ρ is the mass density, C is the specific heat, \dot{q} (in W m^{-3}) is the amount of heat produced per unit time inside the material due to an internal energy source, and $\alpha = \kappa / \rho C$ (m^2s^{-1}) is the thermal diffusivity. The term ρC , known as volumetric heat capacity, represents the thermal energy stored per unit volume. In the one-dimensional (1D) case and under steady-state conditions,

$$\frac{d^2 T}{dx^2} + \frac{\dot{q}}{\kappa} = 0. \quad (5)$$

On the other hand, if there is no heat source in the material, we have the partial differential equation:

$$\frac{\partial T(x, t)}{\partial t} = \alpha \frac{\partial^2 T(x, t)}{\partial x^2}. \quad (6)$$

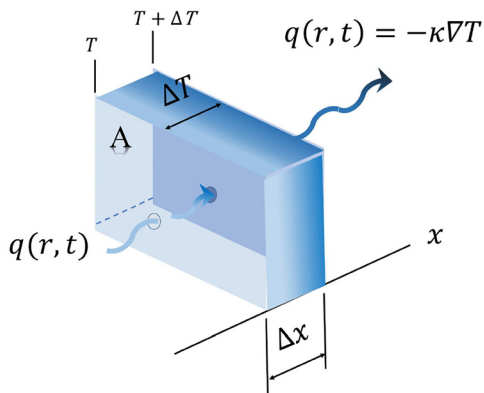


FIG. 1. Illustration of Fourier's law. The heat flows through the sample from the source (left-hand side) to the sink (right-hand side).

Under the boundary conditions $T(x, t) \rightarrow 0$ when $x \rightarrow \infty$ (semi-infinite plane) and $T(x, 0) = T_0\delta(x)$, i.e., there is a temperature pulse at $t = 0$, the partial differential equation can be solved using Fourier transform techniques. The resulting solution can be written as

$$T(x, t) = \frac{T_0}{\sqrt{4\pi\alpha t}} e^{-x^2/4\alpha t}. \quad (7)$$

Other boundary conditions give rise to different solutions. The temperature decays by a factor e at $\ell = \sqrt{4\alpha t}$. This quantity is referred to as the diffusion length. Alternative definitions such as $\sqrt{\pi\alpha t}$, $\sqrt{2\alpha t}$ are also used in the literature, reflecting the fact that the governing partial differential equations have multiple solutions.³⁸ In Sec. II B, we will analyze the case of a harmonic solution. In this case, the diffusion length increases with time as heat continues to spread through the material. As $t \rightarrow \infty$, the diffusion length approaches infinity, resulting in a uniform temperature distribution across the entire material. The analysis can be further extended by expressing the heat equation in cylindrical coordinates.

In cylindrical coordinates (see Fig. 2), with \mathbf{u}_r , \mathbf{u}_ϕ , and \mathbf{u}_z representing the unit vectors in the r , ϕ , and z directions, respectively, Fourier's law becomes

$$\mathbf{q}(r, \phi, z) = -\kappa \nabla T = -\kappa \left(\frac{\partial T}{\partial r} \mathbf{u}_r + \frac{1}{r} \frac{\partial T}{\partial \phi} \mathbf{u}_\phi + \frac{\partial T}{\partial z} \mathbf{u}_z \right), \quad (8)$$

with the heat flux components in the radial, azimuthal, and axial directions given by

$$q_r = -\kappa \frac{\partial T}{\partial r}, \quad q_\phi = -\frac{1}{r} \frac{\partial T}{\partial \phi}, \quad q_z = -\kappa \frac{\partial T}{\partial z}. \quad (9)$$

The heat-diffusion equation takes the form:

$$\frac{1}{r} \frac{\partial}{\partial r} \left(r \frac{\partial T}{\partial r} \right) + \frac{1}{r^2} \frac{\partial}{\partial \phi} \left(\frac{\partial T}{\partial \phi} \right) + \frac{\partial}{\partial z} \left(\frac{\partial T}{\partial z} \right) + \frac{\dot{q}}{\kappa} = \frac{1}{\alpha} \frac{\partial T}{\partial t}. \quad (10)$$

In fundamental research, Fourier's law has been highly effective in describing heat conduction in macroscopic systems. However, at the micro- and nanoscale, additional effects such as size dependence³⁹ and thermal rectification⁴⁰ become significant (see Sec. II E). Moreover,

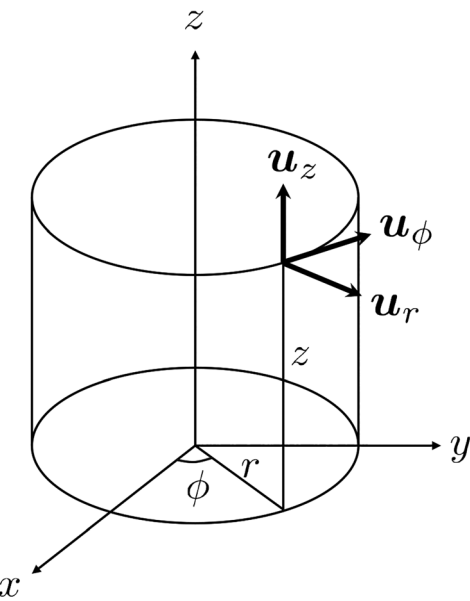


FIG. 2. Unit vectors in cylindrical coordinates referred to Cartesian coordinates.

when the characteristic length of the temperature gradient becomes comparable to the phonon wavelength or mean free path (MFP), or when scattering processes are limited or absent,^{41–45} Fourier's law no longer provides an accurate description of heat transport. Consequently, understanding heat transfer at the nanoscale is crucial for ensuring the reliable operation of modern electronic, electromechanical, and energy conversion devices. Over the past three decades, research in nanoscale heat transfer has progressed rapidly, uncovering a wide range of novel and intriguing phenomena (see Sec. II D).^{14,18,35}

Consider the simple case of a hollow cylinder with wall height h , inner radius r_1 , and outer radius r_2 . A heat source is applied at the inner wall, producing a radial heat flow $Q(r)$ (W) that dissipates outward, as illustrated in Fig. 3.

If there are no heat losses, the radial heat flow rate remains constant at all radii, since the product of the heat flux and the lateral surface area, $q_r \times 2\pi rh$, must be conserved.

$$r \frac{dT}{dr} = C_1, \quad (11)$$

where C_1 is the constant of integration. Solving this equation yields

$$T(r) = C_1 \ln r + C_2, \quad (12)$$

where C_2 is a second integration constant. The two constants, C_1 and C_2 , can be determined from the boundary conditions $T(r_1) = T_1$ and $T(r_2) = T_2$. Applying these conditions gives

$$T(r) = T_1 + (T_2 - T_1) \frac{\ln(r/r_1)}{\ln(r_2/r_1)}, \quad (13)$$

which can be written as

$$\frac{T_1 - T(r)}{T_1 - T_2} = \frac{\ln(r/r_1)}{\ln(r_2/r_1)}. \quad (14)$$

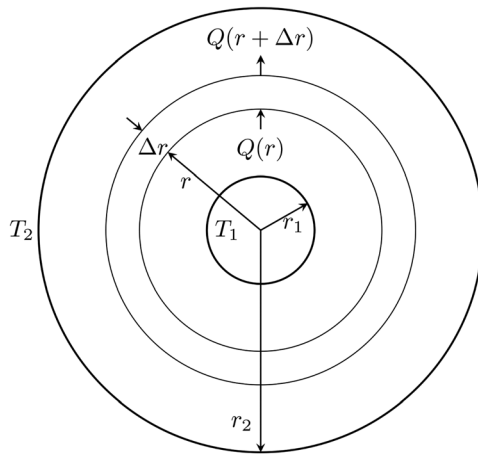


FIG. 3. Heat diffusion in a hollow cylinder.

From the $T(r)$ dependence, we can calculate the flow rate as

$$Q = 2\pi h \kappa \frac{T_1 - T_2}{\ln(r_2/r_1)}. \quad (15)$$

Let us now rewrite the result in terms of the thermal conductance G_{th} introduced above. By definition, G_{th} is the ratio of the total heat flow to the temperature difference across the cylinder walls, such that

$$G_{th} = \frac{Q}{\Delta T}. \quad (16)$$

Let us instead express the result in terms of the thermal resistance R_{th} , defined as the reciprocal of the thermal conductance,

$$R_{th} = \frac{1}{G_{th}}. \quad (17)$$

The thermal resistance R_{th} has, therefore, units of KW^{-1} . From Eq. (15), the thermal resistance can be written as

$$R_{th} = \frac{\ln(r_2/r_1)}{2\pi h \kappa}. \quad (18)$$

However, what does thermal resistance physically represent? From Eq. (18), it is evident that if the thermal conductivity were infinite, heating the cylinder at r_1 would cause heat to reach r_2 instantaneously. Conversely, if the thermal conductivity were zero, no heat would ever reach r_2 . Thus, the thermal resistance quantifies a measure of the difficulty or opposition encountered by heat as it flows between r_1 and r_2 .

From the perspective of phonon transport, the picture becomes even clearer. At low temperatures, the limited phonon population restricts thermal conductivity. As temperature increases, the growing phonon population enhances heat transport. However, when phonon propagation is hindered by nanostructuring, the thermal conductivity is suppressed, leading to a higher thermal resistance. Therefore, the primary role of nanostructuring is to enhance thermal resistance, or equivalently, to reduce thermal conductivity (see Sec. II D).

Thus, Eq. (18) shows that the thermal conductivity κ of a material can be determined once its thermal resistance is known. The derivation

presented here demonstrates this relationship for the specific case of a cylinder with radial symmetry:

$$\kappa = \frac{\ln(r_2/r_1)}{2\pi h R_{th}} = \frac{\ln(r_2/r_1)}{2\pi h} G_{th}. \quad (19)$$

Thermal resistance should not be confused with thermal boundary resistance (TBR), which refers specifically to the resistance encountered by heat as it crosses the interface between two materials (see Sec. II G).

B. Harmonic heat transfer

Consider a semi-infinite solid whose surface is subjected to a periodic, uniform heat flux of the form $I_0 \cos \omega t = I_0 \Re[e^{i\omega t}]$, generating a surface temperature $T(0, t)$, which varies periodically with time (see Fig. 4). The temperature distribution within the material can be expressed as

$$T(x, t) = T_{amb} + \Delta T_{DC} + \Delta T_{AC}, \quad (20)$$

with T_{amb} being the ambient temperature, ΔT_{DC} a constant temperature offset, and ΔT_{AC} is the temperature component oscillating at the frequency ω .

In the absence of internal heat sources, the heat-diffusion equation [Eq. (4)] takes the form:

$$\frac{\partial^2 \vartheta}{\partial x^2} - \frac{1}{\alpha} \frac{\partial \vartheta}{\partial t} = 0, \quad (21)$$

where we have introduced a complex temperature function $\vartheta(x, t)$. The real part of $\vartheta(x, t)$ corresponds to the physically meaningful temperature variation in the solid with respect to the ambient temperature T_{amb} . Thus,

$$T(x, t) = T_{amb} + \Delta T_{DC} + \Re[\vartheta(x, t)]. \quad (22)$$

Let us assume that the time-dependent and spatial-temperature components of $\vartheta(x, t)$ can be separated, $\vartheta(x, t) = \vartheta(x)e^{i\omega t}$. Equation (21) can be simplified to

$$\frac{d^2 \vartheta(x)}{dx^2} - \frac{i\omega}{\alpha} \vartheta(x) = 0 \rightarrow \frac{d^2 \vartheta(x)}{dx^2} = k^2 \vartheta(x), \quad (23)$$

a second-order ordinary differential equation, where

$$k = \sqrt{\frac{i\omega}{2\alpha}} = (1+i)\sqrt{\frac{\omega}{2\alpha}} \equiv (1+i)\beta, \quad (24)$$

with $\beta = \sqrt{\omega/2\alpha}$ being the propagation factor ($2\pi/\lambda$). Using the flux continuity at the surface as a boundary condition,

$$\kappa \frac{\partial \vartheta(x, 0)}{\partial x} \Big|_{x=0} = \frac{I_0}{2}, \quad (25)$$

the temperature can be written as^{46,47}

$$\begin{aligned} \Delta T_{AC}(x, t) &= \Re[\vartheta(x, t)] \\ &= \frac{I_0}{2\kappa} \sqrt{\frac{\alpha}{\omega}} e^{-x/\delta} \cos\left(\omega t - \beta x - \frac{\pi}{4}\right), \end{aligned} \quad (26)$$

which is the expression of an attenuated plane wave. The factor $\delta \equiv 1/\beta = \sqrt{2\alpha/\omega}$ in Eq. (26) is called penetration depth of the heat

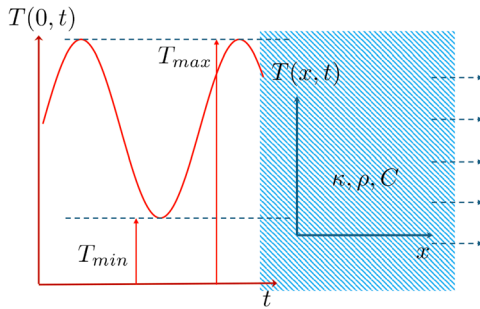


FIG. 4. Geometry of a semi-infinite solid with a periodic temperature variation $T(0, t)$ at its surface. The amplitude $\Delta T(0) = (T_{\max} - T_{\min})/2$.

wave.⁴⁸ δ represents the depth at which the temperature amplitude is reduced by a factor e . In the case of harmonic plane waves, the attenuation is exponential and the decay factor δ has the same definition of the diffusion length since we are dealing with a diffusion process. On the other hand, Eq. (26) accounts for the phase difference between the heat excitation and the resulting thermal response of the solid, given by $(\beta x + \pi/4)$.

The simulation results are exemplified in Fig. 5(a), illustrating that the temperature oscillation in the solid is completely damped at depths of at most several δ .

It is well known that the constitutive Fourier law given by Eq. (1) yields a parabolic heat conduction equation, which means that heat pulses propagate with infinite speed. To overcome this problem, Cattaneo and Vernotte^{49–51} proposed to replace Eq. (1) by an evolution equation taking into account a time delay τ between the temperature gradient and the heat flux. Since this is a diffusion process, τ must be somehow related to the diffusion coefficient; we will come back to the meaning of τ later. Following Cattaneo's work, Fourier's law can be rewritten as

$$\mathbf{q}(\mathbf{r}, t) + \tau \frac{\partial \mathbf{q}(\mathbf{r}, t)}{\partial t} = -\kappa \nabla T(\mathbf{r}, t). \quad (27)$$

This relation, which is commonly referred to as the Cattaneo–Vernotte equation, leads to hyperbolic-type heat conduction and predicts thermal oscillations propagating at a finite speed.⁵² Indeed, in this case, Eq. (21) can be rewritten to give the wave equation as

$$\frac{\partial^2 \vartheta'}{\partial x^2} - \frac{1}{\alpha} \frac{\partial \vartheta'}{\partial t} - \frac{\tau}{\alpha} \frac{\partial^2 \vartheta'}{\partial t^2} = 0. \quad (28)$$

Expressing $\vartheta'(x, t) = \vartheta'(x) e^{i\omega t}$ yields

$$\frac{d^2 \vartheta'(x)}{dx^2} - \frac{i\omega}{\alpha} (1 + i\omega\tau) \vartheta'(x) = 0, \quad (29)$$

and assuming $\vartheta'(x) = A e^{kx+i\phi}$ with the boundary condition

$$\left. \frac{\partial \vartheta'(x, 0)}{\partial x} \right|_{x=0} = (1 + i\omega\tau) \frac{I_0}{2}, \quad (30)$$

the solution for k is

$$k = \sqrt{\frac{\omega}{\alpha}} [1 + \omega^2 \tau^2]^{1/4} e^{i\pi} e^{(i/2)\arctan\omega\tau} \quad (31)$$

in polar form and

$$k = \sqrt{\frac{\omega}{2\alpha}} \left[\sqrt{\sqrt{1 + \omega^2 \tau^2} - \omega\tau} + i\sqrt{\sqrt{1 + \omega^2 \tau^2} + \omega\tau} \right] \quad (32)$$

in binomial form. The corresponding phase factor $\phi = -\pi/4 + (1/2)\arctan\omega\tau$. In contrast to the parabolic solution, where the real and imaginary parts of k were identical, the hyperbolic solution introduces an additional term in which the real and imaginary components differ in the sign of the $\omega\tau$ term inside the square root. Taking the real part of the complex temperature yields⁴⁶

$$\begin{aligned} \Delta T'_{AC}(x, t) = & \frac{I_0}{2\kappa} \sqrt{\frac{\alpha}{\omega}} \sqrt{1 + \omega^2 \tau^2} \exp \left[-x \sqrt{\frac{\omega}{2\alpha}} \sqrt{\sqrt{1 + \omega^2 \tau^2} - \omega\tau} \right] \\ & \times \cos \left(x \sqrt{\frac{\omega}{2\alpha}} \sqrt{\sqrt{1 + \omega^2 \tau^2} + \omega\tau} - \omega t + \frac{\pi}{4} - \frac{1}{2} \arctan\omega\tau \right). \end{aligned} \quad (33)$$

Yuen and Lee⁵³ also provide a thorough derivation of this relationship.

The variation of the temperature difference (amplitude and phase) as a function of frequency is illustrated in Fig. 6. In the low-frequency regime ($\omega\tau \ll 1$), Eq. (33) simplifies to Eq. (26), producing an overlap between solid and dotted lines in Fig. 6. In this frequency range, $\Delta T'_{AC}$ decreases with increasing ω while the phase shift between surface temperature and heat excitation remains unchanged and equal to $-\pi/4$. The penetration depth of the temperature oscillations depends on the modulation frequency of the heat excitation since the thermal penetration depth in Eq. (33) is $\delta \sim \omega^{-1/2}$.

In the high frequency limit ($\omega\tau \gg 1$), the hyperbolic solution for $\Delta T'_{AC}$ is given by⁴⁶

$$\Delta T'_{AC}(x, t) = \frac{I_0 \sqrt{\alpha\tau}}{2\kappa} e^{-x/\sqrt{4\alpha\tau}} \cos \left(\sqrt{\frac{\tau}{\alpha}} \omega x - \omega t \right). \quad (34)$$

The amplitude remains independent of the modulation frequency [solid line in Fig. 6(a)]. In contrast, the phase lag approaches zero [solid line in Fig. 6(b)], indicating that the surface temperature oscillations are synchronized with the modulated heat input. Since $\arctan 0 = 0$ and $\frac{1}{2}\arctan\infty \rightarrow \pi/4$, the phase factor $\pi/4$ is exactly compensated. Equation (34) further indicates that the penetration depth

$$\delta' = \sqrt{4\alpha\tau} \quad (35)$$

is independent of the modulation frequency.

Moreover, the dependence of $\Delta T'_{AC}$ on the normalized depth x/δ' , shown in Fig. 5(b), reveals that, unlike the low-frequency behavior shown in Fig. 5(a), the temperature undergoes multiple oscillations before their amplitude becomes significantly reduced. In addition, both the penetration depth δ' and the temperature amplitude given by Eq. (34), which scale with $\sqrt{\tau}$, vanish in the limit of small τ .

It is important to note that the penetration depth has the same definition as the thermal diffusion length introduced after Eq. (7), with the substitution t by τ . Consistently, the diffusion time can be expressed as $\tau = \ell^2/\alpha$.

Historically, Joseph and Preziosi⁵⁴ provided a comprehensive review of the thermal response of solids to sudden changes in surface temperature. Since then, the Cattaneo–Vernotte framework has been

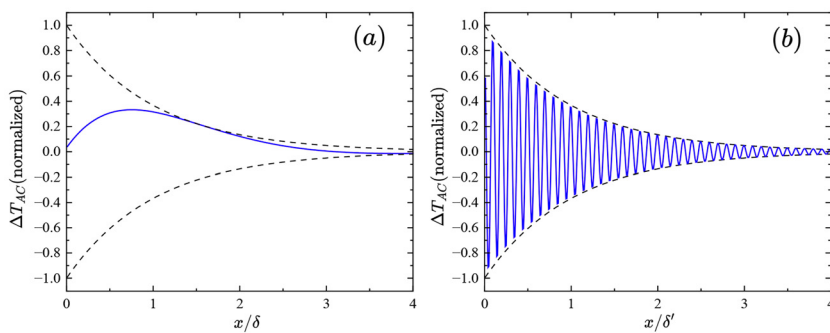


FIG. 5. Normalized (without the pre-factor) $\Delta T_{AC}(x, t)$ as a function of x/δ (x/δ') in a semi-infinite stainless-steel sample ($\delta = \sqrt{2\alpha/\omega}$, $\delta' = \sqrt{4\alpha\tau}$). (a) Calculated using Eq. (26) with $f = 100$ Hz and $t = 3.7 \times 10^{-3}$ s. (b) Calculated using Eq. (33) with $\tau = 10^{-10}$ s, $f = 5 \times 10^{10}$ Hz, and $t = 1.9 \times 10^{-11}$ s.

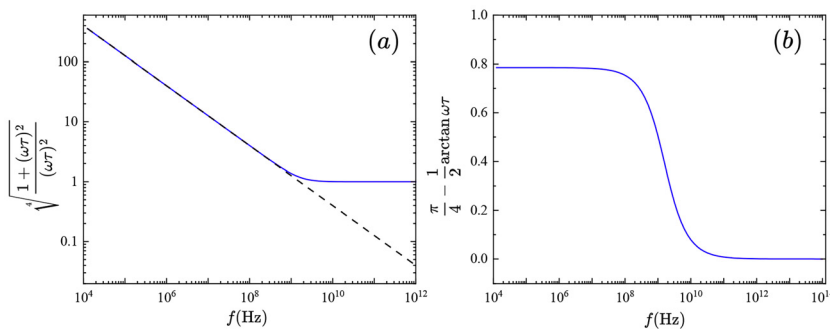


FIG. 6. (a) Amplitude and (b) phase of $\Delta T_{AC}(0, 0)$ on the surface ($x = 0$, and at $t = 0$) of a semi-infinite stainless-steel sample vs modulation frequency in a double logarithmic plot using a value of $\tau = 10^{-10}$ s. In the low frequency range (< 10^8 Hz in stainless steel), the hyperbolic (33) and parabolic (26) solutions coincide. At higher frequency (> 10^{10} Hz in stainless steel), the amplitude becomes constant and the phase goes to zero.

analyzed and generalized in several directions, including the works of Straughan,⁵⁵ Eltayeb,⁵⁶ Capriz *et al.*,⁵² Herron and Mickens,⁵⁷ and Nascimento *et al.*⁵⁸

The Cattaneo–Vernotte model resolves the paradox of instantaneous heat propagation, yet it gives rise to other nonphysical effects, such as interference between temperature waves, boundary reflections, and shock-like heat waves. To address these issues, Mironov⁵⁹ recently proposed a modification of the hyperbolic heat equation, in which the temperature gradient at time t depends on the flux at $t \pm \tau$. This formulation preserves a finite rate of energy transfer while avoiding solutions in the form of real harmonic waves, thereby eliminating the aforementioned paradoxes.

C. Coupled thermoelastic effects

Foundational theories of thermoelasticity address the coupling between thermal and mechanical effects, extending classical elasticity to account for temperature-induced stresses and deformations.⁶⁰ Biot's classical thermoelastic theory⁶¹ modifies Fourier's law by introducing a strain-rate term, leading to a diffusion-type equation. However, because it assumes no thermal relaxation time, the theory reduces to Fourier heat conduction, predicting infinite propagation speed. In the harmonic heat transfer case discussed in Sec. II B, this corresponds to undamped temperature oscillations with zero phase shift.⁶²

To address the limitations of Biot's model, Lord and Shulman and Green and Lindsay⁶³ developed generalized thermoelasticity theories that introduce a finite thermal relaxation time. This modification transforms the heat conduction equation into a hyperbolic form, ensuring finite thermal propagation speed and providing a more accurate framework for describing rapid transient phenomena in elastic

and composite materials. The concept of thermal relaxation time—also referred to as thermal diffusion or impulse relaxation time—has since become central in contexts such as the selection of laser pulse durations.

Chandrasekharaiyah and co-workers^{64–66} have briefly reviewed this topic. Over the decades, the framework has been extended to multidimensional and anisotropic materials, demonstrating its versatility in modeling complex behaviors of nanostructures and porous media under extreme thermal and mechanical conditions.^{67–74}

Recent advances in thermoelasticity have explored nonlocal and fractional theories that incorporate long-range interactions and memory effects,⁶⁹ as well as advanced numerical techniques, such as finite element analysis, multiscale modeling, and normal-mode or harmonic methods,^{70,75,76} to analyze complex systems including multilayered and porous semiconductor structures. In addition, the Green–Naghdi theory of generalized thermoelasticity^{77–79} has been applied to predict the behavior of nanostructures both with⁸⁰ and without^{81,82} energy dissipation.

Among the various configurations, the thermoelastic response of thin membranes has attracted particular attention. For instance, Soranzio *et al.*⁸³ investigated transient grating dynamics in a bare Si membrane and a Si membrane with a MoS₂ ML transferred to the surface, as illustrated in Fig. 7(a).

The transient grating (TG) is a third-order non-linear optical technique, belonging to the class of four-wave mixing processes. In this method, two pulses of identical wavelength λ_0 (the pump beams) are overlapped, both temporally and spatially, on the sample at a crossing angle 2θ [see Fig. 7(b)]. For parallel polarizations, their interference produces a spatial modulation in light intensity with a periodicity given by

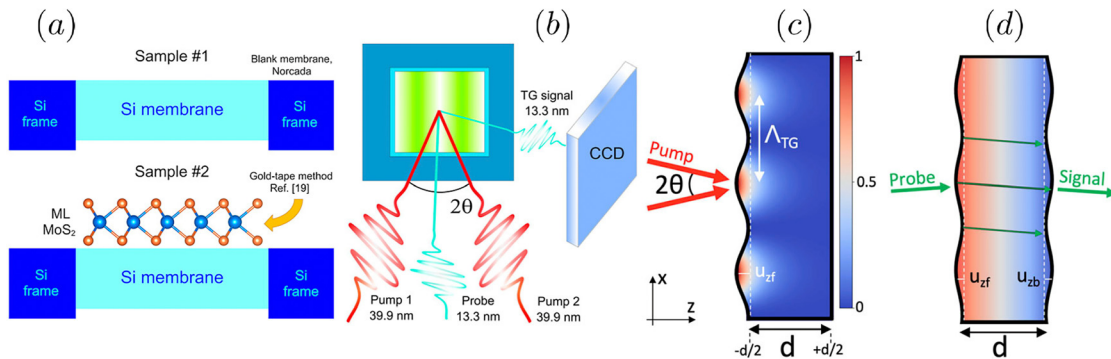


FIG. 7. (a) Samples: #1 a blank Si membrane and #2 MoS₂/Si membrane. (b) Scheme of the transient grating setup. (c) Schematic femtosecond extreme UV pulse excitation configuration. Two pump beams create an intensity grating with a period Λ_{TG} , resulting in an initial thermal gradient given by the sample absorption and causing thermal expansion that generates acoustic modes. (d) Sample after the pump pulse is passed. Heat propagates along a horizontal direction reaching the opposite end of the sample in about 5 ns. The thermoelastic response driven by the transient grating is probed by a third pulse, the probe, and detected in a forward diffraction geometry by a CCD shown in (b). Reprinted from Soranzio *et al.*, ACS Appl. Nano Mater. 7, 15317–15324 (2024),⁸³ licensed under a Creative Commons Attribution (CC BY) license.

$$\Lambda_{TG} = \frac{\lambda_0}{2 \sin \theta}, \quad (36)$$

as illustrated in Figs. 7(c) and 7(d). This periodic excitation pattern forms a transient diffraction grating within the material. A third pulse (the probe), with wavelength λ_{pr} and variable delay, is then diffracted by this grating, generating a fourth pulse, the signal beam. See Fig. 7(b) for a schematic representation.

The results in Fig. 8 reveal a pronounced difference in the surface thermoelastic responses of the two samples shown in Fig. 7(a). For the blank membrane, two acoustic modes with their overtones are sufficient to reproduce the transient grating signal in Fig. 8(a). The discrete Fourier transform of the residual signal (inset) is well described by the sums and differences of two frequencies, $f_1 \approx 102$ GHz and $f_2 \approx 60$ GHz—namely, $f_1 - f_2$, $2f_2$, $f_1 + f_2$, and $2f_1$. Similar multimode responses have been reported in other materials by Janušonis *et al.*,⁸⁴ Maznev *et al.*,⁸⁵ Brioschi *et al.*,⁸⁶ Foglia *et al.*,⁸⁷ Bencivenga *et al.*,^{88,89} and Fainozzi *et al.*⁹⁰ The two dominant acoustic modes correspond to the surface-skimming longitudinal wave at f_1 and the Rayleigh surface acoustic wave at f_2 , the latter involving elliptical displacements combining longitudinal and transverse motion.

The results in Fig. 8(b) show how a MoS₂ ML can significantly alter the near-surface response of the Si substrate. In sample #2, the relative contribution of the f_2 mode is enhanced, as shown in the inset. The MoS₂ ML almost completely suppresses the Rayleigh-type surface wave, characterized by elliptical motion localized underneath the Si surface, while the longitudinal wave, whose displacement is parallel to the surface, remains largely unaffected.

Finally, a slower decay of the non-oscillating background, typically associated with thermal transport,⁹¹ is observed beneath the periodic modulations due to the Si/MoS₂ coating of the membrane.⁸³ This way, the transient grating technique offers the nanoscale sensitivity and necessary temporal resolution to access the dynamics of the thermoelastic response in the picosecond timescale. In general, the use of ultrafast coherent extreme UV sources to generate spatially periodic nanoscale excitations and monitor their dynamics enables thermal transport measurements on the ~ 10 nm scale and provides a powerful

approach to investigate other nanoscale phenomena with non-trivial behavior.⁹¹

Kroonblawd *et al.*⁹² developed an approach to directly determine the thermal transport properties of explosive hot spots with realistic initial structures through the combination of molecular dynamics (MD) and diffusive heat equation modeling. Effective thermal conductivity is determined by fitting heat equation models to MD simulations of hot-spot relaxation over extended timescales. This approach is applied to the molecular crystalline explosive 1,3,5-triamino-2,4,6-trinitrobenzene (TATB), considering a range of shock strengths and two limiting impact orientations. TATB has a layered crystal structure composed of nearly planar sheets connected by a two-dimensional hydrogen-bonding network, where each molecule interacts with six neighbors through intermolecular hydrogen bonds between nitro and amino groups. Adjacent molecules from neighboring layers interact primarily through weak van der Waals forces. TATB is a prototypical energetic material, notable for its exceptional stability under high temperatures, shocks, and impacts.^{93,94} This makes TATB an ideal model system for investigating the thermal physics of hydrogen-bonded materials.

Figure 9 shows a prediction for the structure of a typical hot spot in TATB, which exhibits a range of sheared states^{95,96} interspersed with crystalline regions. The combined effect of plastically deformed regions and their boundaries may considerably reduce the apparent thermal conductivity from the values for the perfect crystal. It is not well understood whether continuum theories for heat transport, such as Fourier's heat law and the diffusive heat equation, hold for nanoscale explosive hot spots and generated shock heat waves. Another important aspect is the quantification of an effective thermal conductivity to describe nanoscale heat transport in explosives during shock initiation and detonation. The anisotropic thermal conductivity of TATB has been extensively characterized through MD simulations as a function of temperature and pressure. Under ambient conditions, κ along the N₍₁₀₀₎ direction within the molecular layers is 64% higher than that in the normal direction along N₍₀₀₁₎.⁹² Modeling estimates for the average phonon MFP in the perfect TATB crystal are on the order of a few nanometers or smaller,⁹⁷ which suggests that thermal relaxation of nanoscale hot spots may be primarily diffusive.

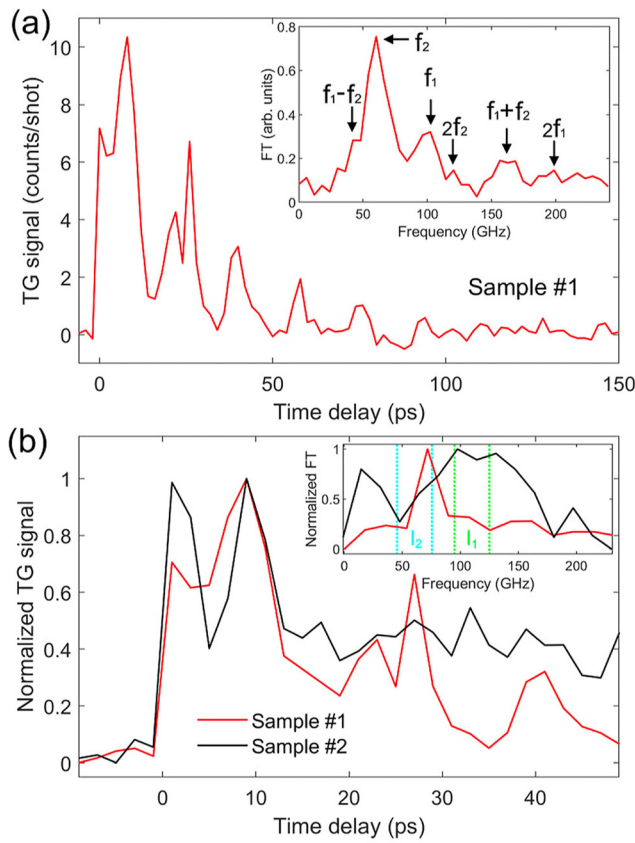


FIG. 8. (a) TG signal from the blank Si membrane (sample #1). Inset: the Fourier transform of the signal after subtracting an exponentially decaying background with ~ 160 ps window. (b) TG signal from the MoS_2/Si membrane (sample #2) compared to that in (a). Inset: the Fourier transform of the two signals after subtracting an exponentially decaying background with ~ 60 ps window. Reprinted from Soranzio *et al.*, ACS Appl. Nano Mater. 7, 15317–15324 (2024),⁸³ licensed under a Creative Commons Attribution (CC BY) license.

Non-reactive MD simulations offer direct predictions of hot spot formation and relaxation, inherently accounting for all mechanical heat generation processes and ballistic transport effects within the classical framework of phonon populations and heat capacity. The initial hot spot structures are sampled by simulations of pore collapse in TATB with two carefully chosen orientations that provide upper and lower bounds for κ anisotropy relative to normal conditions. Kroonblawd *et al.*⁹² showed that, despite significant simplifications, diffusive heat equation models can capture the thermal physics of nanoscale explosive hot spots with surprising accuracy.

Heat maps of the MD and heat equation model temperature profiles (T_{MD} and T_{HEq} , respectively) are shown in Fig. 10 at early and late times after impact, along with the difference between them ($T_{MD} - T_{HEq}$). Both qualitative trends and substantial quantitative agreement are observed between the MD predictions and the heat equation models. At 50 ps, the heat equation model underestimates the MD temperatures at the hot-spot core ($T_{MD} - T_{HEq} > 0$) but overestimates them just outside the core ($T_{MD} - T_{HEq} < 0$). By 1000 ps,

these discrepancies are significantly reduced across all regions. Temperature-difference maps reveal that early-time transport in MD is slower than predicted by the globally fitted conductivity. For crystalline TATB, the effective phonon MFP is only a few nanometers,⁹⁷ suggesting that Fourier heat transfer should remain valid even at the nanoscale. However, conductivities obtained from hot-spot relaxation simulations often approach limiting liquid-state values, reflecting the highly disordered nature of sheared TATB in and around the hot-spot core.^{96,98} Overall, TATB conductivity spans a broad range (0.2–1.6 W m⁻¹ K⁻¹) across different density states.⁹² Since the density near a collapsed pore depends strongly on loading orientation and shock strength, this disorder likely contributes to the relative success of isotropic heat transfer models in describing hot spots.

D. Nanoscale heat transfer

At micro- and nanoscales, the sample size becomes comparable to the phonon mean free path (Λ), leading to the breakdown of purely diffusive transport. At these length scales, the deviation from the Fourier law gives rise to a variety of non-diffusive phenomena.^{99,100} In low-dimensional materials, non-Fourier heat conduction can be classified basically into two regimes: (i) Casimir–Knudsen regime and (ii) Coherent transport, quantization, and localization. In the Casimir–Knudsen regime, the phonon mean free path Λ is comparable to or larger than the sample dimensions, phonons scatter mainly with the boundaries instead of internally, and the transport becomes ballistic or quasi-ballistic. A Knudsen number $Kn = \Lambda/d > 1$, where d specifies the sample dimensions, characterizes this regime. The thermal conductivity is reduced with respect to the bulk and can exhibit a strong anisotropy.

Phonons exhibit both particle-like and wave-like behavior. Their particle-like nature is evident in scattering processes, while their wave-like character is demonstrated, for instance, by the folding of acoustic phonons in a superlattice (SL). The imposed periodicity of the SL creates mini-Brillouin zones, where phonons are folded back into the reduced zone. This folding modifies phonon group velocities and, consequently, heat transport. Moreover, the emergence of a phonon bandgap arises from wave interference effects.¹⁰¹ To preserve phonon coherence, however, interfaces must be nearly perfect to ensure specular reflection.

At very low temperatures, the heat conductance can be quantized. The quantum of thermal conductance (QTC) is given by the expression:¹⁰²

$$G_0 = \frac{\pi^2 k_B^2 T}{3h} \quad (37)$$

per transport channel, where k_B is the Boltzmann constant and h is the Plank constant. To experimentally observe the quantization, several conditions must be satisfied: (i) the transport must be quasi one dimensional (nanowires, CNTs, GNRs); (ii) the transport must be ballistic, i.e., without scattering; (iii) the system must be at very low temperatures (typically below 1 K) where only a few acoustic phonons can be excited and the presence of optical phonons is completely negligible; and (iv) a nearly perfect thermal isolation is needed. In the work of Polanco *et al.*,¹⁰² there is an interesting discussion on the measurements and the different theoretical approaches. The first observation of the QTC was provided by Schwab *et al.*¹⁰³ Zhang¹⁰⁴ *et al.* studied the phonon transport in SiGe NWs as a function of the Ge content

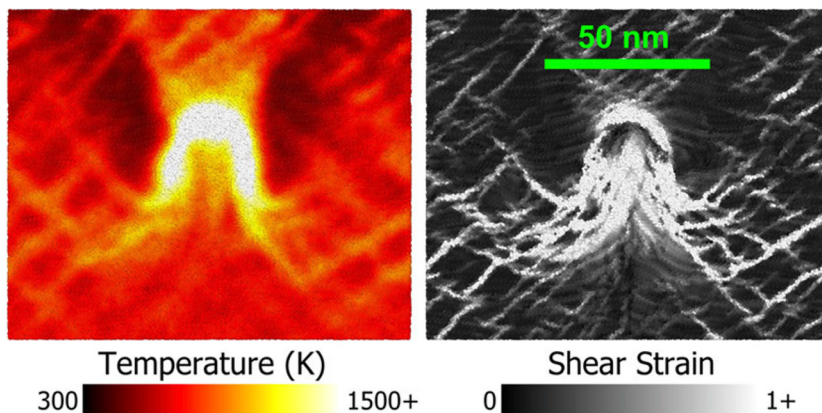


FIG. 9. Computed temperature and shear strain distributions of a TATB hot spot formed from shock-induced pore collapse. The shear strain is unitless and should be interpreted qualitatively as a precise numerical value depending on parameters in the analysis. The hot spot was generated for a shock aligned with the (001) crystal face normal vector $N_{(001)}$ with a 2.0 km s^{-1} impact speed. Reprinted from Kroonblawd *et al.*, J. Phys. Chem. C **125**, 20570–20582 (2021).⁹² Copyright 2021, with permission from American Chemical Society.

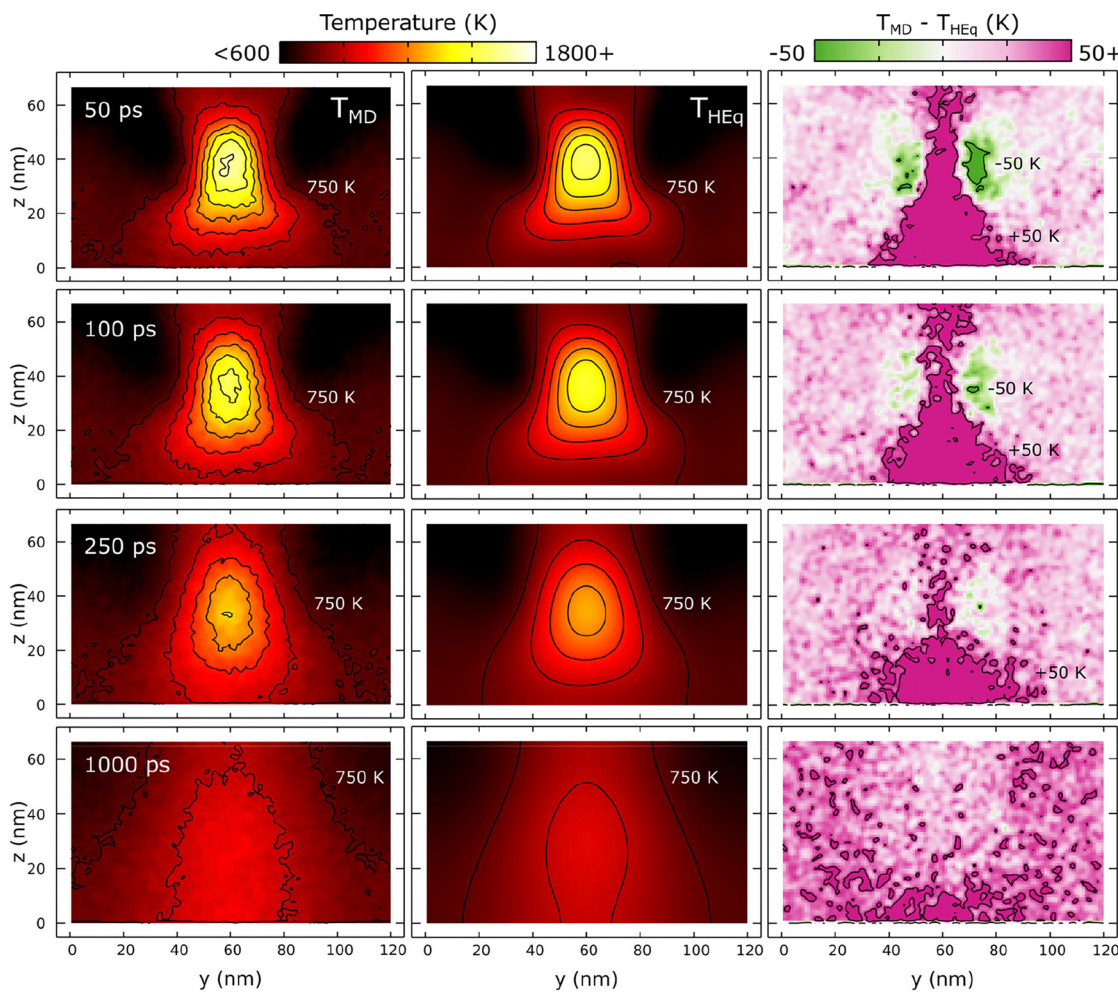


FIG. 10. Comparison of temperature profiles from MD and an isotropic fitted heat equation (HEq) model for the case with $N_{(001)}$ and 2.0 km s^{-1} impact speed. Columns include the MD temperature profile T_{MD} (left), the HEq temperature profile T_{HEq} (middle), and the difference between MD and HEq profiles $T_{MD} - T_{HEq}$ (right). Results at 50, 100, 250, and 1000 ps after impact are, respectively, shown in the rows from top to bottom. Contours are drawn in 150 K increments starting at 750 K for both T_{MD} and T_{HEq} . Reprinted from Kroonblawd *et al.*, J. Phys. Chem. C **125**, 20570–20582 (2021).⁹² Copyright 2021, with permission from American Chemical Society.

and frequency. At low frequencies, $\text{Si}_{1-x}\text{Ge}_x$ NWs exhibit ballistic transport. As the Ge content increases, the range of ballistic transport extends up to frequencies approaching 1 THz. At high frequencies, however, the exponential decay of the transmission indicates Anderson localization, leading to a sharp reduction of the thermal conductivity.

In metals, heat is primarily transported by electrons, while in semiconductors and insulators, phonons are responsible for heat transport. In the framework of the simple kinetic theory of gases, the ability of solids to conduct heat can be expressed as

$$\kappa = \frac{1}{3} C v \Lambda, \quad (38)$$

where v is the average velocity of phonons (or electrons) and Λ is their mean free path, defined as the average traveling distance between two scattering events.

In non-metallic solids, when the characteristic system size is much larger than the phonon mean free path, heat transfer occurs in the macroscopic diffusive regime, where the classical heat diffusion equation provides an accurate description.¹⁵ When the system size becomes comparable to Λ , phonon ballistic transport—commonly known as the classical size effect—emerges, and the Boltzmann transport equation (BTE) is required to capture the underlying physics. As the system size further approaches the phonon wavelength, the wave nature of phonons must be explicitly accounted for.⁴¹

Another source of size-dependent effects is the presence of interfacial thermal resistance—commonly termed as thermal boundary resistance (TBR) or Kapitza resistance. When phonons scatter across the interface, a temperature discontinuity arises, giving rise to interfacial thermal resistance. Notice that the interfacial thermal resistance exists even at atomically perfect contacts and should be distinguished from contact resistance coming from imperfect physical contact (roughness or disorder at the interface). Typical values of interfacial thermal resistance range from 10^{-9} to $10^{-6} \text{ m}^2 \text{K W}^{-1}$.¹⁰⁵ While this resistance is often negligible at microscopic scales, it becomes important when interfaces become densely packed, with separation from nanometers to micrometers.¹⁰⁶

Based on the phonon BTE, within the single-mode relaxation time approximation, the thermal conductivity is given by¹⁵

$$\begin{aligned} \kappa &= \frac{1}{3(2\pi)^3} \sum_{\nu} \int C_{k\nu}(T) v_{g,k\nu}^2 \tau_{k\nu}(T) d\mathbf{k} \\ &= \frac{1}{3(2\pi)^3} \sum_{\nu} \int C_{k\nu}(T) v_{g,k\nu} \Lambda_{k\nu}(T) d\mathbf{k}, \end{aligned} \quad (39)$$

where $v_g = \nabla_{\mathbf{k}}\omega_0$ is the phonon group velocity with angular frequency ω_0 , τ is the lifetime of the phonon ($k\nu$), \mathbf{k} the phonon wave vector, and $\Lambda_{k\nu} = v_{g,k\nu} \tau_{k\nu}$. The summation is over all phonon branches ν in the first Brillouin zone. The phonon-specific heat C for each mode is computed according to the Bose–Einstein distribution as

$$C = k_B \left(\frac{\hbar\omega_0}{k_B T} \right)^2 \frac{e^{\hbar\omega_0/k_B T}}{(e^{\hbar\omega_0/k_B T} - 1)^2}, \quad (40)$$

where \hbar is the reduced Planck constant. κ is obtained from Eq. (39) by summing over all phonon modes and integrating across the Brillouin zone along the direction of interest. Consequently, κ is governed by the phonon dispersion relations, which are inherently determined by

the crystal structure and its corresponding space group. The integrand in Eq. (39) consists of a product of the specific heat, the group velocity squared, and the lifetime defined for each branch of the phonon motion signified by the dispersion spectrum.

The phonon properties C , v_g , and τ , which feature in Eq. (39), can be determined theoretically. The total lattice energy is given by the Taylor series expansion of atomic displacement components u_i as

$$U \approx U_0 + \frac{1}{2!} \sum_{ij} \Phi_{ij} u_i u_j + \frac{1}{3!} \sum_{ijk} \Phi_{ijk} u_i u_j u_k, \quad (41)$$

where Φ_{ij} and Φ_{ijk} are the harmonic and third-order force constants, respectively. Using the harmonic force constants, the phonon dispersion relation can be calculated, from which the group velocity and specific heat are obtained. The impact of the third-order term on the specific heat and the group velocity of phonons is usually small; however, it dominates phonon–phonon scattering, and anharmonic force constants can be used to evaluate phonon–phonon relaxation times using Fermi’s golden rule.

At the nanoscale, heat conduction can be effectively tuned by modifying τ . However, achieving such control is inherently difficult, as the dominant thermal phonons usually have very short wavelengths, which makes them highly susceptible to scattering events. This challenge has attracted considerable attention, especially with recent advances in nanostructured and compositionally graded thermoelectric materials. Some aspects of this manipulation in nanophononic crystals are illustrated in Fig. 11. These nanostructures can be classified as 1D crystals, where periodic property variations occur along a single axis [Fig. 11(a)], 2D nanostructures [Fig. 11(b)], or 3D structures [Fig. 11(c)]. The resulting interference of phonon waves can lead to remarkable phenomena such as Brillouin zone folding and bandgap opening, which are absent in bulk materials. In the 1D case, the thermal conductivity of a W/Al₂O₃ SL is approximately four times lower than the simple series average of the conductivities of tungsten and alumina.¹⁰⁷ The minimum in thermal conductivity observed in Fig. 11(a) marks the transition from diffusive to coherent phonon transport. As the temperature decreases, this minimum shifts to lower values and coincides with a reduction in the number of interfaces, supporting the idea that coherent wave effects play a significant role.¹⁰⁸ In 2D, κ remains substantially lower than that of the corresponding bulk materials over a broad temperature range from 0.1 to 300 K.¹⁰⁹ As shown in Fig. 11(b), the low-temperature data closely follow the theoretical predictions represented by the solid and dashed curves.¹⁰⁹ In 3D, silicon crystals with embedded pores exhibit exceptionally low thermal conductivity, as illustrated in Fig. 11(c). Finally, Fig. 10(d) presents results for membranes patterned with single- and double-sided pillars, where the thermal conductivity is reduced by nearly two orders of magnitude compared to a uniform membrane of the same thickness.

Both phonon interference and diffusive scattering can lead to a reduction in thermal conductivity κ . In the case of interference, this reduction arises from a decrease in the group velocity v_g caused by band flattening in the phonon dispersion. For diffusive scattering, the decrease in κ is instead attributed to the limited mean free path and lifetime of phonons.⁵

Periodic pillars embedded in a host material can act as local resonators, introducing additional flat branches in the phonon dispersion at their characteristic resonance frequencies [see Fig. 11(d)]. Coupling

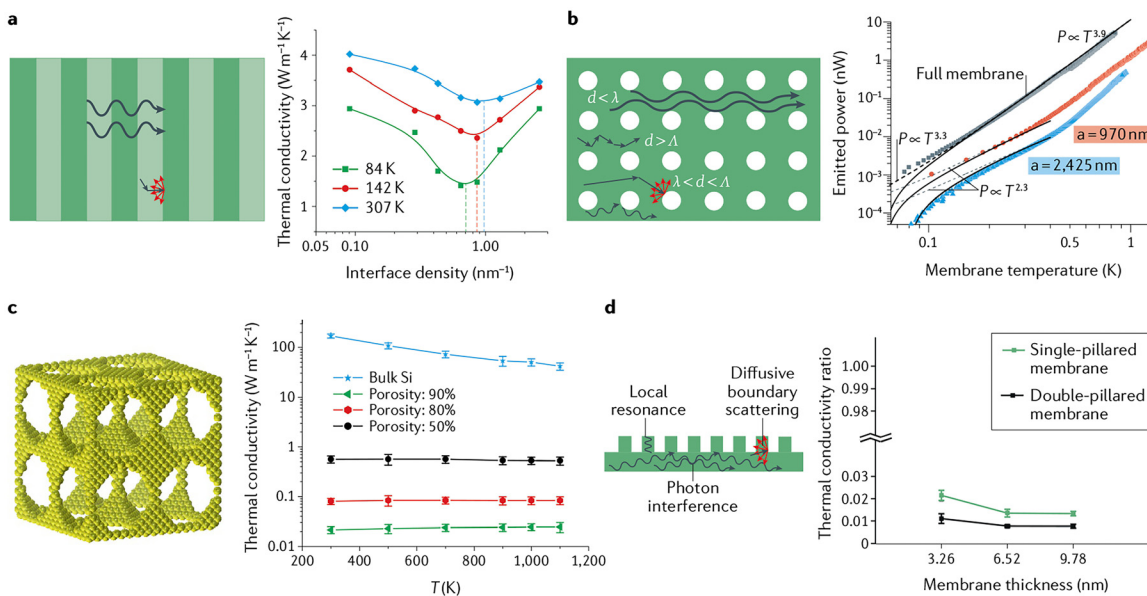


FIG. 11. Microscopic description of heat conduction. (a) Coherent (wavy lines) and diffusive (straight lines) phonon scattering in 1D SLs (left). Measured κ in $(\text{SrTiO}_3)_n/(\text{CaTiO}_3)_n$ SLs as a function of the interface density at different temperatures (right). (b) The different regimes of phonon transport in the 2D case depend on the relationship between the phonon wavelength λ , phonon MFP Λ , and periodicity d (left). Measured emitted phonon power vs temperature (right). The squares indicate data for the full membrane, whereas the circles and triangles for two square nanophononic crystals with a periodicity of 970 and 2425 nm, respectively. (c) Thermal conductivity of 3D bulk and porous Si as a function of temperature. (d) Schematic sketch of the three mechanisms that induce a reduction in κ in pillar-based nanostructures (left). Pillared membranes exhibit extremely low thermal conductivities (right). Reprinted from Li *et al.*, Nat. Rev. Mater. **6**, 488 (2021).⁵ Copyright 2021, with permission from Springer Nature.

20 December 2025, 13:48:09

between local resonances and the underlying vibrational modes eliminates dispersion crossings, thereby opening bandgaps and flattening phonon branches near the resonance frequencies. This effect reduces the group velocity, v_g , and consequently suppresses the thermal conductivity, κ .¹¹⁰

More advanced studies of pillar-based structures are needed, with the focus on identifying the mechanism behind the observed reduction in thermal conductivity. Experimentally disentangling the effects of local resonances, phonon interference, and diffusive scattering remains challenging. Moreover, a growing body of literature indicates that, owing to the short wavelengths of thermal phonons, even subtle variations in surface structure or geometry can alter phonon coherence lengths, potentially accounting for inconsistencies in experimental observations. Hence, directly detecting the phonon coherence length can provide a more accurate evaluation of the underlying mechanisms. Finally, due to the coupling between longitudinal and transverse modes, an additional resonance mechanism has been reported to reduce heat conduction in core-shell nanowires.^{101,111} The factors governing phonon transport in pillar-based structures are similarly applicable to other low-dimensional multiphase systems.

E. Non-reciprocal heat transport

Recently, asymmetric quantum heat transfer has been realized by manipulating charge-carrier scattering, arising from both phonons and electrons, particularly, in nanoscale systems.^{112–115} This phenomenon offers great potential for achieving ultrahigh thermal rectification, thereby enabling advances in micro/nanoelectronic thermal management^{116,117} and in source-free thermal computing architectures.^{118,119}

At the nanoscale, carriers can propagate along nearly straight trajectories, giving rise to ballistic transport,^{120–122} a behavior that sharply contrasts with the diffusive observed in macroscopic systems. At larger length scales, carriers undergo inevitably multiple scattering events, such as the scattering by defects, Umklapp scattering, and others, that drive heat transport back into the disordered diffusive regime, therefore suppressing non-reciprocal effects. Nevertheless, achieving efficient and robust non-reciprocal heat transfer across a broad temperature range remains an open challenge.¹²³

Non-reciprocal heat transport in uniform systems has recently attracted significant research attention, since most existing theories address the diffusive regime. Zhou *et al.*¹²⁴ recently demonstrated a mechanism for nonreciprocal charge transport in the ballistic regime, driven by band structure asymmetry. The band asymmetry generates unequal Coulomb potentials when the bias voltage imposed by the electrodes is reversed. Consequently, the energy bands shift differently depending on the current direction, leading to pronounced nonreciprocal behavior.

Inspired by the transformative role of electric diodes in modern electronics, extensive research has been devoted to achieving rectification across diverse transport processes, including charge, mass, and heat flow.^{118,125} Among these, thermal rectification has drawn particular interest. It refers to a diode-like effect in which the heat current depends asymmetrically on the direction of the applied temperature bias: large in one orientation and suppressed in the reverse. Ideally, a thermal rectifier would exhibit strongly directional transport, acting as a good conductor in one direction while functioning as an effective insulator in the other. Such behavior promises substantial technological impact. For example, thermal rectification could provide a key

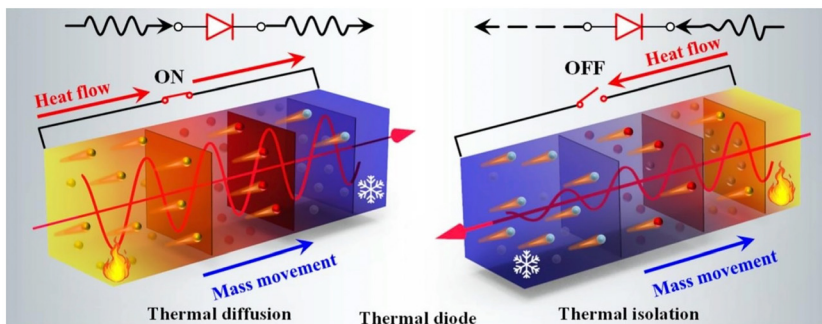


FIG. 12. Schematic of nonreciprocal heat transfer via mass flow. When the heat flow is aligned with the mass movement (left), heat transfer is enhanced and the thermal diode remains “on.” When the heat flow opposes the mass movement (right), heat transfer is suppressed and the diode turns “off.” Reprinted from Zhang *et al.*, Chem. Eng. J. **522**, 167537 (2025);¹²³ licensed under a Creative Commons Attribution (CC BY) license.

strategy for managing heat in miniaturized electronic devices, where conventional cooling methods become increasingly inadequate as chip dimensions shrink. Beyond thermal management, it also opens the possibility of autonomous, heat-driven computing architectures that may complement—or under certain conditions, even substitute—traditional electronic systems.

An illustrative concept of thermal rectification, reviewed by Zhang *et al.*,¹²³ is presented in Fig. 12. By designing heterogeneous metamaterials with regions of positive and negative thermal expansion, the authors introduced directed mass transport that breaks spatial inversion symmetry in the distribution of thermal properties. This asymmetry gives rise to nonuniform variations in key thermal parameters—such as heat capacity and thermal conductivity—across the material. Consequently, the conventional reciprocity between heat flux and temperature gradient, as prescribed by Fourier’s law, no longer holds strictly. Instead, the system acquires a directional dependence in its thermal response, functioning analogously to an electronic diode but for heat transport. To further strengthen this analogy, Zhang *et al.* establish a theoretical correspondence between the built-in electric field of semiconductor junctions and the directed mass field emerging in thermal metamaterials, thereby offering a unified framework for understanding non-reciprocal heat transport.

A large body of theoretical and experimental studies has predicted or demonstrated the occurrence of thermal rectification in both bulk and nanoscale systems, the majority of which involve either heterojunctions or compositionally graded structures.^{125–128} In bilayer systems, the observed thermal rectification has generally been attributed to differences in the temperature dependence of the thermal conductivity between the two dissimilar materials.^{129,130} At interfaces, the effect is often interpreted in terms of asymmetric phonon spectra mismatch when the direction of the applied temperature bias is reversed.¹³¹ Another contributing factor is phonon localization effects.^{132,133} Theoretical studies in recent years have further suggested that asymmetric pristine carbon nanostructures can exhibit thermal rectification.^{132,134,135} These systems, composed of a single material, are particularly appealing due to their structural simplicity and inherently high thermal conductance.

Wang *et al.*¹²⁸ investigated various asymmetric nanostructures—including nonuniform nanowires, thin films, and quantum dots, as illustrated in Fig. 13—which can exhibit thermal rectification when operating in the phonon confinement regime, i.e., when the lateral dimension is sufficiently small compared to the MFP. Their theoretical analysis demonstrated that phonon lateral confinement is the fundamental origin of rectification in such asymmetric homogeneous

materials. This confinement gives rise to three interconnected rectification mechanisms: phonon spectra overlap, the inseparable dependence of thermal conductivity on temperature and position, and phonon edge localization.

In parallel with these theoretical advances, significant experimental efforts have been pursued over the past decade. A notable study by Tian *et al.*¹³⁶ reported thermal rectification in large-area reduced GRO, attributing the effect primarily to asymmetric geometry. This interpretation was later challenged by Wang *et al.*,¹²⁸ who highlighted the critical influence of factors such as defects, interfacial properties, and structural inhomogeneities. Since then, numerous investigations have examined different aspects of non-reciprocal heat transport, collectively shaping our understanding of thermal rectification.

Wang *et al.*¹¹³ experimentally demonstrated thermal rectification in ML GR by introducing structural asymmetry through three approaches: nanopores patterned on one side, asymmetric nanoparticle deposition, and tapered geometries. The GR samples with

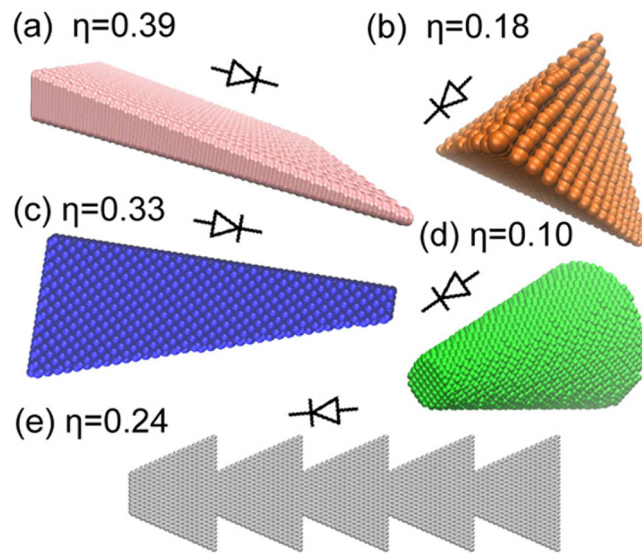


FIG. 13. Schematics of homogeneous nanostructure thermal rectifiers: thin films (a) and (c), quantum dots (b), and nanowires (d) with geometric asymmetry; (e) graphene-based rectifier series with smooth edges. Rectification factors η are obtained with the optimized Tersoff potential at 300 K and $\Delta T = 90$ K. Reprinted from Wang *et al.*, Nano Lett. **14**, 592–596 (2014).¹²⁸ Copyright 2014, with permission from American Chemical Society.

engineered asymmetry are shown in Fig. 14. Using FIB modification, three ML samples (#1–3) were patterned with nanopores of different sizes and densities: sample #1 contained 14 nanopores (~ 100 nm in diameter), sample #2 had six nanopores (~ 200 nm), and sample #3 included three nanopores (~ 400 nm).

The experimental results of the thermal conductivity of the samples are shown in Fig. 15. In pristine ML GR, no thermal rectification was observed, as the thermal conductivities measured in opposite heat-flow directions (solid and open symbols) differed by less than 2%. After patterning through nanopore drilling on one side of the samples, a clear directional dependence emerged. Specifically, the thermal conductivity in the direction from the nanopore-patterned region to the pore-free region (solid symbols) was consistently higher than that measured in the reverse direction (open symbols). The preferred direction of heat flow corresponding to the higher conductivity is illustrated by the red arrows in Fig. 14. The average rectification factor was approximately 26%, which is substantially higher than the experimental uncertainty of $\sim 5\%$. These results suggest that suspended ML GR provides a compelling route toward the design of 2D thermal rectifiers, offering prospects for autonomous heat-flow regulation and improved energy-harvesting efficiency. There are also theoretical proposals that exploit thermal rectification to enable independent control of forward and backward heat fluxes. Thus, the theoretical work by Wu *et al.*¹³⁷ on a 3D hybrid structure composed of GR and BN nanotubes (GR-BNNTs) provided an interesting perspective on the field and advances the understanding of phonon transport mechanisms in columnar hybrid structures.

As shown schematically in Fig. 16, the lattice mismatch GR and BN systems is minimal, allowing for almost seamless structural integration. However, when combined with GR-BNNT hybrids, this structural compatibility does not translate easily into efficient thermal transport. Instead, the substantial mismatch in their phonon spectra imposes a serious limitation as it hinders effective phonon coupling

across the interface and consequently leads to a marked reduction in the overall thermal conductivity of the hybrid material. Notably, this spectral mismatch can create favorable conditions for the emergence of thermal rectification. In contrast to previous investigations on CNT–GR hybrids,¹³⁷ the present study uncovers a distinctive regulation mechanism that allows forward and backward heat fluxes in thermal rectification to be controlled independently. Specifically, modulation of phonon transport within the interlayer BNNTs primarily governs the forward heat flux, exerting only a negligible influence on the backward flux. Conversely, adjustments to phonon transport in the underlying GR layers predominantly determine the backward heat flux, with little effect on the forward direction. This decoupled behavior highlights the complementary roles of BNNTs and GR in shaping directional heat transport, providing new insight into the design of hybrid nanostructures with tunable rectification characteristics.

The interlayer BNNTs exhibit remarkable capability in suppressing the backward heat flux from penetrating into the upper GR layer through the interlayer connector. This property provides an attractive means of decoupling and independently regulating the forward and backward heat transport channels. As shown in Fig. 17(a), the heat flux exchanged between the green and red cuboid regions is denoted as q_T , while that between the blue and red cuboid regions is labeled as q_B . To further probe these transport pathways, the spectral thermal conductivities of the interlayer BNNTs and the underlying GR regions under forward heat flux are displayed in Figs. 17(b) and 17(c). The results demonstrate that the phonons associated with q_T can effectively propagate from the hot bath in the upper GR layer, traverse the interlayer BNNTs and reach the cold bath in the bottom GR layer. In contrast, phonons excited by q_B largely avoid the BNNT connector, instead traveling directly along the bottom GR layer to the cold bath. This distinction highlights how the BNNTs interlayer selectively mediates phonon transport, thereby enabling an independent route to control forward vs backward heat fluxes.

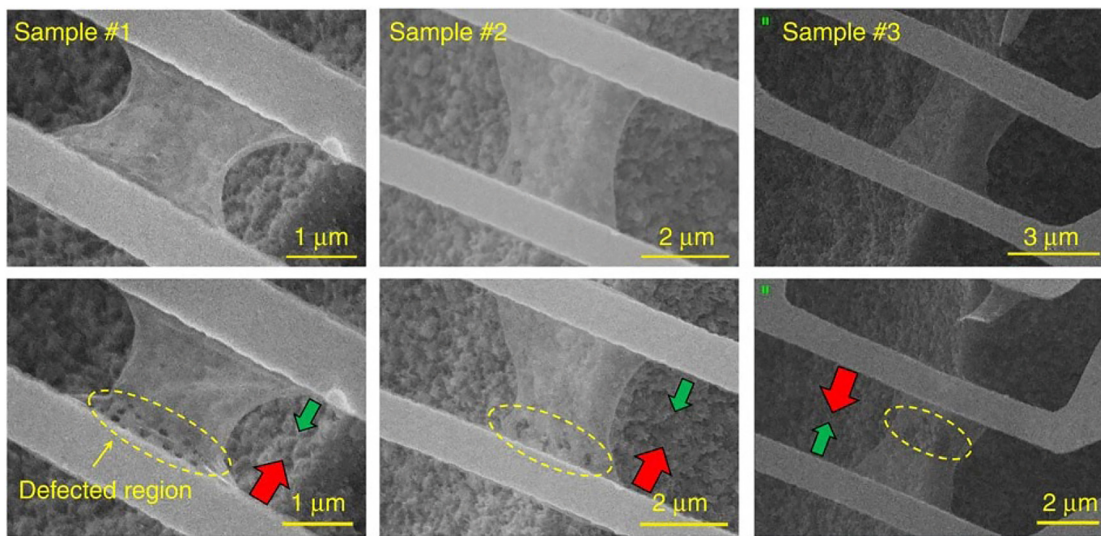


FIG. 14. SEM images of GR before and after FIB nanopore patterning (yellow dashed circles) in samples #1–3. Thermal conductivity was measured along opposite directions, with large red arrows showing the higher-conductivity direction and small green arrows the lower one. Reprinted from Wang *et al.*, Nat. Commun. **8**, 15843 (2017);¹¹³ licensed under a Creative Commons Attribution (CC BY) license.

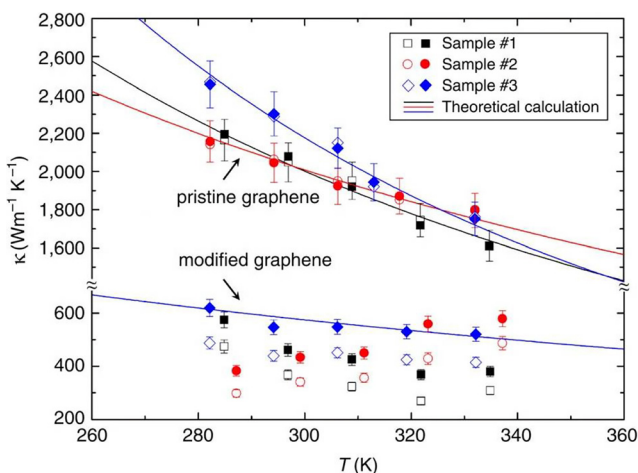


FIG. 15. Thermal conductivity of pristine and nanopore-patterned graphene. Pristine graphene showed nearly identical values in opposite directions (solid and open symbols). After nanopore patterning, the conductivity was higher from the nanopore side toward the pore-free side (solid symbols), generating rectification factors of 28%, 26%, and 25% for samples #1–3, respectively. Solid lines denote the predictions of the lattice dynamics model. Reprinted from Wang *et al.*, Nat. Commun. **8**, 15843 (2017);¹¹³ licensed under a Creative Commons Attribution (CC BY) license.

The work by Ma and Tian¹²² provided an interesting perspective of the field, giving an in-depth theoretical description of thermal rectification in tapered bottlebrush polymer chains shown in Fig. 18. They incorporate side chains with systematically varied molecular weights, forming a cone-like asymmetric macromolecule at the nanoscale.^{138,139} Using large-scale MD simulations, Ma and Tian investigated heat transport in these structures along opposite directions, defining the forward direction as heat flow from the wide end to the narrow end, and the backward direction as the reverse. The simulations revealed an unconventional rectification behavior in which the backward direction supported a larger heat flux than the forward direction. This counter-intuitive effect was attributed to the presence of a structural disorder gradient along the molecule, which induces nonlinear heat transfer. Furthermore, they reported a pronounced length dependence of the

rectification ratio, as illustrated in Fig. 19(a). The analysis uncovered a new transport mechanism: thermal transport remained diffusive in the forward direction but progressively transitioned to ballistic transport in the backward direction as the system length increased.

At short lengths ($l < 10$ nm), the thermal conductivities in both directions were nearly identical, resulting in a negligible rectification ratio $\eta \approx 0$ in Fig. 19(a) because structural asymmetry was minimal. In this regime, κ remained constant in both directions, characteristic of purely diffusive transport. As l increased, however, the structural asymmetry became more pronounced, giving rise to a markedly different length dependence of κ [see Fig. 19(b)]. While the forward-direction thermal conductivity, κ^+ , remained nearly unchanged with length, the backward-direction conductivity, κ^- , increased steadily, providing direct evidence for the coexistence of diffusive and ballistic transport. This behavior indicates a transition from diffusive-dominated conduction at short lengths to ballistic-dominated conduction in the backward direction at longer lengths. When l is small, the ballistic contribution is masked by diffusive scattering, but as l increases, ballistic transport becomes predominant, consistent with the length-dependent rise in κ^- .

The tunability of bottlebrush polymer architectures thus provides a unique platform for probing the interplay of diffusive and ballistic heat transport within a single molecular system. Moreover, this structural flexibility offers opportunities to actively engineer and control heat flow at the molecular scale, opening new avenues for thermal management and nanoscale phononics.

F. Simulating heat transfer

Simulations of nanoscale thermal properties can be broadly classified into two categories: (i) continuum simulations and (ii) atomistic simulations. The continuum approach includes the direct solution of the wave equation and BTE. By treating phonons as acoustic waves with linear dispersion relations and neglecting nonlinearity and phonon–phonon scattering,¹⁵ the continuum approach offers a highly simplified theoretical framework. Since phonons have a broad wavelength spectrum, exhibit nonlinear dispersion relations, and phonon–phonon scattering cannot be neglected, the wave equation is rarely used to describe phonon transport.¹⁴⁰ In contrast, the BTE, which is based on particle dynamics and neglects wave effects,¹⁴¹ is widely employed to

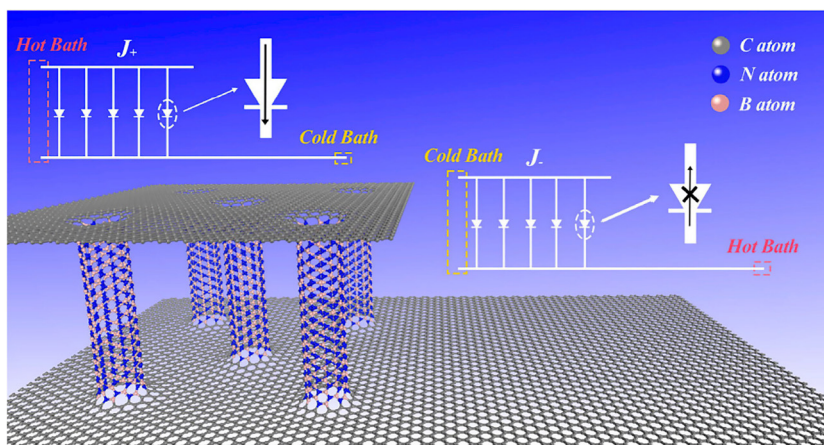


FIG. 16. Schematic illustration of the GR-BNNT architecture demonstrating the thermal rectification phenomenon. Reprinted from Wu *et al.*, ACS Appl. Mater. Interfaces **16**, 42660–42673 (2024).¹³⁷ Copyright 2024, with permission from American Chemical Society.

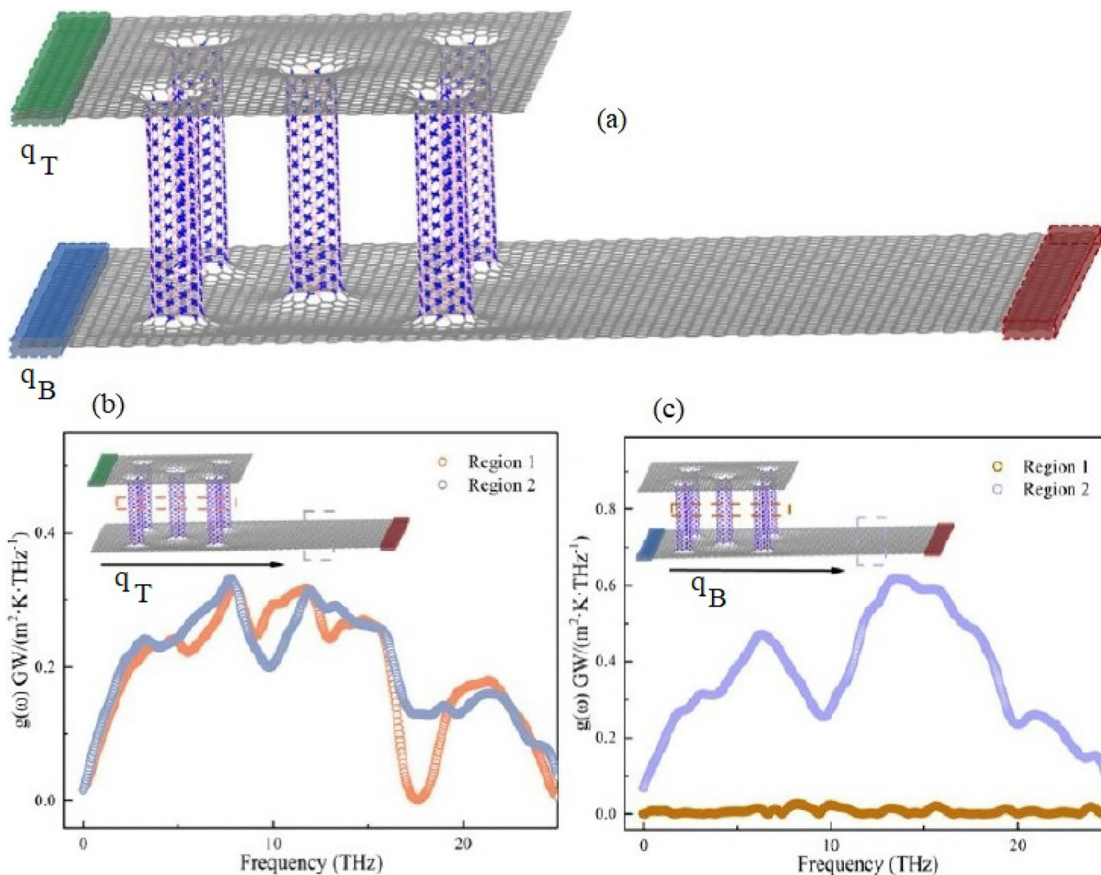


FIG. 17. (a) Schematic illustration of the heat bath configuration that generates the heat fluxes q_T and q_B in GR-BNNTs. (b) and (c) Spectral thermal conductivities of the GR-BNNTs under q_T and q_B conditions, showing contributions from the BNNTs and the underlying GR. Region 1 corresponds to the upper GR area at the hybrid interface, whereas Region 2 represents the molecular junctions where the BNNTs are connected to the GR layer. Reprinted from Wu et al., ACS Appl. Mater. Interfaces **16**, 42660–42673 (2024).¹³⁷ Copyright 2024, with permission from American Chemical Society.

20 December 2025, 13:48:09

simulate mesoscopic conduction processes due to its effectiveness in describing transport and scattering of energy carriers in solids.¹⁴²

Assuming phonons do not interact with external forces and that no source term is present, the phonon BTE can be written as

$$\frac{\partial n}{\partial t} + v_g \cdot \nabla n = \left(\frac{\partial n}{\partial t} \right)_s, \quad (42)$$

where n is the phonon distribution function, t is the time, and $(\partial n / \partial t)_s = \tau_s^{-1}$ denotes the scattering rates, with τ_s being the phonon relaxation time. To solve this equation, boundary and interface conditions are used to model the phonon-boundary scattering. Once the distribution function is obtained by solving the BTE, the temperature distribution and heat flux can be extracted. In principle, the BTE is not limited by the size of the simulation domain, provided that each discretized element contains enough particles to properly define the distribution function $n(r, p, t)$, which depends on the phonon position r , momentum p , and time t . The solution of BTE converges to the macroscopic heat diffusion equation when the simulation domain is much larger than the phonon MFP. Therefore, BTE is usually applied for

systems larger than the atomic scale, but not reaching the diffusion regime.

In contrast, atomistic simulations treat the atomic structures of materials, including interfacial structures, with high accuracy. Key computational approaches including molecular dynamics (MD) simulations, lattice dynamics simulations, and non-equilibrium Green's function (NEGF) formalism have been used to describe thermal conductivity. MD simulation uses a system typically composed of several thousands of atoms with a given interatomic potential. Atomic motion is governed by simple Newton law equations of motion and follows Maxwell-Boltzmann classical statistics, limiting MD methods to $T > \Theta_D/3$,¹⁴³ Θ_D being the Debye temperature. Two main approaches, nonequilibrium MD (NEMD) and equilibrium MD (EMD), are used.^{144–147} NEMD is typically characterized by hot and cold thermal reservoirs on either side of the simulation cell. The temperature is calculated over the length between the heat source and the sink, and the interfacial temperature drop is extracted. EMD can be used to determine thermal properties by looking at fluctuations of atomic energy around the equilibrium. Both techniques are relatively

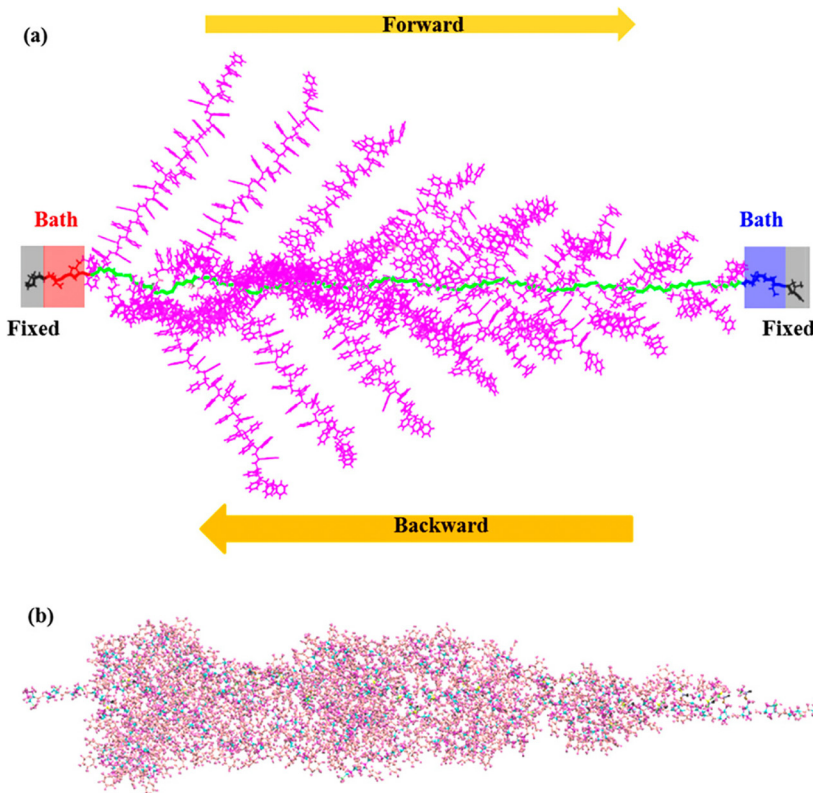


FIG. 18. (a) Optimized structure of a tapered bottlebrush polymer device with heat baths and fixed ends prior to MD simulations. The backbone is shown in green, side chains in pink, heat baths in red and blue (40 atoms each), and fixed boundaries in black. Yellow arrows indicate heat flux directions. (b) Snapshot of the same device during MD simulations. Reprinted from Ma and Tian, *Nano Lett.* **18**, 43–48 (2018).¹²² Copyright 2018, with permission from American Chemical Society.

simple to implement and require many time steps to ensure the system is thermalized.

Computational methods, including lattice dynamics, use force constants given by Eq. (41) from empirical force fields or first-principles calculations. In recent years, lattice dynamics with input from atomistic models, especially density functional theory (DFT) calculations, has significantly improved the accuracy of predicted phonon properties and thermal conductivity of materials.^{148–151}

The NEGF approach is an efficient tool for calculating the phonon transmission coefficient, particularly when elastic scattering dominates the transport process. NEGF is especially powerful for investigating heat conduction in interfaces and nanostructures, making it useful for exploring phonon transport in the quasi-ballistic regime. It has been successfully applied to low-dimensional materials, interfaces between dissimilar materials, and multilayer structures, and the dependence of the detailed atomic configurations on the phonon transmission and thermal conductance across these structures has been investigated. The implementation of mode-decomposed phonon transmission makes it possible to integrate NEGF with BTE-based methods to model phonon transport in more complicated nanostructures.

The NEGF approach models vibrational energy propagation across nanostructured materials from a quantum-mechanical perspective. Two types of NEGF simulations are commonly used: anharmonic NEGF (a-NEGF) and harmonic NEGF (h-NEGF). a-NEGF incorporate inelastic interactions arising from anharmonic atomic potentials, but its computational cost is high. Thus, the vast majority of NEGF simulations use h-NEGF, which relies on harmonic atomic potentials

that neglect inelastic interactions. Over the past decades, h-NEGF has become a key tool to understand thermal transport across low-dimensional materials.^{152–158} Unlike classical MD and semiclassical BTE methods, NEGF is a purely quantum mechanical approach. Therefore, NEGF can correctly capture vibrational energy transport at low temperatures, unlike most MD implementations. Moreover, NEGF treats vibrational energy carriers as quantum mechanical waves and does not need to assign them to particular positions in space. Thus, it can compute vibrational energy transport in spatially varying systems, such as superlattices, without forcing energy carriers to behave like particles, a limitation of BTE approaches. Being an atomistic and fully quantum mechanical formalism, NEGF provides valuable insights into unresolved challenges in nanoscale thermal transport.

G. Interface thermal conductance

As mentioned above, heat-flow resistance at an interface is generally termed thermal boundary resistance (or Kapitza resistance) R_K . The thermal transport efficiency at interfaces between dissimilar materials is also quantified by the thermal boundary conductance h_K (TBC), which is simply the inverse of TBR, $h_K = 1/R_K$ (with units of $\text{W m}^{-2}\text{K}^{-1}$), which describes the relationship between heat flux and the temperature difference across the interface. The TBC is defined as $h_K = q_{\perp}/\Delta T$, where ΔT is the temperature drop in the interfacial region and q_{\perp} (with units of W m^{-2}) is the heat flux across the interfacial region.^{159,160}

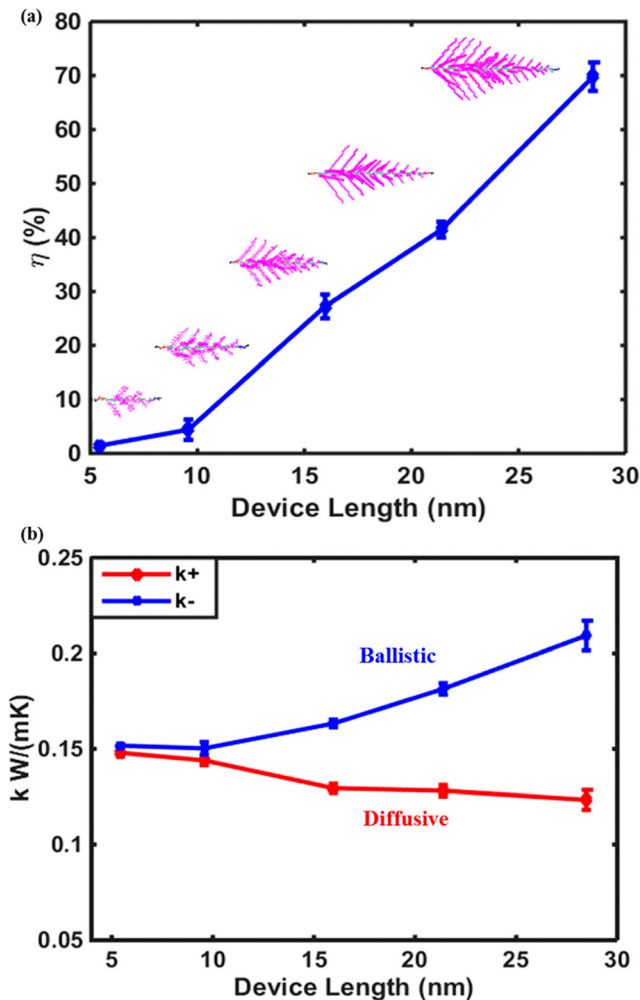


FIG. 19. (a) Thermal rectification ratio (η) as a function of device length. (b) Thermal conductivity vs device length in tapered bottlebrush polymers, where κ^+ and κ^- denote the conductivity in the forward and backward directions, respectively. Reprinted from Ma and Tian, *Nano Lett.* **18**, 43–48 (2018).¹²² Copyright 2018, with permission from American Chemical Society.

There is a distinction between the thermal boundary resistance and the thermal contact resistance. For a macroscopic thermal contact between two bodies, usually with very rough surfaces whose root mean square roughness is greater than $0.5 \mu\text{m}$, asperities on each side of the interface prevent intimate contact between the two solids.^{161,162} Even when pressure is applied to bring the surfaces together, most of the interface remains separated by air gaps. In regions of intimate contact, solid thermal conduction is the dominant heat transfer mechanism between the two materials. However, in areas where surfaces do not touch, conduction through the intermediate gas region dominates. To reduce thermal resistance between heat-generating microprocesses and the heat sink, the air gap between components is filled with a high-thermal-conductivity material known as a thermal interface material (TIM). Commercial TIMs are often polymeric elastomers filled with high thermal conductivity materials such as silver nanoparticles. The

incorporation of novel nanomaterials has shown great promise for the development of next-generation TIMs.^{163–165}

In contrast, thermal boundary resistance refers to the resistance at the interface between two materials when they are in perfect contact. In practice, this interface can be atomically smooth, or with a roughness from a few tenths of a nanometer to several nanometers. Even for a smooth interface, reflections occur when phonons travel toward the boundary because of the difference in the acoustic properties of adjacent materials.

The main factors that control h_K in solid/solid interfaces are (i) the respective phonon dispersion and phonon/electron DOS in the two adjacent materials and the interphase region near the interface; (ii) the interface roughness, which can affect the strength of interatomic interactions at the interface and the vibrational properties of the solid as shown in Fig. 20(a); and (iii) the temperature.^{159,166} Figure 20(b) displays typical values of h_K ranging from 20 to $300 \text{ MW m}^{-2} \text{ K}^{-1}$ for crystalline interfaces where thermal transport is dominated by lattice vibrations.

The heat flux across an interface from material 1 to material 2 can be given in the framework of the Landauer formalism.¹⁵ The inclusion of a transmission probability which governs all interactions at the interface gives the following expression for the thermal boundary conductance:¹⁵⁹

$$h_K = \frac{1}{8\pi^3} \sum_{\nu} \int \hbar\omega_{k\nu} g_{k\nu} \frac{\partial f_{0,kT}}{\partial T} v_{g,k\nu} \zeta_{k\nu} dk, \quad (43)$$

where ν is the phonon polarization (TA or LA), $g_{k\nu}$ is the partial density of states, f_0 the equilibrium Bose–Einstein distribution function, and $\zeta_{k\nu}$ is the transmission coefficient from material 1 to material 2.

The transmission coefficient ζ_k can be estimated using the acoustic or diffuse mismatch models for phonon–phonon scattering¹⁶⁷ (see Fig. 21). In these models, interfacial phonon flux is limited by mismatches in acoustic properties or phonon DOS. Analogous to the mismatch in the refractive indices between two optical media, the resistance at the interface between two solids under the acoustic mismatch model (AMM) is due to the difference in the sound velocities that result from the acoustic impedances. The probability of phonon transmission is determined by the ratio of acoustic impedances, $Z_{1,2} = \rho_{1,2}v_{1,2}$, at the interface, where ρ is the mass density and v is the velocity of the acoustic phonon. The transmission coefficient is given by

$$\zeta_{\text{AMM}} = \frac{4Z_1Z_2}{(Z_1 + Z_2)^2}. \quad (44)$$

Under the AMM, no atomistic properties intrinsic to the interface are considered. This model has been successfully used to describe low-temperature measurements of h_K . However, it is no longer valid at temperatures above approximately 30 K, even for ideal interfaces.¹⁶⁹ To accommodate real imperfect interface behaviors, the diffuse mismatch model (DMM) is the most widely used.

The basic assumption of the DMM is that phonons are scattered diffusively at the interface (see Fig. 21), causing them to lose their memory of incoming direction and polarization. Furthermore, a key assumption is elastic two-phonon scattering, where a phonon of frequency ω_0 transfers energy only to a phonon of the same frequency on the opposite side. This constraint means that the phonon

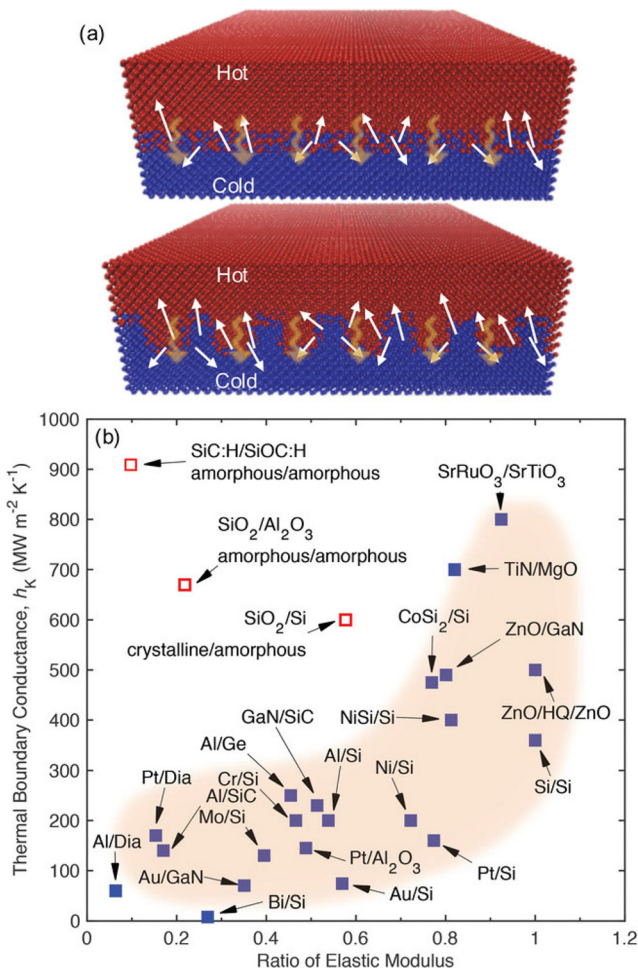


FIG. 20. (a) Imperfect interfaces with localized interfacial modes (arrows) that enhance thermal boundary conductance. (b) Measured TBC vs elastic modulus ratio for different materials interfaces. Reprinted from Giri and Hopkins, *Adv. Funct. Mater.* **30**, 1903857 (2020).¹⁵⁹ Copyright 2020, with permission from John Wiley and Sons.

population in the material with the lower Debye temperature (or cutoff frequency) governs the temperature dependence of h_K . Consequently, in the elastic scattering limit, h_K becomes temperature-independent once the lower Debye temperature is exceeded. The DMM has had some success in the interpretation of experimental measurements of h_K .¹⁰⁵

With the above assumptions, the phonon transmission probability is determined by the mismatch of the partial phonon DOS, $g_{1,2}(\omega_{k\nu}, T)$, summed over all phonon branches:¹⁶⁷

$$\zeta_{\text{DMM}}(\omega_{k\nu}) = \frac{g_2(\omega_{k\nu}, T)}{g_1(\omega_{k\nu}, T) + g_2(\omega_{k\nu}, T)}. \quad (45)$$

Since the bulk material and interfaces are in series in the Landauer-type models, the total thermal resistivity of the material is given by the sum of the bulk and interface resistivities:¹⁷⁰

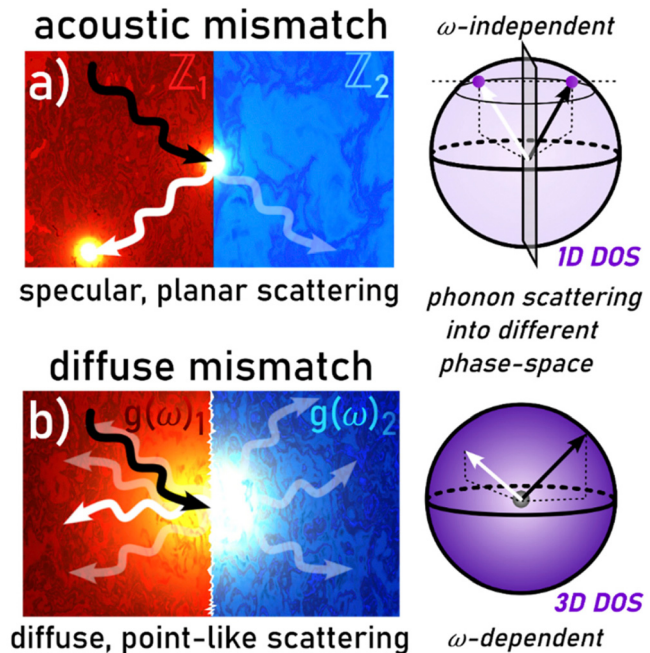


FIG. 21. Commonly used thermal boundary scattering models: (a) acoustic mismatch model (AMM) and (b) diffuse mismatch model (DMM). At the interface of materials 1 and 2, phonons (black) are either reflected or transmitted (white or pale blue) according to the transmission probability. Within the AMM, phonon transmission depends on the acoustic impedance mismatch between materials 1 and 2 (Z_1 and Z_2) and remains frequency independent (left). Due to its planar character, the scattering channels phonons into the 1D DOS (right). Within the DMM, the transmission probability is governed by the mismatch in the frequency-dependent phonon DOS of materials 1 and 2, $g_1(\omega_{k\nu}) - g_2(\omega_{k\nu})$ (left). Point-like scattering finally directs phonons into the 3D DOS (right). Reprinted from Stamper *et al.*, *Appl. Phys. Rev.* **11**, 021336 (2024);¹⁶⁸ licensed under a Creative Commons Attribution (CC BY) license.

$$\kappa(\omega_{k\nu})^{-1} = \kappa_{\text{bulk}}(\omega_{k\nu})^{-1} + (L_z h_K(\omega_{k\nu}))^{-1}, \quad (46)$$

where L_z is the linear spacing between interfaces.

Unlike the semi-classical AMM and DMM models, which neglect the detailed structure and properties of the interface, the quantum interfacial perturbation approach considers the dimensionality, spatial extent, and physical origin of the interface. This method employs the Peierls–Boltzmann transport equation, treating the material as a homogeneous solid with a relaxation time modified by additional interfacial scattering according to Mattheissen's rule. The rough interface is modeled as a perturbation by introducing a scattering potential encountered by an incoming wave packet and induces a scattering probability and relaxation time through quantum perturbation theory.¹⁷⁰ However, the differences between the Landauer and perturbation models demonstrated negligible differences in ζ .^{170,171}

The interface and elastic scattering processes described above do not provide a complete picture, as inelastic interactions can significantly influence the theoretical modeling of h_K .¹⁷² Inelastic processes occur when bulk vibrational modes couple to interfacial vibrational modes, defined as eigenmodes with large displacements of interfacial atoms, which form due to the higher degree of anharmonicity at the

interface relative to the bulk.^{172,173} Molecular dynamics simulations have been used to explore these inelastic contributions to interface thermal conductance.

MD simulations can compute h_K directly from the simulation temperature profile once the steady state has been reached. The common strategy involves adding and subtracting a portion of energy from a thin slab of atoms on either side of the boundary,¹⁷⁴ which fixes the heat flux at the interface $q_{\perp} = -h_K \Delta T$, where q_{\perp} is the heat flux normal to the interface, and ΔT is the temperature drop across the interface. The temperature discontinuity at the interface is then calculated from the temperature profile (ΔT) and h_K is obtained with the last equation.

Understanding TBR has historically been challenging, since measuring the heat flow across a single interface requires specialized equipment and techniques such as ultra-fast time-domain thermoreflectance.¹⁶⁶ It is a matter of current computational strategy to understand the most fundamental phonon and electron interactions involved in TBR and thus surpass simple models of TBR.^{159,175}

Figures 22 and 23 summarize the simulation data for the thermal conductivity of bulk silicon and the Si/h-Si (h-Si or heavy Si is a Si isotope with a larger atomic mass) interface.¹⁷⁶ Figure 22(a) shows the simulation domain for MD and NEGF simulations. Silicon is placed on the left side and heavy silicon (h-Si) on the right, with the interface located at $x = 0$. The mass ratio is defined as $MR = M_{h\text{-Si}}/M_{\text{Si}}$ and is varied within the range $1 \leq MR \leq 10$. The Tersoff potential is used to provide a comprehensive view of the thermal conductivity. The thermal boundary resistance extraction details are illustrated in Fig. 22(b). MD simulations are conducted using the LAMMPS package,¹⁷⁷ while NEGF simulations use the NEMO⁵¹⁷⁸ nanodevice simulation tool.

The prediction of NEGF of the bulk Si thermal conductivity agrees with the MD solution, as shown in Fig. 23(a). Figure 23(b) shows that the TBR as a function of MR calculated with NEGF is quantitatively in agreement with the MD predictions. For both methods, the thermal boundary resistance increases with MR and vanishes for a homogeneous system when MR tends to unity. The minor discrepancy between the MD and NEGF results may be due to different treatments of the phonon modes perpendicular to the transport direction x and the open boundary conditions in the transport direction.¹⁷⁶

H. Strategies for measuring thermal conductivity

The thermal conductivity κ of different materials can be measured using various characterization techniques. The choice of method depends on factors determined by the underlying heat transfer mechanism, including sample size and shape, composition, and the temperature and pressure conditions of the measurements.

The main experimental techniques for measuring κ in solids can be broadly classified into optical and electrical methods, each of which can be implemented in either steady-state or transient mode. In steady-state methods, a fixed temperature gradient is imposed to extract thermal properties, whereas transient methods probe the temporal response of energy dissipation. The suitability of each approach depends on its inherent advantages and limitations, as well as on factors such as sample geometry, thermal characteristics, and temperature range.¹⁷⁹

Optical techniques include the ultrafast laser transient thermoreflectance (TTR) available in the time domain (TDTR)^{180–183} and frequency domain (FDTR),^{184,185} laser flash,¹⁸⁶ Raman thermometry,²²

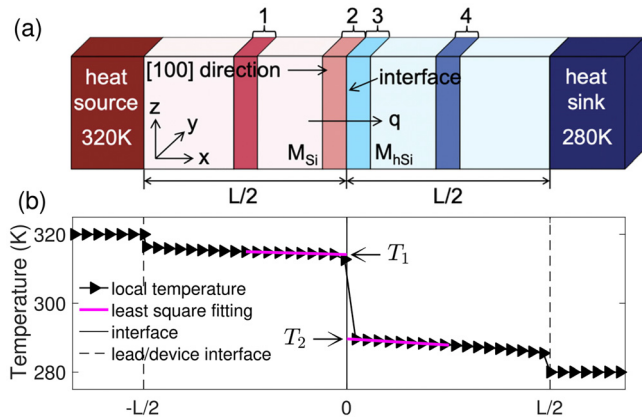


FIG. 22. (a) Simulation domain: regions 1–4 are three atomic layers located in Si (layer 1), in the Si-hSi interface (layers 2 and 3) and in h-Si (layer 4). (b) TBR extraction schematics. Reprinted from Chu *et al.*, Appl. Phys. Lett. **115**, 231601 (2019). Copyright 2019, with permission from AIP Publishing.

and various advanced pump-probe techniques, as reported by Li *et al.*,¹⁸⁷ Pérez *et al.*,¹⁸⁸ Jiang *et al.*,^{189–191} Feser and Cahill,¹⁹² Feser *et al.*,¹⁹³ Tang and Dames,¹⁹⁴ Rodin and Yee,¹⁹⁵ Rahman *et al.*,¹⁹⁶ and Qian *et al.*,¹⁹⁷ The most remarkable advantage of optical methods is the flexibility to adjust the relative positions of pump and probe laser spots on the sample surface, and the elliptical eccentricity of laser spots, thereby directly achieving a 360° scan of the in-plane anisotropic thermal conductivities.^{190,194}

The challenge in interpreting the data comes from the fact that probe signals in these optical techniques commonly utilize high repetition frequencies and are thus sensitive to the thermal conductivity and heat capacity of the metal transducer. Moreover, the thermal boundary resistance between the transducer and the sample poses additional errors in the measured κ .¹⁹⁸ Another challenge is the fact that optical techniques employ multivariate fitting algorithms to obtain κ , which inevitably affects the accuracy of the measured value. Even at low frequencies, these techniques suffer from insufficient sensitivity to measure the cross-plane thermal conductivity.¹⁹¹

Methods for extracting κ using electrical circuits typically include the 3 ω technique,^{10,11} microfabricated suspended device,^{28,199} and further advancements in light of the numerous works, for example, by Kurabayashi *et al.*,²⁰⁰ Borca-Tasciuc *et al.*,²⁰¹ Slomski *et al.*,²⁰² Su *et al.*,²⁰³ Yamaguchi *et al.*,²⁰⁴ Forsythe *et al.*,²⁰⁵ Peri *et al.*,²⁰⁶ Mishra *et al.*,²⁰⁷ Kommandur and Yee,²⁰⁸ Ramu and Bowers,^{209,210} Handweg *et al.*,²¹¹ Mazzelli *et al.*,²¹² and comprehensive reviews of the topic, e.g., by Dames²¹ and Bhardwaj and Khare *et al.*²¹³

However, almost all the above electrical methods are affected by the error propagation from the thermal resistance of superficial structures (insulation layer, sensor-sample interface, etc.) to the final measurement results.^{209,210} Similar to the optical methods, these electrical methods also depend on multivariate fitting algorithms, which seriously challenge the accuracy of measured results.

Table I summarizes some of the most widely used experimental techniques for measuring thermal conductivity. The primary advantages and limitations of these methods are illustrated in Fig. 24. Although substantial information is already available—some of which is summarized in Table I and discussed in greater detail in Sec. III—a

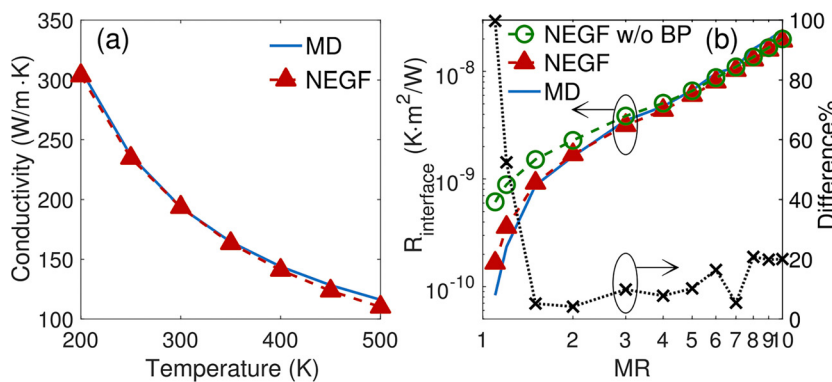


FIG. 23. (a) MD (blue line) and NEGF (triangles) results for the thermal conductivity of bulk Si. (b) MD (blue line) and NEGF results (green circles without Büttner probe (BP) self-energy, black triangles include BP) for Si/h-Si thermal boundary resistance vs mass ratio. Crosses indicate the relative difference between MD and NEGF. Consequently, the impact of scattering on the thermal boundary resistance declines with increasing mass of h-Si. Reprinted from Chu *et al.*, Appl. Phys. Lett. 115, 231601 (2019).¹⁷⁶ Copyright 2019, with permission from AIP Publishing.

universally applicable, high-precision experimental technique for measuring the thermal conductivity of low-dimensional materials remains lacking.

Using the steady-state strategy, κ is obtained by measuring the temperature difference ΔT at a particular distance of interest under a steady-state heat flow through the sample. The thermal conductivity is then given by the slope of the power vs the temperature gradient between the separation distance.²¹⁷ The steady-state methods are based on Fourier's law to measure low thermal conductivities. However, these techniques require large samples and prolonged measurement times.¹⁷⁹ They also suffer from parasitic heat losses and the thermal contact resistance between the sample and the thermometer. The steady-state methods take full advantage of the one-directional heat flow over a larger area, which is designed for the measurement of samples with anisotropic κ and large-area composite materials.

A range of transient techniques have been developed to mitigate the drawbacks of steady-state methods, such as heat losses, sensor contact resistance, and long stabilization times. The sample is heated using continuous wave or pulsed sources, resulting in periodic or transient temperature changes.¹⁷⁹ These methods determine the thermal diffusivity α as a measure of how quickly a material can respond to changes in temperature. The value of α is related to the mass density ρ and specific heat capacity C by

$$\alpha = \frac{\kappa}{\rho C}. \quad (47)$$

Therefore, κ governs heat transfer, while α describes the speed of propagation of temperature through the sample. Consequently, thermal conductivity is more relevant for steady-state heat transfer problems, while thermal diffusivity is more pronounced for transient heat transfer behavior.

Many of the discoveries described here have resulted from advances in 3ω , TDTR, and FDTR techniques. Their versatility allows for the thermal characterization of a wide range of materials, from bulk samples to thin films, spanning thicknesses from a few nanometers up to several hundred micrometers. Thin film layers provide many examples in which a quantitative understanding of heat transfer phenomena is achieved. Thin films can exist in several configurations: supported on a substrate, suspended as free-standing layers, or arranged in multi-layer stacks. When the film thickness becomes smaller than the MFP

of the dominant heat carriers—electrons in conductors and phonons in insulators—the thermal conductivity decreases relative to the bulk value, as geometric confinement restricts carrier transport. As a result, thin films typically exhibit both thickness-dependent and anisotropic thermal conductivity, with κ_{\perp} (cross-plane, also referred to as out-of-plane or through-plane) often differing significantly from κ_{\parallel} (in-plane).

III. THERMAL CONDUCTIVITY IN THIN FILMS

To characterize the cross-plane thermal conductivity κ_{\perp} of a thin film, a temperature drop ΔT should be created and measured throughout the film. This task becomes particularly challenging when the sample thickness ranges from a few nanometers to tens of micrometers.^{179,215} The measurement of the in-plane thermal conductivity κ_{\parallel} introduces important challenges, the most significant being the accurate evaluation of parasitic heat losses through the substrate. Volklein *et al.*²¹⁸ proved that the measurement accuracy can be improved if the condition $\kappa_{\parallel}d_f \geq \kappa_s d_s$ is satisfied, where d_f and d_s are the thin film and substrate thicknesses, and κ_s is the thermal conductivity of the substrate. However, the parasitic heat losses are completely removed if the film is suspended across a hole in the substrate, complicating the sample preparation.

The most common procedures used to measure the thermal conductivity of thin films include the 3ω method and time-domain thermoreflectance. This Section provides a comprehensive overview of these techniques and several other approaches to thermal conduction research on thin films, focusing on understanding the strategies of extracting κ of a thin film and the differences between measurements and predictions.

A. 3ω technique

1. Principles of the 3ω technique

The 3ω method (or transient hot wire method) was proposed by Corbino in 1910, who introduced the third harmonic component of the voltage when applying an AC to a heater for calculating the thermal diffusivity of metal filaments in light bulbs.^{219,220} This technique was further developed by Cahill and Pohl^{10,11} at the Laboratory of Atomic and Solid State Physics at Cornell University in 1987, and later extensively discussed in the literature to estimate the cross-plane κ of thin films.^{221,222} The 3ω method is one of the most powerful

TABLE I. Key aspects of the methods for measuring in-plane ($\kappa_{||}$) and cross-plane (κ_{\perp}) thermal conductivities.^{7,44,198,214,215}

Method	Measurement of κ	Sample structure	Advantages	Limitations
TDTR	Mainly κ_{\perp} of thin films, it can be adapted to measure $\kappa_{ }$	Supported	Non-contact method; κ can be obtained without knowing C; high adaptability for sub-micrometer films, SLs, and bulk; works for inorganic and hybrid materials	High precision optics required; metal film deposition needed; large uncertainty for $\kappa_{ } < 5 \text{ W/mK}$; cannot measure monolayer 2D materials
FDTR	Mainly κ_{\perp} of thin films, it can be adapted to measure $\kappa_{ }$	Supported	Fast and non-contact; suitable for sub-micrometer films and bulk materials; simpler than TDTR	Requires metallic coating; large uncertainty for $\kappa_{ } < 5 \text{ W/mK}$; specific heat data needed
Raman thermometry	Key technique for measuring $\kappa_{ }$	Supported suspended	Allows monolayer resolution; simple sample prep	Inaccurate results due to laser absorption coefficient; low phonon shift materials are hard to measure
Laser flash	Mainly κ_{\perp}	Suspended	Fast and easy; measures κ of small samples; suitable for wide temperature range (up to 700 °C)	Hard to quantify κ due to heat flow measurement complexities; thickness limitation
Conventional 3 ω	Mainly κ_{\perp} of films but can measure $\kappa_{ }$ in bulk materials	Supported	Suitable for sub-micrometer films; high signal-to-noise ratio	Needs microfabrication for sensors; sample electrical isolation may reduce accuracy
Microfabricated suspended device	κ_{\perp} of NWs, nanotubes; $\kappa_{ }$ for thin films	Suspended	Eliminates substrate effects; suitable for nanoscale samples	Laborious sample prep; sensitive to thermal contact resistance

techniques to measure κ_{\perp} in thin films. Although it was used primarily to determine the cross-plane thermal conductivity of thin films, it can also be used to measure the in-plane $\kappa_{||}$ by adjusting the heater width and heating frequency.²¹

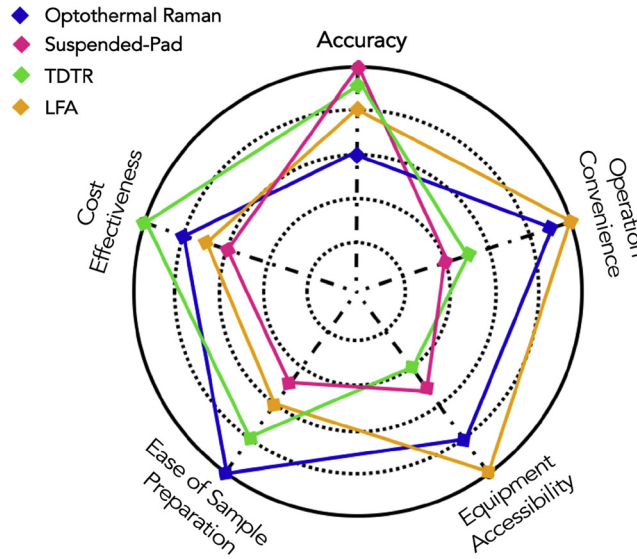


FIG. 24. A comparison is made among four commonly used methods for measuring thermal conductivity, considering factors such as accuracy, operational simplicity, equipment availability, sample preparation requirements, and cost. Reprinted from Song *et al.*, Joule 2, 442–463 (2018).²¹⁶ Copyright 2018, with permission from Elsevier.

The 3 ω method uses a microfabricated metallic line that acts as a heater and thermometer (see Fig. 25). The resistance of the metallic line, with value R_T , is fed with a sinusoidal current of frequency ω ($I_{1\omega}$ in the figure), which produces a Joule effect that causes a temperature increase (a DC component ΔT_{DC}) and temperature fluctuations at 2ω with amplitude $\Delta T_{AC}(2\omega)$. Detecting the third harmonics in voltage ($V_{3\omega}$ in the figure), the amplitude of the temperature oscillations and the thermal conductivity can be found.

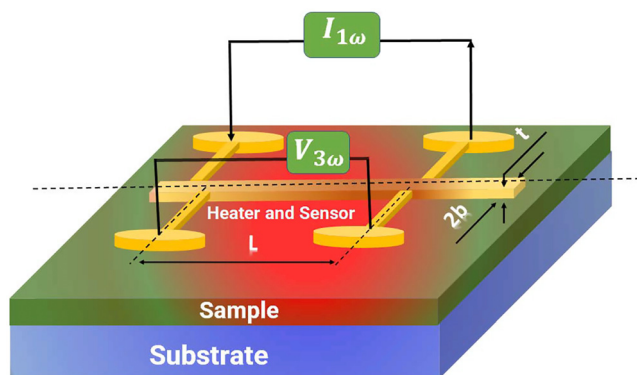


FIG. 25. Schematics of the standard 3 ω technique showing a long and thin metallic bridge or thermometer with specific width $2b$, length L , and thickness t . Commonly used metals for the RT element are gold (Au)²²³ and platinum (Pt)²²⁴ since the metallic line should be highly resistant to oxidation (ideally inert) and have a well-defined temperature-dependent electrical resistance to accurately measure the temperature.^{225,226}

Specifically, an AC of frequency ω , $I(t) = I_0 \cos \omega t$, is passed through the metallic line or resistance thermometer (RT) with electrical resistance R_T . Because the ultimate objective is to detect the third harmonic of the response signal, it is important to ensure that the input current remains purely harmonic. This precaution prevents the generation of undesired higher harmonics that could otherwise arise from waveform distortion. The dissipated power $P(t)$ in the RT strip can be written as

$$P(t) = I^2(t)R_T = \frac{1}{2}I_0^2R_T(1 + \cos 2\omega t). \quad (48)$$

As previously noted, the current contains both DC and AC components. The temperature variation due to the Joule effect is

$$\Delta T(t) = \Delta T_{DC} + \Delta T_{AC} \cos(2\omega t + \phi), \quad (49)$$

where ϕ is the phase shift between the temperature oscillations and the excitation current. This, in turn, produces harmonic variations in the resistance given by²²⁷

$$R_T(t) = R_0[1 + \beta_R \Delta T_{DC} + \beta_R \Delta T_{AC} \cos(2\omega t + \phi)], \quad (50)$$

where R_0 is the heater resistance in the absence of current and β_R is the temperature coefficient of the resistance ($\beta_R = 0.0034 \text{ K}^{-1}$ for gold and 0.00392 K^{-1} for platinum²²⁸). Hence, as the temperature of the RT element increases, RT oscillates at 2ω and exhibits a linear dependence on T . However, because of the additional contribution from the DC term, it is essential, in practical applications, to calibrate the RT element by characterizing its dependence on frequency.

The resulting voltage across the sensor is obtained by multiplying the input current by the heater resistance, which yields

$$V(t) = I_0 R_0 \left[(1 + \beta_R \Delta T_{DC}) \cos \omega t + \frac{1}{2} \beta_R \Delta T_{AC} \cos(\omega t + \phi) + \frac{1}{2} \beta_R \Delta T_{AC} \cos(3\omega t + \phi) \right]. \quad (51)$$

The voltage component at 3ω results from the multiplication of the oscillating current by the periodic portion of $R_T(2\omega)$. One is, therefore, able to obtain the in-phase and out-of-phase components of $\Delta T(t)$ by measuring the 3ω component of the voltage:

$$V_{3\omega} = I_0 R_0 \frac{1}{2} \beta_R \Delta T_{AC} = \frac{1}{2} V_0 \beta_R \Delta T_{AC}, \quad (52)$$

where $V_0 = R_0 I_0$, I_0 and R_0 are the DC components of the current and resistance, respectively, and ΔT_{AC} is the amplitude of the temperature rise of the heater. Rearranging Eq. (52) gives

$$\Delta T_{AC} = \frac{2V_{3\omega}}{V_0 \beta_R}. \quad (53)$$

The measurement of the voltage signal at 3ω is a challenging process since $V_{3\omega}$ is usually 100–1000 times smaller than the voltage signal at ω due to the low value of β_R .^{21,229} Meanwhile, $V_{3\omega}$ is directly proportional to the temperature oscillation at 2ω thus acting as a direct thermometer of ΔT_{AC} . The 3ω component can be measured using standard AC lock-in techniques, which can also be supplemented by a Wheatstone bridge²³⁰ to remove the large V_0 before measuring the third harmonic signal $V_{3\omega}$. For conductive or doped semiconducting films, an insulating layer must be introduced

between the heater and the sample to prevent electrical short-circuiting.

Both the magnitude and phase of the temperature oscillations vary with ω , depending on the thermal diffusion time of the material, $\tau_D = \ell^2/\alpha$, the time required for the heat to propagate over a distance ℓ , the diffusion length ($\ell = \sqrt{2\alpha/\omega}$). In the limit of infinite thermal diffusivity α , that is, infinite κ , $\tau_D \rightarrow 0$, heat propagates with infinite velocity, and the temperature will be constant throughout the sample. This leads to undamped temperature oscillations with zero phase shift. In turn, the $\alpha \rightarrow 0$ case, that is, nearly zero diffusivity, results in very low heat propagation, almost zero oscillation amplitude, and a very large phase lag.

The most obvious challenge in these measurements is to determine the temperature drop across the film. Approximate analytical expressions were obtained to determine the cross-plane and in-plane thermal conductivities. A complete solution of the oscillating temperature field, through which the thermal conductivity of the sample can be found based on 2D heat diffusion, can be determined in various cases, such as a semi-infinite medium, or a substrate with finite thickness but infinite lateral size. For example, Borca-Tasciuc *et al.*²⁰¹ presented a general semi-analytical solution for heat conduction in a multilayer film-on-substrate system. Dames²¹ also described the general case of the framework of thermal and electrical transfer functions.

According to Cahill,^{11,231} for a finite width heater deposited on the substrate surface, the average temperature ΔT_{AC} in the heater is

$$\Delta T_{AC} = \frac{P}{L\pi\kappa} \int_0^\infty \frac{\sin^2 kdk}{k^2 \sqrt{k^2 + i\Omega}}, \quad (54)$$

where P is the amplitude of the power dissipated by the heater line at a frequency ω , L is the length of the line, and $\Omega = b^2\omega/\alpha$ is the reduced frequency. The integral can be expressed in terms of the Meijer G-function, a special function that is readily available in standard mathematical libraries or symbolic computation software such as *Mathematica*.²³²

$$\int_0^\infty \frac{\sin^2 kdk}{k^2 \sqrt{k^2 + i\Omega}} = \frac{1}{4} G_{24}^{22} \left(i\Omega \middle| \begin{matrix} 0 & 1 \\ 0, 0, -1, -\frac{1}{2} \end{matrix} \right). \quad (55)$$

In the low frequency limit ($\Omega \ll 1$ or $\omega \ll \alpha/b^2$), the approximate value of the ΔT_{AC} is²³³

$$\Delta T_{AC} \approx \frac{P}{L\pi\kappa} \left[-\frac{1}{2} \ln \Omega + \frac{1}{2} \zeta - i \frac{\pi}{4} \right], \quad (56)$$

where $\zeta = 3 - 2\gamma \approx 1.84557$, with γ being the Euler number. Figure 26 presents the real (in-phase) and imaginary (out-of-phase) components of $(L\pi\kappa/P)\Delta T_{AC}$, evaluated numerically from Eq. (55) and from the low-frequency approximation in Eq. (56), as a function of the excitation frequency. It exhibits a linear regime in a semi-logarithmic plot at low frequencies (larger thermal penetration depths) when the in-phase temperature decays logarithmically. The out-of-phase component is $-\pi/4$, in agreement with Eq. (56). At higher frequencies (small thermal penetration depths), the in-phase and out-of-phase temperature components are relatively close but opposite in sign, finally leveling off to zero with increasing frequency. The thermal conductivity of the substrate can be determined from either the real or imaginary part.

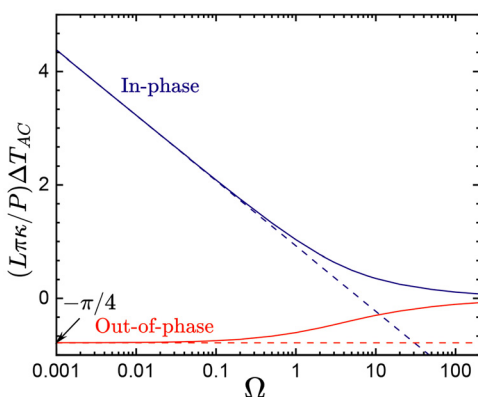


FIG. 26. In-phase and out-of-phase components of the temperature oscillations $(L\pi\kappa/P)\Delta T_{AC}$ (dimensionless temperature) vs the reduced thermal excitation frequency Ω calculated from Eq. (55), solid lines, and (56) dashed lines.

However, experimentally, it is more reliable to consider the data obtained from the real contribution.¹¹ By inserting Eq. (56) into Eq. (52) and introducing the substitution $\Omega = b^2\omega/\alpha$,⁴⁸

$$V_{3\omega} = -\frac{V_0^3 \beta_R}{4\pi L\kappa R_0} \left[\ln \omega + \ln \frac{b^2}{\alpha} - \xi \right] - i \frac{V_0^3 \beta_R}{8L\kappa R_0}. \quad (57)$$

Hence, by measuring the third-harmonic signal at two different heating frequencies ω_1 and ω_2 , one can find from Eq. (57)¹⁰

$$\kappa = \frac{\beta_R V_0^3 \ln(\omega_2/\omega_1)}{4\pi L R_0 (V_{3\omega,1} - V_{3\omega,2})}, \quad (58)$$

where $V_{3\omega,1}$ and $V_{3\omega,2}$ are the third-harmonic voltages for frequencies ω_1 and ω_2 , respectively. In practice, instead of using two frequencies, the third harmonic signal is collected over a range of frequencies, and the thermal conductivity is obtained by a least squares fitting of the function $V_{3\omega}(\omega)$. For example, Fig. 27(b) displays the measured 3ω voltage in self-standing iron oxide thin films as a function of ω on a semi-logarithmic scale. The results show that the $V_{3\omega}$ signal closely follows a $\ln \omega$ dependence, from which the thermal conductivity κ was determined from the slope of the curves.

2. In-plane and cross-plane thermal conductivity

Thin film studies often focus on cross-plane thermal conductivity, while in-plane conductivity measurements in anisotropic films are less common due to their greater complexity and experimental challenges.²¹ A central difficulty lies in performing cross-plane and in-plane measurements simultaneously without physically altering the sample.

The 3ω method is a well-established electrothermal technique for determining the cross-plane thermal conductivity (κ_{\perp}) of thin films. These measurements are most straightforward in relatively thick, low- κ films. Critical requirements include the use of a sufficiently wide heater line to promote one-dimensional heat flow, a substrate thick enough to be approximated as semi-infinite, and the avoidance of excessively high excitation frequencies.²¹

Figure 27(d) shows the temperature dependence of the cross-plane thermal conductivity of three Fe_3O_4 films and a simple

theoretical calculation based on the Callaway model²³⁴ (solid lines), demonstrating the typical $\kappa(T)$ behavior due to phonon-scattering processes and their regimes of dominance.¹⁴¹ Starting from $T \rightarrow 0$, $\kappa \rightarrow 0$ due to the freezing out of phonon modes (the limiting value of κ is given by the finite size of the sample). As the temperature increases, the initial increase in κ is a specific heat effect. Then the phonon-grain boundary scattering prevails. Finally, the impurity, electron, and inter-phonon U-processes dominate. The maximum value of κ usually occurs at $\sim 0.1\Theta_D$, Θ_D being the Debye temperature. The high temperature variation is dominated by interphonon scattering and has a behavior T^{-1} , sometimes referred to as the Slack relation.^{235,236}

It is well established that the significant reduction in the thermal conductivity of thin films, compared to their bulk counterparts [Fig. 27(d)], arises primarily from enhanced phonon-boundary scattering associated with finite crystal dimensions and grain-size effects. The results predicted by the Callaway model agree reasonably well with the experimental data in Fig. 27(d), including the results for bulk Fe_3O_4 .²³³ Employing the analysis framework established around the Callaway phonon conductivity model, the total combined phonon scattering rate can be given the form:²³³

$$\tau_s^{-1} = v \left(\frac{1}{d_1} + \frac{1}{d_f} \right) + A\omega_0^4 + B\omega_0^4 Te^{-\Theta_D/3T}, \quad (59)$$

where d_1 denotes the grain size of the thin films, while A and B are fitting parameters. The parameter A corresponds to the scattering by impurities or isotopes, whereas the parameter B represents the scattering due to U-processes. As shown in Fig. 27(d), the simulated results are in reasonable agreement with the measured data, although the experimental values are somewhat lower, especially for the 100-nm film.

By measuring the temperature drop across the thin film, one can estimate its cross-plane thermal conductivity $\kappa_{f\perp}$. The temperature at the top surface of the film is usually taken to match the heater/sensor temperature due to minimal contact resistance, $10^{-8}\text{--}10^{-7} \text{ m}^2 \text{ K W}^{-1}$.¹² The temperature at the bottom surface is typically determined from the measurement of the heat flux and the known thermal conductivity of the substrate κ_s , which can be obtained from the literature or measured independently using the 3ω method. Under the assumption of one-dimensional heat flow through the thin film, κ is given by¹⁷⁹

$$\Delta T_{s+f} = \Delta T_s + \frac{Pd_f}{2bL\kappa_{f\perp}}, \quad (60)$$

where subscripts f and s denote the thin film and substrate properties, respectively.

Measurements of the in-plane thermal conductivity are less common than those for the cross-plane direction, while the methods used are more diverse. In-plane thermal conductivity measurements can be broadly classified into two categories: those conducted on suspended films and those carried out on supported films. In general, suspended film methods are more sensitive, accurate, and flexible, but the micro-fabrication of the film to suspend is sometimes a serious challenge.²¹ For suspended films, the most important concern is making the length of suspended film long enough so that the spreading and contact resistances at the edge support substrate and the heater can be neglected,

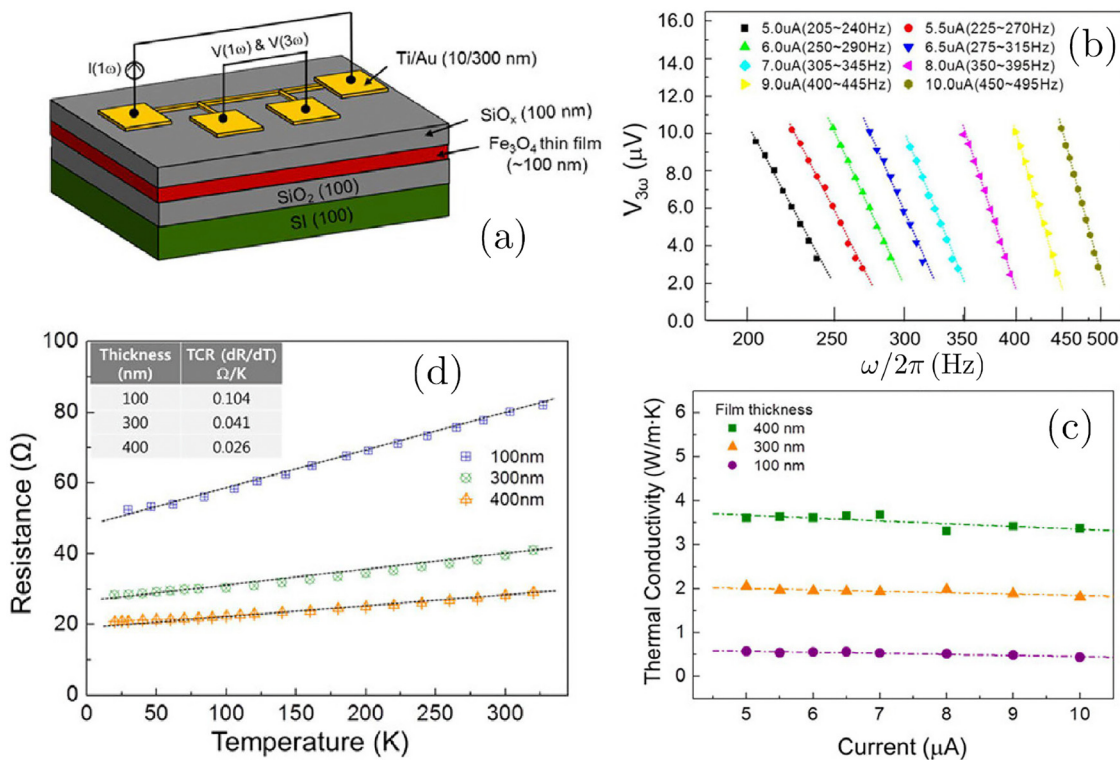


FIG. 27. (a) Schematic of the 3ω measurement setup for determining the cross-plane thermal conductivity of epitaxial Fe_3O_4 thin films grown on SiO_2/Si (100) substrates. (b) Semi-logarithmic plots of $V_{3\omega}$ as a function of ω for input currents ranging from 5 to $10 \mu\text{A}$. (c) Thermal conductivity κ of Fe_3O_4 films with varying thicknesses as a function of the applied current, indicating that the observed variation arises primarily from measurement uncertainties. (d) Temperature-dependent κ of Fe_3O_4 films with thicknesses of 100, 300, and 400 nm, together with Callaway-model fits accounting for impurity scattering, Umklapp (U) processes, and boundary scattering. Reprinted with permission from Park *et al.*, *Nanoscale Res. Lett.* **9**, 1–8 (2014);²³³ licensed under a Creative Commons Attribution (CC BY) license.

20 December 2025, 13:48:09

but still short enough to ignore radiation losses and 2D effects due to the finite heater length.

The techniques for measuring the in-plane thermal conductivity of supported films are more specialized and include the variable line-width 3ω method and the heat spreader method.²¹ Compared with approaches applied to suspended films, the corresponding methods for supported films are inherently less sensitive. However, the need for relatively narrow and/or closely spaced heating/sensing lines must not be overlooked. Both methods for supported films perform best with relatively thick films exhibiting high in-plane thermal conductivity ($\kappa_{f\parallel}$); however, their respective requirements for cross-plane thermal conductivity ($\kappa_{f\perp}$) differ significantly. The variable line width 3ω method works best for films with small $\kappa_{f\perp}$, which must be accurately known. However, the heat spreader method works better for films with moderate to large size $\kappa_{f\perp}$. Finally, error analysis for supported-film configurations remains comparatively underdeveloped in the literature, particularly relative to the extensive treatment of the cross-plane 3ω method. Given the complexity of such samples, rigorous analyses are likely to require numerical rather than purely analytical approaches.^{21,237}

The 3ω method is also widely employed in the measurement of $\kappa_{f\parallel}$. Compared to the cross-plane measurement of $\kappa_{f\perp}$, a much narrower heater is used to measure $\kappa_{f\parallel}$ so that the heat transfer process

within the film is sensitive to the thermal conductivity of both the in-plane and the cross-plane. The half-width b of the heater should be narrow enough to satisfy²¹

$$\frac{b}{df} \sqrt{\frac{\kappa_{f\perp}}{\kappa_{f\parallel}}} \leq 0.1. \quad (61)$$

A description of the technical details and recent advances has been covered in previous reviews.^{21,179}

It is worth mentioning a modified 3ω method developed by Wang *et al.*,²³⁸ which facilitates the measurement of in-plane thermal conductivity in thin films. This method resembles the cross-wire geometry approach for measuring the thermal conductivity of micro-wires.²³⁹ In both methods, a microscale heating wire serves both as a thermometer and as a heater. An AC flows through the heating wire, with two ends mounted on the heat sinks. The test film is suspended on insulating ceramic sheets. The heating wire is placed at an angle relative to the magnetic field \mathbf{B} to ensure that the resulting Ampère force is directed downward [see Fig. 28(a)]. The heating wire should first be calibrated, for example, using the standard 3ω method. Then a relatively large DC is fed into the heating wire, forcing it to contact the test film with the aid of interstitial materials under Ampère's force [see Fig. 28(b)]. The temperature rise of the heating wire will then decrease,

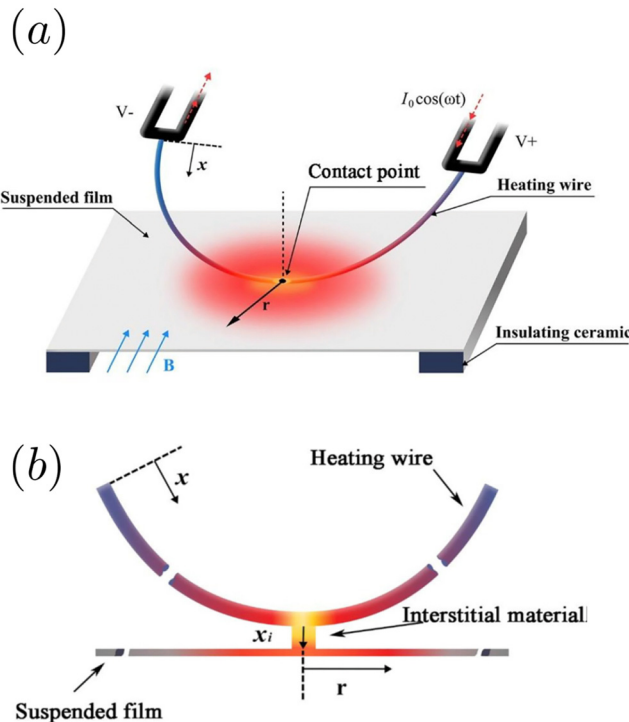


FIG. 28. (a) Principle for a modified 3ω method with the coordinate system. $V+$ and $V-$ indicate the positive and negative voltages, B is the magnetic field strength, and x and r are the coordinates of the heating wire and test film, respectively. (b) Enlarged schematic of the heating wire and interstitial material. Reprinted from Wang *et al.*, Int. J. Heat Mass Transfer **219**, 124870 (2024).²³⁸ licensed under a Creative Commons Attribution (CC BY) license.

as a part of the heat flows through the film. By comparing the 3ω voltage before and after contacting the test film, the value of $\kappa_{f||}$ can be obtained from the slope of the real part of the thermal impedance plotted against the logarithm of the heating frequency. A thorough theoretical analysis conveniently matched the analysis framework of a T-type probe using the periodic heating method established by Wang *et al.*²⁴⁰ Introducing the dimensionless frequency

$$\Omega = \frac{l_h}{\delta} = l_h \sqrt{\frac{\omega}{2x}}, \quad (62)$$

where l_h is the length of the hot wire, the wire resistance

$$R_h = l_h / \kappa_h A_h, \quad (63)$$

with A_h being the section of the wire and κ_h its thermal conductivity, we can introduce the dimensionless thermal transfer:²⁴¹

$$Z = \frac{\Delta T}{I_{rms}^2 R_0 R_h} = \frac{1}{i\Omega^2} \left[1 - \frac{\sqrt{2}(1-i)}{2\Omega} \tanh\left(\frac{\sqrt{i}}{2}\Omega\right) \right]. \quad (64)$$

Here, I_{rms} is the root mean square value of the heating current.

Figure 29 shows the experimental results for the stainless-steel film. They indicate that the measured function Z can be well predicted by fitting thermal conductivity and thermal diffusivity, as shown by the dashed line in Fig. 29. In contact conditions, the value of Z is

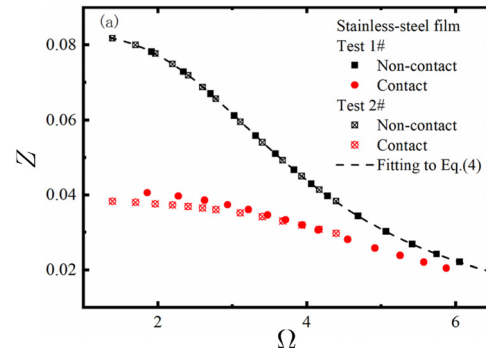


FIG. 29. Measured dependence of the dimensionless thermal transfer function on dimensionless frequency for a stainless-steel film with a thickness of about $10.0 \mu\text{m}$. Dashed line is fitted by Eq. (64). Reprinted from Wang *et al.*, Int. J. Heat Mass Transfer **219**, 124870 (2024).²³⁸ Copyright 2024, with permission from Elsevier.

markedly decreased compared to that of the bare heating wire. It appears that the difference in Z is not very significant under different contact conditions, especially in the high-frequency range (squares and circles in the lower two curves of Fig. 29). The authors therefore conclude that this method can be more reliable in measuring thin films with low thermal conductivities.

For many samples, a differential 3ω method is the best way to extract κ_f .^{21,242–244} To have a confident value of the thermal conductivity of a thin film, we have to use the 3ω method to obtain the thermal conductivity κ_s of the substrate and measure a set of films of various thicknesses on the substrate (SiN, Si, SiC, and c-cut sapphire are commonly used). The amplitude of the temperature oscillations at the frequency 2ω throughout the structure of the film on a substrate (ΔT_{s+f}) and the reference substrate (ΔT_s) can be obtained using Eq. (53). Then, the temperature oscillations caused by the thin film can be written as

$$\Delta T_f = \Delta T_{s+f} - \Delta T_s, \quad (65)$$

which yields κ for the film in the form²²¹

$$\kappa_f = \frac{Pd_f}{2b\Delta T_f}. \quad (66)$$

In some reports, measured data on the thermal resistance of a thin film have been analyzed based on the apparent thermal conductivity affected by an additional thermal resistance at the interfaces between the film and the substrate and the interface between the metal heating strip and the film.^{221,245} In the case of the 3ω technique, the existence of a boundary layer between a film and a substrate adds a thermal resistance R_{sf} to the resistance of the film in a one-dimensional heat diffusion model. In this case, if $d_f \ll 2b$, heat flow in the film is one-dimensional, and the apparent thermal conductivity κ_a of the layer can be found using²²¹

$$\Delta T_f = \frac{P}{\kappa_a} \frac{d_f}{2b}. \quad (67)$$

The presence of R_{sf} and κ_a is represented by^{221,246}

$$\kappa_a = \frac{\kappa_i}{1 + R_{sf} \kappa_i / d_f}, \quad (68)$$

where κ_i is the intrinsic thermal conductivity of the film, assumed to be independent of d_f , and κ_a is derived from Eq. (67).

Bogner *et al.*²⁴³ measured κ of aluminum nitride (AlN) and silicon nitride (Si_3N_4) thin films on silicon (Si) substrates using this method. Figure 30 shows the experimental data for ΔT_s and ΔT_{s+f} measured in the frequency range of 100 Hz to 8 kHz. The temperature difference corresponding to the film can be obtained by subtracting these two temperatures, as exemplified in Fig. 30.

The resulting κ of both AlN and Si_3N_4 increase with film thickness, between 5.4 and 17.6 W m⁻¹ K⁻¹ for AlN and from 0.8 to 1.7 W m⁻¹ K⁻¹ for Si_3N_4 , with thicknesses varying from 300 to 1000 nm. The reduction of κ with decreasing film thickness was shown to be attributed to the shorter mean free path of the phonon due to the grain boundary scattering in thinner films.

Recent work in applying the thermo-resistive atomic force microscopy (AFM) probe to replace the metal heater demonstrates the promise of the 3ω microscopy and AC-modulated scanning thermal microscopy (SThM) techniques.^{247–249} To investigate the local thermal properties, the thermo-resistive probe, which is operated simultaneously as both a heater and a thermometer, has to be in contact with the surface of the sample. If the AFM is operated in contact mode, the conventional 3ω method can be applied to the resistive probe. In this case, an AC with an angular modulation frequency ω is driven through the thermo-resistive probe that causes Joule heating and generates a temperature oscillation at a frequency 2ω . This results in a voltage oscillation along the resistive probe with a frequency-dependent third harmonic voltage component $V_{3\omega}$, which depends on the thermal probe temperature oscillation.²⁴³ Section VD attempts to provide further details on this rapidly developing area.

Next, there are some specific requirements for the 3ω setup. The general working frequency range for this method is typically 0.01 Hz to 5 kHz.²⁵⁰ The dimensions of the thermal resistor (specifically, width and thickness) must be chosen to be appropriate to the working limit of the technique. Thus, the thickness of the RT element must be smaller than the thermal penetration depth of the heat wave. Otherwise, the heat wave may not penetrate the sample beneath the surface, as discussed above. Typically, the width $2b$ varies between 2

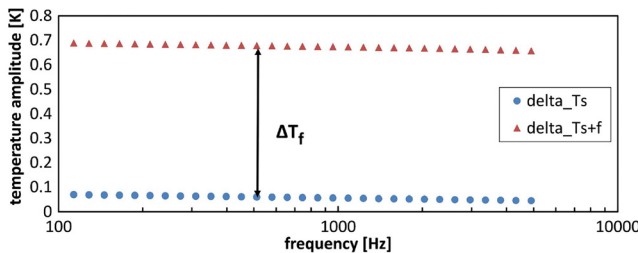


FIG. 30. Measured temperature rise amplitudes for the substrate and film-on-substrate structure with a 1001-nm-thick Si_3N_4 thin film. Triangles represent ΔT_{s+f} of the film-on-substrate structure, which is experimentally measured by detecting the 3ω voltage across the 5.5 μm wide Au heater. The thermal conductivity of the Si_3N_4 is determined by comparing the film-on-substrate structure's temperature amplitude with the Si substrate's corresponding value (circles). Reprinted from Bogner *et al.*, *Thin Solid Films* **591**, 267–270 (2015).²⁴³ Copyright 2015, with permission from Elsevier.

and 500 μm ,^{251,252} the thickness d ranges from 100 to 500 nm,^{243,250} and the length L lies in the range of 3–5 mm.²²⁵

Based on Eq. (52), the real part (in-phase component) of the temperature oscillation remains a linear function of $\ln(2\omega)$ over the frequency range given by²⁵³

$$\frac{25\alpha}{2d_s^2} \leq \omega \leq \frac{\alpha}{50b^2}, \quad (69)$$

where d_s is the substrate thickness. For this, the half-width of the heater b must be much smaller than the penetration depth δ . Moreover, the penetration depth of the thermal oscillation must be smaller than the thickness of the substrate d_s to avoid back-surface reflection. The combined effect of b , δ , and ω on temperature oscillations is illustrated in Fig. 31.

However, the boundaries of the linear regime can only be accurately determined if the value of α is known. Otherwise, a quick frequency sweep can be done to get an experimental linear region. Then, a second and finer frequency sweep is applied to get finer data points.²⁵⁴

Finally, heat losses can be minimized by placing the sample in a vacuum chamber within a temperature-controlled environment.²⁴² Radiative losses can be suppressed by appropriately shielding the 3ω device, while convective losses are minimized by performing measurements in a high-vacuum environment (pressures below 10^{-5} Pa). Conductive losses can be reduced through the use of fine-diameter alloy wires, such as manganin or phosphor bronze.²⁴¹

Advantages of the 3ω method

1. Non-destructive testing technique, it does not change the attributes of the sample after the experiment.²⁵⁵

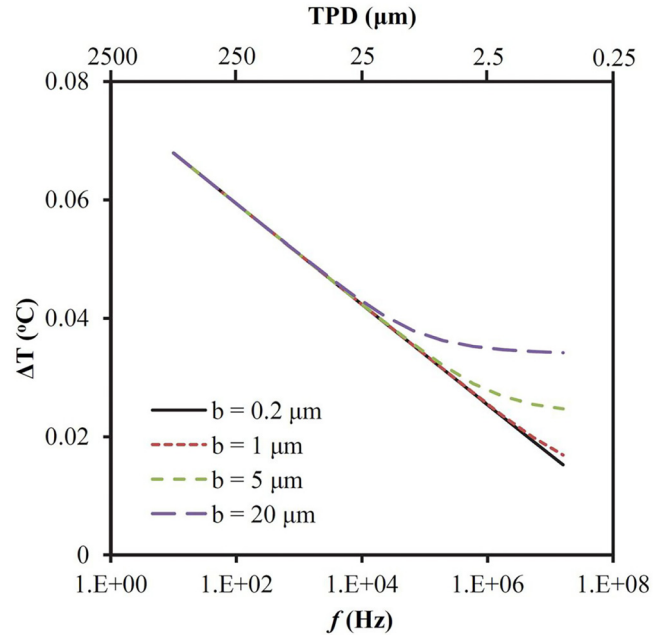


FIG. 31. Effect of width, thermal penetration depth, and frequency of the RT element on the temperature oscillations. Reprinted from Moridi *et al.*, *Surf. Coatings Technol.* **334**, 233–242 (2018);²⁵⁵ licensed under a Creative Commons Attribution (CC BY) license.

2. The RT element is typically maintained within 1 °C of the ambient temperature, thereby minimizing heat loss from the sample to the environment arising from temperature gradients.
3. The small thermal penetration depth associated with AC heating results in negligible radiative and convective losses. Moreover, the region surrounding the heating stripe that is most affected by heat dissipation remains very limited in extent.^{10,21} Consequently, the method can, in principle, be applied under both ambient and vacuum conditions.
4. The error associated with radiative heat losses, when scaled by the characteristic length of the experimental geometry, is substantially reduced. As a result, the contribution of radiation to the overall measurement error remains below 2%, even at elevated temperatures up to 1000 K.^{6,10}
5. Measurements of dielectric, semiconducting, and electrically conducting thin films are possible. For electrically conducting and semiconducting materials, samples must be electrically isolated from the metallic heater/sensor with an additional insulating layer (e.g., a 180-nm-thick film of a-SiO₂).^{256–258}

Limitations of the 3 ω method

1. Although reliable for materials with moderate thermal conductivities,^{10,11,201} the method exhibits reduced accuracy when applied to materials with high thermal conductivity.^{10,255}
2. The differential 3 ω method is only suitable for films with thermal conductivity much lower than the thermal conductivity of the substrate.²⁵⁸
3. Controlling heat penetration at the substrate–film interface presents a significant experimental challenge.¹¹
4. To keep the uncertainty of the differential method within acceptable limits, the temperature drop across the film must exceed both the drop across the dielectric layer and that within the substrate.²⁵⁸
5. Introducing an additional insulating layer for measuring κ in conducting films—used to prevent current leakage through the sample and the generation of spurious third-harmonic signals—inevitably introduces extra thermal resistance, thereby reducing both sensitivity and measurement accuracy.^{48,259}
6. A rough sample surface can cause mechanical failure or rupture of the deposited metal line.

B. Laser flash analysis

In 1961, Parker *et al.*²⁶⁰ introduced the contactless laser flash analysis (LFA) technique, which employs transient heat flux to determine thermal properties. The LFA is a non-steady technique for evaluating the thermal diffusivity, heat capacity, and thermal conductivity of solid materials.^{186,261} The sample is usually planar for thermal conductivity tests and multilayered for thermal contact resistance measurements.¹⁷⁹ The method has also been used to investigate heat transport in composite materials and liquids in a broad temperature range.^{2,7,262,263}

An *et al.*²⁶⁴ reported an effective *in situ* method for κ measurements based on laser-excited Raman spectroscopy, which has the advantages of non-contact, nondestructive, facile preparation, easy operation, and the capability of a large measurement range. At room temperature, the measured thermal conductivities (κ) of Si,

SiC, polycrystalline diamond, and single-crystalline diamond are 140.2 ± 14.4 , 414.7 ± 26.2 , 1372.3 ± 229.0 , and 1734.9 ± 280.6 W m⁻¹ K⁻¹, respectively.²⁶⁴ These results highlight the reliability of Raman spectroscopy for characterizing semiconductor materials, particularly those with high thermal conductivity.

The experimental setup is given in Fig. 32(a). A short-duration laser beam hits the front surface of the sample under study and causes an instantaneous temperature rise on the rear side, which is sensed by an infrared (IR) detector. A typical time-dependent temperature increase on the rear surface is shown in Fig. 32(b).

Uniform surface heating is assumed, reducing heat transfer to a one-dimensional conduction problem. A thin high-emissivity coating, such as graphite, is applied to maximize light absorption on the front surface and enhance infrared emission from the rear.^{179,266} This coating improves the absorption of the laser pulse and infrared emission, both are critical for accurate measurements of κ . The thickness of this coating is important; it must be thin enough to avoid acting as a thermal barrier, yet thick enough to ensure uniform energy absorption. If too thick, it can skew the results by preventing effective heat transfer, but, if too thin, it may not adequately enhance the surface absorptivity and emissivity. Therefore, optimal coating thickness is essential for precise measurements of κ .

Consider a thin film of thickness d , which is instantaneously heated across its entire surface at $t = 0$. The subsequent temperature evolution at time t and depth x can be expressed as

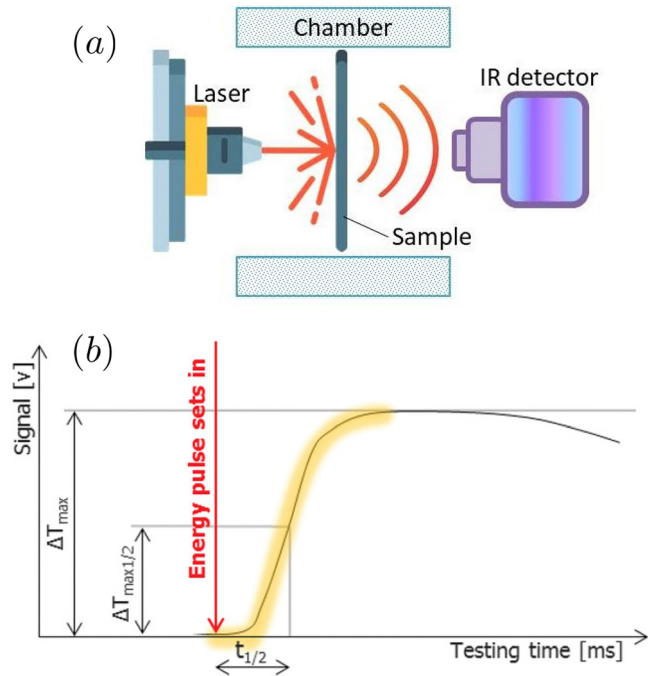


FIG. 32. (a) Schematic of the LFA method. (b) A typical time evolution of the rear side temperature, as sensed by an infrared detector. An increase in thermal diffusivity leads to faster heat propagation and a more rapid rise in the rear-side temperature. Laser icon in (a)—Free PNG from www.freepik.com/icons/laser. Reprinted from Weingrill *et al.*, Macromol. Mater. Eng. **304**, 1800644 (2019),²⁶⁵ licensed under a Creative Commons Attribution (CC BY) license.

$$\vartheta(\xi, \tau) = \int_0^1 \vartheta(\xi', 0) d\xi' + 2 \sum_{n=1}^{\infty} e^{-n^2 \pi^2 \tau} \cos n\pi\xi \int_0^1 \vartheta(\xi', 0) \cos n\pi\xi' d\xi', \quad (70)$$

where the following dimensionless variables are introduced: $\vartheta = \rho CT/Q$, with Q being the applied heat flux; $\xi = x/d$, the normalized spatial coordinate; and $\tau = \alpha t/d^2$, the normalized time, with d denoting the slab thickness, ρ the mass density, C the specific heat capacity, and α the thermal diffusivity. At $\xi = 1$,

$$\vartheta(1, \tau) = 1 + 2 \sum_{n=1}^{\infty} (-1)^n e^{-n^2 \pi^2 \tau}. \quad (71)$$

The thermal diffusivity is computed from the temperature rise vs time as²⁶⁷

$$\alpha = 0.138795 \frac{d^2}{t_{1/2}}, \quad (72)$$

where $t_{1/2}$ is the time taken to the rear surface to attain half its maximum temperature [see Fig. 33]. Once the density ρ and specific heat capacity C are determined, the thermal conductivity can be obtained from $\kappa = \alpha \rho C$.

The LFA method is widely employed to characterize a broad range of materials, but its applicability is limited by sample thickness. This restriction arises from the finite duration of the heating pulse and the response time of the infrared detector. Conventional instruments are typically suited for samples with thicknesses on the order of 10–100 μm or greater, depending on the material's thermal conductivity.²⁶⁶ Nonetheless, several studies have demonstrated that LFA can also provide valuable measurements of κ in nanostructured materials (see Sec. V G).

Advantages of LFA

- Neither absolute temperatures nor heat measurements are necessary. The thermal diffusivity is measured by capturing the relative temperature change as a function of time. Consequently, the relative measurement uncertainties are only 3–5% even at high temperatures.^{268,269}

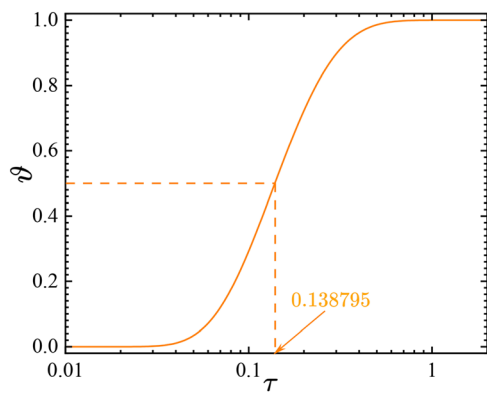


FIG. 33. $\vartheta(1, \tau)$ as a function of τ . The value of τ corresponding to $\vartheta = 1/2$ is indicated with a dashed line in the graph.

- Easy sample preparation, high accuracy, and repeatability.²⁷⁰
- Advantages of the contactless approach with non-destructive high-accuracy temperature sensing.²⁷¹
- During the measurement, the convective heat transfer can be neglected.
- The measurement time is typically as small as 1–2 s for most materials, thus minimizing the heat losses.
- Measurements can be made in a spacious temperature range, spanning from high (3000 °C) to cryogenic (−125°C) temperatures,^{7,214,272} and wide range of thermal diffusivities (0.1–1000 mm^2/s).²⁷³

Limitations of LFA

- The boundary conditions for the LFA technique require the heat pulse to be uniform and of short duration compared to the transient time through the sample, which itself should be sufficiently short to avoid heat losses. Since ideal boundary conditions are rarely met in experiments, real-life corrections are needed to improve the accuracy.^{261,267}
- Material density and specific heat must be separately measured to obtain κ , which may reduce the accuracy of the technique.
- Experimentally, measuring α in thin films with $d < 1 \mu\text{m}$ remains highly challenging.
- Estimating sensitivity and correcting for errors such as heat loss and finite heating pulses is inherently complex.^{267,274,275}

C. Time-domain thermoreflectance

A noncontact optical heating and sensing technique called transient thermoreflectance was first developed in the 1970s and 1980s and is used to quantify thermal characteristics (such as thermal conductivity, heat capacity, and interfacial thermal conductance) in both bulk and thin film materials. The thermoreflectance approach implies sample heating by continuous wave (CW) light.^{276,277} Transient thermoreflectance can be implemented in either the time or frequency domain. TDTR is a robust way to measure thermal transport using temperature-variated reflectance. In 1986, Paddock and Eesley²⁷⁸ introduced TDTR to measure the thermal diffusivity of metallic thin films using transient picosecond thermoreflectance. TDTR has been applied to analyze the acoustic and thermal properties of a wide range of materials, including thin films,^{279,280} bulk samples,²⁸¹ liquids,²⁸² and interfaces.²⁸³ Recently, TDTR has been used in a diamond anvil cell to measure the thermal conductivity as a function of pressure.²⁸⁴

TDTR is a transient, non-contact optical technique that determines κ using pump-probe measurements with mode-locked laser oscillators. In a TDTR setup, the light source is a mode-locked Ti:sapphire laser oscillator with an ultrafast speed and exceptional beam quality. Figure 34(a) shows a typical schematic of the TDTR setup. In this configuration, the laser beam (150 fs pulses at an 81 MHz repetition rate) is shaped into a circular profile using cylindrical lenses. The pump is modulated between 0.2 and 20 MHz via an electro-optical modulator (EOM), while the probe can be delayed by up to 12 ns. Both beams are focused onto the sample at spots separated by 4 mm. Similar setups can be found in the literature.^{285–288} The use of cylindrical lenses also allows to measure the in-plane anisotropy.¹⁸⁹ In the TDTR technique, the sample should be metallic or have a metallic coating on top with a typical thickness of around 50–100 nm. This

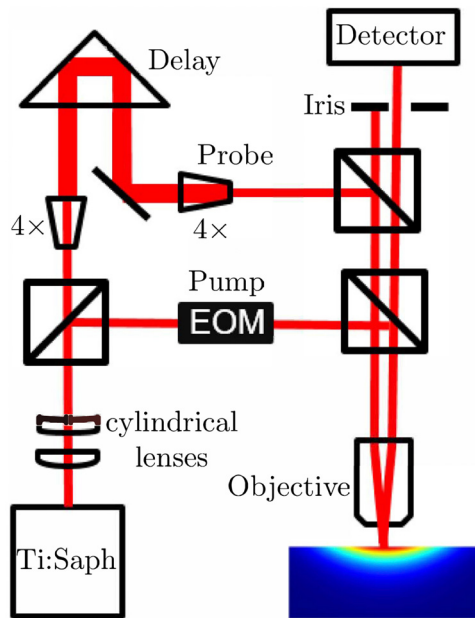


FIG. 34. Schematic of the TDTR setup. Reprinted from Jiang *et al.* Rev. Sci. Instrum. **88**, 074901 (2017).¹⁸³ Copyright 2017, with permission from AIP Publishing.

layer behaves as a temperature transducer layer that absorbs the heating pump beam as well as converts the oscillations of the surface temperature into variations in the reflected probe beam intensity.²⁵⁸ In this way, irradiation by a laser pulse produces a transient oscillatory temperature change that alters the surface reflectance, which is monitored by the probe beam. The probe, carrying a frequency component corresponding to the pump modulation, is then directed onto a photodetector. Since reflectance changes are on the order of 10^{-4} K^{-1} ,²⁸⁹ a lock-in amplifier is used to detect the small variations in probe intensity filtering the strong background noise.²⁹⁰ The pump modulation signal is introduced into the lock-in amplifier as a reference signal. The concentrically aligned reflected intensity signal has both in-phase (V_{in}) and out-of-phase (V_{out}) voltage components without errors arising from the spot size of a laser.²⁹¹ After heating by the laser pulses, there will be a sudden jump in surface temperature followed by a moderate cooling process, as shown in Fig. 35. The cooling process is recorded by tracking the variations in the in- and out-of-phase voltage components, $R = -V_{in}/V_{out}$, of the lock-in amplifier while changing the time delay between the probe and pump beams.^{183,258,292} Finally, the thermal properties can be extracted (κ as well as interfacial thermal resistance of the sample) by fitting the voltage ratio R to theoretical models of heat transfer and optimizing the free parameters.^{179,287,291}

To demonstrate this approach, Jiang *et al.*²⁹⁰ used the TDTR method on a GaN substrate with 100-nm Al as a transducer layer. The measured ratio R of the in-phase and out-of-phase voltage components is compared with thermal models to extract the κ of GaN, as shown in Fig. 36.

The thickness range of the samples that can be measured using TDTR is only constrained by the thermal penetration depth δ , given by Eq. (26), i.e.,

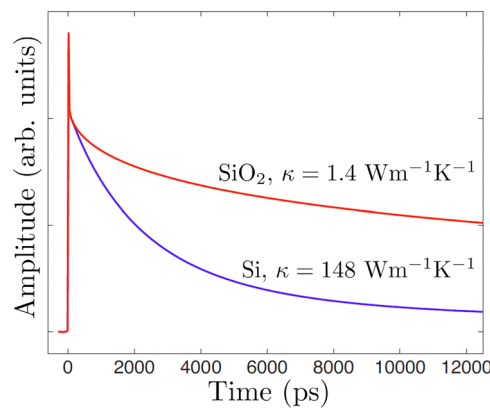


FIG. 35. Diagram showing how the thermoreflectance signal has evolved for a sample consisting of a 100-nm Al layer on Si and SiO_2 substrates. Reprinted from Schmidt *et al.*, Rev. Sci. Instrum. **79**, 114902 (2008).¹⁸⁰ Copyright 2008, with permission from AIP Publishing.

$$\delta = \sqrt{\frac{2\alpha}{\omega}} = \sqrt{\frac{2\kappa}{\rho C \omega}}. \quad (73)$$

By varying the modulation frequency of the pump, one can change the thermal penetration depth, allowing the study of buried interfaces and defects located at various depths below the surface of the sample.²⁹³ Boughez *et al.*²⁹⁴ used the TDTR method to measure κ and thermal boundary resistance of GaN thin films, grown by MOCVD on Si substrates, with thicknesses ranging from 0.31 to $1.27 \mu\text{m}$. The measured κ values do not change with thickness and show excellent agreement with the literature values (Fig. 37).²⁹⁴

By adjusting the laser spot size and modulation frequency, TDTR can probe various thermal properties under various regimes of heat transport.^{180,295} The heat transport regime is primarily determined by two length scales: the laser spot size r_0 , affecting lateral spreading, and the thermal penetration depth δ , set by periodic heating. In TDTR measurements, when the laser spot size is much larger than the thermal penetration depth in the cross-plane direction, heat flow is effectively confined to one dimension, producing a primarily cross-plane temperature gradient [see Fig. 38(a)]. In this case, the surface temperature change is predominantly affected by the cross-plane thermal conductivity κ_{\perp} . In contrast, if the laser spot is tightly focused such that its radius r_0 is of the order of the thermal penetration depth δ , heat spreads both laterally and vertically, producing a three-dimensional temperature gradient, as shown in Fig. 38(b). In this mode of heat transfer, the surface temperature response depends on both κ_{\parallel} and κ_{\perp} , which can be extracted by conducting measurements with two different spot sizes. By adjusting the modulation frequency, the penetration depth can be controlled following $\delta \sim \omega^{-1/2}$ [see Eq. (26)]. Accordingly, in anisotropic TDTR measurements, the standard procedure is to determine κ_{\perp} under conditions of a large spot size and high modulation frequency, where cross-plane transport dominates. This value is then fixed in the heat transfer model to extract κ_{\parallel} from measurements performed with a small spot size and low modulation frequency.¹⁸⁰ However, it is important to note that this approach assumes κ_{\perp} remains the same under both measurement conditions, even though experimental^{296–299} and theoretical^{300,301} studies indicate that, for some materials, κ_{\perp} can vary with the modulation frequency.

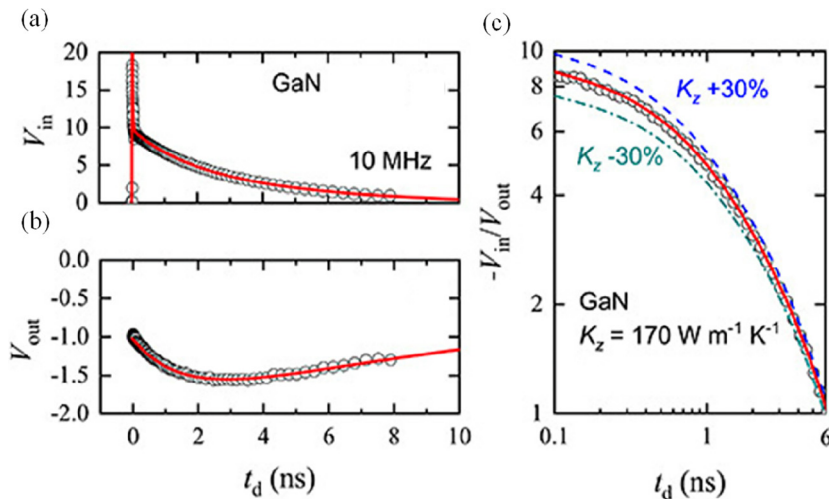


FIG. 36. (a,b) An illustration of in-phase and out-of-phase data as a function of delay time for GaN substrate. (c) Ratio $R = -V_{in}/V_{out}$ as a function of delay time, fitted to the expected thermal behavior to deduce the thermal conductivity of the GaN substrate. Reprinted from Jiang *et al.*, J. Appl. Phys. **124**, 161103 (2018)²⁹⁰. Copyright 2018, with permission from AIP Publishing.

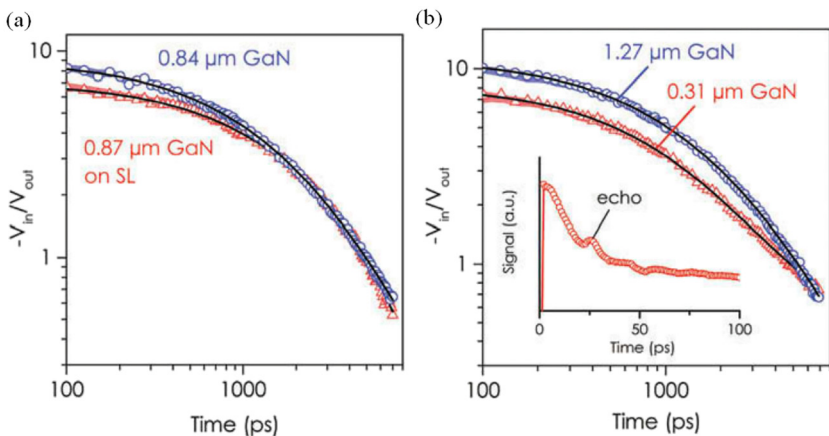


FIG. 37. TDTR data for different thicknesses of the GaN thin films. Reprinted from Boughe *et al.*, Nanoscale and Microscale Thermophys. Eng. **20**, 22–32 (2016)²⁹⁴. Copyright 2016, with permission from Taylor & Francis.

Advantages of TDTR

1. A fully non-contact technique with high spatial resolution, capable of measuring κ without prior knowledge of the volumetric heat capacity C .³⁰²
2. Unlike the 3ω method, TDTR is more flexible regarding sample dimensions, requiring only an optically smooth area smaller than $100 \times 100 \mu\text{m}^2$.¹⁸³

Limitations of TDTR

1. The TDTR technique relies on pulsed laser heating, with changes in reflectance measured as a function of the temporal delay between the pump and probe beams. The range of thermal conductivity values that TDTR can accurately resolve is limited by both the modulation frequency and the laser spot size. In TDTR, the modulation frequency typically ranges from 0.2 to 20 MHz. Operating below 0.2 MHz is challenging because the $1/f$ noise degrades the signal-to-noise ratio, while the accumulation of strong pulses introduces significant phase uncertainty. At modulation frequencies above 20 MHz, TDTR measurements are limited by weak out-of-phase signals as well as the high

susceptibility of detectors and cables to radio-frequency noise.^{180,290,295}

2. Drawbacks of TDTR include its complex experimental setup, sophisticated data reduction process, and the need for surface coating.
3. The sample surface must be smooth to minimize diffuse reflections during TDTR measurements.^{290,295}

D. Frequency-domain thermoreflectance

A related thermoreflectance approach is the frequency-domain thermoreflectance (FDTR), in which measurements are based on the dependence of the thermoreflectance signal on the pump beam modulation frequency. Schmidt *et al.* first introduced the method in 2009.¹⁸⁴ More recently, Kirsch *et al.*³⁰³ provided a detailed account of unpublished insights and institutional knowledge that are critical for achieving accurate and repeatable measurements of thermal properties using FDTR. This versatile technique is closely linked to TDTR, since the same experimental setup (see Sec. III C) can be adapted for FDTR by fixing the delay stage at a specific position and sweeping the

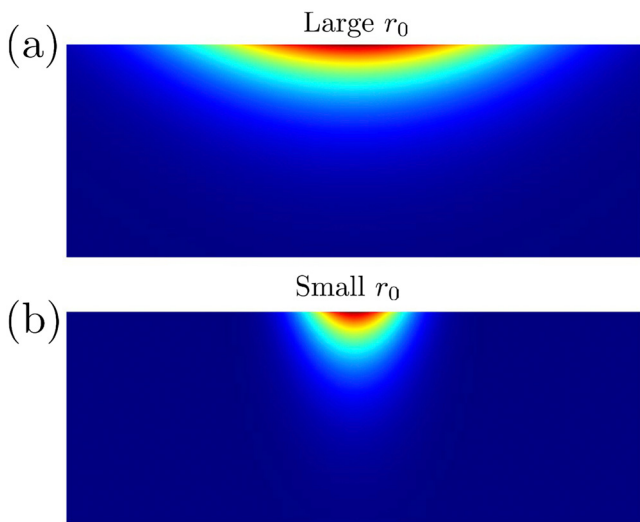


FIG. 38. Different heat transport regimes achieved by changing the laser spot size from (a) a large (which is mainly one-dimensional) to (b) a tightly focused (three-dimensional). Reprinted from Jiang *et al.*, Rev. Sci. Instrum. **88**, 074901 (2017).¹⁸³ Copyright 2017, with permission from AIP Publishing.

modulation frequency. Unlike TDTR, however, FDTR uses a fixed probe delay, thereby eliminating complications such as beam drop and divergence that are typically associated with a mechanical delay stage. An FDTR system can also be realized with cost-effective CW lasers, enabling thermal conductivity measurements of bulk materials and sub-micrometer films with accuracy comparable to that of TDTR. FDTR employs the same spot geometry and analytical framework as TDTR; however, the independent experimental variable is the modulation frequency rather than the pump–probe time delay.¹⁸⁴ To ensure optical opacity of the transducer film and to suppress spurious thermoreflectance contributions from the underlying temperature field, the film thickness is typically required to exceed 50 nm.³⁰⁴

In FDTR, the sample surface is periodically heated by an intensity-modulated pump laser, as shown in Fig. 39. The periodic excitation generates thermal oscillations that propagate through the material, producing a temperature field that varies both spatially and temporally. This thermal response is then monitored by a probe beam, enabling the extraction of the material's thermal properties.

In the following discussion, the thermal penetration depth, as defined in Eq. 73, must be considered. When the modulation frequency is below (above) the critical frequency, the sample is classified as thermally thin (thick). As in TDTR, the sample surface in FDTR is typically coated with a thin metal transducer film, which functions as an absorbing layer to ensure efficient pump-laser absorption.

A continuous-wave (unmodulated) probe laser is employed to monitor the thermal response of the sample. The probe wavelength must be carefully selected to maximize the thermoreflectance signal, as the reflectivity of the metal transducer film—and thus the measurement sensitivity—depends on this wavelength. For a typical probe wavelength of 532 nm, gold is widely regarded as the ideal transducer material.³⁰⁵ The thermoreflectance signal is influenced by multiple factors, including optical absorption, light polarization, electronic band transitions, and electron–phonon coupling.³⁰⁶ Consequently, the

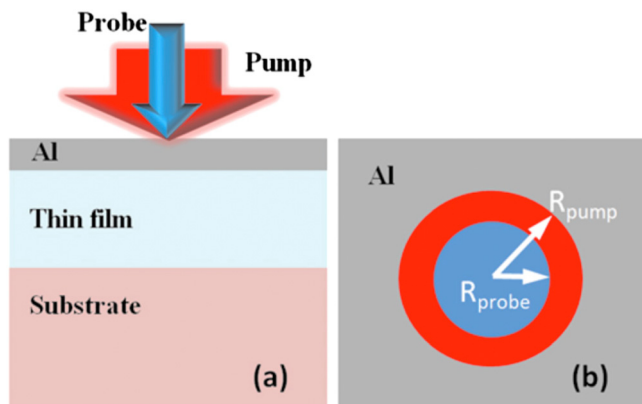


FIG. 39. Schematic view of the sample for FDTR experiment: (a) sectional view and (b) top view. Reprinted from Zhu *et al.*, J. Appl. Phys. **108**, 094315 (2010).²⁸⁷ Copyright 2010, with permission from AIP Publishing.

choice of transducer material and probe wavelength plays a critical role in measurement accuracy. Temperature-induced strain at the sample surface alters the optical constants, leading to a corresponding change in reflectivity ($\Delta\mathcal{R}$), a phenomenon known as the thermoreflectance effect.³⁰⁷ Within the transducer, the relative change in reflectivity ($\Delta\mathcal{R}/\mathcal{R}$) varies linearly with small temperature fluctuations (ΔT).⁸

$$\frac{\Delta\mathcal{R}}{\mathcal{R}} = \left(\frac{1}{\mathcal{R}} \frac{\delta\mathcal{R}}{\delta T} \right) \Delta T = \beta_{TR} \Delta T, \quad (74)$$

where β_{TR} denotes the thermoreflectance, which typically ranges from 10^{-5} to 10^{-3} K⁻¹. Both the pump and probe beams are focused through a single microscope objective on spots with $10 - 20 \mu\text{m}$ in diameter. The laser beams can be either CW or pulsed as suggested by Schmidt *et al.*¹⁸⁴ The corresponding setups for FDTR are shown in Fig. 40. In a continuous-wave laser configuration, two CW lasers are employed. The pump beam is modulated by the EOM, producing a periodic heat flux on the sample surface, while the probe beam is directed onto the surface without passing through a mechanical delay stage. Compared to frequency-domain thermoreflectance (FDTR) systems that rely on ultrafast lasers and mechanical delay stages, this arrangement is simpler, more cost-effective, and easier to implement. Despite its reduced complexity, it has been successfully applied to measure the thermal conductivity of various thin-film materials with a precision comparable to that of TDTR.^{279,287,308}

The second configuration employs a pulsed laser and is closely analogous to the TDTR setup. In this approach, the pump and probe beams are typically derived from the same laser source and separated using a beamsplitter. The temporal separation between pump and probe pulses is controlled by an optical delay line, which introduces a delay time τ_d .

A lock-in amplifier records the amplitude and fundamental phase lag between the reflected probe beam and thermal oscillation at the modulation frequency as shown in Fig. 41. To extract the thermal properties of the sample, the measured phase lag is fitted over a range of modulation frequencies using appropriate heat conduction models.^{180,195,279,291,309,310} In practice, parameters such as the volumetric heat capacity, density, and dimensions of the sample, along with the

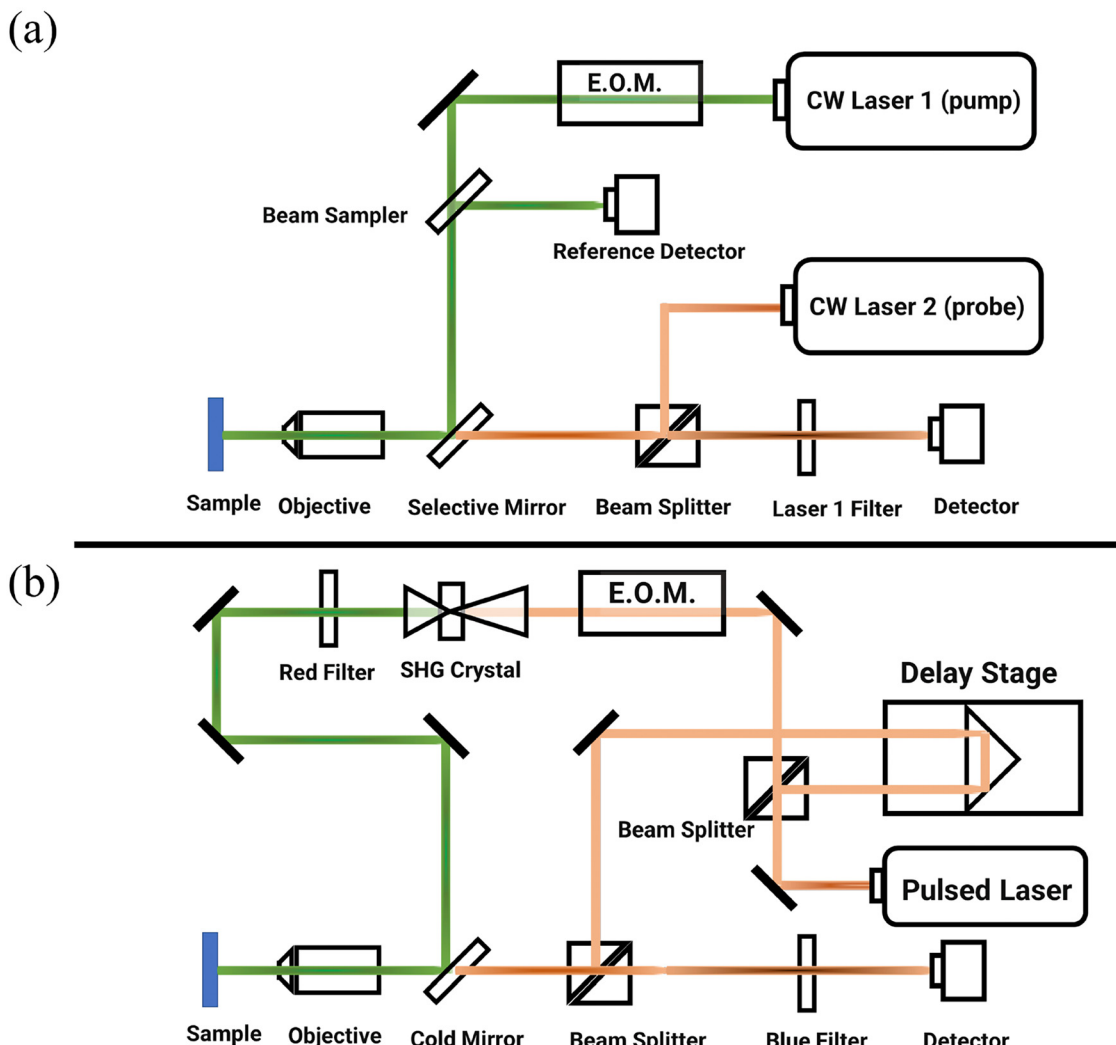


FIG. 40. (a) CW laser-based FDTR system. The pump laser (1) is modulated via an electro-optic modulator (EOM), while the probe laser (2) detects the thermoreflectance signal. Both beams are coaxially focused onto the sample through a single objective, and a reference detector determines the pump phase in the sample. (b) Pulsed laser FDTR setup. Each pulse is split into pump and probe, with the probe delayed by a mechanical stage. The pump passes through an EOM and a second harmonic generation crystal before reaching the sample. Reprinted from Schmidt *et al.*, Rev. Sci. Instrum. **80**, 094901 (2009).¹⁸⁴ Copyright 2009, with permission from AIP Publishing.

20 December 2025 13:48:09

thermal properties of the transducer film, are incorporated into these models to determine the thermal conductivity (κ). Because pulsed and CW FDTR systems yield different phase responses, it is essential to apply the appropriate analysis framework when interpreting the signals from each configuration.

A central question is whether pump-probe thermoreflectance techniques can truly achieve the precision necessary for accurate determination of thermal parameters, given the persistent challenges of signal interpretation, model assumptions, and experimental uncertainties. Recently, Chatterjee *et al.*³¹¹ have made advances in achieving high precision measurements with a new fitting algorithm concurrently incorporating both phase and amplitude for the assessment of cross-plane thermal transport properties. The errors in estimating thermal conductivity, thermal boundary resistance and thermal diffusivity are

approximately 2.4%, 2.5%, and 3.0%, respectively. The application of extended data analysis techniques, particularly through advanced deep learning approaches, can significantly enhance the accuracy and precision of thermoreflectance techniques. Although deep learning models have demonstrated improvements in fitting quality and in the precision of uncertainty estimation compared with traditional Monte Carlo simulations, their performance remains strongly dependent on the quality of the training data, the choice of network architecture, and the potential for overfitting.

Advantages of FDTR

1. Building on the advantages of TDTR, FDTR likewise provides a non-contact technique that requires only a minimal surface area for heating and probing.

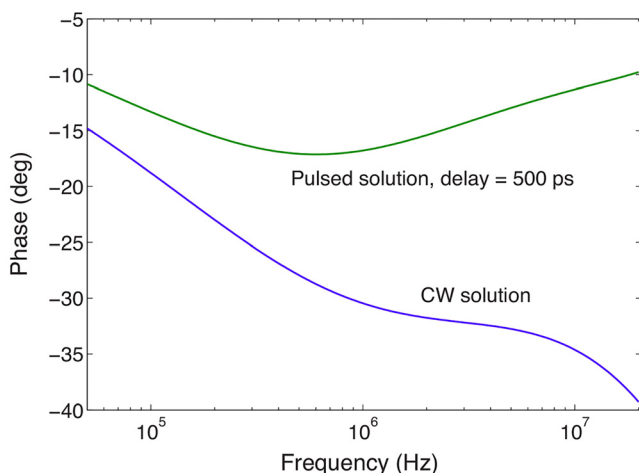


FIG. 41. Phase response for continuous-wave and pulsed FDTR measurements of 100-nm Al on sapphire with the frequency range of 50 kHz–20 MHz. Reprinted from Schmidt *et al.*, Rev. Sci. Instrum. **80**, 094901 (2009).¹⁸⁴ Copyright 2009, with permission from AIP Publishing.

- Many limitations of TDTR can be avoided by employing FDTR, which enables the characterization of the thermal properties of both bulk materials and thin films without the need for a moving stage or an ultrafast pulsed laser.²⁸⁷
- FDTR is simpler to implement, as it does not involve the complexity of a lengthy mechanical time delay. Unlike TDTR, it does not require an expensive pulsed laser.
- FDTR is capable of measuring a wide range of thermal conductivity values, from approximately 1 to 250 W m⁻¹K⁻¹.²⁸⁷
- In addition to bulk materials, FDTR can accurately measure thin films with thicknesses from tens of nanometers to several micrometers, allowing for precise determination of the thermal penetration depth.^{184,279}

Limitations of FDTR

- The method typically requires a thin metal transducer layer (~100 nm) on the sample, serving as an absorbing layer with a high thermorelectance coefficient at the probe wavelength.³¹² However, recent advances have shown that the transducer layer can be omitted for opaque samples, significantly improving sensitivity to in-plane thermal transport.¹⁹⁷
- Similarly to TDTR, FDTR can be costly and challenging to operate, as it generally requires detection of the phase shift of the signal while accounting for instrument-induced electronic phase shifts, in addition to requiring prior knowledge of the heat capacity of the material.⁸

IV. THERMAL CONDUCTIVITY IN ULTRA-THIN MATERIALS

With their precisely controllable thickness, 2D materials exhibit remarkable electrical,^{313,314} thermal,^{315–318} optical,^{319,320} and mechanical^{321,322} properties. The advent of 2D materials has opened a new frontier in integrated flexible technologies.³²³ Owing to these unique

attributes, they are highly attractive for diverse applications, including wireless health monitoring systems,^{324–327} flexible bioelectronics,^{328–330} and origami-inspired device architectures designed for unconventional and demanding environments.^{331–333} A wide variety of 2D materials have been extensively investigated for such purpose (Fig. 42), including graphene, transition-metal dichalcogenides (TMDs), transition-metal oxides (TMOs), black phosphorus (BP), hexagonal boron nitride (hBN), MXenes, and 2D perovskites.^{334,335}

Because of their ultrathin nature, the thermal properties of 2D materials are strongly governed by surface scattering of acoustic phonons. Consequently, precise thermal characterization techniques are critical for understanding and optimizing heat transport in these systems.

As in many other materials, when the characteristic dimensions of a sample become comparable to the average length of the phonon scattering or the mean free path Λ , the assumptions underlying the classical heat conduction models begin to break down; see Sec. II D). In this regime, thermal transport can no longer be fully described by bulk parameters such as the thermal conductivity, which assume diffusive phonon motion and size-independent behavior. Instead, boundary scattering, phonon confinement, and nondiffusive heat flow give rise to pronounced size effects, making the effective thermal properties strongly dependent on the sample geometry and characteristic length scales. Simply put, when the characteristic sample length in the direction of heat flow, l , becomes much smaller than the phonon MFP, the nature of thermal transport undergoes a fundamental change. In this regime, phonons propagate ballistically, that is, without undergoing internal scattering events, and the thermal conductance approaches the ballistic limit G_{bl} , which is determined solely by the available phonon modes and their temperature-dependent occupation. If the conventional diffusive relation between thermal conductivity and conductance given by Eq. (2), is naively applied to such short samples, the inferred thermal conductivity becomes explicitly size-dependent. As l decreases further into the deep ballistic limit, this effective conductivity approaches zero, illustrating that thermal conductivity, as a property of the bulk-defined material, loses its physical meaning in this regime. Recent efforts have characterized ballistic thermal conductance in one- and two-dimensional systems with relatively simple geometries, including carbon nanotubes,^{13,337} silicon nanostructures,³³⁸ and in-plane transport in graphene.³³⁹ These studies have provided valuable benchmarks for understanding the maximum heat carrying capacity of materials at the nanoscale. However, the ballistic thermal limits of other two-dimensional systems, particularly along their cross-plane transport direction, remain largely uncharted. This knowledge gap is significant because layered materials exhibit highly anisotropic phonon dispersions, and their cross-plane transport is often dominated by weak van der Waals interactions, which may fundamentally alter ballistic transport behavior compared to their in-plane counterparts. In a broader context, while the concept of ballistic transport is well established and widely studied in the field of electrical conduction, the corresponding understanding of phonon-mediated heat conduction is much less mature. This disparity highlights the need for systematic studies of ballistic thermal transport across different material classes and dimensionalities, as such insights are essential not only for advancing fundamental phonon physics but also for guiding the thermal management strategies of next-generation nanoscale and quantum devices, where size effects dominate energy dissipation.

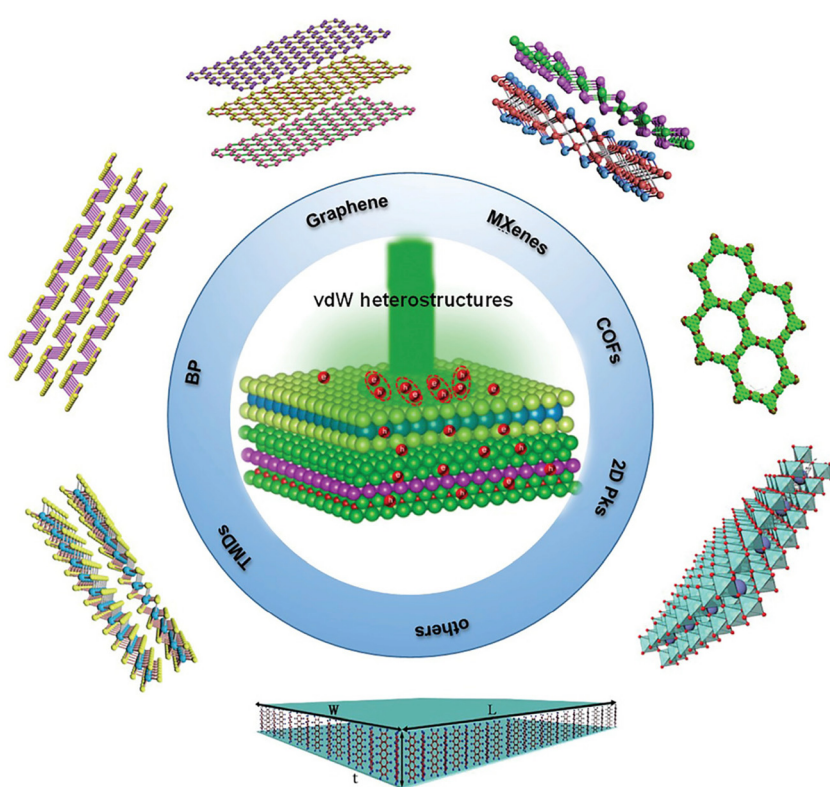


FIG. 42. Schematic illustration of various kinds of 2D materials. Reprinted from Zhang et al., *Adv. Sci.* 7, 2002697 (2020).³³⁶ licensed under a Creative Commons Attribution (CC BY) license.

Experimentally, however, probing ballistic heat transport remains a highly challenging task. Measurements in this regime demand precise control over sample dimensions and surface quality to minimize unintended scattering, as well as ultrahigh spatial and temporal resolution to isolate ballistic contributions from diffusive backgrounds. Additional complications arise from thermal contact resistance at interfaces, which can obscure intrinsic transport properties, and from the difficulty of accurately calibrating temperature gradients at the nanoscale. These obstacles explain why the experimental literature on ballistic phonon transport is still relatively sparse and why theoretical predictions often precede experimental verification.

It is well-known that individual 2D materials tend to exhibit characteristic limitations in certain devices. However, as soon as they are rationally stacked or assembled with two or more 2D materials, synergistic effects can arise, thus greatly enhancing their performance.³³⁴ Therefore, numerous 2D heterostructures involving well-defined heterojunctions and heterointerfaces were manufactured using various preparation techniques, for example mechanical exfoliation, aligned transfer, chemical vapor deposition, liquid phase exfoliation and layer-by-layer assembly, and advanced characterization techniques have been designed. So far, numerous experimental techniques have been developed to characterize thermal conductivity in 2D materials. However, performing reliable thermal transport studies over a broad thickness range, down to the molecular monolayer, is challenging. Experimental approaches can be susceptible to thickness-dependent artifacts and require reproducible fabrication of many clean samples with controlled thicknesses.

In this section, we begin with a review of optical methods, including Raman thermometry, the bolometric method, and time-domain thermoreflectance. We then examine electrical techniques, such as the suspended thermal bridge method and the 3ω method.

A. Raman thermometry technique

Raman spectroscopy is certainly a very direct technique of examining molecular vibrational modes and phonons in solids. It is probably the most powerful technique for studying the effect of stress in semiconductor nanostructures, originated by lattice mismatch or differences in the expansion coefficients of their components. This technique involves the analysis of inelastically scattered light produced by a monochromatic laser beam interacting with a material.

Recently, the Raman thermometry technique has become a common method to determine the thermal conductivity in 2D materials, reaching the limit of a monolayer-thick material.^{30,340–348} The heating of the sample by the laser beam affects the peak position of the phonons due to anharmonicity and lattice expansion. Thus, monitoring the peak position can be the most straightforward method of determining temperature. This method requires a previous calibration of the phonon shift with temperature.

Another method is to determine the temperature from the ratio of the anti-Stokes to Stokes signal strengths of a given Raman peak based on the Boltzmann distribution. The Stokes shift corresponds to phonon emission and the scattered efficiency contains the term $N + 1 \approx 1$ in most cases, where N is the phonon population, while the

efficiency of the anti-Stokes component is directly proportional to the phonon population N , thus at low temperatures the anti-Stokes signal is very weak. In thermal equilibrium, the phonon population is replaced by the Boltzmann distribution function.

The relative occupation of the phonon absorption term divided by that of the phonon emission can be derived from the Boltzmann distribution such that

$$\frac{I_{AS}}{I_S} \propto e^{-\hbar\omega_0/k_B T}, \quad (75)$$

where I_S and I_{AS} are the Stokes and anti-Stokes Raman intensities, respectively, and $\hbar\omega_0$ is the phonon frequency.

The frequency dependence of the inelastic Stokes and anti-Stokes Raman scattering processes depend on the laser and scattered frequencies^{349,350}

$$I_S \propto \omega_l(\omega_l - \omega_0)^3 \quad (76)$$

while

$$I_{AS} \propto \omega_l(\omega_l + \omega_0)^3, \quad (77)$$

where ω_l is the frequency of the incident laser light, and $\omega_l - \omega_0$ and $\omega_l + \omega_0$ are the scattered frequencies of the Stokes and anti-Stokes components, respectively. Combining Eqs. (75)–(77) results in the following ratio of the anti-Stokes/Stokes Raman intensities:

$$\frac{I_{AS}}{I_S} = \frac{(\omega_l + \omega_0)^3}{(\omega_l - \omega_0)^3} e^{-\hbar\omega_0/k_B T}. \quad (78)$$

In this method, the detection scheme of the Raman signal plays a critical role. When the spectra are acquired using a charge-coupled device (CCD) detector, which is a photon counting device, Eq. (78) is more appropriate for the analysis of the data while the following expression is derived for an energy-based detection of the scattered light:³⁵¹

$$\frac{I_{AS}}{I_S} = \frac{(\omega_l + \omega_0)^4}{(\omega_l - \omega_0)^4} e^{-\hbar\omega_0/k_B T}. \quad (79)$$

The Maxwell-Boltzmann distribution function is applicable to values of $k_B T \gg \hbar\omega_0$, otherwise the Bose-Einstein statistics must be applied, although the difference between applying these two distributions disappear when the I_{AS}/I_S ratio is applied.³⁵⁴

Once the vibrational frequency and intensity ratio are known, the temperature is extracted without material-dependent parameters. Raman measurements using the anti-Stokes/Stokes ratio can be spatially resolved to nanometer length scales³⁵⁵ or temporally resolved to nanosecond³⁵⁶ or picosecond time scales.³⁵⁷ Meanwhile, there are several key challenges in the practical implementation of this technique.^{352,353} First, a significant difference exists between the Stokes intensities, even at low or room temperature, owing to the low phonon population. In materials with multiple phonon modes, the low-energy phonons contribute more strongly to the anti-Stokes signal. Second, the relationship between the anti-Stokes-to-Stokes intensity ratio and temperature becomes increasingly complex over a broad temperature range. This complexity arises from phonon frequency shifts induced by anharmonic effects and thermal expansion, which reduce the suitability of low-frequency optical phonons for accurate temperature

measurements. Third, the high-temperature limit of the technique is often determined by the black-body emission of the sample that competes with the ability to measure Raman signals. Low-level fluorescence, comparable to the Raman intensity, is often observed at all temperatures and must be isolated to determine accurate Raman intensities.

To analyze the heating effect on the Raman shift, consider the schematic design of a graphene sheet suspended on a hole with radius R made in a Au-coated SiN_x support, serving to ensure good thermal contact, as shown in Fig. 43(a). The calculation of κ is based on the heat diffusion equation, solved in cylindrical coordinates [Fig. 43(b)]. For the steady-state heating of a thin film, e.g., the graphene layer shown in Fig. 43(a), the energy transport in the sample is governed by the radial (r) component of the differential equations given in Sec. II A. For simplicity, we assume that the laser beam is focused in the center of the suspended graphene at $r = 0$. The measured Raman shift is markedly smaller when the laser is focused on supported graphene compared with the center of suspended graphene. This reduction arises because heat transfer from the supported graphene to the underlying metal substrate [Au in Fig. 43(a)] lowers the temperature rise, $\Delta T_2(r) = T_2(r) - T_0$, in the supported region relative to that in the suspended graphene, $\Delta T_1(r) = T_1(r) - T_0$, where T_0 denotes the ambient temperature in the absence of laser irradiation (typically room temperature).

The measured Raman shift is much smaller when the laser beam is focused on the supported graphene than at the center of the suspended graphene because heat transfer from the supported graphene to the metal support [Au in Fig. 43(a)] results in lower temperature rise $\Delta T_2(r) = T_2(r) - T_0$ in the supported graphene than in the suspended graphene $\Delta T_1(r) = T_1(r) - T_0$ with T_0 being the temperature without laser irradiation (typically room temperature). To calculate the in-plane thermal conductivity, one must analyze the temperature distribution across the sample in both the suspended and supported regions. After the thermal map or local temperature rise is obtained, the thermal properties of the sample can be deduced using an appropriate heat diffusion model.

To model the temperature distribution in the suspended region, the heat diffusion equation is used as follows:^{340,358}

$$\frac{\kappa}{r} \frac{d}{dr} \left[r \frac{d\Delta T_1(r)}{dr} \right] = -q_r \quad \text{for } r \leq R, \quad (80)$$

where q_r is the heat flux due to laser-induced heating, which may be written as

$$q(r) = \frac{P}{\pi r_0^2 d_f} e^{-r^2/r_0^2}, \quad (81)$$

where P is the absorbed laser power at the center of the beam spot, and

$$r_0 = \frac{\lambda_0}{\pi N A} \quad (82)$$

is the linewidth of the laser spot (the Airy disk is replaced by a Gaussian spot, neglecting the small fluctuations at the surroundings of the spot), NA is the numerical aperture of the objective, and λ_0 is the laser wavelength. In writing Eq. (81), one assumes that the heating laser beam is a pure TEM00 Gaussian mode that requires high-quality lasers.

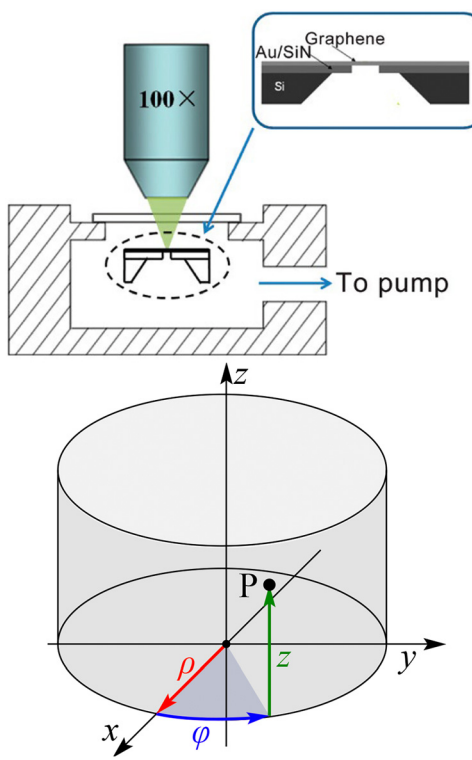


FIG. 43. (a) Schematic setup of the Raman thermometry measurement of suspended graphene. Laser light is focused on a suspended flake of graphene placed in a vacuum chamber (b) Cylindrical coordinate system used for calculating κ (from Wikimedia Commons, the free media repository). Reprinted from Chen et al., ACS Nano 5, 321 – 328 (2011).³⁴¹ Copyright 2011, with permission from American Chemical Society.

In the supported region, the heat diffusion equation is

$$\frac{\kappa' d}{r dr} \left[r \frac{d\Delta T_2(r)}{dr} \right] - \frac{h_K}{d_f} \Delta T_2(r) = 0 \quad \text{for } r \geq R, \quad (83)$$

where h_K is the TBC between the film and the substrate, and we have assumed that the laser spot is completely confined in the suspended region (not the temperature variation). The above suggests that the thermal conductivity of the supported region (κ') can differ from that of the suspended region (κ).

The general solution of Eq. (80) is

$$\Delta T_1(r) = \frac{P}{4\pi\kappa d_f} \text{Ei}\left(-r^2/r_0^2\right) + c_1 \ln \frac{r}{r_0} + c_2, \quad (84)$$

while that of Eq. (83) becomes

$$\Delta T_2(r) = c_3 \text{I}_0(\beta r) + c_4 \text{K}_0(\beta r), \quad (85)$$

where $\text{Ei}(x)$ is the exponential integral, $\beta = \sqrt{h_K/\kappa' d_f}$, and $\text{I}_0(x)$ and $\text{K}_0(x)$ are Bessel functions of the first and second kind, respectively. Here, c_1 , c_2 , c_3 , and c_4 are constants to be determined from the obvious boundary conditions:

(i) The temperature must have a maximum at $r = 0$,

$$\left. \frac{d\Delta T_1}{dr} \right|_{r=0} = 0. \quad (86)$$

(ii) The temperature variation must be continuous,

$$\Delta T_1(R) = \Delta T_2(R). \quad (87)$$

(iii) The heat current must also be continuous,

$$\kappa \left. \frac{d\Delta T_1}{dr} \right|_{r=R} = \kappa' \left. \frac{d\Delta T_2}{dr} \right|_{r=R}. \quad (88)$$

(iv) The temperature must tend to T_0 far away from the spot,

$$\lim_{r \rightarrow \infty} \Delta T_2(r) = 0. \quad (89)$$

The final solutions of Eqs. (80) and (83) matching these boundary conditions are

$$\begin{aligned} \Delta T_1(r) = & \frac{P}{4\pi\kappa d_f} \left\{ \left[\text{Ei}\left(-\frac{r^2}{r_0^2}\right) - \text{Ei}\left(-\frac{R^2}{r_0^2}\right) - 2\ln \frac{r}{R} \right] \right. \\ & \left. + \frac{2\kappa}{R} \sqrt{\frac{d_f}{h_K \kappa'}} \frac{\text{K}_0(\beta R)}{\text{K}_1(\beta R)} (1 - e^{-R^2/r_0^2}) \right\} \end{aligned} \quad (90)$$

and

$$\Delta T_2(r) = \frac{P}{2\pi d_f R} \sqrt{\frac{d_f}{h_K \kappa'}} (1 - e^{-R^2/r_0^2}) \frac{\text{K}_0(\beta r)}{\text{K}_1(\beta R)}. \quad (91)$$

Recognizing that

$$\Delta T_1(R) = \Delta T_2(R) = \frac{P}{2\pi d_f R} \sqrt{\frac{d_f}{h_K \beta}} (1 - e^{-R^2/r_0^2}) \frac{\text{K}_0(\beta R)}{\text{K}_1(\gamma R)}, \quad (92)$$

Eq. (90) can be rewritten as

$$\Delta T_1(r) = \Delta T_1(R) + \frac{P}{4\pi\kappa d_f} \left[\text{Ei}\left(-\frac{r^2}{r_0^2}\right) - \text{Ei}\left(-\frac{R^2}{r_0^2}\right) - 2\ln \frac{r}{R} \right]. \quad (93)$$

Despite the assumptions underlying the analysis and the inherent limitations discussed below, this approach provides a practical framework for interpreting the thermal behavior of real samples. Upon heating, Raman modes soften due to anharmonic effects and thermal expansion. Because laser excitation generates a non-uniform temperature distribution across the sample surface, an average temperature can be defined within the illuminated spot as

$$T_{\text{spot}} = \frac{\int_0^R T(r) e^{-r^2/r_0^2} r dr}{\int_0^R e^{-r^2/r_0^2} r dr}. \quad (94)$$

If $R \gtrsim 3r_0$, the integral for the radial variable can be extended to infinity with an error smaller than 10^{-4} , then

$$\int_0^\infty e^{-r^2/r_0^2} r dr = \frac{r_0^2}{2}. \quad (95)$$

On the other hand,

$$\int_0^\infty e^{-x^2} [\text{Ei}(-x^2) - \ln x^2] x dx = \frac{1}{2} [\gamma - \ln 2], \quad (96)$$

where γ is the Euler's constant. The full expression of the average spot temperature is

$$\Delta T_{\text{spot}} = \Delta T(R) + \frac{P}{4\pi\kappa d_f} [-0.115932 + 2\ln(R/r_0) - \text{Ei}(-R^2/r_0^2)], \quad (97)$$

with $\Delta T(R) = T(R) - T_0$.

The thermal resistance of the film, R_f , is defined as the ratio of the temperature rise at the spot relative to that at the hole radius to the applied heat flux.

$$R_f = \frac{T_{\text{spot}} - T(R)}{q_r} = \frac{\Delta T}{P} = \frac{\ln(R/r_0)}{2\pi\kappa d_f} \left[1 + \frac{\gamma - \ln 2 - \text{Ei}(-R^2/r_0^2)}{2\ln(R/r_0)} \right], \quad (98)$$

where ΔP is the absorbed laser power (heat flux). For a typical value of $R/r_0 \sim 4$, the term in brackets gives $0.958 \sim 1$. Therefore, Eq. (98) can be simplified to yield

$$\kappa = \frac{\ln(R/r_0)}{2\pi d_f R_f} = \frac{\ln(R/r_0)}{2\pi d_f} \frac{P}{\Delta T} = \frac{\ln(R/r_0)}{2\pi d_f} G_{\text{th}}, \quad (99)$$

where the thermal conductance $G_{\text{th}} = \Delta P/\Delta T$ must be extracted from the experiment. We proceed as follows: first, we measure the variation of the phonon frequency with temperature and determine the slope, χ_T , from this dependence. Then, at a fixed temperature, we vary the laser power and extract the corresponding slope of the phonon frequency as a function of the laser power, χ_P . The thermal conductance is then obtained as

$$G_{\text{th}} = \frac{\chi_P}{\chi_T}. \quad (100)$$

Thus, Raman thermometry provides a powerful approach, allowing both temperature monitoring via the Stokes/anti-Stokes intensity ratio and the determination of thermal conductivity through suitable physical models.

In certain cases, it is essential to determine the surface temperature of a device. Surface temperature mapping can be performed using infrared techniques (IR imaging) or Raman spectroscopy (Raman thermography), the latter relying on Stokes/anti-Stokes signals to extract the temperature. A recent modification of the Raman thermography technique, called 2D Raman thermography (2DRT) was proposed by Lundh *et al.*³⁵⁹ It consists of placing a monolayer of a 2D material, for instance MoS₂, on top of the device to be mapped, to improve the accuracy of the surface temperature. MoS₂ absorbs visible light and the Raman signal will be stronger. They apply the technique to a β -Ga₂O₃ MODFET device, where the visible light produces Joule heating tens of nanometers below the surface. Thermal mapping revealed local temperature rises near the gate region and showed that conventional Raman thermometry can underestimate peak device temperatures by up to $\sim 30\%$ in metals or low absorbent materials.

Sullivan *et al.*³⁶⁰ employed Raman thermometry on suspended GR to analyze the frequencies and intensity of first- and second-order

Raman peaks, providing insights into the origin of its exceptionally high thermal conductivity. Graphene synthesized on copper foil via low-pressure CVD was transferred onto a 400-nm-thick low-stress silicon nitride membrane patterned with arrays of holes (5–20 μm in diameter) using focused ion beam milling, as shown in the right-hand inset of Fig. 44. The main panel presents a representative Raman spectrum of graphene, with the characteristic G and 2D peaks clearly resolved.

The inset on the left shows the Stokes and anti-Stokes G-band signals, corresponding to phonon emission and absorption processes, respectively, following photon absorption. The Raman spectra were obtained using a 532-nm laser and a $50 \times$ objective giving a spot of 360 ± 3 nm measured with a cover glass.³⁶⁰ The measurements were performed under vacuum in a high temperature stage. With increasing temperature or laser power, the G-band shifts to lower frequencies, and the anti-Stokes intensity I_{AS} grows relative to the Stokes intensity I_S , as illustrated in the left-hand inset of Fig. 44.

Second-order Raman peaks, corresponding to two-phonon processes at the Brillouin zone boundary, were also measured to extract temperatures associated with different phonon modes. A first-principles-based multi-temperature model was used to fit and interpret the data, predicting the heating and thermalization behavior of various phonon polarizations (LO, TO, ZO, LA, TA, and ZA). The study found that, because Raman thermometry primarily probes the hottest phonons (LO/TO, LA/TA), it tends to overestimate the overall lattice temperature, which is lower when the contributions of ZA phonons are included.

Using Eqs. (99) and (100) to determine the thermal conductivity of suspended graphene, Sullivan *et al.*³⁶⁰ obtained the apparent thermal conductivity κ_a . Figure 45 shows the result for κ_a as a function of the so-called “apparent temperature” measured at the highest laser power (4.7 mW). The apparent temperature measured from the shift of the $\omega_{D+D''}$ peak is lower than that measured from the shift of the ω_G peak. Higher apparent temperatures correspond to lower apparent thermal conductivities. In the figure, T_O (O means optical phonon) represents the temperature extracted from the G-band shift. A linear

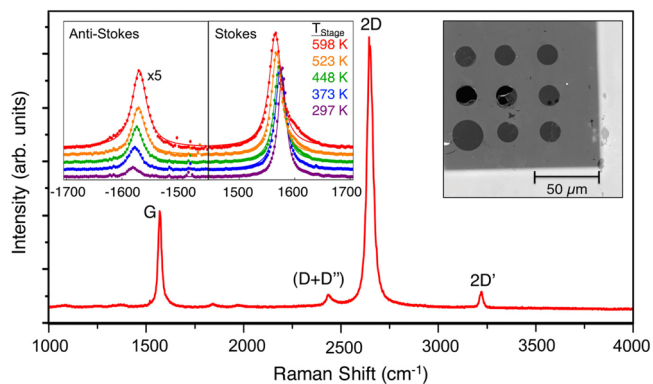


FIG. 44. Raman spectra of the suspended graphene sample acquired at a stage temperature of 598 K. The top-left inset shows the Stokes and anti-Stokes G-band³⁶¹ measured at an incident laser power of 4.7 mW and varying temperatures. The top-right inset presents an SEM micrograph of the graphene sample supported on a holey silicon nitride membrane. Reprinted from Sullivan *et al.*, Nano Lett. 17, 2049–2056 (2017). Copyright 2017, with permission from American Chemical Society.

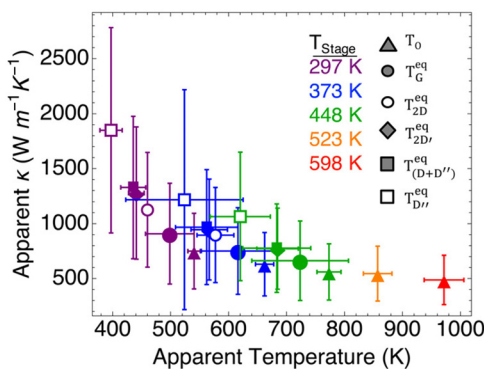


FIG. 45. Apparent thermal conductivity value of the suspended graphene as a function of the apparent temperature measured using different phonon temperatures extracted from the Raman spectra, as indicated in the legend. Reprinted from Sullivan *et al.*, Nano Lett. **17**, 2049 – 2056 (2017).³⁶⁰ Copyright 2017, with permission from American Chemical Society.

fit of the temperature values obtained by increasing the stage temperature at the lowest laser power yields χ_T [see Eq. (100)]. The equilibrium temperature T^{eq} is obtained as

$$T^{eq} = T_{Stage} + \frac{\omega - \omega_0}{\chi_T}. \quad (101)$$

We have described Raman thermometry as a steady-state measurement method using CW lasers, requiring a relatively long accumulation time to collect the Raman signal. Steady-state heat transfer models are then used to describe thermal transport and calculate κ of the material. However, there are currently few alternative approaches in the literature employing pulsed laser excitations, and such transient techniques to perform Raman thermometry measurements remain a largely unexplored area. Appropriate methods for extracting thermal information have already allowed for a whole range of novel experiments, including, for example, transient optical heating and Raman probing,^{362,363} frequency-resolved transient Raman thermal probing technique,³⁶⁴ picosecond energy transport state-resolved Raman (ET-Raman)^{365,366} and frequency domain ET-Raman (FET-Raman).^{367,368}

To extend Raman thermometry beyond steady-state measurements, one can examine its application to transient thermal behavior. This can be achieved by employing a modulated (pulsed) laser for both heating and Raman excitation. This method has been used by Li *et al.*³⁶³ to study the thermal conductivity of CNT fibers. In this experiment, the sample was suspended between two heat sinks with large heat capacity and high thermal conductivity, ensuring that the fiber ends remain at room temperature [see Fig. 46(a)]. Since the length of the sample, L , is much larger than its diameter, a one-dimensional model can be used to describe the time-dependent heat transport along the sample, resulting in the spatially averaged temperature rise in the heated region given by³⁶²

$$\overline{\Delta T}(t) = \frac{2\dot{q}L^3}{\kappa(x_2 - x_1)} \sum_{m=1}^{\infty} \frac{1}{\pi^4 m^4} \left[1 - \exp\left(-\frac{\pi^2 m^4 \alpha t}{L^2}\right) \right] \times \left(\cos \frac{\pi m}{L} x_1 - \cos \frac{\pi m}{L} x_2 \right)^2, \quad (102)$$

where \dot{q} is the heat generation rate [see Eq. (3)], α is the thermal diffusivity [see Eq. (4)], and x_1 and x_2 are the beginning and end of the laser spot, respectively, as shown in Fig. 46(a). Increasing excitation time t_e shifts the D and G Raman peaks to shorter wavenumbers, as depicted in Fig. 46(c). This shift is attributed to the increase in temperature at the heating point with increasing t_e . A gain in the Raman intensity is also observed with an increase in t_e due to appropriately longer light excitation and signal collection times. The thermal diffusivity of the sample can be fitted from the normalized temperature rise given by

$$\begin{aligned} \overline{\Delta T} &= \frac{\overline{\Delta T}(t)}{\overline{\Delta T}(t \rightarrow \infty)} \\ &= \frac{\sum_{m=1}^{\infty} \frac{1}{\pi^4 m^4} \left[1 - e^{-\pi^2 m^4 \alpha t/L^2} \right] \left(\cos \frac{\pi m}{L} x_1 - \cos \frac{\pi m}{L} x_2 \right)^2}{\sum_{m=1}^{\infty} \frac{1}{\pi^4 m^4} \left(\cos \frac{\pi m}{L} x_1 - \cos \frac{\pi m}{L} x_2 \right)^2}. \end{aligned} \quad (103)$$

The time-dependent temperature variation is well illustrated in Fig. 47(a). During t_e , the temperature increases rapidly when the light is turned on, gradually decreasing during t_r when the laser excitation is turned off. The average temperature over t_e is measured using the position of the G peak, which varies linearly with temperature.³⁶³ The measurement results, shown in Figs. 47(b) and 47(c), yields a thermal diffusivity of $(1.74 \pm 0.20) \times 10^{-5} \text{ m}^2 \text{ s}^{-1}$, based on the fitting curve in Fig. 47(c). This appears to agree well with the value $\alpha = (1.76 \pm 0.06) \times 10^{-5} \text{ m}^2 \text{ s}^{-1}$ obtained by Li *et al.*³⁶³ on the same CNT fibers using the transient electrothermal technique.³⁶⁹

Upon finding a good agreement between the two transient methods, it is useful to compare these measurement results with those obtained by conventional steady-state Raman thermometry, which gave $\kappa = (34.3 \pm 0.4) \text{ W m}^{-1} \text{ K}^{-1}$.³⁶³ A rough approximation of the thermal diffusivity of a CNT fiber can be estimated as $\alpha = \kappa/\rho C$. Choosing another material, multi-walled CNT arrays,³⁷⁰ fairly similar to what was studied by Li *et al.*,³⁶³ can help to some extent. Taking the volumetric heat capacity $\rho C \approx 1170 \text{ kJ m}^{-3} \text{ K}^{-1}$ reported by Xie *et al.*³⁷⁰ results in $\alpha = 2.9 \times 10^{-5} \text{ m}^2 \text{ s}^{-1}$, finding some correspondence to the above two values of α . Here it is important to remark that the very low thermal conductivity of CNT fiber ($\approx 34 \text{ W m}^{-1} \text{ K}^{-1}$) in comparison with that of individual CNT, exhibiting $\kappa \sim 10^3 \text{ W m}^{-1} \text{ K}^{-1}$,^{27,28} may arise from the thermal contact resistance between individual nanotubes in the fiber.

Hence, while similar experimental and computational approaches are often already well described,^{32,358,367,371–376} there is a clear evidence that there are many uncertainties in the measurement of the thermal conductivity using Raman thermometry. For example, Beechem *et al.*³⁴³ discussed the validity of the models used in the analysis of thermal conductivity in suspended wafers by comparing them with results from finite element modeling (FEM). Although the authors did not take into account some important sources of error, like convection losses or radiation, they claim that important errors can be made by averaging the temperature in the suspended region or neglecting the mechanical stress produced by laser heating. In recent work by Reig *et al.*³⁵⁸ a careful analysis of the procedure to obtain the thermal conductivity in bulk and the limit of monolayer thicknesses using Raman thermometry has been performed. The authors conclude that the

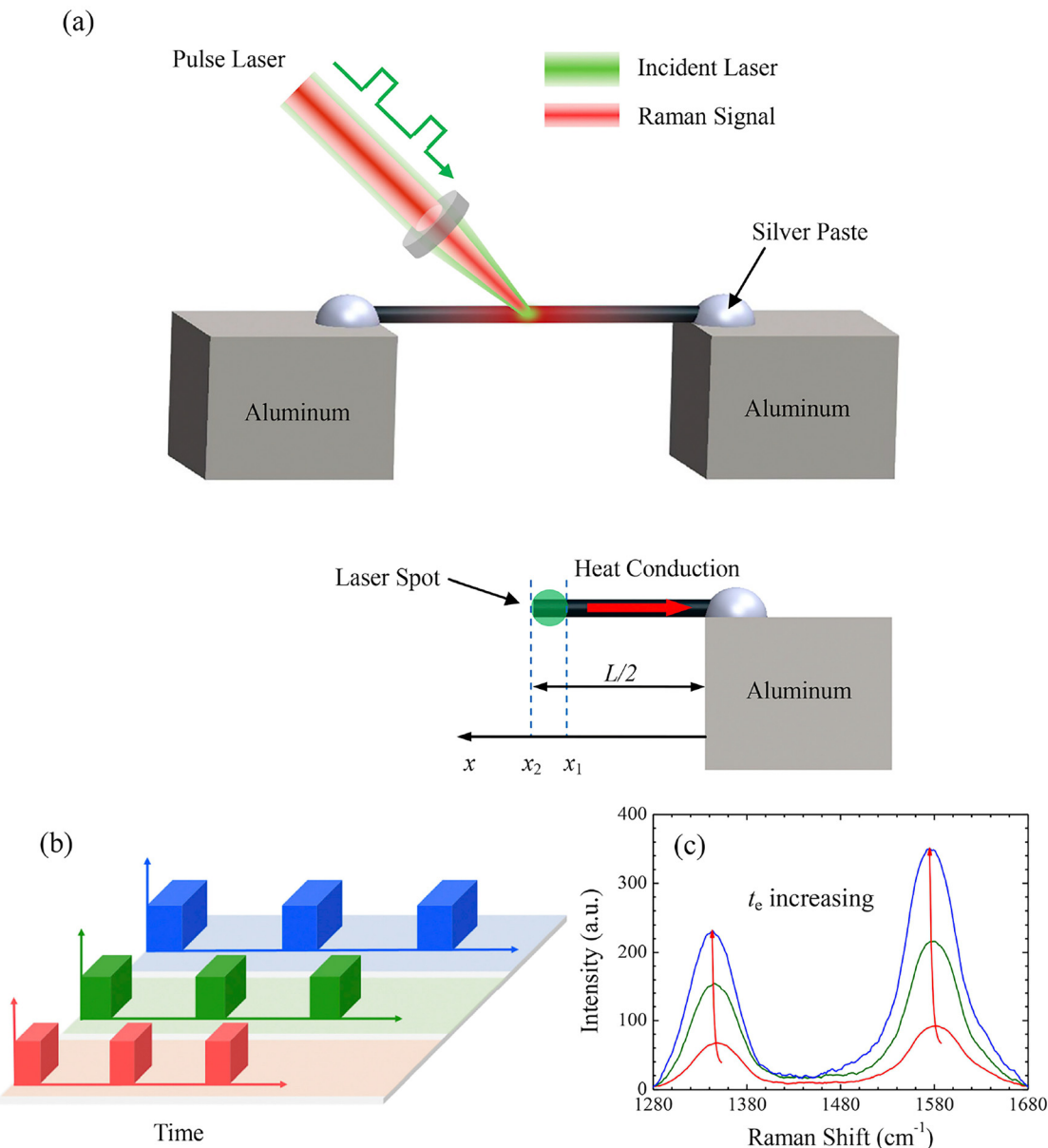


FIG. 46. (a) Schematic setup used for transient Raman measurement. (b) Three selected square pulse lasers of different excitation times (t_e) for both heating and Raman excitation measurement. (c) The corresponding Raman spectrum of the CNT fiber sample for one "heating and cooling" cycle. The Raman peaks shift to shorter wavelength and the Raman intensity increases with increasing t_e . Reprinted from Li et al., Carbon **103**, 101–108 (2016).³⁶³ Copyright 2016, with permission from Elsevier.

convection losses can be important; the thermal conductivity is slightly higher in air than in vacuum for thick flakes. Still, it is almost an order of magnitude higher in a MoSe₂ monolayer. Finally, the heat loss induced by thermal radiation from the sample surface is proportional to $4\sigma_{SB}T^3\Delta T$ or $T^4 - T_0^4$, σ_{SB} being the Stefan–Boltzmann constant, but even if $T - T_0 = 265$ K, the maximum temperature difference they have reached, the radiation losses have been estimated as $\sim 1\%$.

Although generally useful, Raman thermal conductivity measurements have a limited range of applicability that must be

considered material by material before the measurements. The uncertainty in Raman thermal conductivity measurements scale directly with the uncertainty in temperature and heat input measurements. Measurements of thermal conductivity using the Raman technique are performance comparable to more traditional techniques that provide an error of 5%–10% with an uncertainty of $\pm 10\%$ for many materials.³⁴³ However, the error can increase to $\sim 40\%$, thus rendering the applicability of the technique when thermomechanical stress substantially biases the measurement of

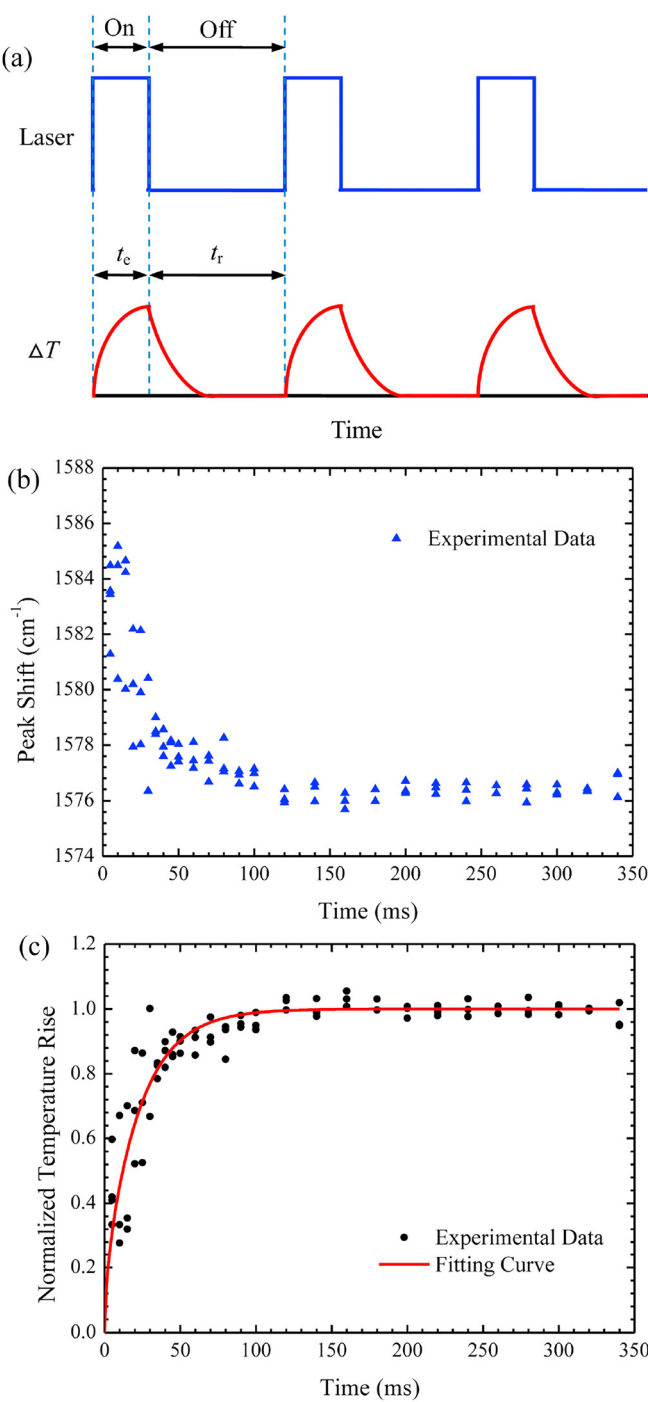


FIG. 47. (a) Schematic illustration of the temperature rise ΔT after the square pulse laser light is turned on during the pulse duration t_e , and the thermal relaxation duration t_r when the laser excitation is turned off. (b) Measured time evolution of the Raman peak shift after the laser light is turned off. (c) Normalized temperature rise and the fitting curve used to measure a CNT fiber's thermal diffusivity. Reprinted from Li *et al.*, Carbon **103**, 101–108 (2016).³⁶³ Copyright 2016, with permission from Elsevier.

temperature or when a material has a thermal conductivity highly dependent on temperature.

Advantages of Raman thermometry

1. It is among the few techniques specifically suited for characterizing 2D materials, allowing measurements down to a single monolayer.
2. Minimal sample preparation is required, generally limited to using a substrate patterned with round holes whose diameters are comparable to the lateral dimensions of the sample.
3. The technique represents a critical frontier for probing in-plane thermal transport in low-dimensional materials.

Limitations of Raman thermometry

1. Non-resonant spontaneous Raman scattering is inherently weak, and small scattering signals can be masked by fluorescence. This limitation can be addressed either by using higher-power lasers to compensate for low non-resonant Raman quantum yields or by employing longer wavelengths to avoid resonant excitation of electronic states that produce fluorescence or phosphorescence.³⁵²
2. The temperature resolution of Raman measurements is typically limited, leading to significant errors and reducing the accuracy of heat transport characterization in 2D materials. Employing optomechanical non-contact methods³¹⁸ to probe the thermal properties of nanomechanical resonators composed of freestanding 2D materials can improve the precision of in-plane thermal conductivity measurements.
3. Accurate determination of thermal conductivity requires a sufficiently sensitive phonon temperature coefficient. A key limitation of this approach is that materials with minimal phonon shifts as a function of temperature produce high uncertainty in κ , making reliable measurements challenging.
4. Despite the increasing use of Raman thermometry, the associated measurement errors and uncertainties remain insufficiently characterized, complicating comparisons with more established thermal measurement techniques.³⁴³

B. Bolometric technique

Langley³⁷⁷ developed the bolometer, a thermal infrared detector that covers the wavelength range up to ~ 5 mm. An electrical resistance thermometer is used in this technique to measure the temperature of the radiation absorber. A calibrated radiation-induced resistance change is used as a temperature indicator. The general working principle is based on the change in transport conductance due to incident radiation termed the bolometric effect.

The bolometer technique can carve its application niche in measuring the thermal properties of low-dimensional materials using a setup shown in Fig. 48. The technique is particularly useful for measuring the thermal properties of electrically conductive metal films with a linear resistance-temperature correlation dependence by probing the electrical resistance change caused by the incident radiation power. One should bear in mind that the bolometric method is not advantageous for bulk materials because there are many more convenient and simple ways to measure thermal conductivity. However, in 2D systems, the number of available methods is limited, thus the bolometric technique may prove useful.³⁷⁸ The resistance change ΔR across the film

induced by the Gaussian laser heating can be sensitively measured with a current preamplifier combined with a lock-in amplifier, consistent with a very large thermal sensitivity. The thermal conductivity can then be extracted from the measured ΔR using numerical thermal simulations. The general theoretical framework is similar to that highlighted in Sec. IV A.³⁷⁹ More details on solving coupled heat diffusion differential equations using FEM with thermal conductivity as a fitting parameter were presented by Kasirga.³⁷⁸

The change in layer conductance induced by light absorption can be due to two mechanisms, a change in carrier mobility μ due to the associated temperature change or a variation in the density of free carriers Δn . Therefore, one notes the fundamental feature of the bolometric effect, which is based on the change in mobility, but not in carrier density, due to heating.³⁸⁰ Freitag *et al.*³⁸¹ showed that these two mechanisms result in bolometric photocurrents of opposite sign: the photo-generated excess carriers induce an enhancement of the conductance, whereas the temperature dependence of μ leads to a reduction of the conductance with increasing T . One can control which mechanism dominates by changing the Fermi energy E_F .

Many previous photothermal (PT) transport measurements in semiconductors have focused specifically on the study of fully coupled photoelectric and photoinduced bolometric effects. The distinguishing feature is that in a thermally mediated transport, the electrons excited by photons relax to a thermal distribution at an enhanced temperature before they are detected in bolometric measurements. In photoelectric response, the nonthermal distribution of excited electrons in the conduction band is detected before it relaxes to the valence band.

In the photoelectric effect, the change in electrical conductivity is $\Delta\sigma = e\mu\Delta n$ where e is the electron charge. For a film of length L and cross-sectional area S , the resulting voltage is

$$\Delta V_{PC} = I\Delta R = I \frac{L}{S} \Delta \left(\frac{1}{\sigma} \right) = -I \frac{L e \mu}{S \sigma^2} \Delta n = -V_0 \frac{\Delta n}{n}, \quad (104)$$

where I is the electrical current and V_0 the voltage without illumination.

For the bolometric response,

$$\Delta V_b = I\Delta R = I \frac{dR}{dT} \Delta T, \quad (105)$$

where ΔT is the temperature change due to light absorption.

Although photoelectric contribution can be very important in semiconducting films, the bolometric technique is yet to be applied in some cases where the bolometric effect is large enough. It may be

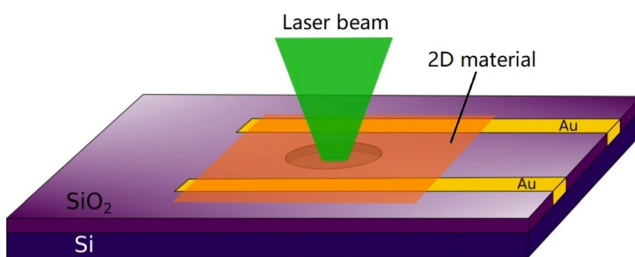


FIG. 48. Schematic of the bolometric setup illustrating a suspended 2D material excited by a laser beam and gold contacts deposited on SiO_2/Si substrate and used to monitor changes in the electrical resistance of the material.

useful to consider materials that have small electron heat capacity and weak electron–phonon coupling, leading to large light-induced changes in electron temperature.

The thermal conductivity of nanosheets and thin flakes has been measured using this technique. A representative example is the determination of the thermal conductivity of a thin metallic flake of 2H-TaS₂. The flake was transferred onto two gold contacts patterned on a substrate that contained a circular hole beneath the suspended region, as shown in Fig. 49. The measurements were carried out using a commercial scanning photocurrent microscope (SPCM) equipped with a $40\times$ objective that focuses a laser beam with a Gaussian profile. The laser served as a localized heat source and was directed onto the flake, centered over the circular hole. The resulting temperature rise across the suspended area was on the order of a fraction of a kelvin.

The electrical resistance of the device was precisely monitored using a lock-in technique to detect changes induced by the local temperature increase under laser irradiation. From these measurements, the thermal conductivity of 2H-TaS₂ at room temperature was determined to be $(13.2 \pm 1.0) \text{ W m}^{-1} \text{ K}^{-1}$, in good agreement with the theoretical values reported by the authors.³⁷⁹

A more comprehensive example is shown in Fig. 50(a). The bolometric response of reduced graphene oxide (rGO) films under black body illumination was measured at temperatures of 50–300 K, reaching a voltage responsivity of up to $82 \times 10^3 \text{ V W}^{-1}$ at 50 K.³⁸² Disordered graphene such as rGO³⁸³ has a strongly temperature-dependent electrical resistance, is a good IR absorber, and has a high thermal resistance.

The samples were clamped between fiberglass (FR-4) and copper laminates and mounted on a cryostat with an IR transmission window. Electrical measurements were made in two- and four-point configurations by applying a bias current and probing a voltage. IR irradiation of the rGO films was performed using a silicon carbide broadband Globar source.

The measured thermal resistance as a function of electrical resistance is shown in Fig. 50(b) illustrating that the thermal resistance is only weakly dependent on electrical resistance. Assuming a simple one-dimensional heat transfer model and using Eq. (63), Dickerson *et al.*³⁸² estimated the value of $\kappa=1.5 \text{ W m}^{-1} \text{ K}^{-1}$ at 60 K. This result shows good agreement with the experimental κ values reported for polycrystalline graphite and amorphous carbon.³¹

Advantages of bolometric technique

1. The bolometric effect underlies many modern technological sensors and devices. A prominent example is the integrated-circuit thermometer, which exploits the well-calibrated resistivity change of a platinum strip.³⁷⁹
2. The temperature response can be obtained through measurements in the infrared spectral range.³⁸²
3. Due to the change in electrical resistance of the active material, a cooled array of high-temperature-coefficient resistance materials can detect infrared radiation with high sensitivity.³⁸⁴
4. In two-dimensional systems, the range of available methods for measuring thermal conductivity is relatively limited. In this context, the bolometric technique offers a distinct advantage. When combined with complementary approaches, bolometric insights provide valuable contributions toward developing a comprehensive understanding of thermal transport in 2D materials.

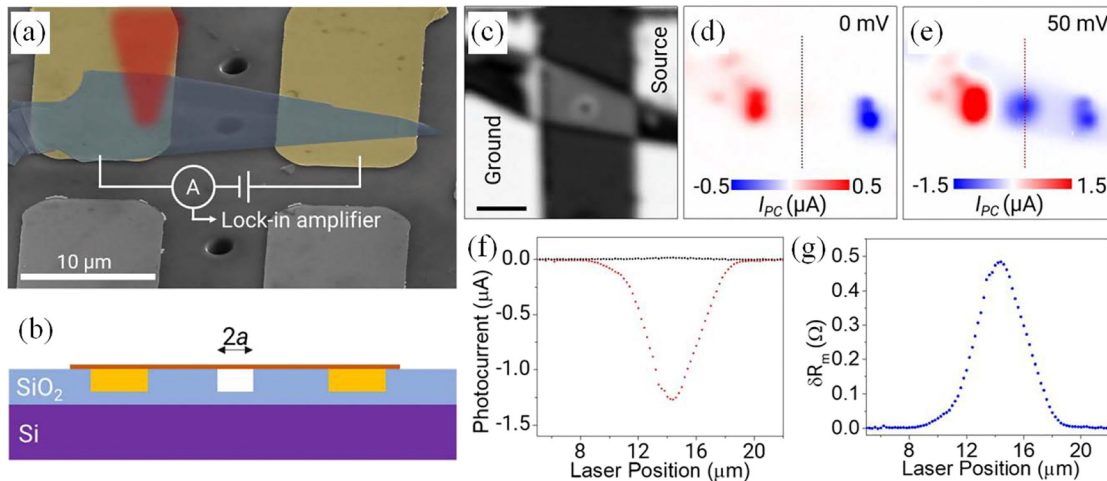


FIG. 49. (a) False-colour SEM image of the 2H-TaS₂ flake bridging the gold contacts. (b) Cross-sectional schematic of the device, showing a circular hole of diameter 2a beneath the suspended region. (c) SEM micrograph of the suspended crystal (scale bar: 5 μm). (d) Photocurrent map acquired at zero bias, revealing Seebeck currents generated at the flake–contact junctions. (e) Photocurrent maps obtained under a 50 mV bias, showing the photoresponse across the crystal and the variation over the hole. (f) Line profiles of the photocurrent generated during laser scans at 0 and 50 mV bias. (g) Variation of the overall device resistance as a function of the laser position. Reprinted from Çakiroğlu *et al.*, 2D Mater. **7**, 035003 (2020).³⁷⁹ Copyright 2020, with permission from IOP Publishing.

Limitations of bolometric technique

1. Calculating the change in overall resistance of the device when the laser is focused on the center of the suspended region of the crystal is challenging.³⁸²
2. These experimental approaches encompass both the sample preparation procedures required for accurate measurements and the experimental setup needed to achieve high sensitivity.³⁸⁵
3. Beyond highly conductive metal films, the applicability of the bolometric method becomes questionable or even invalid. A major limitation arises when this technique is applied to semiconductors, as significant challenges may occur. In such cases, it is often necessary to incorporate an electrically conductive feature with a small electron heat capacity and weak electron-phonon coupling, which can lead to pronounced light-induced changes in electron temperature.

C. Time- and frequency-domain thermoreflectance

Over the past two decades, ultrafast laser-based transient thermoreflectance (see Secs. III C and III D) has emerged as a highly effective and adaptable technique for measuring thermal properties of a wide variety of 2D materials with a thickness down to ~ 20 nm.^{290,386,387} For example, Schmidt *et al.*³⁸⁸ measured the interface conductance between metal and highly ordered pyrolytic graphite as an excellent approximation to the thermal interfaces with the side-wall of multi-walled carbon nanotubes (MWCNTs)³⁸⁹ and multilayer graphene sheets.³⁹⁰ These methods have also been applied to measure the thermal conductivities of other 2D materials, such as MoS₂,²⁹⁷ tungsten ditelluride (WTe₂),³⁹¹ and rhenium disulfide (ReS₂).³⁹²

Sood *et al.*³⁹³ employed the TDTR technique [see Fig. 51(a)] to measure the cross-plane thermal conductivity of MoS₂ films with thicknesses ranging from 20 to 240 nm, as shown by the circles in Fig. 51(b). First-principles DFT simulations, represented by the dashed

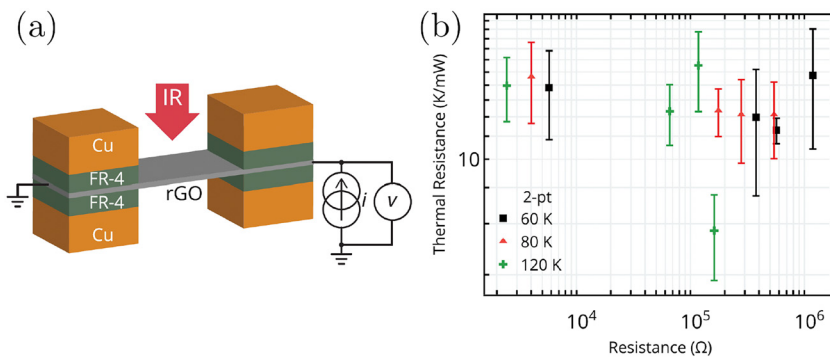


FIG. 50. (a) Schematic of free-standing rGO clamped by laminates of electrically insulating, thermally conducting fiberglass and copper. The electrical circuit consists of a current-biased film with a voltage readout. (b) Measured thermal resistance as a function of low-bias 2-point (2-pt) resistance for five rGO samples at 60, 80, and 120 K. Reprinted from Dickerson *et al.*, Appl. Phys. Lett. **107**, 243103 (2015).³⁸² Copyright 2015, with permission from AIP Publishing.

line in Fig. 51(b), capture the thickness-dependent trend of κ_{\perp} and yield quantitatively reliable values of thermal conductivity.

The values of κ_{\perp} decreases from $\sim 2 \text{ W m}^{-1} \text{ K}^{-1}$ for the thickest film ($d_f = 240 \text{ nm}$) to $0.9 \text{ W m}^{-1} \text{ K}^{-1}$ for $d_f = 20 \text{ nm}$, consistent with phonon transport along the c -axis in the quasi-ballistic regime and suggesting that the dominant heat-carrying phonon modes have MFPs of at least several tens of nanometers.³⁹³ The κ_{\perp} values in Fig. 51(b) for the thickest films are nearly identical to those obtained by Liu *et al.*³⁹⁴ ($\sim 2 \text{ W m}^{-1} \text{ K}^{-1}$) and Muratore *et al.*³⁹⁵ ($\sim 2.5 \text{ W m}^{-1} \text{ K}^{-1}$) in bulk MoS₂. However, these values are considerably smaller than the cross-plane thermal conductivity of $\kappa_{\perp} \sim 4.8 \text{ W m}^{-1} \text{ K}^{-1}$ reported by Jiang *et al.*,²⁹⁷ and the value of $\sim 5.1 \text{ W m}^{-1} \text{ K}^{-1}$ predicted by DFT calculations from Lindroth *et al.*³⁹⁶

This apparent discrepancy in the reported values of κ_{\perp} may arise from the combined influence of modulation frequency (ω) dependence and the finite thermal penetration depth.³⁹³ Although near-interfacial phonon nonequilibrium effects warrant closer investigation, a simplified model assumes that phonons with $\Lambda_{\perp} > d_f$ are suppressed under high-frequency pumping, thereby reducing the apparent cross-plane thermal conductivity κ_{\perp} . For low κ materials with relatively wide MFP distributions, this assumption is reasonable, it is consistent for instance with the discussion given by Sun *et al.*²⁹⁶ and Koh *et al.*²⁹⁸

In the same work of Sood *et al.*,³⁹³ they report, from DFT calculations, that almost 50% of the heat in MoS₂ is carried by phonons with MFPs exceeding 200 nm, nearly two orders of magnitude higher than the predictions of kinetic theory. As a result, quasi-ballistic effects cause the cross-plane thermal conductivity κ_{\perp} of nanometer-thin MoS₂ films to scale with thickness, with the volumetric thermal resistance saturating at a finite value of $\sim 10 \text{ m}^2 \text{ K GW}^{-1}$. For a 20-nm film, up to 30% of the total thermal resistance arises from this contribution, while the remainder is dominated by the SiO₂ substrate and the aluminum transducer interfaces.

These insights may motivate further research into strategies for tailoring the phonon spectrum. The dominant contribution to κ_{\perp} of phonons with long MFP suggests that introducing disorder or defects along the c -axis could strongly suppress cross-plane heat conduction³⁹⁷ without substantially degrading electronic transport. Such behavior is highly advantageous for cross-plane thermoelectric devices based on layered 2D materials,³⁹⁸ offering new opportunities for energy harvesting and electronic cooling.

Frequency-domain thermoreflectance has recently been recognized as another attractive technique for studying thermal transport in

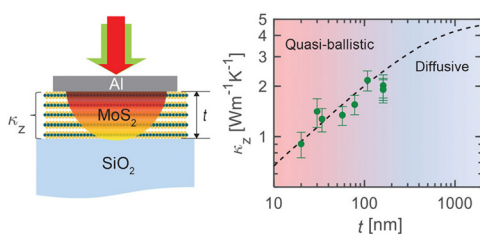


FIG. 51. (a) Schematic of the TDTR setup to measure the MoS₂ films. (b) Measured thickness-dependent cross-plane thermal conductivity of MoS₂ films. Reprinted from Sood *et al.*, Nano Lett. **19**, 2434 – 2442 (2019).³⁹³ Copyright 2019, with permission from American Chemical Society.

2D materials. Using FDTR, as illustrated in Fig. 52(a), Chavez-Angel *et al.*³⁹⁹ demonstrated the ability to engineer extremely insulating van der Waals heterointerfaces based on atomically thin lattice-mismatched Bi₂Se₃/MoSe₂ superlattices (SLs) and GR/PdSe₂ heterostructures with exceptional thermal resistances ($70\text{--}202 \text{ m}^2 \text{ K GW}^{-1}$) and ultralow cross-plane thermal conductivities ($0.012\text{--}0.07 \text{ W m}^{-1} \text{ K}^{-1}$) at room temperature, comparable to those of amorphous materials.

In this example, the FDTR setup combines simultaneous κ_{\perp} and interface thermal conductance measurements.^{403,404} For the case of SLs, multilayer structures consist of Au (transducer), SLs, and substrate stacks as shown in Fig. 52(a). The effective κ_{\perp} and the thermal resistances between Au and SLs (R_1) and SLs and substrate (R_2) were obtained for each SL following a three-dimensional multilayer heat diffusion model.¹⁸⁴ Examples of the measured phase signal and the best model fits are shown in Fig. 52(b). The procedure used to extract the thermal parameters of the sample was justified by El Sachat *et al.*,⁴⁰³ Xiao *et al.*,⁴⁰⁴ and Schmidt *et al.*^{180,184}

In Bi₂Se₃/MoSe₂ SLs, κ_{\perp} increases slightly with increasing thickness ranging from 0.059 to $0.07 \text{ W m}^{-1} \text{ K}^{-1}$, as seen in Fig. 52(c). In GR/PdSe₂ heterostructures, κ_{\perp} exhibits a pronounced thickness dependence, increasing by nearly a factor of six as the PdSe₂ thickness increases from a single layer to seven layers.

Notice how the weak thickness dependence of κ_{\perp} in SLs can be understood by considering both the interface-phonon scattering and the size effects. In the case of diffusive thermal transport, short-wavelength thermal phonons are scattered by multiple Bi₂Se₃/MoSe₂ interfaces reducing their contribution to cross-plane thermal transport with increasing film thickness. In turn, as the volume fraction of the constituent SLs increases, more long-wavelength phonons are allowed to propagate and contribute to κ_{\perp} until they are scattered at the sample boundaries. These opposite effects resulted in the suppressed thickness-dependent trend of κ_{\perp} observed in Fig. 52(c). This prediction is in agreement with the experiments by Koh *et al.*⁴⁰⁵ on short-period AlN/GaN SLs and Cheaito *et al.*⁴⁰⁶ on SiGe SLs illustrating that the transmission of phonons across SLs strongly depends on the wavelength of the phonons, suggesting that long-wavelength phonons are the dominant heat carriers. Molecular dynamics simulations by Chalopin *et al.*⁴⁰⁷ have also confirmed the predominant role of Si/Ge interfaces with large phonon MFPs in thermal conductivity.

In pure Bi₂Se₃ and GR/PdSe₂, the absence or minimal presence of mismatch interfaces enables most thermally excited phonons to participate in cross-plane transport. As a result, κ_{\perp} is governed primarily by finite-size effects, leading to different rates of increase in κ_{\perp} , as shown in Fig. 52(c).

Chavez-Angel *et al.*³⁹⁹ quantified the impact of cross-plane ballistic phonon transport on the total thermal resistance in epitaxial films. The total thermal resistance per unit area ($R_{tot} = R_K + R_f$) is the sum of the combined thermal resistance of the interface $R_K = R_1 + R_2$ that includes the above resistances between Au and SLs (R_1) and SLs and substrate (R_2), and volumetric cross-plane thermal resistance $R_f = d_f / \kappa_{\perp}$.^{393,403} As observed in Fig. 52(d), R_{tot} is proportional to the total thickness of the SL. Similarly, R_K increases with increasing thickness of short-period SLs.^{402,405} This increase is most likely due to enhanced phonon-interface scattering in large lattice-mismatched Bi₂Se₃/MoSe₂ interfaces ($\sim 20\%$ mismatch).

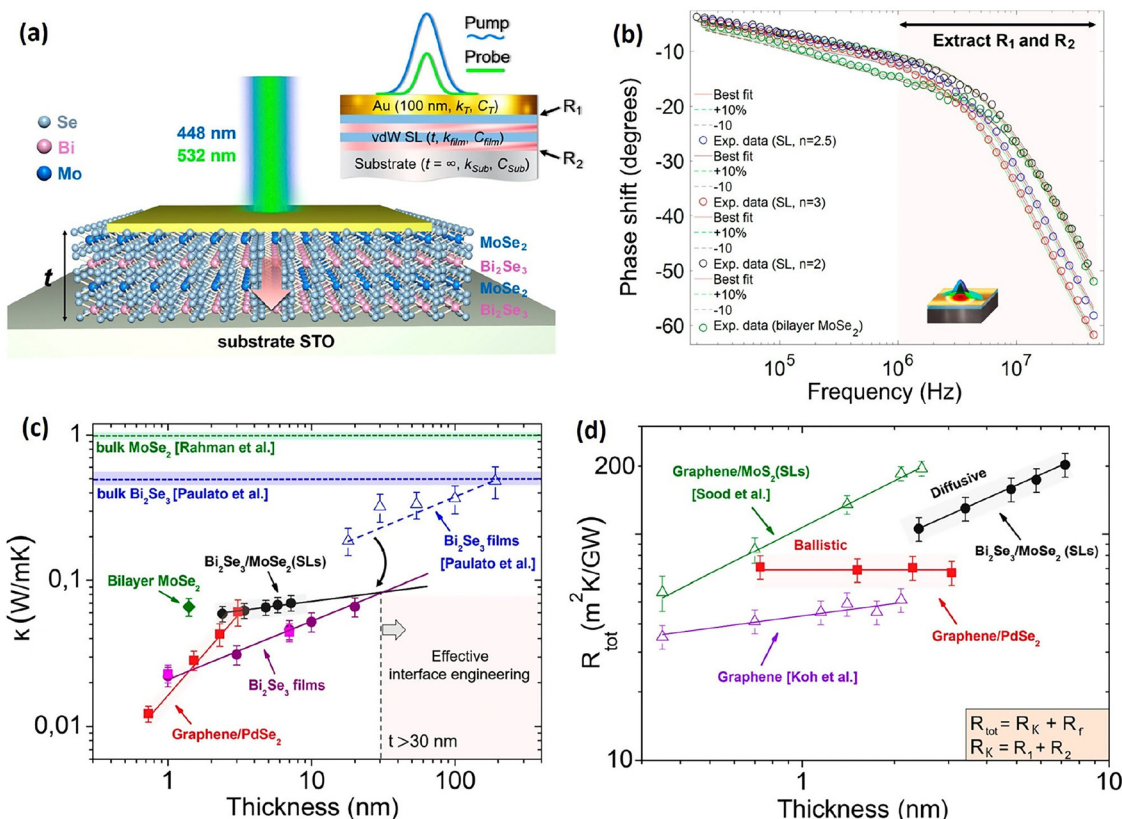


FIG. 52. (a) Schematic of the FDTR technique and Bi₂Se₃/MoSe₂ multilayer system of the SLs. (b) Typical FDTR data measured in bilayer MoSe₂ (green circles) and Bi₂Se₃/MoSe₂ SLs with periods $n = 2, 2.5$, and 3 and the corresponding best model fits. (c) Cross-plane thermal conductivity vs film thickness measured in bilayer MoSe₂ (rhomb), Bi₂Se₃/MoSe₂ SLs (black circles), graphene/PdSe₂ heterostructures (red squares), and Bi₂Se₃ films on strontium titanate (STO) (purple circles), and sapphire (pink squares) substrates. Triangles show previously reported κ_{\perp} values measured in thicker Bi₂Se₃ films.⁴⁰⁰ (d) Total thermal resistance R_{tot} of the Bi₂Se₃/MoSe₂ SLs (circles) and graphene/PdSe₂ heterostructures (squares) vs film thickness. Appropriate R_{tot} measurements in Au/graphene/SiO₂⁴⁰¹ (purple triangles) and Al/graphene-MoS₂ (SLs)/SiO₂⁴⁰² (green triangles) are included for comparison. Reprinted from Chavez-Angel *et al.*, Nano Lett. **23**, 6883–6891 (2023); licensed under a Creative Commons Attribution (CC BY) license.

From the different slopes in Fig. 52(d), Chavez-Angel *et al.*³⁹⁹ deciphered different thermal transport regimes. Thus, unchanged R_{tot} in GR/PdSe₂ indicates strong ballistic thermal transport taking into account the variations of both R_K and R_f with thickness observed by the authors. Similarly, cross-plane ballistic or quasi-ballistic thermal transport has been found in graphene,⁴⁰¹ MoS₂,³⁹³ and PtSe₂⁴⁰³ thin films. However, the increased values of R_{tot} with increasing thickness observed in SLs indicate subsidiary phonon scattering in the diffusive regime. The authors attributed this result to the scattering of high-frequency phonons at multiple Bi₂Se₃/MoSe₂ interfaces illustrating that the lattice mismatch destroys the coherence of high-frequency phonons.

These advancements in the quantitative understanding of interfacial thermal transport across atomically thin van der Waals films would add to the above phonon engineering approach, enabling a promising route for realizing a wide variety of nanoscale electronic and thermoelectric devices.

D. Suspended thermal micro bridge method

In order to eliminate parasitic heat transfer from the sample to the substrate, a steady-state method based on microfabricated

suspended devices has been developed to measure the in-plane thermal conductivity of narrow thin films and κ in nanowires or nanotubes along their axial direction.^{199,408–411} The temperature sensing of this technique is performed at both ends of the sample and all measurements are carried out in the vacuum environment to reduce convective heat loss.

The suspended microbridge method was first used by Kim *et al.*²⁸ in 2001 to measure the thermal conductivity of a single multi-walled nanotube. In the years since the first measurements, substantial progress has been made in both theory and experiments. Shi *et al.*¹⁹⁹ employed this technique to measure κ of graphene on a SiO₂ substrate, Wang *et al.*²³ measured κ in the 77–350 K temperature range for suspended and supported few-layer graphene using a thermal bridge technique, and further improvements were achieved by measuring κ in MoS₂, hBN,^{412,413} and other 2D materials.^{414,415}

More details on the bridge method are shown in Fig. 53. Two configurations proposed by Shi *et al.*¹⁹⁹ and Sultan *et al.*⁴⁰⁹ are typically used. One of them schematically shown in Fig. 53(a) consists of two adjacent suspended SiN_x membranes, each supported by five identical long and thin SiN_x beams. A platinum resistance arm is fabricated on

each membrane to serve as a microheater and thermometer. The sample is mounted on the device to bridge the two membranes, one is used as a heating membrane due to the resistance of Pt heated by a DC in the μA range, while another is used as a sensing membrane fed with an AC source in the nA range.¹⁹⁹ It is assumed that the temperature rise on both membranes is uniform and the heat losses due to gas flow, convection, and radiation can be neglected. The five beams transfer a certain amount of Joule heat from the heating membrane directly to the environment. The rest flows into the sensing membrane through the sample and is finally moved to the environment through the five beams connected to the sensing membrane.

The thermal model of the device in Fig. 53(a) was developed extensively and confirmed by experiments and simulations.^{199,315,409,417–419} There are particularly simple forms of the measured thermal conductance of the sample G_{th} such as⁴¹⁷

$$G_{th} = \frac{\Delta T_c(P_H + P_L)}{\Delta T_h^2 - \Delta T_c^2}, \quad (106)$$

where ΔT_h and ΔT_c are the temperature rise at the heating and sensing membrane, respectively, and P_H and $2P_L$ are the Joule heating power applied to the heater and the two Pt current leads on the heating membrane, respectively. Both ΔT_h and ΔT_c can be measured from the resistance change of the Pt resistance thermometer. On the other hand, the resulting thermal resistance G_{th}^{-1} is formed by the intrinsic thermal resistance of the sample R_{th} , and the thermal contact resistance between the sample and the two membranes, $R_{contact}$, so

$$G_{th}^{-1} = R_{th} + R_{contact}. \quad (107)$$

When only $R_{contact}$ is small enough, the thermal conductivity of the sample κ can be found as

$$\kappa = \frac{L_s}{R_{th}A_s} \approx \frac{L_s G_{th}}{A_s}, \quad (108)$$

where L_s and A_s are the length and cross-sectional area of the sample, respectively.

The question of how to reduce $R_{contact}$ is the most important concern using this technique. This can be done by depositing metal or amorphous carbon in the sample-membrane contact area.¹⁹⁹ Alternatively, R_{th} and $R_{contact}$ can be approximated by measuring the Seebeck coefficient and computing the temperature drops at the contacts.^{411,420}

An important role is played by the sensitivity of the method, which determines the lowest limit of thermal conductivity that can be detected with this technique.⁴²¹ The sensitivity of the measurement is limited by various factors, such as the heat transfer that occurs through residual gas molecules, the radiation emitted from the membranes, and the fluctuations in temperature of the sample environment.⁴²²

Recent advances in technical details are illustrated in Fig. 53 for ultrathin van der Waals NbSe₃ nanowires. In this case, covalently bonded 1D molecular chains are assembled together via van der Waals interactions to form NbSe₃ nanowires.⁴²³ The temperature dependence of κ is illustrated in Fig. 54. For NWs wider than 26 nm in diameter

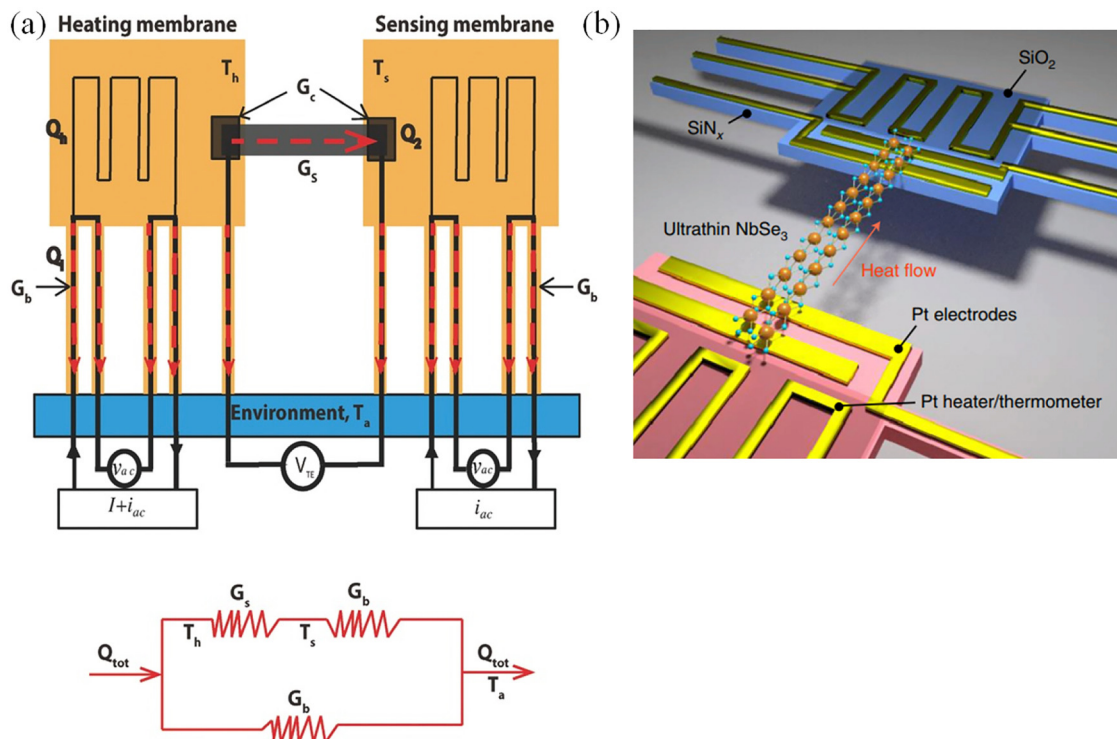


FIG. 53. (a) Schematic illustration of the suspended thermal micro bridge method including heating and sensing membranes (top) and corresponding thermal resistance equivalent circuit (bottom). Reprinted from Wang *et al.*, Adv. Funct. Mater. **27**, 1604134 (2017).³¹⁵ Copyright 2017, with permission from John Wiley and Sons. (b) 2D NbSe₃ device. Reprinted from Yang *et al.*, Nat. Nanotechnol. **16**, 764 (2021).⁴¹⁶ Copyright 2021, with permission from Springer Nature.

(lower panel), κ decreases with T in the range of 50–300 K, which has an Umklapp scattering signature. However, below 26 nm (top panel), κ follows the increasing linear trend in this temperature range, most obvious for the 6.8-nm NW. This behavior is drastically different from the T^{-2} dependence obtained in κ measured in single-walled carbon nanotubes (SWCNTs), where U-scattering dominates phonon transport.²⁹

As shown by Yang *et al.*,⁴¹⁶ this behavior can be reasonably explained by an increased population of 1D phonon modes along the molecular chain for ultrathin wires, which in turn may be due to an increase in the Debye temperature Θ_D . Consequently, Θ_D would increase from the bulk value of about 200 K in NbSe₃⁴²³ since $\Theta_D \propto \sqrt{Y}$,²³⁵ where Y is the Young modulus. This phenomenon known as elastic stiffening^{424,425} was directly observed by Yang *et al.*⁴¹⁶ using a three-point bending scheme with an atomic force microscope.

Elastic stiffening affects the thermal conductivity of the lattice in several ways. First, the enhanced Y corresponds to a higher sound velocity, which is directly proportional to thermal conductivity [see Eqs. (38) and (39)]. Second, the higher Θ_D shifts the phonon spectrum to lower wave vectors at any given T . This increases the energy difference between the acoustic and optical branches, which contributes to a reduced Umklapp scattering rate.⁴²⁶ These factors may help enhance κ as observed in fact in Fig. 54.

The method has been shown to improve an understanding of the physical mechanisms governing heat conduction in nanofilms,^{419,420} 2D materials, such as graphene,^{427,428} boron nitride,⁴¹³ and TMDs.⁴²⁹

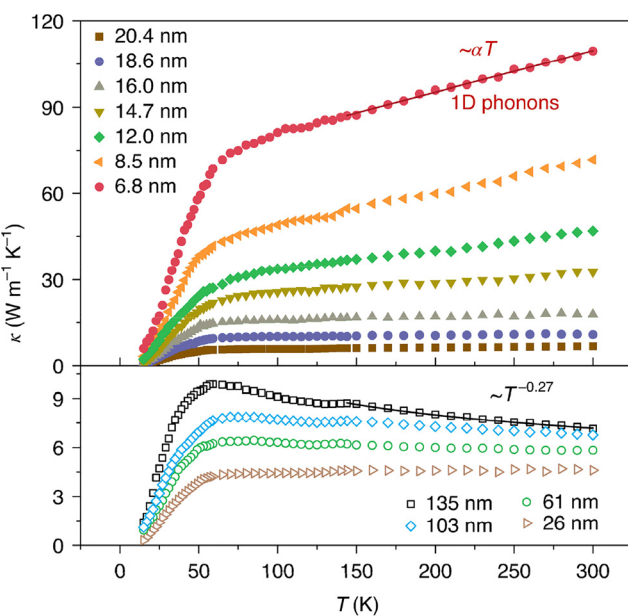


FIG. 54. $\kappa(T)$ for NbSe₃ nanowires with different diameters (the suspended length is about 15 μm for all samples). The line shows the linear trend of κ with a constant α . The measured κ for the thickest nanowire (135 nm) demonstrates an $\sim T^{-0.27}$ dependence from 170 to 300 K, signifying the importance of Umklapp scattering. Reprinted from Yang *et al.*, Nat. Nanotechnol. **16**, 764 (2021).⁴¹⁶ Copyright 2011, with permission from Springer Nature.

Figure 55(b) shows the $\kappa(T)$ behavior for the bilayer and single layer GR samples, approximating the dependence $\kappa \sim T^{1.5}$ at temperatures between 50 and 125 K.

If edge scattering with a constant mean free path Λ_b is the dominant phonon scattering process for the acoustic phonon modes at low temperatures, the scattering rate $\tau_s^{-1} \approx v_g \Lambda_b$ remains approximately constant for the LA and TA branches since v_g is nearly independent of ω , and is proportional to $\sqrt{\omega}$ for the quadratic ZA branch. Regarding the role of edge scattering, Pettes *et al.*⁴³¹ concluded that to most closely match the measured dependencies $\kappa(T)$ in Fig. 55(b), Λ_b should be ~ 150 –200 nm, much smaller than the actual micrometer widths and lengths of the suspended graphene samples. Although edge scattering enables us to explain the behavior of $\kappa \sim T^{1.5}$ at low T due to the dominant contribution of the ZA modes, it cannot explain the observed suppressed κ values in Fig. 55(b) compared to that for bulk allotropes of carbon materials.⁴³¹ Specifically, the measured low temperature values of κ are more than an order of magnitude smaller than those calculated for pristine single-layer graphene and the basal-plane value measured in high-quality graphite. To account for the observed discrepancy, Pettes *et al.*⁴³¹ used the fact that the residual polymer layer was not effectively removed during the graphene assembly process. Considering scattering processes by the residual polymer layer leads to the correct account of the observed thermal conductivity data. It seems reasonable to address interlayer coupling in bilayer samples, which can also break the reflection symmetry of single-layer graphene, reducing the ZA contribution and resulting in suppressed κ .^{430,432} It turns out, however, that this effect is not strong enough to decrease κ well below the value for the basal plane of graphite.⁴³³

A similar discrepancy between theory and experiment, attributed to strong phonon scattering from surface disorder induced by residual polymer and oxide layers, has also been reported for suspended MoSe₂ and MoS₂ monolayers grown by CVD.^{429,434} In simulations, the thermal conductivity decreases sharply with increasing temperature due to the dominance of Umklapp scattering, whereas the experimentally measured $\kappa(T)$ exhibits a much flatter dependence. This difference arises because DFT and BTE frameworks cannot fully capture the impact of surface disorder on phonon scattering. Achieving a complete understanding of these effects remains both fundamentally significant and technologically important, particularly since graphene supported on amorphous SiO₂ constitutes one of the most widely used device architectures.

Advantages of suspended bridge method

- When measuring the axial thermal conductivity of NWs and CNTs, or that of narrow thin films, parasitic heat transfer to the substrate is effectively eliminated.^{199,409–411}
- The technique is applicable over a wide temperature range, from approximately 4 to 400 K.^{28,199}
- It is also well suited for simultaneous measurements of the Seebeck coefficient and electrical conductivity.⁴¹⁴

Limitations of suspended bridge method

- Experimentally, accurately quantifying the two main contributions to thermal contact resistance is challenging: (i) the resistance at the ends of the suspended sample in contact with the SiN_x membranes (heater and sensor) and (ii) the thermal resistance at the sample–membrane and thermometer interfaces. Several studies have proposed models and strategies to improve

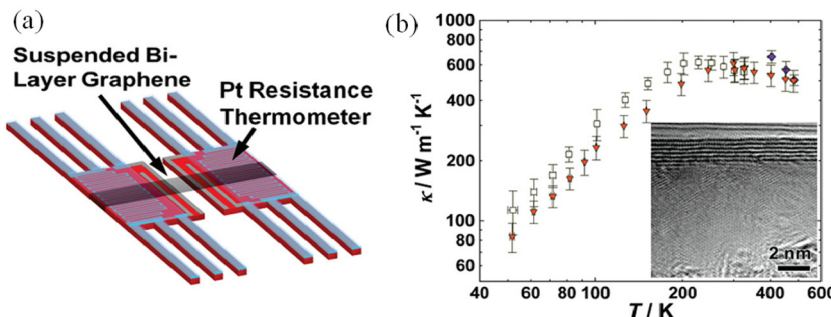


FIG. 55. (a) 3D view of the bilayer GR suspended between two microthermometers. (b) $\kappa(T)$ for the bilayer (BLG2) and single-layer (BLG1) GR samples. For comparison, the measured κ values of a graphene single-layer supported on SiO_2 are shown by circles.⁴³⁰ Solid and dashed lines show the BTE simulated curves for supported and suspended graphene, respectively.⁴³⁰ Reprinted from Pettes *et al.*, Nano Lett. 11, 1195 (2011).⁴³¹ Copyright 2011, with permission from American Chemical Society.

- membrane temperature uniformity and mitigate these additional resistance contributions.^{413,428,435}
- Sample fabrication may involve the clean transfer of 2D materials onto the bridge structure using the dry transfer method. However, this process is both challenging and time-consuming, often resulting in polymer residues, defects, and irregular sample edges, all of which significantly affect the measured thermal conductivity.^{180,431,436,437}
 - An alternative fabrication approach utilizes a sharp probe tip to pick up the sample and place it across the two suspended membranes. Nevertheless, handling samples with thicknesses below 50 nm remains challenging due to limitations in probe tip sharpness and the mechanical fragility of the sample material.⁴¹⁴
 - The relatively large experimental heater and sensor areas are highly susceptible to radiative and convective losses, making vacuum conditions essential during measurements.⁴³⁸
 - The thermal contact resistance between the sample and the two membranes, R_{contact} , must be minimized. Incorporating high thermal conductivity materials into the membrane can further reduce these parasitic resistance components.⁴²⁸

E. 3ω technique

Given the apparently complicated lithography of the RT element in 2D flakes, it is perhaps not surprising that much of the potential of the 3ω technique in these materials has yet to be developed.^{44,378} Meanwhile, the compelling results of Eriksson's group at UW-Madison^{439–441} indicate that the technique is a useful path to provide accurate thermal results well into the future. These works published by Jaffe *et al.*^{439–441} are an excellent introduction to the field of thermal transport across nanometer films of 2D materials such as hBN and graphite. These films are so thin that most phonons travel ballistically across the entire film without scattering. In this quasi-ballistic transport regime, the thermal properties of materials strongly diverge from those of large bulk crystals.

Figures 56(a) and 56(b) show the experimental setup for the measurement of κ_{\perp} of a 585-nm-thick hBN flake as a function of temperature, the experimental results are displayed in Fig. 56(c). A differential 3ω measurement was used, where the temperature of a reference heating wire on the bare sample substrate is subtracted from the temperature increase in the heating wire on the hBN flake, as shown in Fig. 56(b). The hBN flakes were exfoliated in a glovebox with N_2 atmosphere and transferred onto SiO_2/Si substrates. The value of κ_{\perp} measured in the 585-nm flake was around a 60% larger than the highest

κ_{\perp} obtained in bulk hBN [see Fig. 56(c)]. Furthermore, the thermal conductivity increases by a factor of ~ 2 between room temperature and 200 K, similar to that of other materials with large phonon MFPs, such as Si.⁴⁴²

Subsequently, κ increases by more than a factor of two as the flake thickness grows from 200 to 585 nm, underscoring the significant contribution of phonons with mean free paths of several hundred nanometers in thicker flakes. Moreover, the thermal conductivity gradually saturates with increasing thickness, consistent with similar trends observed in graphite.⁴⁴⁵ The suppressed contributions of phonons with long MFPs in a film of finite thickness yield a satisfactory description of the observed values of κ .

The scattering of phonons at the grain boundary in stack faults (planar twist interfaces) has been proposed as a limiting factor of the phonon MFPs in 2D materials.^{386,445,446} Using a heterostructure consisting of five exfoliated hBN flakes shown in Fig. 57(a), it is possible to control heat conduction through twist interfaces. Figure 57(c) compares the measured cross-plane thermal conductivity of the stack with that of individual flakes of similar thickness as a function of temperature. Phonon scattering at the twist interfaces markedly reduces the phonon mean free paths, thereby lowering the thermal conductivity, as evidenced in Fig. 57(c). Furthermore, the κ values of the stack show no increase at lower temperatures, indicating that interface scattering dominates the thermal transport.

The measured cross-plane thermal conductivity of the stack and individual flakes of similar thicknesses as a function of temperature is compared in Fig. 57(c). Strong phonon scattering at the twist interfaces drastically reduces the phonon MFPs, thereby reducing the thermal conductivity, as evidenced by the data points shown in Fig. 57(c). Furthermore, the κ values of the stack do not increase at lower temperatures, suggesting that thermal conductivity is dominated by interface scattering.

V. THERMAL CONDUCTIVITY IN NANOSTRUCTURES

The advances in nanotechnology have resulted in novel materials (called nanostructures) and their miniaturized devices with much smaller length scales but improved functionalities. There are various types of nanostructures: superlattices, NWs, nanomeshes (NMs), nanopillars, nanorods, nanotubes, 0D quantum dots (QDs), etc., with different shapes, geometries, and compositions. Due to the size or phonon confinement effect, when the characteristic lengths of the materials are shrunk to the microscale and below, their thermal properties drastically change compared to their bulk counterparts.^{447–450} Their larger specific surface area, smaller size, and quantum confinement

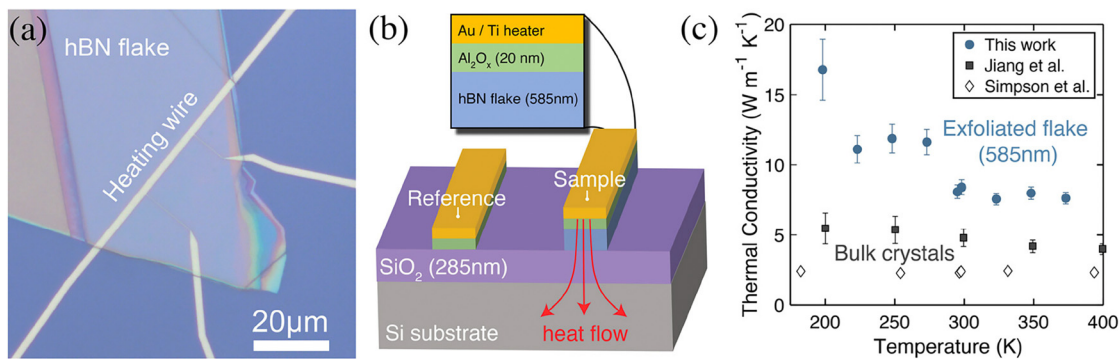


FIG. 56. Measurement of κ_{\perp} of a 585-nm-thick hBN flake. (a) Optical image of a gold RT metal line on an AlO_x encapsulated hBN flake transferred on a SiO_2/Si substrate. (b) Schematic of a reference heating wire on a AlO_x strip covered SiO_2 substrate and a second wire on the encapsulated hBN sample. The wire transfer heat cross-plane through the hBN, which then dissipates into the substrate, as illustrated by the arrows. The heat from the wire flows cross-plane through the hBN and dissipates into the substrate as shown by arrows. (c) κ_{\perp} measurements in the hBN flake. The cross-plane κ_{\perp} values of bulk hBN crystals ($> 10 \mu\text{m}$ thick) shown for comparison, were reported by Jiang *et al.*⁴⁴³ and Simpson *et al.*⁴⁴⁴ Reprinted from Jaffe *et al.*, ACS Appl. Mater. Interfaces 15, 12545 – 12550 (2023);⁴⁴¹ licensed under a Creative Commons Attribution (CC BY) license.

effects that alter the states of photons and electrons in the smallest structures make them advantageous for packing more devices into a given area. As a result, nanostructures have been extensively studied as promising components for future thermoelectric devices.^{451,452}

The implementation of traditional thermal measurement methods employing a contact heating source or probing sensor is restricted by the small size of micro- and nanomaterials. Therefore, non-contact thermal measurement techniques are beneficial for the thermal characterization of microscale and nanoscale materials. There are some reliable methods for measuring κ of these nanostructures. We have listed them as follows: 3ω method, electron beam self-heating, bolometric, and photothermal techniques.

A. Self-heating DC and 3ω technique

The DC self-heating method utilizes a current applied to the test sample and detects the sample's average temperature from its electrical resistance.^{453,454} Although experimentally feasible, it only applies to conducting materials with stable resistance–temperature relationships and perfect sample-electrode contacts.⁴⁵⁵

In the DC self-heating method, the temperature coefficient of the sample resistance should be known before the experiment. It is illustrated in Fig. 58 for a hot wire that is self-heated by Joule effect under a DC voltage. According to Fourier's law, the temperature profile in the wire with uniform internal heat generation is parabolic with the two contacts kept at the temperature of the heat sink T_0 . The average temperature rise of the wire is determined by measuring the change in its electrical resistance.

Using the one-dimensional steady-state heat conduction given by Eq. (5) and assuming the wire ends are kept at a fixed temperature $T = T_0$ yields⁴⁵⁵

$$\kappa = \frac{\dot{q}l^2}{12(\bar{T} - T_0)}, \quad (109)$$

where l is the wire length and \bar{T} is the average wire temperature.

Using the DC self-heating technique, Li *et al.*⁴⁵⁴ studied the thermal transport properties of quasi-one-dimensional suspended graphene nanoribbons (GNR) with $0.25 \mu\text{m}$ length and $\sim 40 \text{ nm}$ width.

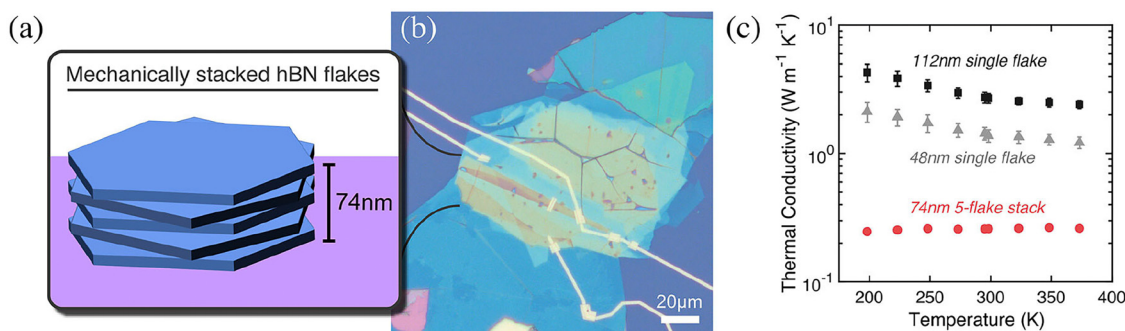


FIG. 57. (a) Schematic of a mechanically assembled stack of five exfoliated hBN flakes with random interlayer rotational misalignments. (b) Optical image of the heating wire fabricated over the five-flake stack. (c) Measured κ_{\perp} as a function of T of the stack shown in (b), which had a total thickness of 74 nm (bottom data points), and individual flakes with thicknesses of 112 and 48 nm (top data points). Reprinted from Jaffe *et al.*, ACS Appl. Mater. Interfaces 15, 12545–12550 (2023);⁴⁴¹ licensed under a Creative Commons Attribution (CC BY) license.

As shown in Fig. 59(a), the thermal conductivity increases with temperature until 320 K followed by a flattening trend.

The temperature dependence of κ implies a transition of thermal conductivity from diffusive to ballistic phonon transport.^{339,389} The measured κ in Fig. 59(a) is (224 ± 16) W m⁻¹ K⁻¹ at 300 K, which is about ten times smaller than that of large pristine graphene, while the electrical conductivity remains high, about 10^6 S m⁻¹.⁴⁵⁴ Still, this result is interesting in the context of potential applications where the heat flow in nanostructures can be effectively tuned through the effects of sample width, length, substrate interaction, and edge disorder. Thus, Bae *et al.*³³⁹ reported that 0.25-μm graphene samples achieve approximately 35% of the ballistic upper bound of thermal transport up to room temperature, enabled by the relatively large mean free path (~ 100 nm) of substrate-supported graphene. In contrast, structuring comparable samples into graphene nanoribbons (GNRs) leads to diffusive heat transport governed by the ribbon width and edge roughness. In the edge-dominated regime, the thermal conductivity of GNRs scales as $\kappa \sim (2b)^{1.8 \pm 0.3}$ for ribbons with a width of 65 nm at 300 K.³³⁹

Quite simply speaking, the reduction in the thermal conductivity of the GNR lattice compared to κ in bulk graphene can arise from (i) a narrow width-induced reduction of phonon MFP due to boundary (edge) scattering (from the rough diffuse edge to the smooth specular edge)⁴⁵⁶ or (ii) a quasi-ballistic effect induced by short lengths. The dominance of each mechanism was evaluated by numerically solving the BTE using a finite-volume method.⁴⁵⁴ The authors considered two extreme cases of edge scattering when all phonons were scattered diffusely (diffuse edges) or elastically (specular edges). The resulting temperature profiles are plotted along the normalized length in Fig. 59(b). The temperature jumps at the contacts, 5.05 K for the diffuse edge and 5.44 K for the specular edge, are originated from quasi-ballistic phonon transport. The average temperature \bar{T} increases 10.22 and 7.30 K for the diffuse and specular edges, respectively. Using Eq. (109), one finds $\kappa = 133$ W m⁻¹ K⁻¹ for the diffuse edge and 186 W m⁻¹ K⁻¹ for the specular edge. The calculated value of κ for the specular case is very close to the measured lattice thermal conductivity (182 ± 16 W m⁻¹ K⁻¹ at 300 K), allowing the authors to conclude that the edge scattering of phonons is very weak in their as-grown GNRs.⁴⁵⁴

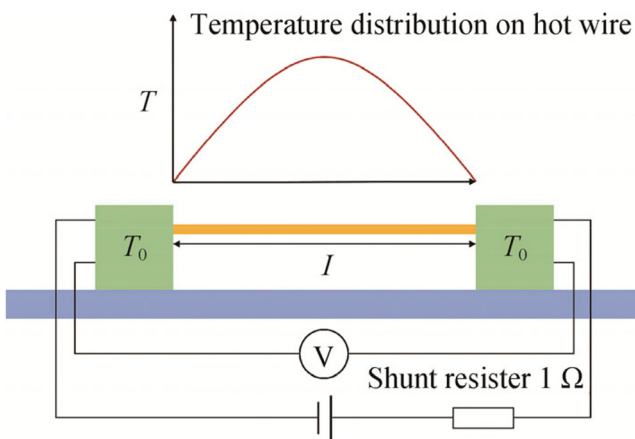


FIG. 58. Schematic showing measurement principle of the DC self-heating method. Reprinted from Abe *et al.*, J. Therm. Sci. **31**, 1037–1051 (2022).⁴⁵⁵ Copyright 2022, with permission from Springer Nature.

In the self-heating 3ω method, the sample itself acts as both heater and thermometer, provided it is electrically conductive and its resistance is temperature dependent.⁴⁵⁷ Similar to the conventional 3ω method (see Sec. III A), applying an AC of the form $I(t) = I_0 \cos \omega t$ to the conductive sample induces a temperature oscillation at frequency 2ω , which in turn produces a resistance fluctuation at 2ω . This results in a measurable voltage response at 3ω across the sample. The technique has been applied to various nanostructures, including platinum wires,⁴⁵⁷ nanoporous Si films,⁴⁵⁸ multi-walled²²⁴ and single-walled⁴⁵⁹ carbon nanotubes, as well as Si nanowires.⁴⁶⁰

The self-heating method was used by Finefrock *et al.*⁴⁶¹ to measure the thermal conductivity of lead telluride-coated glass fibers (PbTe). Figure 60 shows cross-sectional SEM images of the cut ends of the fiber sample. The four-probe configuration used to measure κ is shown in Fig. 60(b). Unlike a conventional four-probe resistance test, the two outside probes feed the electric current, and the two inside probes measure the voltage across the fiber.

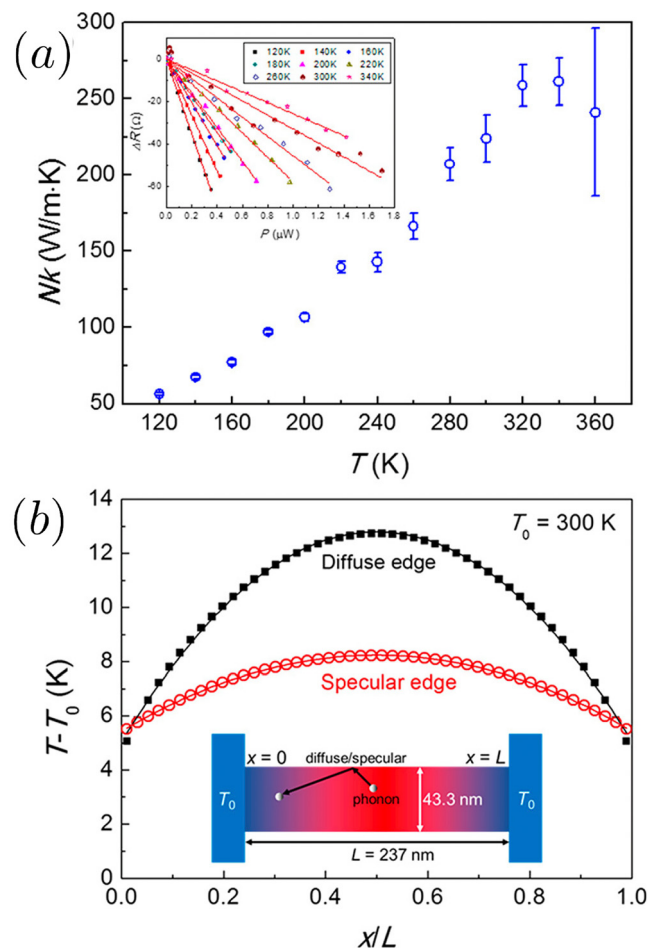


FIG. 59. (a) Temperature-dependent thermal conductivity of a free-standing single-layer graphene nanoribbon. (b) Temperature profiles across GNR simulated by phonon Boltzmann transport approach at the internal heat power $1 \mu\text{W}$ at 300 K. Reprinted from Li *et al.*, ACS Nano **13**, 9182–9189 (2019).⁴⁵⁴ Copyright 2019, with permission from American Chemical Society.

However, in contrast to electrical resistance measurement, the thermal setup requires that (i) the sample in between the two voltage probes must be suspended to allow a temperature variation, (ii) all probes must be extremely thermally conductive to ensure effective heat transfer between the sample and the substrate, and (iii) measurement must be performed under high vacuum and the entire setup must be thermally shielded to the substrate temperature to minimize radial thermal leakage via convection or radiative transfer.⁴⁵⁷

Explicit solutions to the 1D heat transfer equations that allow the calculation of the thermal conductivity with an analysis that bridges the high- and low-frequency limits of the solutions were reviewed by Lu *et al.*⁴⁵⁷

Finefrock *et al.*⁴⁶¹ developed an accurate thermal transport model that accounts for radiation heating and employs the finite-difference method to simulate the 3ω measurement process. This approach yields the thermal conductivity of PbTe-nanocrystal-coated glass fibers as a function of PbTe volume fraction, as shown in Fig. 60(d). The bare glass fiber exhibits a thermal conductivity of $0.70 \pm 0.10 \text{ W m}^{-1} \text{ K}^{-1}$. With the addition of a thin PbTe nanocrystal layer, κ initially increases to $0.93 \pm 0.14 \text{ W m}^{-1} \text{ K}^{-1}$ at 5.8% PbTe, but then decreases to $0.55 \pm 0.12 \text{ W m}^{-1} \text{ K}^{-1}$ at 35.8% PbTe. This reduction is attributed to cracking in thicker PbTe coatings, which impedes efficient heat transport.

Zhuge *et al.*⁴⁶⁰ reported the κ of B-doped Si nanowires with $45 \pm 5 \text{ nm}$ diameter and $\delta-$ modulated dopant distribution on the wire surface. A suspended Si NW structure was made to avoid unguarded thermal dissipation to the adjacent Si/SiO₂ substrate, as schematically shown in Fig. 61(a). The electrode contacts to the NW were then made using 20 nm Pt and 300 nm Au. The SEM image of the four-terminal device from the tilted view (top view in the inset) is shown in Fig. 61(b). The floating height of the NW is about 270 nm. A

high-resolution transmission electron microscopy (HRTEM) image of the nanowire is shown in Fig. 61(c) illustrating subsurface oxide ($\sim 1.5 \text{ nm}$) and thin disordered crystalline ($\sim 2 \text{ nm}$) layers developed due to the high concentration of dopant B atoms.

The κ results are summarized in Fig. 62. The authors also observed that κ remained nearly constant at NW lengths larger than $\approx 2 \mu\text{m}$, indicating that the thermal transport is in the diffusive regime. Taking into account the thermal contact resistance carefully, the inherent room temperature κ of a 45-nm wire was estimated to be $22-24 \text{ W m}^{-1} \text{ K}^{-1}$, which agrees fairly well with those of previous reports for vapor-liquid-solid (VLS) grown Si nanowires with smooth surfaces⁴⁶² and those with wet etching⁴⁶³ given in Fig. 62(a).

A key challenge in interpreting these results lies in the interplay between ballistic and diffusive conduction regimes, as illustrated in Fig. 61(a). In the diffusive regime, phonons undergo strong boundary scattering at the surface, which dominates over impurity scattering. Moreover, because dopants are confined to the surface boundary layer, their influence on thermal transport is further reduced relative to surface-induced boundary scattering. The wire diameter (d) changes in the phonon MFP (Λ_{NW}) can be written under Matthiessen's rule as^{464,465}

$$\frac{1}{\Lambda_{NW}} = \frac{1}{\Lambda} + \frac{1-p}{(1+p)d}, \quad (110)$$

where p is the surface specularity and Λ is the phonon MFP in bulk Si. The thermal conductivity of the NW is then calculated using the Born-von Karman-Slack (BvKS) model and the phonon MFP spectra of bulk Si.^{466,467}

As indicated by the dashed lines in Fig. 62(a), the measured κ values are well fitted using $p \approx 0.1$, indicative of the nearly diffusive phonon regime at the surface of the Si NW even with a smooth surface.

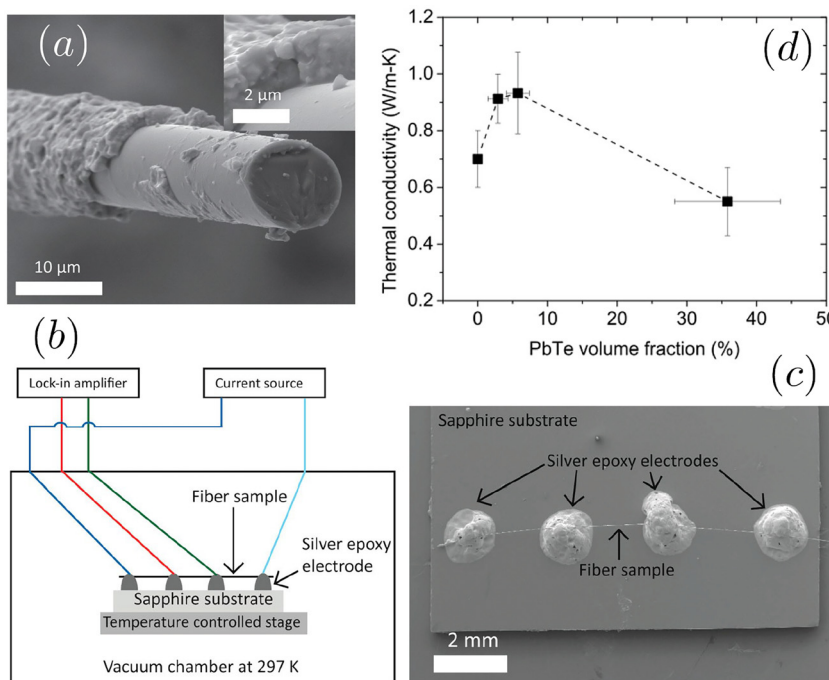


FIG. 60. (a) Cross-section SEM images of cut ends of glass fiber covered with 35.8% PbTe by volume. (b) Schematic of the four-probe configuration for measuring the thermal conductivity of a rod-like sample. The sample is heat sunk to the sapphire substrate through the four electric contacts, but the part in between the two voltage contacts needs to be suspended to allow the temperature variation. (c) SEM image of the fiber sample, electrodes, and substrate. (d) κ of PbTe coated glass fiber as a function of PbTe volume fraction at about 300 K. Reprinted from Finefrock *et al.*, Nano Lett. 13, 5006–5012 (2013).⁴⁶¹ Copyright 2013, with permission from American Chemical Society.

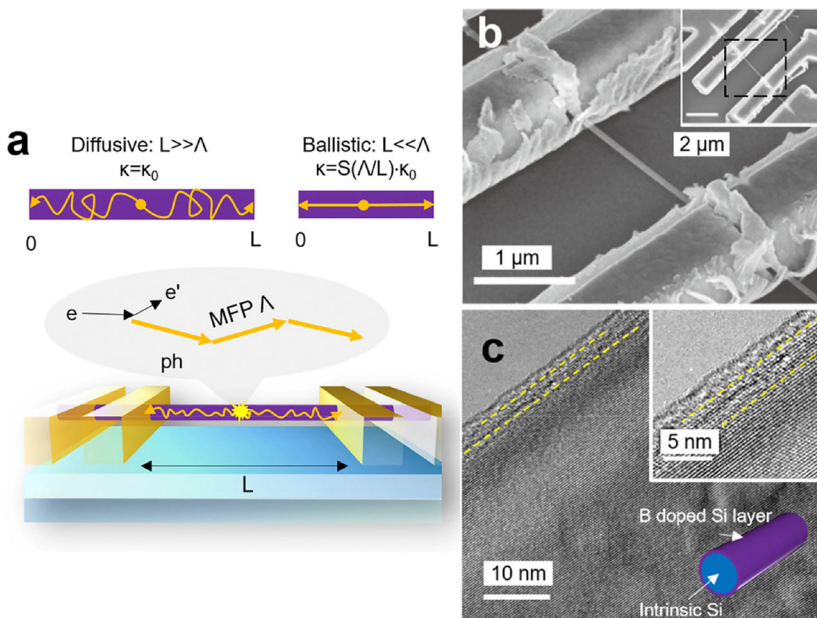


FIG. 61. (a) Schematic of the suspended Si nanowire with the illustration of diffusive and ballistic thermal transport in the self-heated nanowire. The nanowire has a resistivity of 10^{-3} – $10^{-2}\Omega\text{ cm}$, corresponding to the dopant concentration of $\sim 10^{18}$ – 10^{19} cm^{-3} . The contact resistance to the nanowire was estimated to be within $\sim 1\%$ to 10% of the total resistance of the nanowire. (b) SEM image of the fabricated four-terminal measurement device. (c) HRTEM image of the δ -doped Si nanowire with an intrinsic core but a heavily B-doped surface layer. Reprinted from Zhuge *et al.*, J. Appl. Phys. **124**, 065105 (2018).⁴⁶⁰ Copyright 2018, with permission from AIP Publishing.

The aspect to notice is the importance of the frequency dependence of surface scattering which is ignored when using the singular specularity p for all phonons in Si.⁴⁶⁵ Meanwhile, this simplified analysis still allows for a qualitative description of the diffusive nature of phonons at the surfaces, which is likely the result of surface roughness and the interface with surface oxides as discussed by Neogi *et al.*,⁴⁶⁸ Martin *et al.*,⁴⁶⁹ He and Galli,⁴⁷⁰ and others.

Figure 62(b) displays the temperature dependence of κ for nanowires of different lengths. For long Si nanowires, the measured $\kappa(T)$ agrees well with the previous report of Li *et al.*⁴⁶² that claimed that κ begins to decrease above $\approx 150\text{ K}$ due to increased Umklapp phonon-phonon interaction, as indicated by gray line in Fig. 62(b). For NWs shorter than $\approx 1\text{ }\mu\text{m}$, κ continuously increases with T , implying the suppressed role of Umklapp scattering during phonon transport.

Phonon transport models were also employed by Zhuge *et al.*⁴⁶⁰ to investigate the influence of ballistic phonons on heat flux in self-heated Si nanowires. As noted by Minnich *et al.*,⁴⁷¹ ballistic carriers can be partially decoupled from the thermalized phonon population. While these ballistic phonons still contribute to heat transport, they carry significantly less heat than predicted by Fourier's law, leading to a reduced apparent thermal conductivity. Consistent with this picture, Zhuge *et al.*⁴⁶⁰ observed an abnormal length dependence of κ in self-heated 1D Si nanowires [Fig. 61(a)], which they attributed to ballistic transport. By contrast, Raja *et al.*,⁴⁷² using the DC self-heating technique, reported no measurable length dependence of κ in highly B-doped (10^{19} cm^{-3}) Si nanowires with an average diameter of 30 nm. These contrasting results highlight the need for further investigation, particularly into the thermalization behavior of Joule-heated phonons under nanoscale confinement and the role of dopant-induced scattering.

It is important to highlight several factors that likely contribute to the discrepancy between the results reported by Zhuge *et al.*⁴⁶⁰ and Raja *et al.*⁴⁷² First, in heavily doped Si nanowires, phonon MFPs are significantly reduced due to strong point-defect scattering. This leads

to predominantly diffusive thermal transport that is effectively independent of wire length. In contrast, the δ -modulated, surface-doped Si nanowires (45 nm diameter) studied by Zhuge *et al.* exhibit less point-defect scattering, allowing phonons with longer MFPs to persist and contribute to heat conduction. As a result, a measurable length dependence can emerge, particularly for wire lengths shorter than $\sim 2\text{ }\mu\text{m}$.⁴⁶⁰

Second, when point defects dominate scattering, the entire MFP spectrum shifts toward shorter values, suppressing any observable length scaling. By comparison, when surface roughness or selective phonon-branch scattering prevails, a high-MFP tail remains, enabling thermal conductivity to increase with length in the sub- μm to μm range.

Third, differences in experimental methodology may influence sensitivity to non-diffusive transport. Zhuge *et al.* employed a self-heated 3ω geometry, where surface-localized heating closely mimics actual device operation and enhances sensitivity to quasi-ballistic effects and non-uniform temperature profiles, especially in shorter wires. Raja *et al.*, by contrast, used a suspended, electrically contacted structure with a DC self-heating technique specifically designed to differentiate diffusive and non-diffusive regimes.

Finally, variations in thermal contact resistance, heat spreading near contacts, and data analysis protocols can obscure or mimic apparent length dependence if not consistently addressed. Differences in analytical assumptions—such as surface specularity, interface resistance, or the MFP cutoff—can also critically affect whether subtle length-dependent trends are observed or overlooked.

B. Electron beam self-heating technique

Another approach to utilize sample self-heating is the electron-beam self-heating technique, as proposed by Wang *et al.*²³ and Liu *et al.*²⁴ This is exemplified in Fig. 63 where the heat is generated by applying a scanning-focused electron beam to a $\text{Si}_{0.7}\text{Ge}_{0.3}/\text{NiSi}_{0.7}\text{Ge}_{0.3}$

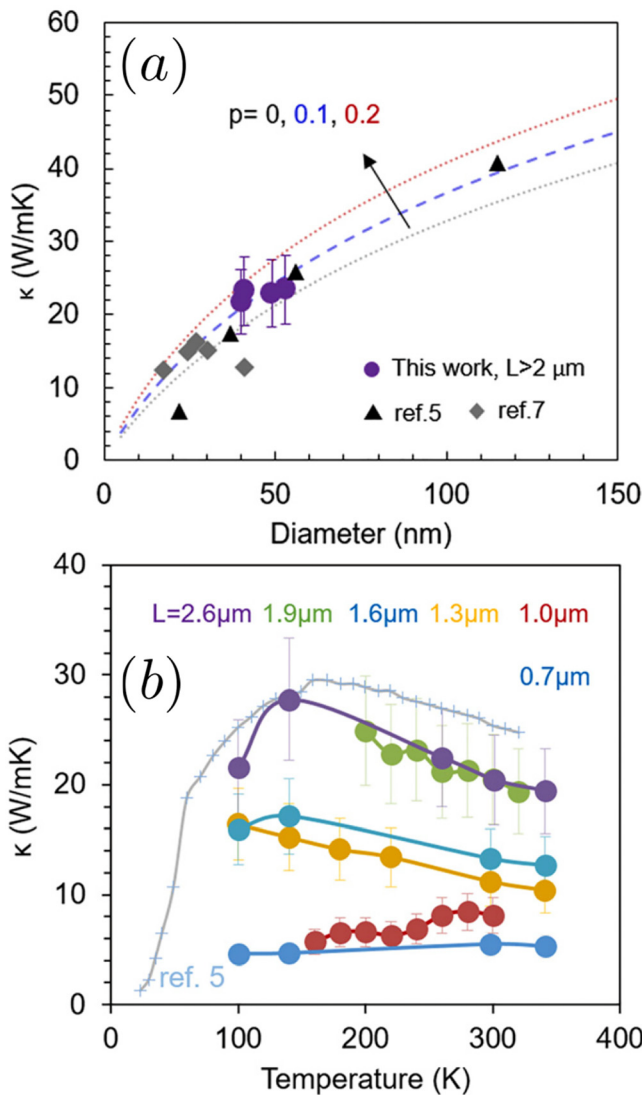


FIG. 62. The measured diameter (a) and temperature (b) dependence of thermal conductivity for Si nanowires of varied lengths from 0.7 to $2.6\mu\text{m}$. The references are from Li *et al.*⁴⁶² and Chen *et al.*⁴⁶³ Reprinted from Zhuge *et al.*, J. Appl. Phys. **124**, 065105 (2018).⁴⁶⁰ Copyright 2018, with permission from AIP Publishing.

NW. As above, the average temperature rise at the NW is deduced from the variation of the electrical resistance. This technique uses thermal isolated microfabricated islands with the NW suspended between two temperature sensors (see Sec. IV D). When the focused electron beam strikes the sample [see Fig. 63(a)], the energy of the electron beam is absorbed at a particular location x_0 along the length of the sample, resulting in the formation of a localized hot spot. The heat generated by the focused electron spot flows to the left and right islands, increasing the temperature at the ends by $\Delta T_L = T_L - T_0$ and $\Delta T_R = T_R - T_0$, respectively [see Fig. 63(b)], where T_0 is the substrate temperature. T_R and T_L can be measured by the traditional thermal bridge method.

At a thermal steady state, the heat flux from the hot spot to the islands equals the heat flux from the two islands to the substrate through the beams suspending the islands. The thermal resistance $R_i(x)$ at any point i on the suspended nanowire can be written as²⁴

$$R_i(x) = R_b \left[\frac{a_0 - a_i(x)}{1 + a_i(x)} \right], \quad (111)$$

where R_b is the equivalent thermal resistance of the six suspension beams that connect the left (or right) island to the outside environment, $a_0 = \Delta T_{L0}/\Delta T_{R0}$, when electrical heating of the left (L) or right (R) island raises its temperature by ΔT_{L0} or ΔT_{R0} , and $a_i(x) = \Delta T_{Li}/\Delta T_{Ri}$ when the electron beam irradiates a spot along the NW at i . Then the thermal conductivity of the suspended NW is

$$\kappa = \frac{1}{A} \frac{1}{dR_i(x)/dx}, \quad (112)$$

where A is the cross-sectional area of the nanowire.

A detailed derivation of these quantities and a more detailed analysis are provided by Wang *et al.*,²³ Liu *et al.*,²⁴ Zhao *et al.*,⁴⁷³ and Aiyiti *et al.*⁴⁷⁴

The values of κ measured in five- (S1) and four-layer (S2 and S3) MoS₂ ribbons using the thermal bridge method and focused electron beam self-heating technique can be directly compared in Fig. 64 (closed and open symbols, respectively) finding good agreement between them and that measured with Raman thermometry.

The room temperature thermal conductivity derived from the four-layer MoS₂ (S2) is $34 \pm 6 \text{ W m}^{-1} \text{ K}^{-1}$ which is comparable to the results reported by Yan *et al.*,³⁴² Wei *et al.*,⁴⁷⁵ and Cai *et al.*⁴⁷⁶ However, this value contrasts to higher values of κ found in other studies. Thus, Sahoo *et al.*⁴⁷⁷ obtained $\kappa = 52 \text{ W m}^{-1} \text{ K}^{-1}$ using Raman thermometry and Jo *et al.*⁴¹² found $\kappa = 44\text{--}50 \text{ W m}^{-1} \text{ K}^{-1}$ with the suspended thermal bridge method. The discrepancy may be observed from different sample seeds, rough sample edges, and different measurement methods.⁴⁷⁴ The first principles calculations of Gu *et al.*⁴⁷⁸ indicate that the basal plane κ of MoS₂ decreases with an increasing number of layers, although there has been some debate as to whether this trend is consistent with the experiment.^{342,394,412,477,479}

Zhao *et al.*⁴⁷³ employed the same strategy and measured the thermal resistance along porous Si NWs, as shown in Fig. 65. The linearity of the dependence implies uniformity in the measured thermal resistance and diffusive phonon transport along the nanowire.

The cross-sectional area A in a porous Si NW is defined as the solid, non porous cross-sectional area. With this definition, and using Eq. (112), Zhao *et al.*⁴⁷³ analyzed how the thermal conductivity is affected by porosity. The simulation and measurement results are included in Figs. 66 and 67. In the NEMD simulation, the two heat baths at temperatures of 310 and 290 K are located at the left and right ends, respectively, as shown in Fig. 66(a). Free boundary conditions are assumed for the surface of the porous Si nanowire, while fixed boundary conditions are considered in the NW direction. Figure 66(a) also shows the simulated temperature profiles of porous and solid nanowires. The resulting κ on porosity is shown in Fig. 66(b), illustrating that increasing porosity enhances phonon-interface scattering, which leads to a sharp reduction of κ .

The relationship between κ and porosity, measured on the same porous nanowire, is summarized in Fig. 67. To account for the unusually low thermal conductivity of porous Si NWs and its dependence on

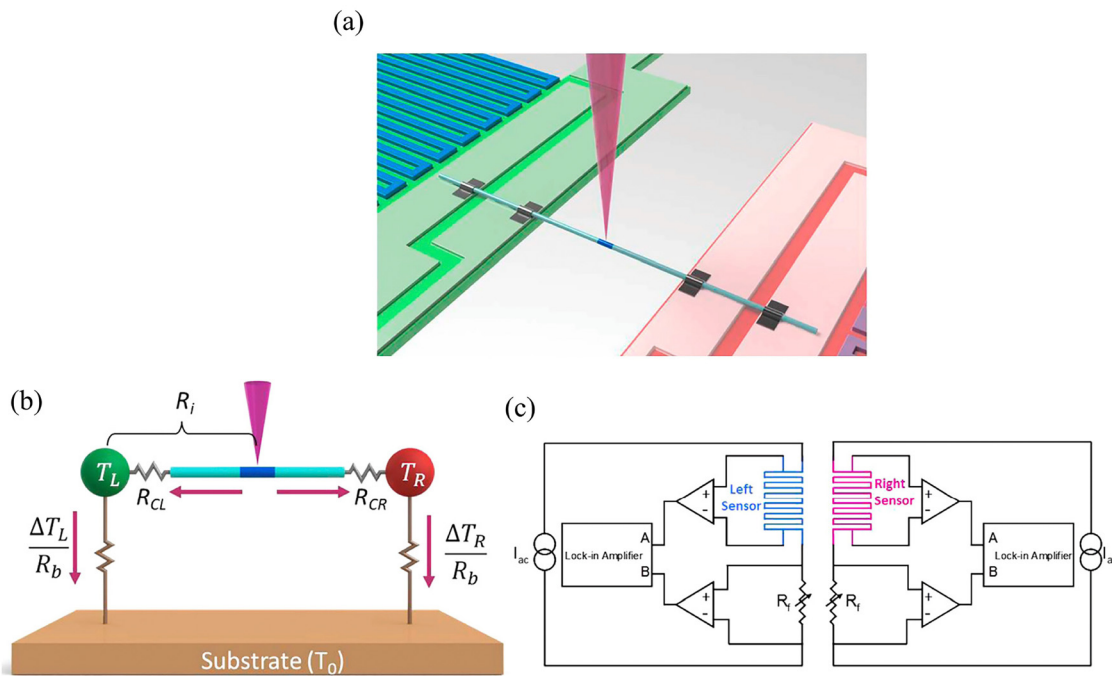


FIG. 63. Experimental setup for electron beam self-heating technique. (a) Schematic of the microfabricated device, including the left and right Pt resistance sensor islands. A focused electron beam (vertical cone) is used as a heat source. (b) Equivalent thermal resistance circuit with the temperature rise of the left (ΔT_L) and right (ΔT_R) sensors. Reprinted from Liu *et al.*, Nano Lett. **14**, 806–812 (2014).²⁴ Copyright 2014, with permission from American Chemical Society.

20 December 2025, 13:48:09

porosity, a modified phonon radiative heat transfer (EPRT) model, originally developed by Majumdar,⁴⁸⁰ can be employed. In the EPRT approach, phonons move ballistically within the crystalline part of the nanowire and scattered diffusively when arrive to the surface of the pores. The phonon MFP are assumed to be frequency dependent (phonons with small frequency have a long wavelength and a large MFP, being the dominant thermal carriers). Zhao *et al.*⁴⁷³ made an elegant and complex effort to show that over a wide range of structure sizes, ranging from about 5 nm to about 500 nm, the EPRT model captures the scaling of the effective κ as a function of structure size very well, particularly for highly porous Si nanowires.

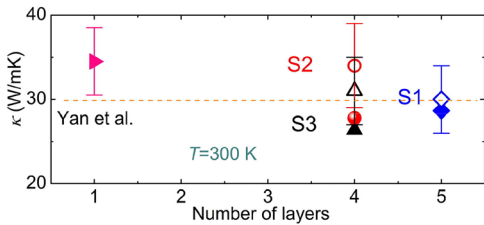


FIG. 64. κ vs number of layers in MoS₂. Closed symbols denote κ measured by thermal bridge method, while open symbols denote the thermal conductivity derived from the focused electron beam self-heating technique. The measured data by Yan *et al.*³⁴² obtained from temperature-dependent Raman spectroscopy are shown for comparison. Reprinted from Aiyiti *et al.*, Sci. Bull. **63**, 452–458 (2018).⁴⁷⁴ licensed under a Creative Commons Attribution (CC BY) license.

Advantages of self-heating method

1. This method allows spatially resolved measurements of the thermal conductivity of a single nanowire with sub-20 nm resolution. It also effectively addresses the long-standing challenge of poorly defined thermal contact resistance between the nanowire and the two islands, a major limitation of conventional thermal-bridge techniques.²⁴

Limitations of self-heating method

1. The primary challenge of this method is generating sufficiently large temperature gradients between the two membranes and the electron-beam spot, especially in thin materials where electron energy absorption is limited. The resulting small temperature rise at the sensors produces a weak signal with a low signal-to-noise ratio, complicating detection.⁴⁸¹
2. This technique requires high-quality samples with clean, flat surfaces, as the electron beam is highly sensitive to rough edges, defects, and polymer residues, all of which can introduce significant errors in the measured thermal resistance signal.⁴⁸¹

C. Suspended thermal micro bridge method

Thermal conductivity measurements of nanowires and nanotubes are often performed using microfabricated suspended island structures, as shown in Fig. 68 (upper inset), with integrated heaters and temperature sensors on each island. An individual MWCNT or a bundle of MWCNTs is placed across the two suspended islands, which

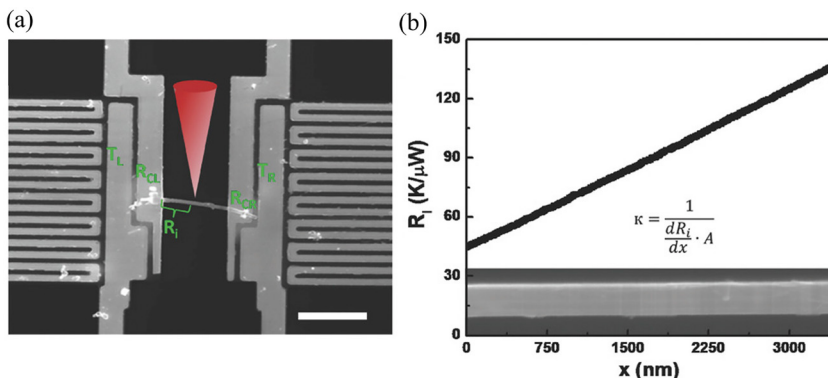


FIG. 65. (a) Diagram of the suspended porous Si nanowire with a focused electron beam. The scale bar is $5\ \mu m$. (b) Measured thermal resistance against the distance along the nanowire. The inset below is an SEM image of the suspended nanowire. Reprinted from Zhao *et al.*, *Adv. Funct. Mater.* **27**, 1702824 (2017). Copyright 2017, with permission from John Wiley and Sons.

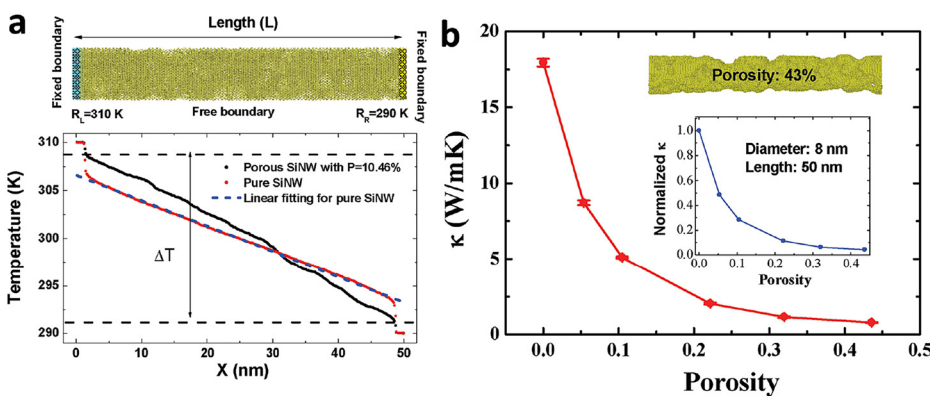


FIG. 66. (a) Structure of porous Si nanowire with porosity 10.46% (upper panel) and the corresponding temperature profile of this nanowire (lower panel). The wire diameter is 8 nm, and the length is 50 nm. (b) κ of porous Si nanowire vs porosity. The inset is the structure of a porous silicon nanowire with a porosity of 43%. Inset: normalized thermal conductivity as the ratio of κ of a porous Si nanowire to that of solid Si nanowire. Reprinted from Zhao *et al.*, *Adv. Funct. Mater.* **27**, 1702824 (2017).⁴⁷³ Copyright 2017, with permission from John Wiley and Sons.

possess high thermal resistance to the environment. When one island is heated, heat is conducted through the nanowire/nanotube to the other island. Using a simple heat transfer model,²⁸ the thermal conductance of both the nanotube connection and the suspended support legs can then be estimated (Fig. 68).

To estimate κ from the measured thermal conductance, both the geometric factors of the MWCNT and the anisotropy of κ must be taken into account. In MWCNTs with good thermal contact to a

thermal bath, the outer walls contribute more significantly to heat transport than the inner walls, while the axial-to-radial conductivity ratio affects the conversion from thermal conductance to thermal conductivity. Neglecting junction conductance and assuming isotropic behavior provides a lower bound for the intrinsic axial thermal conductivity, as shown in the lower inset of Fig. 68. As the diameter of a MWCNT bundle increases, κ becomes similar to the bulk value.⁴⁸²

The phonon MFP can be expressed as $\Lambda^{-1} = \Lambda_{st}^{-1} + \Lambda_U^{-1}$, where Λ_{st} and Λ_U denote the static and Umklapp scattering lengths, respectively. At low temperatures, Umklapp processes are strongly suppressed, giving $\Lambda \approx \Lambda_{st}$ and a thermal conductivity $\kappa(T)$ that follows the temperature dependence of the specific heat. Below the Debye temperature of the interlayer phonon mode, $\Theta_{D\perp}$, $\kappa(T)$ displays a weakly three-dimensional character, scaling as $\kappa \sim T^{2.5}$ (see the low-temperature fit in Fig. 68), consistent with graphite single crystals.⁴⁸³ For $T > \Theta_{D\perp}$, the interlayer phonon modes become fully populated, and $\kappa(T) \sim T^2$, reflecting the quasi-two-dimensional nature of thermal transport in MWCNTs.²⁸ At higher temperatures, enhanced phonon–phonon Umklapp scattering reduces Λ_U , and once $\Lambda_{st} > \Lambda_U$, κ decreases with increasing T .

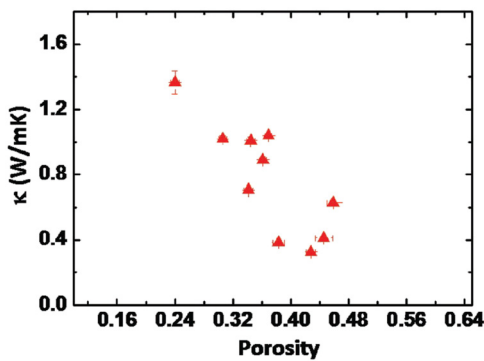


FIG. 67. Measured κ as a function of porosity for ten different porous Si nanowires. Reprinted from Zhao *et al.*, *Adv. Funct. Mater.* **27**, 1702824 (2017). Copyright 2017, with permission from John Wiley and Sons.

D. Scanning thermal microscopy

In contrast to far-field optical techniques, scanning thermal microscopy (SThM) is not limited in lateral resolution by optical diffraction at a few hundred nanometers. It can perform thermal imaging and measurements far beyond the micrometer scale. Scanning thermal

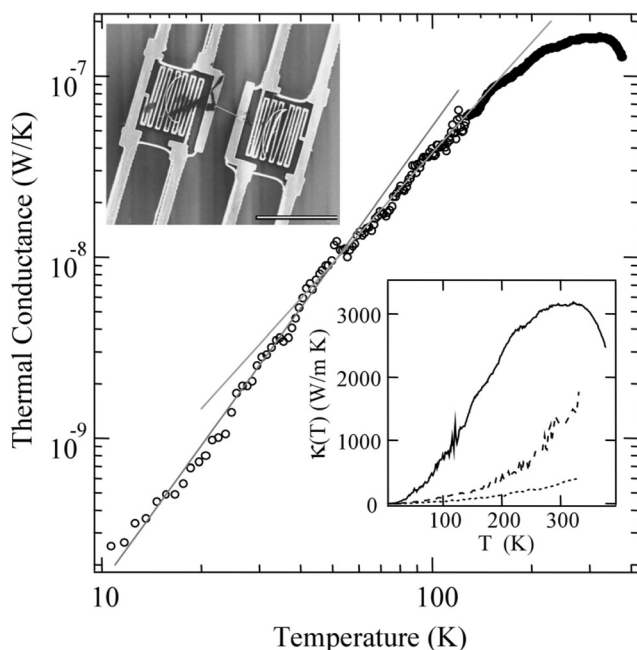


FIG. 68. Thermal conductance of an individual MWCNT, 14 nm in diameter. The solid lines represent the linear fits to the data in logarithmic scale, with slopes of 2.50 and 2.01 in different temperature ranges. Lower inset: Temperature-dependent $\kappa(T)$ of the same MWCNT (solid line), compared with small (80 nm, broken line) and large (200 nm, dotted line) MWCNT bundles. Upper inset: SEM image of the suspended islands with the individual MWCNT; scale bar: 10 mm. Reprinted from Kim *et al.*, Phys. Rev. Lett. **87**, 215502 (2001).²⁸ Copyright 2001, with permission from APS.

microscopy techniques are based on scanning probe microscopy (SPM)⁴⁸⁴ with a spatial resolution that depends on the characteristic lengths associated with the heat transfer between the small thermal probe and the sample. SThM probes can be engineered with tip curvatures radii on the order of 10 nm.⁴⁸⁵

The first SPM instrument for nanoscale thermal measurements was invented in 1986 by Williams and Wickramasinghe,⁴⁸⁶ soon after the invention of scanning tunneling microscopy. Since the 1990s, it has been actively developed and applied in various areas such as microelectronics, optoelectronics, polymers, and CNTs.⁴⁸⁵ There are passive and active SThM operation modes. In the passive, or temperature-contrast mode, the probe monitors the local temperature to map the spatial temperature profile of the sample surface. In the active, or conductivity-contrast mode, the probe simultaneously heats the sample and measures its temperature. The efficiency of heat dissipation from the probe into the sample depends, among other factors, on the thermal properties of the sample. Therefore, this mode provides the distribution of local thermal conductivity and allows visualization of areas exhibiting different thermal properties.

The scanning thermal microscopes are frequently based on scanning tunneling microscopy (STM) or atomic force microscopy with the tip replaced by a thermal probe when measurements are performed as a function of the tip-sample force and distance using various types of sensors placed at the tip of an AFM probe. A thermocouple

comprising two wires is frequently used and these two wires provide a stiffness coefficient that is large enough to form the cantilever required for an AFM setup. The setup of an AFM-based SThM system is exemplified in Fig. 69.

Typically, the cantilever tip is heated by direct laser irradiation while the sample is maintained at room temperature, and the tip is raster-scanned across the surface to acquire spatial data. A thermocouple attached to the cantilever measures the temperature change at the tip during scanning. Thermal images can also be obtained by recording variations in thermoelectric voltage using an electronic bridge circuit as exemplified in Fig. 70. Depending on whether the laser beam is modulated or not (DC or AC modes), the image will reflect either the thermal conductivity or the thermal diffusivity of the sample.⁴⁸⁸ Enhanced heat dissipation during tip-sample indicates higher thermal conductivity of the sample, leading to a faster temperature drop at the probe tip. The SThM images in Figs. 69(c), 69(e), and 69(g) demonstrate the strong capability of this technique to map thermal conductivity, exemplified by the increase in κ due to rGO loading, as commonly observed in graphene-based composites.⁴⁸⁹

In the setup of Fig. 69, cantilever deflections are probed by reflecting a laser beam on a tiny mirror toward a photodetector. Other deflection measurement systems can involve piezoresistive cantilevers.⁴⁹¹ The probe deflection generates an electrical signal that is detected. Piezoelectric scanners are used to move the sample vertically and to scan its surface laterally. In the imaging mode, the deflection signal is used in a feedback control loop to maintain a constant tip-sample contact force while the tip scans laterally. The combination of the scan position data $x - y$, the force feedback signal, and the thermal signal measured by the sensor at the tip or on the cantilever yield the topography and thermal images of the surface.⁴⁸⁵ As above, the thermal image contrast reflects the change in the amount of heat locally exchanged between the tip and the sample.

SThM measurements usually require various thermosensitive sensors that can be separated into groups such as Seebeck thermovoltage (thermocouple junctions), variation in electrical resistance (thermoresistive probes), fluorescence, or thermal expansion (dynamic cantilevers).^{485,492} The thermal probe of an SThM system determines its capability, range of operation, and measurement quality. The most critical parameters of an SThM probe are the tip radius and probe material. The radius of the tip limits the spatial resolution⁴⁸⁴ and restricts the heat transfer between the tip and the sample.⁴⁸⁸ The probe material affects the performance of SThM by controlling the thermal transfer mechanism. The highly productive SThM tip-developing research has enriched the field with various probe techniques, although extensive research is still under way in this area.

Könemann *et al.*⁴⁹⁰ described the temperature-dependent thermal conductivity of a self-heated MWCNT supported on a silicon substrate from SThM measurements (see Fig. 70). The technique used a microcantilever with an integrated resistive sensor coupled to a Si tip. The applied bias V_{tot} induced significant heating, so the sample temperature was modulated by applying an AC with a frequency ω across the MWCNT. This resulted in periodic Joule self-heating at frequency 2ω . A local spot on the sample surface with temperature T_{sample} was thermally coupled through the tip to a resistive sensor integrated into the Si microelectromechanical systems (MEMS) cantilever. Changes in the sensor temperature T_{sensor} led to changes in its electrical resistance, which were tracked using a Wheatstone bridge circuit. The DC change

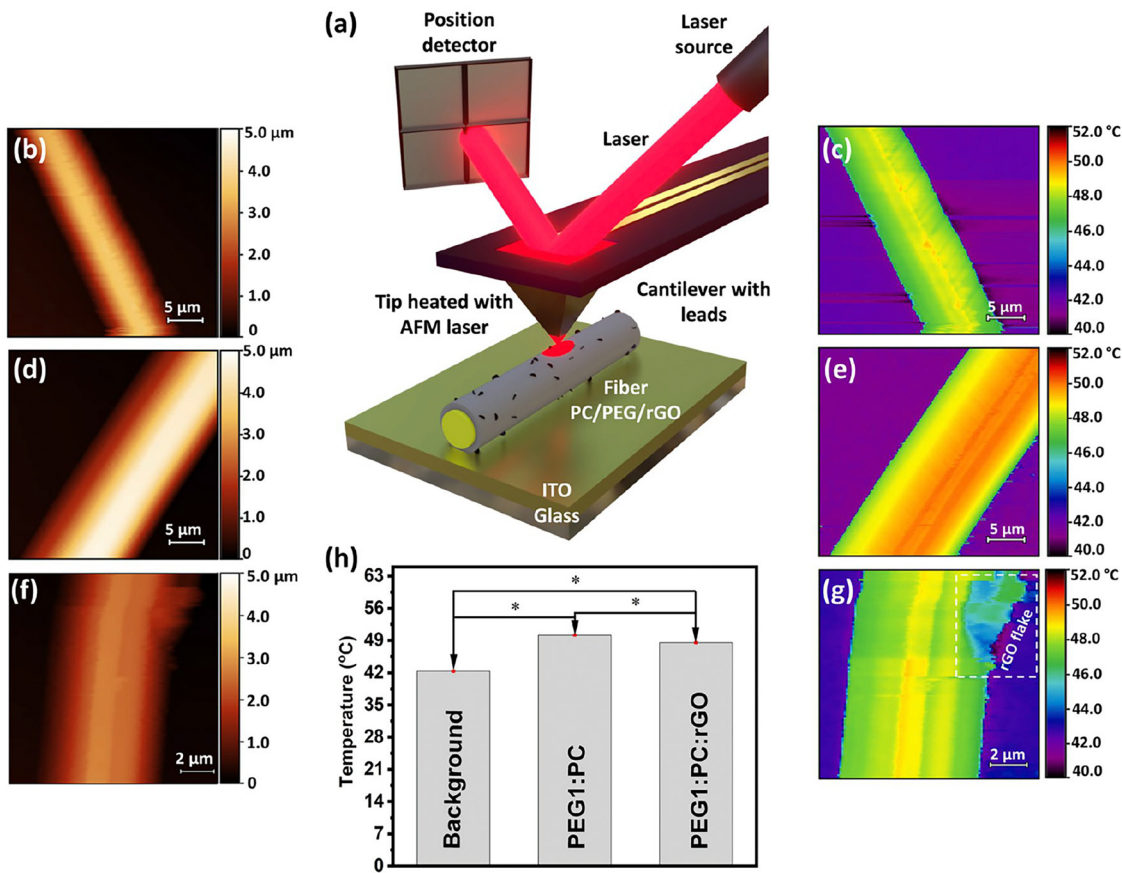


FIG. 69. Schematic showing the major components of the AFM tool for acquiring the SThM images of core-shell fiber with an optical beam deflection system (a) along with SThM and topographic micrograph images (b)–(g) of individual fibers from polyethylene glycol (PEG) as core and rGO-polycarbonate (PC) as shell. (b) Topographic and (c) SThM images of PEG1:PC:rGO single fiber. (d) Topographic and (e) SThM images of PEG1:PC single fiber. Enlarged topographic (f) and SThM (g) images of PEG1:PC:rGO fiber indicate the attachment of rGO flakes on the fiber's surface. (h) Bar diagram of the average surface temperature of the fiber with and without rGO along with the background temperature. Reprinted from Das *et al.*, *Adv. Compos. Hybrid Mater.* **7**, 123 (2024).⁴⁸⁷ licensed under a Creative Commons Attribution (CC BY) license.

in voltage V_{DC} between the Wheatstone bridge legs and its AC amplitude V_{AC} at 2ω then relates the local sample temperature T_{sample} to the known and constant out-of-contact sensor temperature.^{490,493} The resulting topography and SThM temperature maps are shown in Figs. 71(a) and 71(b), respectively.

A carbon particle originating from the CNT growth is seen close to the left contact in both images. By contrast, the Joule heating map in (b) shows a hot spot centered between the contacts, coinciding with a deliberately introduced amorphous carbon segment deposited using a focused ion beam, with functions as an integrated nanoheater. The temperature in this hot spot is ~ 50 K higher than that in the adjacent defect-free sections. Elevated temperatures are also observed in the regions where the contacts bury MWCNT. This observation suggests either that charge carriers dissipate heat along the entire CNT, with the electrical current density decaying over micrometer length scale, or that a large thermal boundary resistance at the CNT-metal interface confines heat within the CNT.⁴⁹⁰

Combining SThM and frequency modulated Kelvin probe force microscopy data and using the one-dimensional heat diffusion model, Könemann *et al.*⁴⁹⁰ obtained temperature-dependent thermal

conductivities, shown in Fig. 72. They are about one order of magnitude smaller than that for free-standing MWCNTs²⁸ (see Sec. V C), consistent with experiments highlighting the substrate-nanotube interaction. This results in the quenching of acoustic phonon modes,⁴⁹⁴ which become no longer available for heat transfer or increasing phonon scattering rates. The temperature behavior of κ also contrasts with that in freely suspended CNTs, when the thermal conductivity increases up to room temperature and then saturate⁴⁹⁵ or even decreases with increasing temperature, which is attributable to Umklapp scattering processes.^{28,29} It is worth noting that the $\kappa(T)$ behavior observed in Fig. 72 above the room temperature is similar to that reported for strongly confined phonon conductors such as Si nanowires, where increasing temperature does not enhance boundary scattering, in contrast to the case of Umklapp scattering.⁴⁹⁰

In 1999, Fiege *et al.*⁴⁹⁶ applied the 3ω approach proposed by Cahill *et al.*¹¹ to process the SThM measurement (for additional discussion, see Sec. III A). In the SThM configuration, an alternating current (AC) $I(\omega) = I_0 \cos \omega t$ is added to the continuous current at the tip. Modulation frequencies between 100 Hz and several tens of kilohertz were used. This frequency range is essentially related to the time

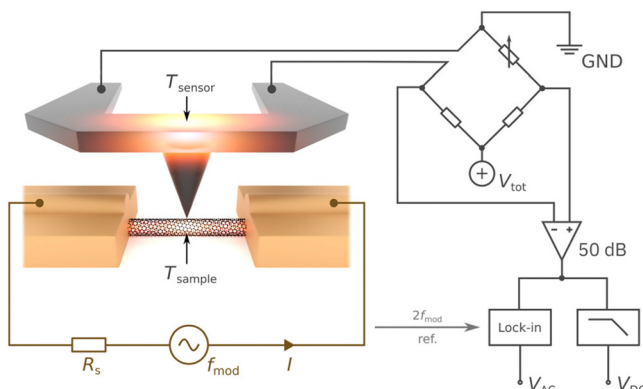


FIG. 70. Schematic of the SThM thermometry technique with an integrated resistive sensor coupled to a silicon tip used to study MWCNTs, about 4 μm in length and 10–50 nm in diameter. The distance between the contacts is $\approx 1 \mu\text{m}$. Reprinted from Könenmann *et al.*, J. Phys. Chem. C **123**, 12460–12465 (2019),⁴⁹⁰ licensed under a Creative Commons Attribution (CC BY) license.

response of the tip and hence to the finite heat capacity of the sensor and the dimensions of the tip.^{496,497} The signals recorded by synchronous detection are the amplitude and phase of the 3ω component of the voltage generated across the tip, whose average temperature T_P is kept constant. Under these conditions, the 2ω component $P_{2\omega}$ of the power dissipated in the probe leads to a modulation of the tip temperature at the same frequency 2ω written as

$$\Delta T_{P_{2\omega}} = T_{P_{2\omega_0}} \cos(2\omega t), \quad (113)$$

where $T_{P_{2\omega_0}}$ is the amplitude of the temperature modulation. Quoting approximate equations used by Cahill *et al.*¹¹ and Fiege *et al.*,⁴⁹⁶ the relation of the amplitude of the second harmonic of the tip temperature $T_{P_{2\omega_0}}$ to that of the power per unit length of the tip filament ($p_{2\omega} = P_{2\omega}/2L$ with L being the tip length) can be given in the form:⁴⁸⁸

$$T_{P_{2\omega_0}} = \frac{p_{2\omega}}{\pi\kappa} (C - \ln \omega), \quad (114)$$

where C is a term independent of the frequency and a function of the thermal diffusivity of the sample and the effective diameter of the tip–surface thermal contact region.

The measured alternating voltage reads⁴⁸⁸

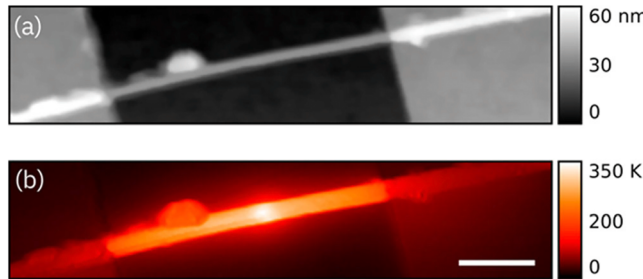


FIG. 71. (a) Topography map and (b) temperature rise due to Joule heating in the MWCNT for a modulation current amplitude $I = 349 \mu\text{A}$. Reprinted from Könenmann *et al.*, J. Phys. Chem. C **123**, 12460–12465 (2019),⁴⁹⁰ licensed under a Creative Commons Attribution (CC BY) license.

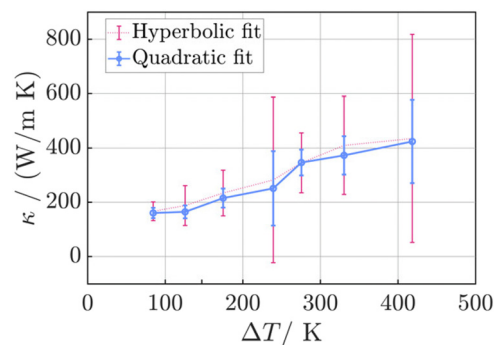


FIG. 72. Temperature-dependent thermal conductivity along the MWCNT out of the amorphous carbon segment. Reprinted from Könenmann *et al.*, J. Phys. Chem. C **123**, 12460–12465 (2019),⁴⁹⁰ licensed under a Creative Commons Attribution (CC BY) license.

$$V_{3\omega}(t) = I_0 \alpha_p \frac{p_{2\omega}}{4\pi\kappa} (C - \ln \omega) \sin(3\omega t - \phi), \quad (115)$$

where α_p is the thermal diffusivity of the tip, ϕ is the phase shift between this voltage and the excitation current $I(\omega)$. By plotting the amplitude of the 3ω signal vs $\ln \omega$, we find a slope inversely proportional to the thermal conductivity of the material.

Since the constant C can be determined from measurements in reference samples, this can be used to calibrate SThM to perform κ measurements, provided that the analyzed samples have roughness and elasticity/hardness similar to the reference samples.

Currently, there are alternative approaches to perform the 3ω -SThM measurements and accurately account for the energy balance near the tip. In this context, it is worth noting the works of Majumdar,⁴⁸⁴ Depasse *et al.*,^{498,499} Lefévre *et al.*,⁴⁹⁷ Hwang *et al.*,⁵⁰⁰ Gomès *et al.*,⁴⁸⁵ Menges *et al.*,⁴⁹³ Hwang and Kwon,⁵⁰¹ Zhang *et al.*,⁴⁹² Swami *et al.*,⁵⁰² and others.

Advantages of SThM

- One experimental technique enables direct observation of nanoscale thermal transport phenomena with high temporal and spatial resolution, featuring thermal time constants in the milli- to microsecond range and nanoscale lateral resolution.^{35,503} The typical lateral thermal resolution is approximately 100 nm,^{421,504} while the use of nanofabricated tips can achieve spatial resolutions approaching 10 nm.^{505,506}
- Following appropriate calibration procedures, passive mode SThM can map the surface temperature distribution of a sample,^{501,507} while active mode SThM can be employed to measure material properties such as thermal conductivity and Seebeck coefficient, as well as to perform surface lithography using specialized high temperature probes.^{508–511}
- The technique is nondestructive and compatible with a wide variety of sample types.
- SThM measurements can be conducted in both contact and non-contact modes.
- It is suitable for operation in various environments, including air, liquids, and rarefied gases.⁵¹²
- Quantitative measurements of thermal conductivity are feasible for materials with low κ (less than $10 \text{ W m}^{-1}\text{K}^{-1}$).⁵¹³

Limitations of SThM

1. The main challenge lies in accurately correlating the sensor signal with the surface temperature. This task is complicated by non-equilibrium processes at nanoscale contacts and the discontinuous temperature distribution across the tip-sample interface.⁴⁸¹ A further difficulty is separating thermal information from topographic data, as the heat flux required to maintain the tip temperature depends strongly on the sample's thermal properties.⁴⁸⁸
2. Another significant limitation is the effect of thermal contact resistance.⁴²¹ Specifically, the signal related to heat flux derived from the temperature difference between the tip and the sample is influenced by the unknown thermal contact resistance,⁵¹⁴ which increases as the contact area between the tip and the sample decreases.
3. Theoretical modeling of SThM data is also complex. Artifacts arising from modulation of the effective tip-sample contact area introduce additional errors in the measured temperatures, making nanoscale temperature measurements challenging.⁴⁸¹
4. Modeling heat transfer between SThM probes and samples becomes even more complex in regimes approaching fully ballistic transport across the tip-sample contact, where conventional diffusive heat transport equations are no longer valid.⁵¹⁵
5. Reducing fluctuations in the tip-sample contact area is another major challenge, as such variations alter the resistance due to topographical effects. Consequently, it becomes necessary to weigh the correlation between the topographic and thermal resistance data. This requirement introduces additional complexity when directly comparing thermal transport information between different SThM.²¹⁵

E. Bolometric technique

The high thermal conductivities of CNTs combined with their electrical and mechanical properties can yield higher-dimensional CNT materials with interesting and unique combinations of properties. Thin films of single-walled carbon nanotubes, as well as composite materials based on SWCNTs, attract research attention in this respect.^{385,516–520} The SWCNT film is a network of individual SWCNTs and SWCNT bundles in which thermal and electrical resistances are dominated by intertube junctions, which in turn are strongly affected by chemical modification of the SWCNTs and film preparation technology.³⁸⁵

Itkis *et al.*³⁸⁵ measured the thermal characteristics of the SWCNT films using the bolometric method. In the experimentation, IR radiation served as the heat source, inducing a triangular temperature distribution across the suspended SWCNTs. The electrical resistance of thin SWCNT films depended strongly on the temperature; the variation was used to measure light-induced temperature modulation ΔT of the film. The temperature data ΔT were extracted directly from the amplitude of resistance modulation ΔR and the temperature dependence of dark resistance dR/dT given by Eq. (105) was obtained. The resulting temperature dependence of the thermal and electrical conductivities is shown in Figs. 73(a) and 73(b), respectively. The $\kappa(T)$ values in Fig. 73(a) were also corrected for radiation heat losses $q_{rad} \propto \cdot T^3 \Delta T$,^{217,385} where ΔT is the average difference between the temperature of the suspended SWCNT film and the temperature of the cold radiation shield surrounding the sample.

Figure 73(a) shows a monotonic increase in κ with increasing T for both AP- (as prepared) and P(purified)-SWCNT films, typical of individual SWCNTs.^{29,521} The value of κ of the thinner AP-SWCNT film is $\approx 30 \text{ W m}^{-1} \text{ K}^{-1}$ at 300 K, which is approximately a factor of three smaller than the value obtained for the thicker P-SWCNT film. These values, in turn, are about two orders of magnitude smaller than κ of individual SWCNTs due to the thermal resistance of the intertube junctions in the SWCNT networks. On the other hand, the observed differences in κ between AP-SWCNT and P-SWCNT films are assumed to be due to the less tightly packed CNT network in the AP-SWCNT film as compared to the highly condensed morphology of the thicker P-SWCNTs.

The authors also analyzed the relative electron and phonon contributions to κ using the Lorenz number, $L_0 = \kappa/\sigma T$. For individual SWCNTs, $L_0 \approx 1 \times 10^{-7} \text{ W } \Omega \text{ K}^{-2}$, compared to $2.45 \times 10^{-8} \text{ W } \Omega \text{ K}^{-2}$ for pure metals, where electrons dominate heat transport.³⁸⁵ This implies that in metallic SWCNTs, the ratio of electron to phonon contributions to κ is roughly 1:3. In contrast, L_0 increases to $7 \times 10^{-6} \text{ W } \Omega \text{ K}^{-2}$ for the P-SWCNT film and $4 \times 10^{-4} \text{ W } \Omega \text{ K}^{-2}$ for the AP-SWCNT network at 300 K. These values indicate that both electrons and phonons contribute to thermal transport in SWCNT networks, but intertube junction resistance strongly suppresses the electronic channel, causing L_0 to rise by two to four orders of magnitude. Moreover, since two-thirds of the SWCNTs in the networks are semiconducting and do not contribute to charge transport, phonons emerge as the principal heat carriers.

F. Photothermal radiometry

Photothermal (PT) radiometry was introduced for the first time by Kanstad and Nordal.⁵²² This work motivated subsequent exploratory studies by Wang *et al.*,^{523,524} which expanded the range of experimental implementations and applications. The PT technique relies on the photothermal effect, where absorption of incident light in a thin subsurface region leads to local heating and enhanced infrared emission, often modeled as surface heating. The resulting temperature rise can be probed through various induced physical processes, including acoustic signals in photoacoustic (PA) techniques,^{277,525,526} or thermal emission from the surface in PT techniques.⁵²⁷ The PA and PT radiation techniques belong to the large branch of laser-assisted noncontact thermal measurement methods discussed above. Unlike PA implementation, the PT acquires thermal radiation in the frequency domain instead of sound waves, which can reduce the complexity of the measurement setup and widen the temperature range for thermal measurement, as the microphone is no longer necessary.⁹ The technique has no frequency limitation, thus it can in principle measure samples with thicknesses ranging from nanoscale to bulk. The PT method is also tailored to accommodate the special surface smoothness requirements compared to thermoreflectance techniques because it detects thermal radiation rather than optical reflections.

The technique uses a laser (usually an IR laser) and the experiment can be done in transmission or reflection, as shown in Figs. 74(a) and 74(b). The usual setup contains a laser, a chopper modulating the frequency of the light, a lock-in and an IR detector. In reflection, the temperature decay of the way through the sample is

$$\Delta T_{AC}(d, t) = \frac{I_0}{2\kappa} \sqrt{\frac{\alpha}{\omega}} e^{-d/\delta} \cos\left(\omega t - d/\delta - \frac{\pi}{4}\right). \quad (116)$$

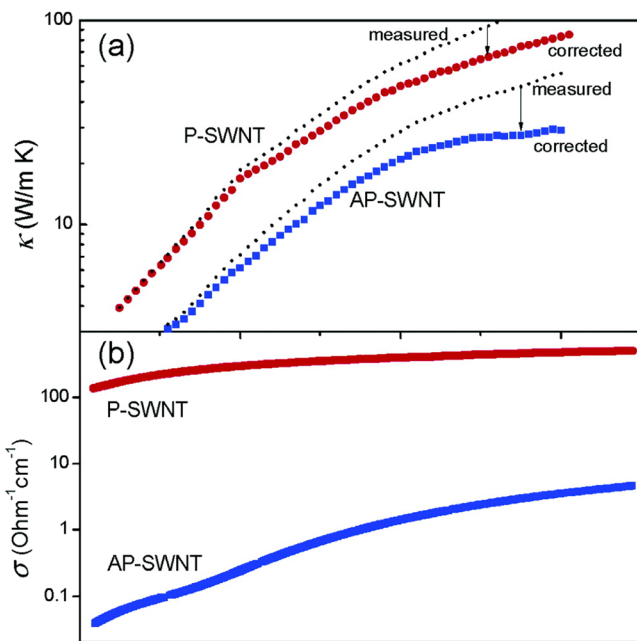


FIG. 73. Temperature dependence of the thermal (a) and electrical (b) conductivities of SWCNT films with thicknesses of 100 nm (P-SWCNT) and 35 nm (AP-SWCNT). Corrected data take into account radiation heat losses. Reprinted from Iltis *et al.*, Nano Lett. 7, 900–904 (2007).³⁸⁵ Copyright 2007, with permission from American Chemical Society.

The phase depends on the frequency. Taking into account the possible frequency shift with the lock-in amplifier,

$$\Delta\phi(\omega) = \frac{d}{\delta} = d\sqrt{\frac{\omega}{2\alpha}}. \quad (117)$$

When the phase lag, $\Delta\phi$, is plotted as a function of the square root of the frequency, the slope yields α , the thermal diffusivity, rather than the thermal conductivity directly. In the reflection configuration, the thermal wave propagates to the end of the sample and returns to the surface, introducing a factor of $1 + Re^{-2d/\delta}$, where R is the thermal reflection at the surface. In this case, the phase lag is still described by Eq. (117). In both cases, depositing a black layer on both sample surfaces is necessary to improve the light absorption and the backside infrared emission. The setups are very similar to the laser flash technique (see Sec. IIIB).

Wang *et al.*⁵²⁴ conducted a PT radiometry experiment to measure the axial thermal conductivity of highly aligned multi-walled carbon nanotubes (CNTs). The CNTs were grown vertically as MWCNTs in Ni catalyst over a thin Cr layer deposited on a Si substrate. Cr plays the role of the radiation layer. A 1064-nm YAG laser was modulated in the 2–70 kHz frequency range. The extracted thermal conductivity of MWCNT was much lower than many theoretical predictions. They attribute the low thermal conductivity to the bad quality of the samples (non-uniform walls, defects, disorder), confirmed by TEM. Wang's group published another work in 2006,⁵²⁸ with slightly better results, but still far from theoretical predictions. The thermal contact resistance at the ends of the nanotubes that are in contact with the thin Si wafer

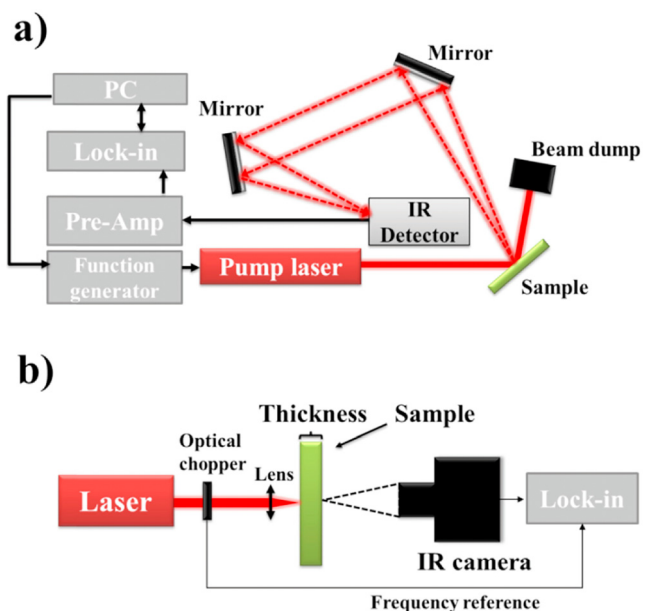


FIG. 74. Schematic of the photothermal emission experimental setup in front (a) and rear (b) configurations. Reprinted from Abad *et al.*, Renewables Sustainable Energy Rev. 76, 1348–1370 (2017).⁷ Copyright 2017, with permission from Elsevier.

substrate was also extracted from the measurement. The Si substrate was chosen because of the limited absorption of the IR laser beam and its transparency to the thermal radiation emitted by the chromium layer. The sample consists of several layers including the air at the top of the CNT array, the Cr film, the Si substrate, and the air below the Si substrate (see Fig. 75).

Wang *et al.*⁵²⁴ studied the thermal conductivity using photothermal spectroscopy. showed that the effective thermal conductivity of the CNT array is $0.145 \text{ W m}^{-1} \text{ K}^{-1}$, while the thermal conductivity of individual CNTs is $27.3 \text{ W m}^{-1} \text{ K}^{-1}$. The latter value for MWCNTs is much smaller than theoretically predicted (3000 – $6600 \text{ W m}^{-1} \text{ K}^{-1}$ ^{127,28,529,530}) for SWCNTs. Note that the previous bulk measurement on MWCNT using the self-heating method yields only $20 \text{ W m}^{-1} \text{ K}^{-1}$ ⁴⁸² while CNT fibers show $\approx 34 \text{ W m}^{-1} \text{ K}^{-1}$ ¹³⁶³ (see Sec. V E), which is close to the value of κ measured in thin SWCNT films³⁸⁵ (more details of these measurements can be found in Sec. IV A). Mehew *et al.*⁵³¹ measured $\kappa \approx 50 \text{ W m}^{-1} \text{ K}^{-1}$ for films composed of double-walled CNTs (DWCNTs) and $\approx 7 \text{ W m}^{-1} \text{ K}^{-1}$ for SWCNT films. They attributed the enhanced κ for DWCNTs to the reduced scattering of phonons by defects and the appearance of an additional conductance channel due to the presence of the second wall in the structure of the nanotube. However, a value two orders of magnitude larger ($\sim 250 \text{ W m}^{-1} \text{ K}^{-1}$) was reported by Hone *et al.*⁵³² in magnetic field-aligned SWCNTs. The MWCNT κ should be lower than that of SWCNTs, consistent with the value of around $15 \text{ W m}^{-1} \text{ K}^{-1}$ for aligned MWCNT measured by Yang *et al.*⁵³³ Meanwhile, several research groups obtained a somewhat higher value of about $25 \text{ W m}^{-1} \text{ K}^{-1}$.^{457,482,534} An especially interesting feature of CNT materials is the thermal conductivity of MWCNT buckypapers. In these samples, the MWCNTs are randomly organized, making it reasonable to

expect κ values lower than those reported for CNT films and fibers. Yue *et al.*⁵³⁵ measured thermal conductivities of about $1\text{--}3 \text{ W m}^{-1} \text{ K}^{-1}$ and attributed the low values to the tangled CNT network and the poor thermal conductance at CNT–CNT contact points, which dominate heat transport in buckypapers.

The small thermal conductivity of the sample in Fig. 75 is likely due in part to the unique structure of CNTs produced by Wang *et al.*⁵²⁴ with Ni nanoparticles at the tip of the CNTs, which yields the contribution of thermal transport across the atomic layer of carbon atoms, and arises in part from poor structural qualities and phonon-defect scattering processes. In addition, the low thermal conductivity could be partially attributed to the inherently disordered nature of some CVD-grown CNTs. Thus, in a similar way to the sample shown in Fig. 75, vertically aligned CNTs grown by CVD on a Si wafer but with 70-nm-thick Ni film as the catalyst exhibit a thermal conductivity of about $40 \text{ W m}^{-1} \text{ K}^{-1}$.⁵²⁸ HRTEM studies revealed the amorphous carbon layer surrounding the graphite layer structure of the CNTs. This isolating layer prevents effective heat transport between CNTs and the Ni film.

Although their interpretation relies on several assumptions, CNT bundles exhibit significantly lower thermal conductivity than individual CNTs. Notwithstanding the many assumptions to interpret, the thermal conductivity of CNT bundles is much lower than that of a single CNT. A significant reason for this is that an ensemble average is typically measured to show the results for various combinations of individual CNTs in the samples having different types and geometry. It is therefore very difficult to develop the analysis methods that can be used to extract the thermal properties of a particular CNT.

Advantages of photothermal emission technique

1. This technique exhibits high sensitivity and enables the detection of subtle temperature variations, which can be converted into thermal conductivity values.
2. It requires relatively low surface smoothness compared to thermoreflectance methods, since it detects thermal radiation rather than optical reflections.
3. It is a nondestructive technique that allows the measurement of cross-plane thermal diffusivity, heat capacity, and thermal

contact resistance in a wide range of materials without compromising their structural integrity.^{524,527,536,537}

4. The technique has the theoretical ability to measure samples with thicknesses ranging from the nanoscale to the bulk scale.⁵²⁷
5. It also enables the study of multilayered samples under the assumption of one-dimensional heat conduction along the thickness direction.⁵²⁷
6. Recent advances have extended the analytical model to allow simultaneous extraction of the optical absorption coefficient and thermal diffusivity in homogeneous and multilayered solids.^{538,539}

Limitations of photothermal technique

1. Depending on the specific implementation, photothermal methods can be complex and may require sophisticated instrumentation, which makes them less accessible to some researchers.
2. The absolute amplitude of thermal radiation cannot be directly used because it depends on many factors, including reflection, absorption, emissivity, experimental setup, and the sensitivity of the sample's IR detector. Instead, the shape of the reduced amplitude as a function of modulation frequency should be employed to determine thermal transport properties.⁵⁴⁰
3. IR thermal radiation is not material-specific. When an individual nanostructure is measured, the IR detector may collect radiation from both the structure itself and its surroundings, leading to measured values that represent averaged thermal properties rather than the intrinsic properties of the nanostructure.⁵²⁷
4. Another important consideration concerns the in-plane thermal conductivity. To validate the use of a one-dimensional heat conduction model, the heating laser spot size should exceed the in-plane thermal diffusion length of each sample layer. However, for materials with high in-plane thermal conductivity, such as graphene, this assumption is violated. In these cases, a three-dimensional heat conduction model must be applied, taking into account the spatial distribution of the heating laser.^{541,542}
5. To accurately determine the thermal properties of one-dimensional materials, extensions of the photothermal (PT) technique, such as the pulsed laser-assisted thermal relaxation (PLTR) method, should be employed.^{543,544} The PLTR2 technique⁵⁴⁵ offers a further advancement, enabling simultaneous measurement of the thermal properties of free-standing films along both in-plane and cross-plane directions.

G. Laser flash analysis

A novel technique, known as the ultrafast laser flash method,^{546–548} has been developed to extend the measurement capabilities of conventional laser flash analysis (LFA) into the thin-film regime. This method employs a picosecond laser as the excitation source and utilizes thermoreflectance for temperature detection. It adopts a rear-heating/front-detection geometry, representing a natural evolution of the traditional laser flash approach.

Ruoho *et al.*²⁶⁶ applied laser flash thermal diffusivity measurements to determine the in-plane thermal conductivity (κ) of ZnO thin films (thickness $<100 \text{ nm}$) grown by atomic layer deposition and deposited on a $20\text{-}\mu\text{m}$ polycarbonate substrate, as illustrated in Fig. 76(a). The substrate thermal diffusivity ($0.078 \text{ mm}^2 \text{ s}^{-1}$) was

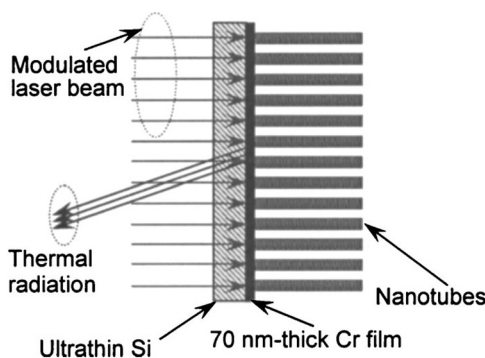


FIG. 75. Schematic of the highly aligned multi-walled CNT sample perpendicularly grown on a 70-nm-thick Cr film coated with a 14- μm -thick Si wafer used to study thermal transport in CNTs. Reprinted from Wang *et al.*, J. Appl. Phys. 97, 064302 (2005). Copyright 2005, with permission from AIP Publishing.

increased to $\approx 0.17 \text{ mm}^2 \text{ s}^{-1}$ for the sample with the thickest ZnO film [see Fig. 76(b)]. The effective thermal conductivity for the composite material can then be calculated using a modified effective medium theory,⁵⁴⁹ which yields $\kappa \sim 2 \text{ W m}^{-1} \text{ K}^{-1}$ for the data presented in Fig. 76(b).²⁶⁶ This is in fair agreement with the lower range of experimental values of κ for ZnO thin films ranging from 1 to $40 \text{ W m}^{-1} \text{ K}^{-1}$.^{550–555}

Recently, MXenes, as an emerging family of 2D metal carbides, nitrides, and carbonitrides, has shown notable potential for thermal management due to their unique 2D nanostructure, adjustable surface chemistry, and high electrical and thermal conductivity.^{556,557} Examples include poly(p-phenylene-2,6-benzobisoxazole) (PBO)/MXene nanocomposite films with a fine PBO nanofibre network on the $\text{Ti}_3\text{C}_2\text{T}_x$ MXene nanosheets exhibiting electrical insulation ($2.5 \times 10^9 \Omega \text{ cm}$) and an in-plane thermal conductivity of about $42 \text{ W m}^{-1} \text{ K}^{-1}$.⁵⁵⁸

The thermal conductivities of the films measured using the LFA method are shown in Fig. 77(a). The $\kappa_{||}$ of the PBO film is $25.6 \text{ W m}^{-1} \text{ K}^{-1}$, exceeding the values for most typical polymers mainly due to the high crystallinity of PBO nano-fibers and the fine 3D PBO nano-fiber network which greatly reduces the phonons scattering.^{559,560} The in-plane κ of the composite films is found to first increase and then decrease with the MXene content.

The PBO/MXene film with a 20 wt. % MXene content shows the highest value of $\kappa = 42.2 \text{ W m}^{-1} \text{ K}^{-1}$. The authors analyzed the results employing a pictorial model shown in Fig. 77(b). The notable improvement of κ in PBO/MXene is related to the strong interaction between MXene nanosheets and PBO nanofibres. As a good thermal conductor, MXene nanosheets act as a thermally conductive bridge in composites, providing a fast phonon/electron channel for heat transfer between PBO nanofibres.⁵⁶¹ It is also apparent that their unique 2D sheet structure would effectively improve the orientation alignment of the PBO nanofibers, thus further increasing the in-plane component of the phonon velocity.^{562,563}

The in-plane thermal conductivity decreases sharply at high MXene contents, as the aggregation between MXene nanosheets increases their thermal resistance and precludes orientational alignment of PBO nano-fibers. The common characteristic of this orientation network structure is that κ of the composite film shows a high degree of anisotropy. The thermal conductivity $\kappa_{||}$ of the PBO/MXene film with a 20 wt. % MXene content is more than 400 times larger than κ_{\perp} , which is $0.103 \text{ W m}^{-1} \text{ K}^{-1}$ in Fig. 77(a).

Generally this is a direct consequence of a layered film microstructure observable in Fig. 77(b). The interconnected PBO nanofibers and MXene nanosheets are highly oriented, so heat carriers can be rapidly conducted in the horizontal direction. However, in the vertical direction, heat conduction considerably slows down as a result of the layered structure with weak interactions (relative to the covalent bonds in the building blocks along the horizontal direction). In addition, the electron conduction between MXene nanosheets is considerably reduced by the barrier of the PBO network. This effect could explain why the PBO/MXene film showed extremely high electrical resistance.

The effect of dissipating heat from the local heat source is illustrated in Figs. 77(c) and 77(d). Since the sample thicknesses are much smaller than the PBO and PBO/MXene film diameters, the contribution of κ_{\perp} to heat dissipation in the thickness direction is negligible.^{564,565} By turning the power supply on/off, the surface temperature

of the bare hot plate rises rapidly in 80 s and then drops slowly in 40 s. Attaching the PBO film to the hot plate significantly suppresses surface temperature fluctuations, with an even stronger effect observed for the PBO/MXene film. This demonstrates an effective strategy for high-temperature thermal management in electronic devices.

VI. MEASURING THERMAL BOUNDARY CONDUCTANCE

Interfaces between dissimilar materials significantly contributes or even dominate the thermal resistance in thin films and nanostructures, where phonons are the primary heat carriers.^{566–568} A deeper understanding of phonon-mediated transport across the interfaces is needed for a more effectively design and implementation of nanostructure devices.¹⁶² Experimental measurements and theoretical predictions of TBCs have made significant progress over the past decades due to significant advances in the research of micro- and nano-scale heat transfer.^{14,569–571} Different theoretical models and methods have been developed to interpret the experimental results on TBC, including the acoustic mismatch model, diffuse mismatch model, atomic Green's function, and molecular dynamics simulations.^{566,569} A recent review of Feng *et al.*⁵⁷² discusses TBC across wide and ultrawide bandgap semiconductor interfaces and provides a comprehensive comparison of various experimental and simulation approaches remarking their benefits and drawbacks. In a similar manner, the work of Yue *et al.*⁵⁷³ conveniently summarizes the experimental results and MD simulations of interfacial thermal transport in atomic-layer materials.

Mehew *et al.*⁵³¹ measured the thermal conductivity of two types of free-standing CNT films containing single- or double-walled CNTs using two-laser Raman thermometry. The effective thermal conductivities of these CNT networks were found to be two orders of magnitude lower than those of isolated CNTs due to the presence of voids and intertube junctions that restrict thermal transport in the CNT network due to the boundary resistance.^{574–577} These junctions also act as phonons filters with MFPs greater than the junction spacing, further reducing the cumulative contribution to κ .⁵⁷⁷

Accurate measurement of boundary conductance is often costly and time-consuming, largely because of the challenge in isolating a single interface. However, significant progress has been made in measuring,^{566,578} modeling,^{171,174,579} and understanding the thermal boundary conductance.¹⁷⁰ Since the TBC is restricted to an interface, methods capable of probing very small volumes are required. A widely exploited strategy is to use transient heating at short time scales (or large frequencies), to control and minimize the thermal penetration depth δ given by Eq. (26). Localizing the thermal excitation and response near an interface makes the measurement more sensitive to TBR.¹⁶⁶ The 3ω method (see Sec. III A), time and frequency domain thermoreflectance (see Secs. III C and III D) are specifically designed to isolate TBR (or TBC) data.

A. 3ω technique

In practice, the 3ω method is limited to frequencies $\omega/2\pi$ smaller than $\sim 10\text{--}100 \text{ kHz}$, imposing a lower bound on the thermal penetration depth⁵⁸⁰ and limiting the minimum detectable TBR. This method requires a careful experimental design. A thin film is often placed between the substrate and the heater line, resulting in two TBRs in series. To ensure accurate measurements, the substrate should have a high thermal conductivity. In one approach, the thermal response is

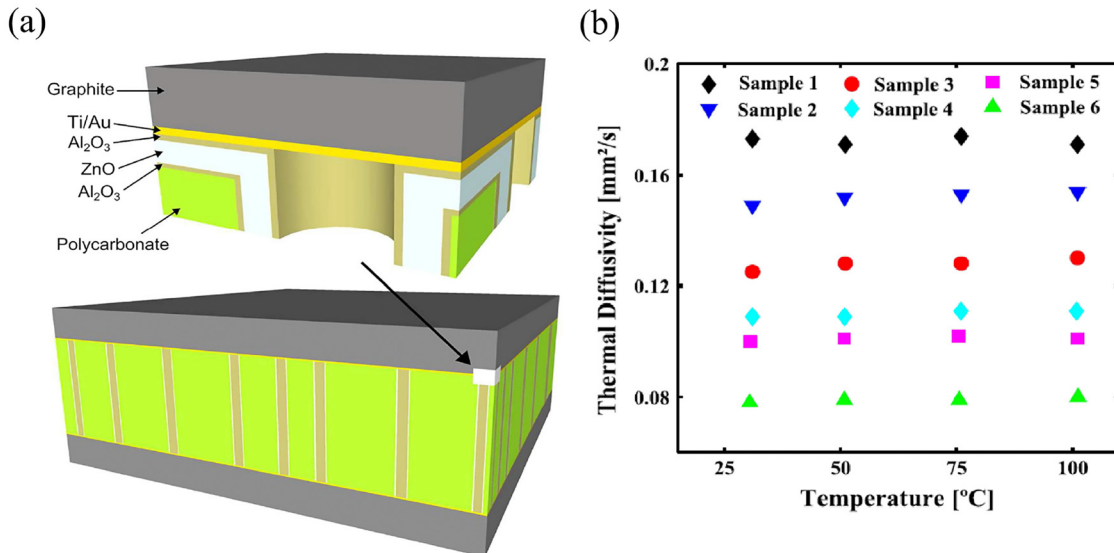


FIG. 76. (a) Schematic of the structure including ZnO thin film with aligned continuous pores deposited on polycarbonate substrate with graphite layers on both sides of the structure. (b) $\alpha(T)$ of the ZnO nanocomposites with the film thicknesses of 102 nm (sample 1), 59 nm (sample 2), 35 nm (sample 3), 17 nm (sample 4), 12 nm (sample 5), and a polycarbonate substrate (sample 6). Reprinted from Ruoho *et al.*, *Nanotechnology* **26**, 195706 (2015). Copyright 2015, with permission from IOP Publishing.

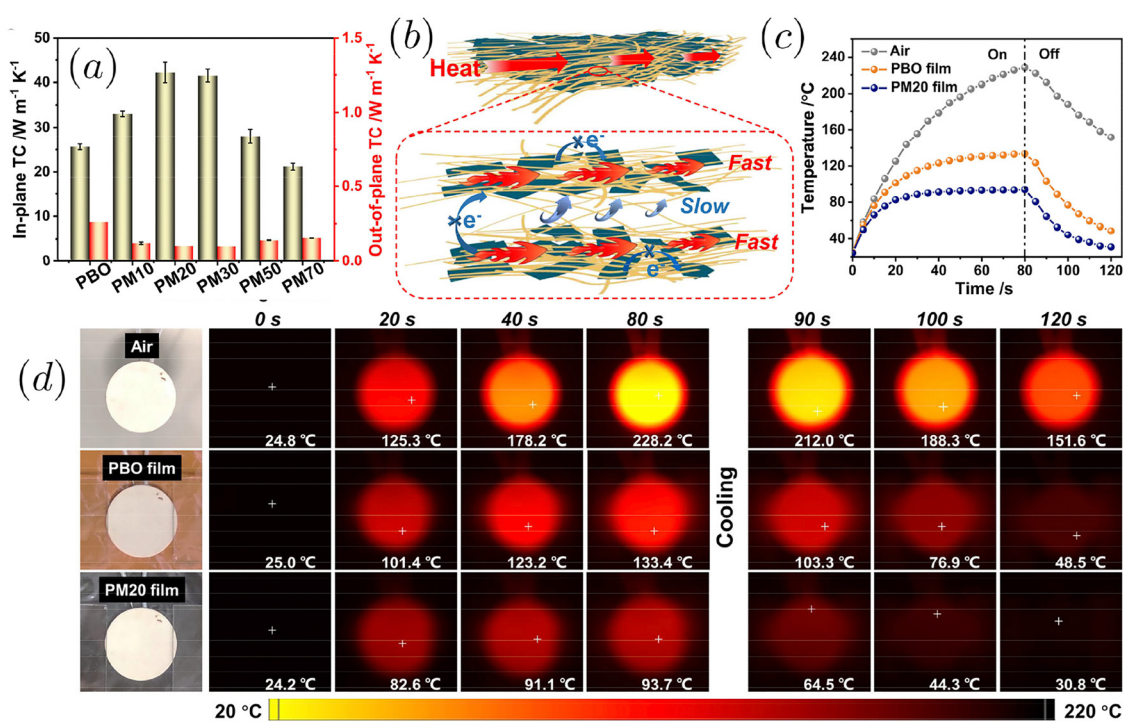


FIG. 77. (a) Thermal conductivity (TC) of PBO/MXene films with different MXene contents, 10, 20, 30, 50, and 70 wt. % for samples PM10, PM20, PM30, PM50, and PM70, respectively. (b) Pictorial model of thermal conduction and electrical insulation of PBO/MXene film. (c) Surface temperature vs time curves of the ceramic plate using air, PBO film, and PM20 film to dissipate heat, respectively. (d) IR thermal images corresponding to T vs t evolution traced in (c). Reprinted from Liu *et al.*,⁵⁵⁸ licensed under a Creative Commons Attribution (CC BY) license.

measured as a function of the thickness of the film (whose κ must remain constant), allowing a subsequent separation between the interface and bulk contributions.^{581,582} If the intervening thin film is sufficiently thin such that $d_f h_K \ll \kappa_f$, the simplified differential 3ω method—comparing paired measurements with and without the film—can be employed.^{390,581,582}

A straightforward estimate of the thermal boundary resistance can be obtained using the film-thickness-dependent relation for the apparent thermal conductivity of thin films [Eq. (68)]. The apparent thermal conductivity κ_a , expressed as a function of the film thickness d_f , reflects an effective value that incorporates both the intrinsic thermal conductivity of the film (κ_i) and the interfacial thermal resistance (R_{sf}). Thus, the total resistance to heat flow from the film into the substrate consists of the intrinsic resistance of the film and the interfacial resistance at the film–substrate boundary. We can then introduce the effective thermal resistance R_{eff} as the sum of the thermal resistance contribution from the film R_f and from the interface R_{sf} :

$$R_{eff} = \frac{d_f}{\kappa_a} = R_f + R_{sf}, \quad (118)$$

where the thermal resistance caused by the film is

$$R_f = \frac{d_f}{\kappa_i}. \quad (119)$$

To date, no widely accepted values of thermal boundary resistance (TBR) exist across a broad range of materials. The parameter R_{sf} is inherently difficult to tabulate for rigorous calculations, as it depends sensitively on both the mechanical contact quality at the interface and the intrinsic properties of the adjoining materials. In low-dimensional systems, the interfacial effect (of both heater/film and film/substrate) should be considered when determining the thermal properties of the thin layer.

One notable application of the 3ω method is the investigation of interfacial effects in thin polyimide C films deposited on borosilicate substrates.²⁵³ Several gold wires with widths $2b$ ranging from 10 to $50\text{ }\mu\text{m}$ were deposited on the sample surfaces. The apparent thermal conductivity κ_a was experimentally determined for polyimide films with thicknesses of 210, 440, and 760 nm. As shown in Fig. 78(a), κ_a increases with increasing d_f , consistent with the prediction of Eq. (68). Figure 78(b) further reveals a linear dependence of R_{eff} on d_f , as expected from Eq. (118). By combining Eqs. (118) and (119), it follows that the intercept of the $R_{eff}(d_f)$ curve with the ordinate axis yields R_{sf} , while its slope provides κ_i .

The value obtained by Guermoudi *et al.*,²⁵³ $R_{sf} \approx 5 \times 10^{-7}\text{ m}^2\text{ K W}^{-1}$ ($h_K \approx 2\text{ MW m}^{-2}\text{ K}^{-1}$), is relatively high compared to typical values reported for other material pairings, as shown in Fig. 20(b). Meanwhile, using the same 3ω approach, Yamane *et al.*⁵⁸³ reported a similar value of TBR ($R_{sf} \approx 5 \times 10^{-7}\text{ m}^2\text{ K W}^{-1}$) in a SiO_2 film with 500 nm thickness grown on a Si substrate. For films much thinner than ~ 20 nm, the estimated R_{sf} was found to be an order of magnitude smaller. Rausch *et al.*⁵⁸⁴ reported $R_{sf} \approx 2 \times 10^{-7}\text{ m}^2\text{ K W}^{-1}$ for poly(3-hexylthiophene) films with thicknesses ranging from 100 to 800 nm deposited on a glass substrate. Xu *et al.*⁵⁷⁸ investigated thermal transport across grain boundaries in polycrystalline Si on a Si wafer using the 3ω technique and provided a comprehensive comparison between experimental measurements and molecular dynamics simulations. The interfacial thermal resistance R_K monotonically decreased

from approximately 7×10^{-8} to $10^{-8}\text{ m}^2\text{ K W}^{-1}$ with an increase in temperature from about 80 to 300 K, depending on the angle of rotation between the film and the wafer. MD simulations support this trend, though the measured values of R_K are much higher than that predicted by MD, presumably due to the underestimated phonon-strain field interaction. This trend was partially attributed to the activation of additional phonon modes at high temperatures, which enhances heat transfer across grain boundaries.

There is also the recent development of Chen *et al.*,³⁹⁰ who measured the thermal contact resistance between graphene and SiO_2 using a differential 3ω method (see Fig. 79). The sample thicknesses were 1.2 (single-layer graphene), 1.5, 2.8, and 3.0 nm. All samples exhibited approximately the same temperature trend from 42 to 310 K, with no clear thickness dependence. The contact resistance at room temperature ranged from 5.6×10^{-9} to $1.2 \times 10^{-8}\text{ m}^2\text{ K W}^{-1}$.

Modeling the thermal contact between graphene and SiO_2 is complicated by the amorphous nature of SiO_2 and the strong anisotropy of graphene. Figure 79 shows that although both the MTM and DMM models capture certain features of the measurements, each has significant limitations. The MTM provides a lower bound and is reliable at temperatures below ~ 60 K. The DMM, while reproducing the overall temperature dependence, overestimates the magnitude by nearly a factor of six across the measured temperature range. This discrepancy is likely due to the omission of inelastic phonon scattering, which may constitute an important channel for heat transfer.⁵⁸⁶

B. Time- and frequency-domain thermoreflectance

Pump-probe thermoreflectance techniques are the most widely used methods for measuring thermal boundary resistance (TBR). In both of their variants, the same considerations apply regarding the real and imaginary components of the reflected intensity, which correspond to the in-phase and out-of-phase signals recorded by the lock-in amplifier (Sects. III C and III D). For quantitative analysis, Cahill developed an analytical thermal model of the sample and solved the diffusion equation numerically.²⁹¹ In this model, each layer is characterized by its thickness, heat capacity, and thermal conductivity, while an interface is represented as a thin layer with small thickness (typically 1 nm) and low heat capacity (typically $1\text{ kJ m}^{-3}\text{ K}^{-1}$ in the calculations).⁵⁸⁷ Most of the model parameters are fixed based on literature values or independent measurements. One then adjusts one or two unknown parameters to fit the model to the experimental data, thereby determining the thermal properties of interest.

However, extracting the target property from the complex thermal model is challenging because it involves several unknown parameters. To reduce the number of parameters is therefore essential in TDTR measurements. The heat capacity is often predetermined using differential scanning calorimetry or taking it from the literature, so that the remaining unknowns are typically limited to $\kappa_{f\parallel}$ and $\kappa_{f\perp}$ and the interface conductance.²⁹⁰ For isotropic samples, fewer parameters are required, since distinguishing between in-plane and cross-plane transport is unnecessary. In addition, employing a large laser spot size ($5 - 20\text{ }\mu\text{m}$) together with a high modulation frequency (1–10 MHz) yields quasi-one-dimensional heat transport. Under these conditions, TDTR signals are more sensitive to cross-plane thermal properties ($\kappa_{f\perp}$ and h_K).

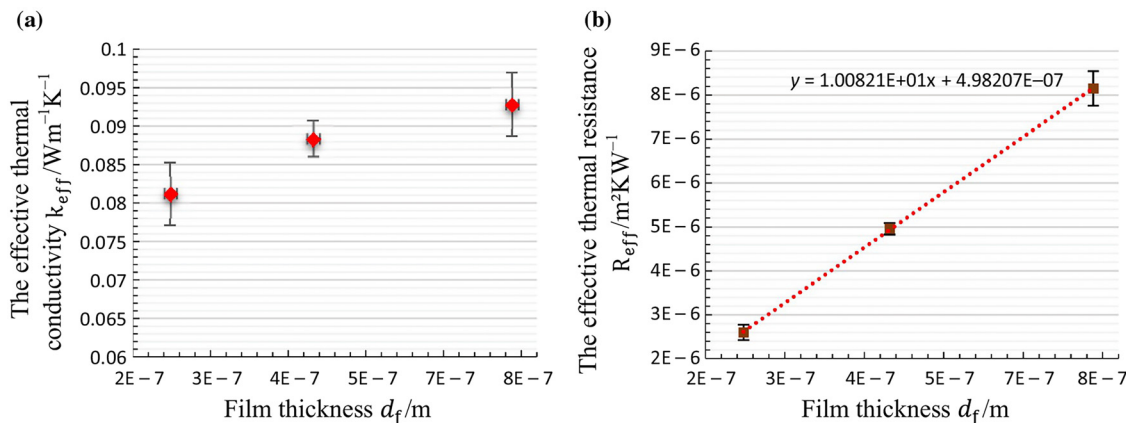


FIG. 78. (a) κ_{eff} of parylene C films on borosilicate substrates as a function of film thickness. (b) R_{eff} of parylene C films vs d_f . Reprinted from Guermoudi *et al.*, *J. Therm. Anal. Calorim.* **145**, 1–12 (2021).²⁵³ licensed under a Creative Commons Attribution (CC BY) license.

Therefore, TDTR is often used to measure the cross-plane thermal conductivity of the sample across the plane and the transducer/sample TBC without extensive elaboration.²⁹⁰

In this way, Cheng *et al.*⁵⁶⁶ measured the TBC of the interface formed by epitaxially growing (111) Al on (0001) ultraclean sapphire substrates using molecular beam epitaxy. Sample Sub100 was grown at 100 °C while in Sub200 the substrate temperature was 200 °C. Interfacial thermal transport involves contributions from elastic phonons, inelastic phonons (phonon–phonon interaction), and electron–phonon coupling across the interface. The relative importance of these

mechanisms in determining TBC remains difficult to quantify.^{166,588} The phonon density of states of Al and sapphire calculated by DFT are shown in Fig. 80(a). Since the maximum phonon frequency of sapphire (about 25 THz) exceeds that of Al (about 10 THz), phonons in the 10–25 THz range of sapphire cannot contribute to TBC under purely elastic scattering.

Heat transport across the Al–sapphire interface is modeled using the thermal resistance circuit shown in Fig. 80(b). In metals such as Al, electrons typically transfer energy to other electrons much more efficiently than to phonons. Therefore, when a temperature difference is applied across the interface, the thermal energy carried by electrons in Al must first be transferred to phonons in Al, since sapphire contains no free electrons. Near the interface, the electron and phonon subsystems in Al can have different temperatures, a situation described by the two-temperature model.⁵⁹² The temperature difference between electrons and phonons near the Al–interface represents a strong local nonequilibrium and gives rise to an electron–phonon coupling thermal resistance within the Al. Phonons on the Al side transfer energy to phonons on the sapphire side through both elastic and inelastic channels. In addition, some theoretical calculations show that electrons on the metal side could directly pass energy to phonons on the nonmetal side. In contrast, some other calculations and experimental data show that the electron–phonon cross-interface coupling does not contribute significantly to TBC.^{588,590,592–594} This possible heat transfer channel has also been contemplated in Fig. 80(b).

A comparison of the measured TBC values at the Al–sapphire interfaces across different experiments is presented in Fig. 80(c). The high-quality interfaces in the Sub100 and Sub200 samples exhibit TBC values exceeding all previously reported values for less perfect Al–sapphire interfaces. For these high-quality interfaces, the TBC reaches a saturation value above room temperature, whereas in other samples reported in the literature [see Fig. 80(c)], TBC increases monotonically with T , a behavior attributed to inelastic phonon scattering.⁵⁹¹ Numerical simulations of the Al–sapphire interface, including results obtained via AGF and the nonequilibrium Landauer method, show good agreement with the experimental data [Fig. 80(d)], indicating that elastic phonon transport predominantly governs heat transfer across high-quality interfaces. The combined contributions of various

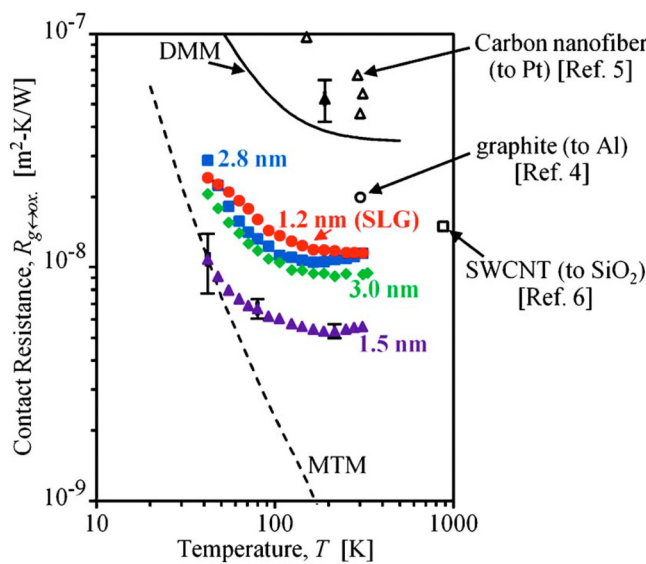


FIG. 79. Measured thermal contact resistance between SiO_2 and graphene, for four samples of different thicknesses. Also included for comparison are literature values of the contact resistances (open points) for carbon nanofibers to Pt,⁴³⁵ graphite to Al,¹⁸⁰ and SWCNT to SiO_2 .⁵⁸⁸ Lines are theoretical curves for the elastic DMM⁵⁸⁶ and the maximum transmission model (MTM).⁴⁶⁸ Reprinted from Chen *et al.*, *Appl. Phys. Lett.* **95**, 161910 (2009). Copyright 2009, with permission from AIP Publishing.

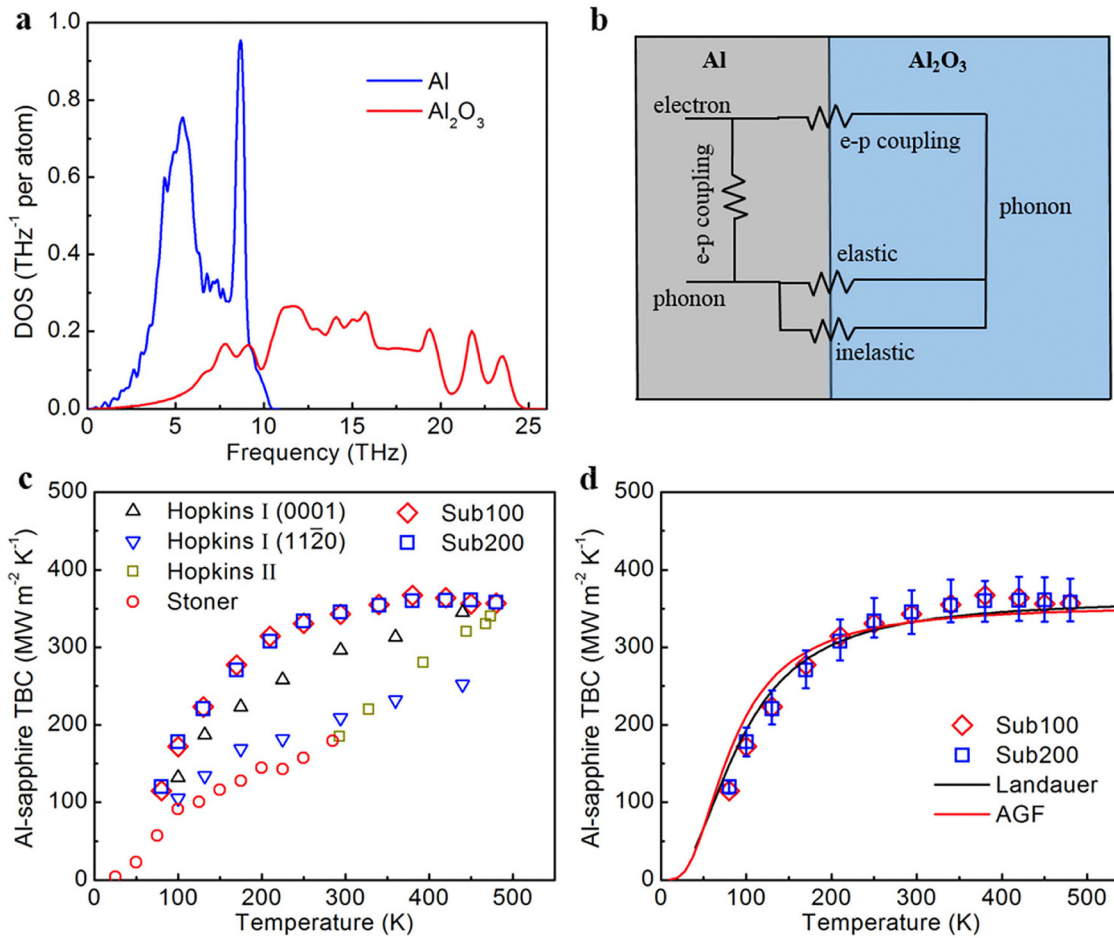


FIG. 80. Thermal transport across Al-sapphire interfaces. (a) Phonon DOS of Al and sapphire. (b) Equivalent thermal circuit of Al-sapphire interfaces. (c) Comparison of temperature-dependent Al-sapphire TBC of samples Sub100 and Sub200 with measured TBC values in the literature: Hopkins I,⁵⁸⁹ Stoner,⁵⁹⁰ and Hopkins II.⁵⁹¹ (d) Comparison of measured Al-sapphire TBC with theoretical values calculated by AGF and non-equilibrium Landauer approach. The substrate temperature for Al growth was kept at 373 K for sample Sub100 resulting in an 83-nm-thick Al and at 473 K for Sub200 (86-nm-thick Al), whereas all the other growth conditions remained the same. Reprinted from Cheng *et al.*, Commun. Phys. **3**, 115 (2020).⁵⁶⁶ licensed under a Creative Commons Attribution (CC BY) license.

20 December 2025, 13:48:09

heat transfer mechanisms, illustrated in Fig. 80(b), are discussed in greater detail by Cheng *et al.*³⁹⁰

Ultrafast lasers have been shown to enable mapping of inhomogeneous samples and probing the relationship between local thermal conductivity variations and microscale structural features such as grain boundaries, composition variations, and interface quality.^{595,596} A substantial body of work has used TDTR for thermal conductivity mapping near the surface of samples,^{597–600} as well as for mapping thermal boundary conductance (TBC) between thin films.^{601,602} In addition, FDTR is sensitive to subsurface interfaces,⁶⁰³ enabling the detection of damage on scales not accessible with TDTR.

Treweek *et al.*⁶⁰⁴ introduced an interesting modification to the FDTR technique, using TBC as a quantitative measure of bond quality.^{159,166} This approach enables the creation of spatially resolved maps of TBC at the boundaries of interest, providing detailed information about local bond quality. In this study, the green and blue lasers are coaxially aligned [see Fig. 81(a)]. The heat dissipates into the sample

with a thermal penetration depth δ given by Eq. (26). The surface temperature changes due to heat dissipation, depending on δ and therefore on both the thermal properties of the sample and $f_{pump} = \omega_{pump}/2\pi$. The modulated surface temperature modifies the surface reflectance, and therefore the reflected probe signal phase lags the incident excitation.

The samples studied by Treweek *et al.*⁶⁰⁴ comprise bulk GaN bonded to commercial diamond (Diamond Foundry) through thermal compression bonding, with both surfaces coated beforehand with an e-beam-evaporated Ti/Au film (5 nm/120 nm) [see Fig. 81(a)]. Finally, FDTR is used to quantify the GaN-diamond interface, with the TBC indicating the quality of the interface.

The phase change variations across each (x, y) map point in the plane were obtained by tuning f_{pump} from 1 kHz to 60 MHz to account for depth-dependent thermal characterization, as shown in Fig. 81(b). For example, at 60 MHz, the Au transducer layer is predominantly sensed. At 1 kHz, the FDTR penetrates approximately 100 μm into the

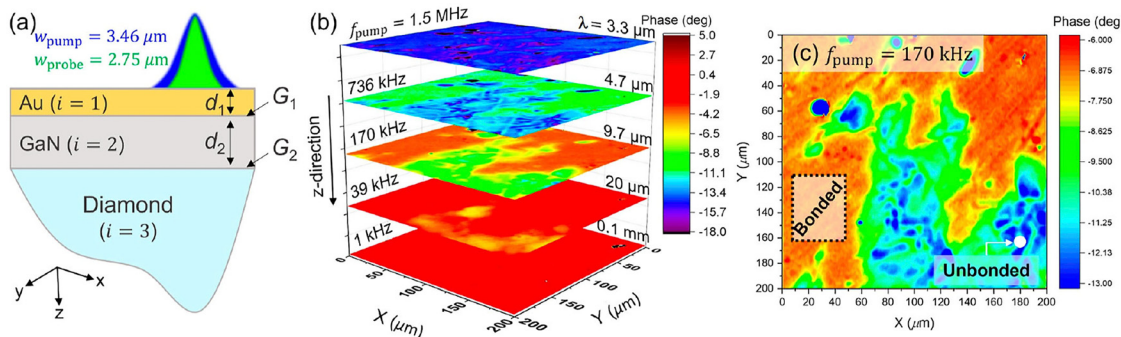


FIG. 81. (a) Schematic of the FDTR experiment on the GaN–diamond thermal compression bonded material system ($d_1 = 120 \text{ nm}$, $d_2 \approx 5 \mu\text{m}$). The pump (blue) and probe (green) beams are focused to the surface of the Au-coated sample. Heat diffuses into the multilayer system, enabling interaction with the GaN–diamond bonded interface. (b) Hyperspectral map showing FDTR images taken at multiple pump frequencies f_{pump} corresponding to different depths into the sample. (c) An FDTR image acquired at $f_{\text{pump}} = 170 \text{ kHz}$ enables visualization of the GaN–diamond interfacial quality, clearly distinguishing bonded and unbonded regions. Reprinted from Treweek *et al.*, ACS Appl. Mater. Interfaces **16**, 4117 – 4125 (2024),⁶⁰⁴ licensed under a Creative Commons Attribution (CC BY) license.

diamond substrate. Here, phase values closer to zero (i.e., red regions) indicate better thermal transport, and vice versa for more negative values. The minimal variation at 1 kHz ($\lambda\delta > 0.1 \text{ mm}$) suggests that the diamond layer is spatially uniform, and the minimal variation above 1.5 MHz ($\delta = 3.3 \mu\text{m}$) suggests that the Au/GaN layers are only slightly spatially nonuniform. Conversely, the phase shift with f_{pump} in the 39–736 kHz range shows the existence of bonded and unbonded regions, most clearly seen at 170 kHz ($\delta = 9.7 \mu\text{m}$) as shown in Fig. 81(c), which is relevant to the GaN–diamond interface.

C. Theoretical simulations

Contemporary theories and simulation approaches have been developed to explain TBC, reflecting the complex nature of interfacial thermal transport. Early efforts demonstrated the capabilities of the acoustic and diffuse mismatch models.¹⁶⁷ More recent approaches include equilibrium and non-equilibrium molecular dynamics,^{605–607} interface conductance modal analysis (ICMA),⁶⁰⁸ the wave packet method,^{609,610} atomistic Green's functions (AGF),^{152,568,611} and the non-equilibrium Landauer approach.^{612,613} However, because of the inherent complexity of interfaces, most theoretical simulations cannot fully capture their detailed atomic-scale features, limiting the extent to which direct comparisons with experimental measurements can yield definitive conclusions.^{105,568}

Prasher *et al.*³⁸⁹ has modeled, using the DMM, the TBR of the graphite and an isotropic substrate. The simulations reproduced very well the TBR of the MWCNT–platinum interface corresponding to the experimental data of Kim *et al.*²⁸ (shown in Fig. 68).

Gaskings *et al.*⁵⁶⁸ measured the TBR in ZnO/GaN heterointerface as a function of temperature using TDTR. For comparison, they also show the data of ZnO/HQ/ZnO interface, where HQ is hidroquinone, extracted from the work of Giri *et al.*⁶¹⁴ The data were compared with the DMM and AGF models. Both the DMM and AGF are rooted in the Landauer formalism, treating TBC as phonon transmission across the interface. In the two extremes of computational rigor considered here, the DMM represents the lower level, modeling phonons as particles, while the AGF provides a higher-level description by accounting for their wave nature. It is important to note that in both models, TBC is evaluated under the assumption of purely elastic

phonon interactions. Figure 82 shows, in a double logarithm scale, the experimental data of h_K as a function of T and the model comparison. The measured values of $h_K \approx 490 \text{ MW m}^{-2} \text{ K}^{-1}$ for ZnO/GaN (red circles) are nearly a factor of two greater than h_K predicted by AGF and DMM in the higher temperature range. The agreement between the AGF and the ZnO/GaN data at low temperatures is due to relatively higher contributions from long-wavelength modes, which also explains the discrepancy with the DMM. At higher temperatures, the disagreement between the data and the models based on the harmonic approximation suggests that inelastic heat flow channels could contribute to h_K across the ZnO/GaN interface at these temperatures.^{593,615–618}

In this case, taking into account the corresponding correction due to phonon anharmonic interactions near the interface is critical for accurate modeling of interfacial thermal transport.⁶¹⁹ Although some authors^{576,588,620–623} have improved these methods to incorporate the inelastic contribution, they cannot include other important phenomena such as the existence of interfacial phonon modes and the local phonon nonequilibrium.⁵⁷²

Inelastic processes arise from the anharmonicity of atomic interactions, leading to phonon–phonon scattering that redistributes both the energy and momentum of phonons. A central outcome of such scattering is the additive behavior of thermal resistances in series, whereby the total thermal resistance can be expressed as the sum of the boundary resistances and the resistance of any intermediate interfacial layer. This principle is well established for macroscopic systems in which the characteristic dimensions are much larger than the mean free path (MFP) of the dominant heat carriers. Under these conditions, heat transport is diffusive and accurately described by Fourier's law. Notably, experimental studies have demonstrated that the additive property remains valid for intermediate layers as thin as 3 nm.¹⁶² Although the fundamental mechanism is not yet fully resolved, equilibrium (EMD) and non equilibrium (NEMD) molecular dynamics and non-equilibrium Green's function (NEGF) simulations indicate that additive behavior is largely preserved at interfaces incorporating ultrathin matching layers.⁶²⁴

In this context, Gordiz *et al.*⁶⁰⁸ introduced interface conductance modal analysis (ICMA), which inherently incorporates anharmonicity and enables the calculation of modal contributions to thermal interface

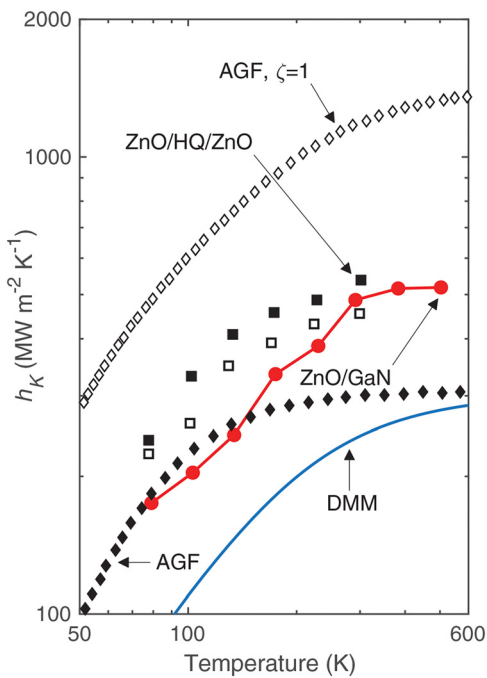


FIG. 82. Measured thermal boundary conductance as a function of temperature for ZnO/GaN (solid circles) compared to data measured across ZnO/HQ/ZnO interfaces.^{568,614} Predictions from the DMM and AGF for ZnO/GaN h_K (solid line and diamond symbols, respectively). The maximum h_K predicted across an ideal ZnO/ZnO interface from the AGF calculations (open diamond symbols) are also shown for comparison.⁵⁶⁸ Reprinted from Giri *et al.*, *Adv. Funct. Mater.* **30**, 1903857 (2019).¹⁵⁹ Copyright 2019, with permission from John Wiley and Sons.

conductance within molecular dynamics simulations. The eigenmodes of vibration were calculated from harmonic lattice dynamics calculations; however, the generality of the ICMA formalism also allows for incorporating anharmonic lattice dynamics results into the calculations. ICMA can be implemented in both equilibrium and non-equilibrium MD simulations, and both methods show qualitative agreement as validated through the study of a simple system of Lennard-Jones solids. The formalism is based on a modal decomposition of the heat flow across the interface, which can then be incorporated into expressions for the conductance using either equilibrium or non-equilibrium MD. As an MD-based approach, it not only captures anharmonic effects but also naturally accounts for the atomic-level details of interface quality.

As an initial application of the ICMA method, Gordiz *et al.*⁶⁰⁸ investigated a simple Lennard-Jones crystal interface, as illustrated in Figs. 83(a) and 83(b). In their EMD simulations, the modal heat flux q_n was recorded over 5 ns in the microcanonical ensemble and subsequently used to compute the modal thermal conductance G_n . The total interfacial conductance was then obtained as $G_{th} = \sum_n G_n$. In their NEMD simulations, the authors evaluated the modal conductance as $G_n = \bar{q}_n / \Delta T$, where \bar{q}_n is the time-averaged modal heat flux and ΔT is the interfacial temperature difference, assumed to be identical for all modes. A thermal power of 6.5 nW was supplied to the system via the hot bath and extracted through the cold bath. The system was first equilibrated for 2 ns to reach a steady state, after which the

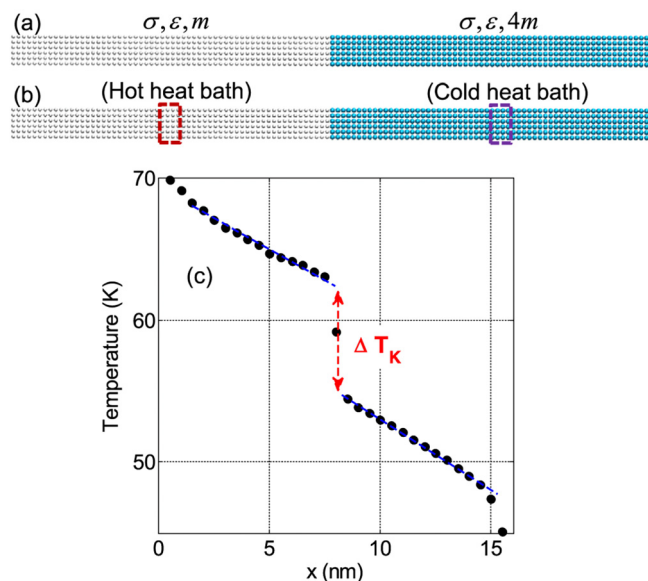


FIG. 83. Schematic of the structures for (a) EMD and (b) NEMD simulations. In (b), hot and cold heat baths are assigned by rectangular blocks on the left- and right-hand sides, respectively. Temperature distribution in (c) illustrates the temperature drop (Kapitza resistance) at the interface. σ_{LJ} and ϵ are parameters of the Lennard-Jones potential.⁶²⁵ An acoustic mismatch exists at the interface because the mass of the atoms on both sides B is different (m_A and $4m_A$). Reprinted from Gordiz *et al.*, *ACS Appl. Mater. Interfaces* **16**, 4117–4125 (2024).⁶⁰⁸ licensed under a Creative Commons Attribution (CC BY) license.

temperature profile, shown in Fig. 83(c), remained constant throughout the structure. By averaging the modal heat fluxes over this steady-state period, the modal contributions G_n to the total interfacial conductance were obtained.

Figure 84 shows the temperature dependence of the modal contributions to G_{th} from the EMD simulations. A reduction in the total thermal interface conductance with decreasing temperature is observed in Fig. 84, consistent with the earlier findings of Duda *et al.*⁶²⁶ In Fig. 84(a), one can also identify the cutoff frequency above which the heavier material [right-hand side in Figs. 83(a) and 83(b)] lacks bulk modes. Beyond this frequency, all contributions to conductance must arise from inelastic (anharmonic) processes, since purely harmonic interactions would yield full accumulation at the maximum frequency of the heavier side ($\omega_{0,\max}$), marked by the vertical dashed line in Fig. 84(a).

Based on these results, we draw important conclusions about the role of anharmonicity. In bulk crystals, anharmonicity is well known to reduce thermal conductivity. At interfaces, however, it plays a different role: anharmonic interactions open additional channels for heat transport by enabling coupling between modes of different frequencies. The net effect is an enhancement of interfacial conductance, as reflected in the higher values of TBC observed at high temperatures, and in particular, by the increased contribution from modes with frequencies above $\omega_{0,\max}$.

VII. CONCLUSIONS AND OUTLOOK

This review highlights the emergence of affordable experimental techniques as versatile and powerful tools for measuring thermal

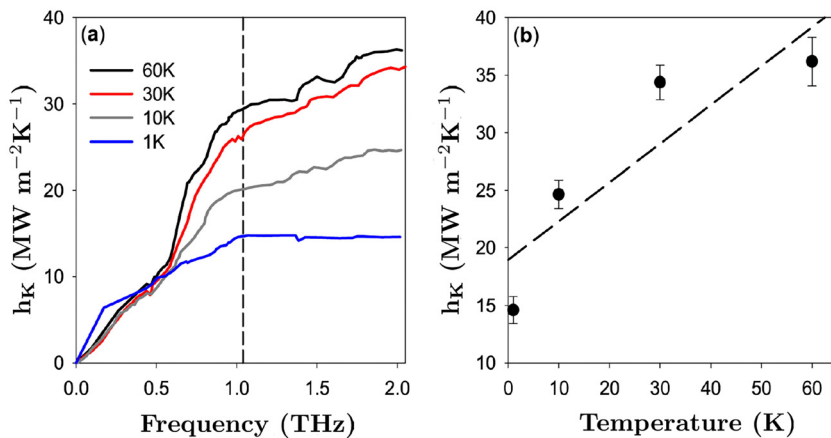


FIG. 84. (a) EMD-calculated interface thermal conductance accumulation functions at the interface of two Lennard-Jones solids at different temperatures. (b) h_K values as a function of temperature. The dashed line represents the linear fit to the data. The intercept of the linear fit and the y -axis can be approximately interpreted as the elastic contribution to the interface thermal conductance.⁶²⁶ The 60-unit cell structure was used in calculations with lattice constants of 5.278, 5.272, 5.267, and 5.264 Å at 60, 30, 10, and 1 K, respectively. Although small differences from EMD and NEMD simulations were reported by Gordiz *et al.*,⁶⁰⁸ the ICMA yielded a similar trend in the normalized modal contributions between the EMD and NEMD approaches. Reprinted from Gordiz *et al.*, ACS Appl. Mater. Interfaces **16**, 4117–4125 (2024).⁶⁰⁸ licensed under a Creative Commons Attribution (CC BY) license.

conductivity in bulk materials and, more importantly, in low-dimensional structures, where heat transport often exhibits unconventional behavior. We have outlined the fundamental working principles of the main techniques, described typical measurement setups, discussed the underlying mathematical frameworks, and presented illustrative examples from the literature. These elements have been examined alongside the advantages and limitations of each method, providing a comprehensive overview of the current state of the field.

As discussed, each technique exhibits distinct strengths and limitations that must be carefully assessed in relation to the experimental context. The suitability of a given method strongly dependent on the characteristics of the sample (such as its dimensionality, size, morphology, mechanical and optical properties, and thermal behavior) and on external factors including the temperature range of interest, the required accuracy, and practical considerations related to instrumentation. Together, these factors provide the basis for selecting the most appropriate experimental approach.

Despite significant progress, accurately measuring thermal contact resistance remains a persistent challenge. Although substantial theoretical and experimental advances have improved understanding of the mechanisms governing heat conduction across and along interfaces, reliable quantification of interfacial resistance is still nontrivial. Addressing this issue is critical because interfacial effects often dominate thermal transport in nanoscale and layered systems, influencing both the interpretation of measurements and the design of future thermal management applications.

Drawing on the comprehensive analysis presented in this Review, it is clear that substantial work remains to advance both theoretical and experimental methodologies for thermal property measurements. Although significant progress has been achieved, reliable characterization of heat transport still faces major challenges, particularly in mitigating parasitic heat losses and addressing the inherent complexity of theoretical models. These issues are expected to become even more critical as research increasingly targets nanostructured materials, where

the pronounced surface-to-volume ratio introduces additional mechanisms that strongly influence heat conduction. Furthermore, the demand for high spatial resolution to probe local temperature fields highlights the need for novel approaches that integrate advanced experimental design with robust theoretical frameworks. In the future, the development of multimodal measurement strategies, the incorporation of emerging computational techniques, and the design of innovative nanoscale probes are likely to play pivotal roles in overcoming current limitations and enabling deeper insights into thermal transport in complex systems.

From the theoretical point of view, the difficulty lies in the fact point about extensive computer resources. The development of the first-principles phonon simulation combining DFT and BTE allows for the prediction of thermal conductivity with high confidence and is free of empirical parameters.⁶ Given high-throughput computational demands, machine learning can efficiently determine the underlying connectivity among enormous data at extremely low cost.^{627,628} Compared with first-principles calculations and MD simulations, the data-driven machine learning models enable high-throughput evaluation of κ with predictive modeling for systems both inside and beyond the training dataset.^{629,630} In addition to directly predicting κ , machine learning can be used to build accurate interatomic potentials for MD simulations.⁴⁴ To optimize the interfacial thermal conductance of composite interfacial structures, newly developed techniques, such as a combination of the atomistic Green function and Bayesian optimization methods,⁶³¹ can be exploited to control interfacial particle scattering and particle wave effects reproducibly.

In experimental research, a substantial body of work has established a range of powerful approaches for measuring the thermal properties of low-dimensional materials, each with distinct advantages and limitations. Electrothermal techniques, for example, provide controlled and well-defined heating, making them highly suitable for studying diverse samples. Steady-state methods are widely employed to determine thermal conductivity using relatively simple physical and

mathematical models; however, they require careful attention to boundary conditions and the use of an ideal heat source to establish a stable and measurable temperature gradient and heat flux across the sample.⁶³² A prominent example is the steady-state microbridge technique, which offers high accuracy and precision over a broad temperature range but also presents inherent limitations that must be carefully considered when interpreting results (see D and C). In particular, further research is needed to enable more comprehensive comparisons between theoretical predictions and experimental data, with an emphasis on mitigating the influence of thermal contact resistance between samples and microdevices.

In contrast, transient techniques, such as the 3ω technique, take full advantage of efficient implementation and easier mechanisms for experimental control. Instead of dealing with the temperature response at a steady state, transient techniques extract the required information by analyzing the response in the time and frequency domains. Due to the improved signal-to-noise ratio in the transient temperature response, the accuracy of the transient techniques is very much improved, even with much less experimental control. However, using transient electrothermal techniques, it is difficult to measure highly electrically resistive or highly conductive samples and those with a very fast thermal transient time. To address this challenge, noncontact techniques employing ultrafast laser heat sources at the nanosecond or picosecond timescale and optically probing the cooling process in the sample offer an important advantage of measuring very fast heat transfer processes and reducing the risk of continuous heat generation and potential damage to the sample. For materials with a weak resistance response to temperature change, Raman-based techniques can be used and have been widely applied to measure 1D and 2D nanoscale materials. One may foresee that transient Raman techniques, including ET-Raman and FET-Raman,^{365,368} may enhance our capability to perform thermal measurements in nanoscale materials. Circumventing the limitations of low Raman signals, an overlap of Raman spectra with fluorescence, bandgap dependence of the laser-induced heating, and some other Raman features is indeed crucial to delivering on its high promises.

Generally, the complexity of the physics and engineering seen in the thermal conductivity literature remains focused on the accurate characterization of thermal properties with high spatial resolution. *In situ* monitoring of transient thermal measurements, along with visualization of thermal properties, is necessary to effectively characterize complex mechanisms and networks of principal relevance for thermal management applications. The continued commitment to improving thermal measurements is of the utmost importance for technical advancement, impacting innovations from nanoelectronics to space exploration.

Given our current state of understanding of the thermal properties of materials, future applications of thermal conductivity measurement techniques can focus on advanced materials, such as those encountered in this review (e.g., nanostructured carbon materials, black phosphorous, MXenes, boron nitride) and composites of increasing complexity where different phases are intermixed on nanometer length scales. Such complex systems may include, for instance, filler-matrix structures with high thermal conductivity nanoparticle fillers such as ceramics, metals, nanotubes, and graphene embedded into an organic polymer matrix. To take advantage of the high thermal conductivity of individual filler particles in real applications, various

methods have been suggested to improve heat conduction, ranging from surface functionalization, filler alignment, and structural optimization.^{168,633–636} The ability to determine superiorities in improving the thermal conductivity of these materials is becoming more and more significant, especially in the higher integration process of chips with thermal dissipation systems.

ACKNOWLEDGMENTS

This work was financed by project No. PROMETEO2019-016 from the Generalitat Valenciana and Nos. RED2022-134448T, TED2021-1292988-I00, and PID2023-146354NB-C41 from the Ministerio de Ciencia, Innovación y Universidades of Spain.

AUTHOR DECLARATIONS

Conflict of Interest

The authors have no conflicts to disclose.

Author Contributions

Ali Sheraz: Conceptualization (equal); Formal analysis (equal); Investigation (equal); Supervision (equal); Validation (equal); Visualization (equal); Writing – original draft (equal); Writing – review & editing (equal). **Oleg Korotchenkov:** Conceptualization (equal); Formal analysis (equal); Investigation (equal); Methodology (equal); Supervision (equal); Validation (equal); Visualization (equal). **Mohammad Ali Nasiri:** Investigation (equal); Writing – original draft (equal). **Marco Antonio López de la Torre:** Conceptualization (equal); Investigation (equal); Methodology (equal); Supervision (equal); Validation (equal); Writing – original draft (equal). **Andrés Cantarero:** Conceptualization (equal); Funding acquisition (equal); Investigation (equal); Methodology (equal); Supervision (equal); Validation (equal); Visualization (equal); Writing – original draft (equal); Writing – review & editing (equal).

DATA AVAILABILITY

The data that support the findings of this study are available from the corresponding author upon reasonable request.

REFERENCES

- ¹H. Mehling and L. F. Cabeza, “Solid-liquid phase change materials,” in *Heat and Cold Storage with PCM: An Up to Date Introduction into Basics and Applications* (Springer, Berlin, Heidelberg, 2008), pp. 11–55.
- ²H. Czichos, T. Saito, and L. Smith, *Springer Handbook of Materials Measurement Methods* (Springer, Berlin, Heidelberg, 2006).
- ³S. Chen, J. Wang, G. Casati, and G. Benenti, “Nonintegrability and the Fourier Heat Conduction Law,” *Phys. Rev. E* **90**, 032134 (2014).
- ⁴I. Chowdhury, R. Prasher, K. Lofgreen, G. Chrysler, S. Narasimhan, R. Mahajan, D. Koester, R. Alley, and R. Venkatasubramanian, “On-chip cooling by superlattice-based thin-film thermoelectrics,” *Nat. Nanotechnol.* **4**, 235–238 (2009).
- ⁵Y. Li, W. Li, T. Han, X. Zheng, J. Li, B. Li, S. Fan, and C.-W. Qiu, “Transforming heat transfer with thermal metamaterials and devices,” *Nat. Rev. Mater.* **6**, 488–507 (2021).
- ⁶X. Qian, J. Zhou, and G. Chen, “Phonon-engineered extreme thermal conductivity materials,” *Nat. Mater.* **20**, 1188–1202 (2021).
- ⁷B. Abad, D.-A. Borca-Tasciuc, and M. Martin-Gonzalez, “Non-contact methods for thermal properties measurement,” *Renewable Sustainable Energy Rev.* **76**, 1348–1370 (2017).

- ⁸J. L. Braun, D. H. Olson, J. T. Gaskins, and P. E. Hopkins, "A steady-state thermoreflectance method to measure thermal conductivity," *Rev. Sci. Instrum.* **90**, 024905 (2019).
- ⁹J. Liu, M. Han, R. Wang, S. Xu, and X. Wang, "Photothermal phenomenon: Extended ideas for thermophysical properties characterization," *J. Appl. Phys.* **131**, 065107 (2022).
- ¹⁰D. G. Cahill and R. O. Pohl, "Thermal conductivity of amorphous solids above the plateau," *Phys. Rev. B* **35**, 4067 (1987).
- ¹¹D. G. Cahill, "Thermal conductivity measurement from 30 to 750 K: The 3ω method," *Rev. Sci. Instrum.* **61**, 802–808 (s).
- ¹²D. G. Cahill, W. K. Ford, K. E. Goodson, G. D. Mahan, A. Majumdar, H. J. Maris, R. Merlin, and S. R. Phillpot, "Nanoscale thermal transport," *J. Appl. Phys.* **93**, 793–818 (2003).
- ¹³A. M. Marconnet, M. A. Panzer, and K. E. Goodson, "Thermal conduction phenomena in carbon nanotubes and related nanostructured materials," *Rev. Mod. Phys.* **85**, 1295–1326 (2013).
- ¹⁴D. G. Cahill, P. V. Braun, G. Chen, D. R. Clarke, S. Fan, K. E. Goodson, P. Kebinski, W. P. King, G. D. Mahan, A. Majumdar, H. J. Maris, S. R. Phillpot, E. Pop, and L. Shi, "Nanoscale Thermal Transport. II. 2003–2012," *Appl. Phys. Rev.* **1**, 011305 (2014).
- ¹⁵G. Chen, *Nanoscale Energy Transport and Conversion: A Parallel Treatment of Electrons, Molecules, Phonons, and Photons* (Oxford University Press, New York, 2005).
- ¹⁶L. Shi, C. Dames, J. R. Lukes, P. Reddy, J. Duda, D. G. Cahill, J. Lee, A. Marconnet, K. E. Goodson, J.-H. Bahk *et al.*, "Evaluating broader impacts of nanoscale thermal transport research," *Nanoscale Microscale Thermophys. Eng.* **19**, 127–165 (2015).
- ¹⁷H. Bao, J. Chen, X. Gu, and B. Cao, "A review of simulation methods in micro/nanoscale heat conduction," *ES Energy Environ.* **1**, 16–55 (2018).
- ¹⁸L. Chen, R. Liu, and X. Shi, *Thermoelectric Materials and Devices* (Elsevier, Amsterdam, 2021).
- ¹⁹S. Sett, V. K. Aggarwal, A. Singha, and A. Raychaudhuri, "Temperature-dependent thermal conductivity of a single germanium nanowire measured by optothermal Raman spectroscopy," *Phys. Rev. Appl.* **13**, 054008 (2020).
- ²⁰Z. Zhang and J. Chen, "Thermal conductivity of nanowires," *Chin. Phys. B* **27**, 035101 (2018).
- ²¹C. Dames, "Measuring the thermal conductivity of thin films: 3 omega and related electrothermal methods," *Annu. Rev. Heat Transfer* **16**, 7–49 (2013).
- ²²H. Malekpour and A. A. Balandin, "Raman-based technique for measuring thermal conductivity of graphene and related materials," *J. Raman Spectrosc.* **49**, 106–120 (2018).
- ²³Z. Wang, R. Xie, C. T. Bui, D. Liu, X. Ni, B. Li, and J. T. Thong, "Thermal transport in suspended and supported few-layer graphene," *Nano Lett.* **11**, 113–118 (2011).
- ²⁴D. Liu, R. Xie, N. Yang, B. Li, and J. T. Thong, "Profiling nanowire thermal resistance with a spatial resolution of nanometers," *Nano Lett.* **14**, 806–812 (2014).
- ²⁵W. Ma, T. Miao, X. Zhang, K. Takahashi, T. Ikuta, B. Zhang, and Z. Ge, "A T-type method for characterization of the thermoelectric performance of an individual free-standing single crystal Bi_2S_3 nanowire," *Nanoscale* **8**, 2704–2710 (2016).
- ²⁶R. S. Ruoff and D. C. Lorentz, "Mechanical and thermal properties of carbon nanotubes," *Carbon* **33**, 925–930 (1995).
- ²⁷S. Berber, Y.-K. Kwon, and D. Tománek, "Unusually high thermal conductivity of carbon nanotubes," *Phys. Rev. Lett.* **84**, 4613–4616 (2000).
- ²⁸P. Kim, L. Shi, A. Majumdar, and P. L. McEuen, "Thermal transport measurements of individual multiwalled nanotubes," *Phys. Rev. Lett.* **87**, 215502 (2001).
- ²⁹E. Pop, D. Mann, Q. Wang, K. Goodson, and H. Dai, "Thermal conductance of an individual single-wall carbon nanotube above room temperature," *Nano Lett.* **6**, 96–100 (2006).
- ³⁰A. A. Balandin, S. Ghosh, W. Bao, I. Calizo, D. Teweldebrhan, F. Miao, and C. N. Lau, "Superior thermal conductivity of single-layer graphene," *Nano Lett.* **8**, 902–907 (2008).
- ³¹A. A. Balandin, "Thermal properties of graphene and nanostructured carbon materials," *Nat. Mater.* **10**, 569–581 (2011).
- ³²A. A. Balandin, "Phononics of graphene and related materials," *ACS Nano* **14**, 5170–5178 (2020).
- ³³P. Huang, Y. Li, G. Yang, Z.-X. Li, Y.-Q. Li, N. Hu, S.-Y. Fu, and K. S. Novoselov, "Graphene film for thermal management: A review," *Nano Mater. Sci.* **3**, 1–16 (2021).
- ³⁴X.-K. Chen, X.-Y. Hu, P.-Z. Jia, and G.-F. Xie, "First-principles determination of high thermal conductivity of PCF-graphene: A comparison with graphene," *Appl. Phys. Lett.* **121**, 182205 (2022).
- ³⁵T. Luo and G. Chen, "Nanoscale heat transfer—from computation to experiment," *Phys. Chem. Chem. Phys.* **15**, 3389–3412 (2013).
- ³⁶J. B. J. Fourier, *Théorie Analytique de la Chaleur* (Gauthier-Villars et fils, 1888).
- ³⁷T. L. Bergman and A. S. Lavine, *Fundamentals of Heat and Mass Transfer* (Wiley, Hoboken, NJ, 2017).
- ³⁸J. L. Braun and P. E. Hopkins, "Upper limit to the thermal penetration depth during modulated heating of multilayer thin films with pulsed and continuous wave lasers: A numerical study," *J. Appl. Phys.* **121**, 175107 (2017).
- ³⁹Y. Kuang, L. Lindsay, S. Shi, X. Wang, and B. Huang, "Thermal conductivity of graphene mediated by strain and size," *Int. J. Heat Mass Transfer* **101**, 772–778 (2016).
- ⁴⁰F. Yousefi, F. Khoeini, and A. Rajabpour, "Thermal conductivity and thermal rectification of nanoporous graphene: A molecular dynamics simulation," *Int. J. Heat Mass Transfer* **146**, 118884 (2020).
- ⁴¹C. de Tomas, A. Cantarero, A. F. Lopeandia, and F. X. Alvarez, "From kinetic to collective behavior in thermal transport on semiconductors and semiconductor nanostructures," *J. Appl. Phys.* **115**, 164314 (2014).
- ⁴²O. Bourgeois, D. Tainoff, A. Tavakoli, Y. Liu, C. Blanc, M. Boukhari, A. Barski, and E. Hadji, "Reduction of phonon mean free path: From low-temperature physics to room temperature applications in thermoelectricity," *C. R. Phys.* **17**, 1154–1160 (2016).
- ⁴³C. Hua, L. Lindsay, X. Chen, and A. J. Minnich, "Generalized Fourier's law for nondiffusive thermal transport: Theory and experiment," *Phys. Rev. B* **100**, 085203 (2019).
- ⁴⁴H. Dai and R. Wang, "Methods for measuring thermal conductivity of two-dimensional materials: A review," *Nanomaterials* **12**, 589 (2022).
- ⁴⁵A. I. Zhamakin, "Heat conduction beyond the Fourier law," *Tech. Phys.* **66**, 1–22 (2021).
- ⁴⁶A. Salazar, "Energy propagation of thermal waves," *Eur. J. Phys.* **27**, 1349–1355 (2006).
- ⁴⁷E. Marín, J. Marín-Antuña, and P. Díaz-Arencebia, "On the wave treatment of the conduction of heat in photothermal experiments with solids," *Eur. J. Phys.* **23**, 523–532 (2002).
- ⁴⁸W. Jaber and P.-O. Chapuis, "Non-idealities in the 3ω method for thermal characterization in the low-and high-frequency regimes," *AIP Adv.* **8**, 045111 (2018).
- ⁴⁹C. Cattaneo, "Sulla conduzione del calore," *Atti Sem. Mat. Fis. Univ. Modena* **3**, 83–101 (1948).
- ⁵⁰C. Cattaneo, "A form of heat-conduction equations which eliminates the paradox of instantaneous propagation," *C. R. Acad. Sci.* **247**, 431–433 (1958).
- ⁵¹P. Vernotte, "Les paradoxes de la théorie continue de l'équation de la chaleur," *C. R. Hebd. Séances Acad. Sci. Paris* **246**, 3154–3155 (1958).
- ⁵²G. Capriz, K. Wilmanski, and P. M. Mariano, "Exact and approximate Maxwell-Cattaneo-type descriptions of heat conduction: A comparative analysis," *Int. J. Heat Mass Transfer* **175**, 121362 (2021).
- ⁵³W. Yuen and S. Lee, "Non-fourier heat conduction in a semi-infinite solid subjected to oscillatory surface thermal disturbances," *J. Heat Transfer* **111**, 178–181 (1989).
- ⁵⁴D. J. Joseph and L. Preziosi, "Heat waves," *Rev. Mod. Phys.* **61**, 41–73 (1989).
- ⁵⁵B. Straughan, *Heat Waves* (Springer Science & Business Media, New York, 2011), Vol. 177.
- ⁵⁶I. Eltayeb, "Convective instabilities of Maxwell-Cattaneo fluids," *Proc. R. Soc. A* **473**, 20160712 (2017).
- ⁵⁷I. H. Herron and R. E. Mickens, "Some exact and approximate solutions to a generalized Maxwell-Cattaneo equation," *Stud. Appl. Math.* **151**, 1550–1568 (2023).
- ⁵⁸J. Nascimento, A. Ramos, A. Campelo, and M. Freitas, "Exact solution of Maxwell-Cattaneo-Vernotte model: Diffusion versus second sound," *Appl. Math. Lett.* **156**, 109135 (2024).
- ⁵⁹V. L. Mironov, "Modified Cattaneo-Vernotte equation for heat transfer in solids," *Therm. Sci. Eng.* **7**, 8050 (2024).

- ⁶⁰D. E. Carlson, "Linear thermoelasticity," in *Linear Theories of Elasticity and Thermoelasticity: Linear and Nonlinear Theories of Rods, Plates, and Shells*, edited by C. Truesdell (Springer, 1973), pp. 297–345.
- ⁶¹M. A. Biot, "Thermoelasticity and irreversible thermodynamics," *J. Appl. Phys.* **27**, 240–253 (1956).
- ⁶²H. W. Lord and Y. Shulman, "A generalized dynamical theory of thermoelasticity," *J. Mech. Phys. Solids* **15**, 299–309 (1967).
- ⁶³A. E. Green and K. Lindsay, "Thermoelasticity," *J. Elast.* **2**, 1–7 (1972).
- ⁶⁴D. Chandrasekharaiyah and H. N. Murthy, "Temperature-rate-dependent thermoelastic interactions due to a line heat source," *Acta Mech.* **89**, 1–12 (1991).
- ⁶⁵D. Chandrasekharaiyah and K. Srinath, "Thermoelastic interactions without energy dissipation due to a point heat source," *J. Elast.* **50**, 97–108 (1998).
- ⁶⁶D. Chandrasekharaiyah and K. Srinath, "Thermoelastic interactions without energy dissipation due to a line heat source," *Acta Mech.* **128**, 243–251 (1998).
- ⁶⁷Y. Song, D. M. Todorovic, B. Cretin, and P. Vairac, "Study on the generalized thermoelastic vibration of the optically excited semiconducting microcantilevers," *Int. J. Solids Struct.* **47**, 1871–1875 (2010).
- ⁶⁸I. A. Abbas and M. Marin, "Analytical solutions of a two-dimensional generalized thermoelastic diffusions problem due to laser pulse," *Iran. J. Sci. Technol. Trans. Mech. Eng.* **42**, 57–71 (2018).
- ⁶⁹M. Marin, A. Öchsner, and M. M. Bhatti, "Some results in moore-gibson-thompson thermoelasticity of dipolar bodies," *ZAMM Z. Angew. Math.* **100**, e202000090 (2020).
- ⁷⁰K. Lotfy, I. S. Elshazly, B. Halouani, P. Ailawalia, and A. A. El-Bary, "Acoustic diffusion of a rotating composite elastic medium subjected to thermal source," *AIP Adv.* **14**, 115231 (2024).
- ⁷¹M. Abi Ghanem and T. Dehoux, "Progress in laser ultrasonics evaluation of micro- and nanoscale interfacial mechanics," *Appl. Phys. Rev.* **11**, 041315 (2024).
- ⁷²J. S. Jin, "Mechanical vibration-induced suppression of transverse acoustic phonons in silicon due to akhiezer damping," *AIP Adv.* **14**, 105332 (2024).
- ⁷³A. M. Alshehri and K. Lotfy, "Mechanical-photoacoustic model for hydro-semiconductor medium subjected to multi-temperatures theory," *Phys. Fluids* **37**, 017146 (2025).
- ⁷⁴M. Nikodemou and N. Nikiforakis, "A unified method for detonation-induced elastoplastic response of multiple interacting materials," *Phys. Fluids* **37**, 016136 (2025).
- ⁷⁵A. Alsisi, I. Abbas, K. Lotfy, A. El-Bary, and M. Ahmed, "The impact of fractional derivative on thermomechanical interactions in two-dimensional skin tissues throughout hyperthermia treatment," *Case Stud. Therm. Eng.* **54**, 104025 (2024).
- ⁷⁶A. Hobiny and I. Abbas, "Eigenvalue approach for investigating thermal and mechanical responses on living tissues during laser irradiation with experimental verification," *Phys. Fluids* **36**, 031906 (2024).
- ⁷⁷A. Green and P. Naghdi, "A re-examination of the basic postulates of thermo-mechanics," *Proc. R. Soc. London Ser. A* **432**, 171–194 (1991).
- ⁷⁸A. Green and P. Naghdi, "On undamped heat waves in an elastic solid," *J. Therm. Stresses* **15**, 253–264 (1992).
- ⁷⁹A. Green and P. Naghdi, "Thermoelasticity without energy dissipation," *J. Elast.* **31**, 189–208 (1993).
- ⁸⁰S. M. Hosseini, J. Sladek, and V. Sladek, "Nonlocal coupled photo-thermoelasticity analysis in a semiconducting micro/nano beam resonator subjected to plasma shock loading: A Green-Naghdi-based analytical solution," *Appl. Math. Model.* **88**, 631–651 (2020).
- ⁸¹A. Zenkour, A. Abouelregal, K. Alnefaie, N. Abu-Hamdeh, A. Aljinaidi, and E. Aifantis, "State space approach for the vibration of nanobeams based on the nonlocal thermoelasticity theory without energy dissipation," *J. Mech. Sci. Technol.* **29**, 2921–2931 (2015).
- ⁸²A. M. Zenkour, "Nonlocal thermoelasticity theory without energy dissipation for nano-machined beam resonators subjected to various boundary conditions," *Microsyst. Technol.* **23**, 55–65 (2017).
- ⁸³D. Soranzio, D. Puntel, M. Tuniz, P. E. Majchrzak, A. Milloch, N. M. Olsen, W. Bronsch, B. S. Jessen, D. Fainozzi, J. S. Pelli Cresi *et al.*, "Impact of MoS₂ monolayers on the thermoelastic response of silicon heterostructures," *ACS Appl. Nano Mater.* **7**, 15317–15324 (2024).
- ⁸⁴J. Janušonis, T. Jansma, C. Chang, Q. Liu, A. Gatilova, A. Lomonosov, V. Shalagatskyi, T. Pezeril, V. Temnov, and R. Tobey, "Transient grating spectroscopy in magnetic thin films: Simultaneous detection of elastic and magnetic dynamics," *Sci. Rep.* **6**, 29143 (2016).
- ⁸⁵A. Maznev, F. Bencivenga, A. Cannizzo, F. Capotondi, R. Cucini, R. Duncan, T. Feurer, T. Frazer, L. Foglia, H.-M. Frey, H. Kapteyn, J. Knobloch, G. Knopp, C. Masciovecchio, R. Mincigrucci, G. Monaco, M. Murnane, I. Nikolov, E. Pedersoli, A. Simonig, A. Vega-Flick, and K. Nelson, "Generation of coherent phonons by coherent extreme ultraviolet radiation in a transient grating experiment," *Appl. Phys. Lett.* **113**, 221905 (2018).
- ⁸⁶M. Brioschi, P. Carrara, V. Polewczuk, D. Dagur, G. Vinai, P. Parisse, S. Dal Zilio, G. Panaccione, G. Rossi, and R. Cucini, "Multidetection scheme for transient-grating-based spectroscopy," *Opt. Lett.* **48**, 167–170 (2023).
- ⁸⁷L. Foglia, R. Mincigrucci, A. Maznev, G. Baldi, F. Capotondi, F. Caporaletti, R. Comin, D. De Angelis, R. Duncan, D. Fainozzi, G. Kurdi, J. Li, A. Martinelli, C. Masciovecchio, G. Monaco, A. Milloch, K. Nelson, C. Occhialini, M. Pancaldi, E. Pedersoli, and F. Bencivenga, "Extreme ultraviolet transient gratings: A tool for nanoscale photoacoustics," *Photoacoustics* **29**, 100453 (2023).
- ⁸⁸F. Bencivenga, F. Capotondi, L. Foglia, R. Mincigrucci, and C. Masciovecchio, "Extreme ultraviolet transient gratings," *Adv. Phys.: X* **8**, 2220363 (2023).
- ⁸⁹F. Bencivenga, R. Cucini, F. Capotondi, A. Battistoni, R. Mincigrucci, E. Giangrisostomi, A. Gessini, M. Manfredda, I. Nikolov, E. Pedersoli, E. Principi, C. Svetina, P. Parisse, F. Casolari, M. Danailov, M. Kiskinova, and C. Masciovecchio, "Four-wave mixing experiments with extreme ultraviolet transient gratings," *Nature* **520**, 205–208 (2015).
- ⁹⁰D. Fainozzi, F. Caporaletti, F. Capotondi, D. De Angelis, R. A. Duncan, L. Foglia, A. Martinelli, R. Mincigrucci, K. A. Nelson, E. Pedersoli *et al.*, "Temperature effects on the nanoscale thermoelastic response of a SiO₂ membrane," *APL Mater.* **12**, 051122 (2024).
- ⁹¹F. Bencivenga, R. Mincigrucci, F. Capotondi, L. Foglia, D. Naumenko, A. Maznev, E. Pedersoli, A. Simonig, F. Caporaletti, V. Chiloyan, R. Cucini, F. Dallari, R. A. Duncan, T. D. Frazer, G. Gaio, A. Gessini, L. Giannessi, S. Huberman, H. Kapteyn, J. Knobloch, G. Kurdi, N. Mahne, M. Manfredda, A. Martinelli, M. Murnane, E. Principi, L. Raimondi, S. Spampinati, C. Spezzani, M. Trovò, M. Zangrandi, G. Chen, G. Monaco, K. Nelson, and C. Masciovecchio, "Nanoscale transient gratings excited and probed by extreme ultraviolet femtosecond pulses," *Sci. Adv.* **5**, eaaw5805 (2019).
- ⁹²M. P. Kroonblawd, B. W. Hamilton, and A. Strachan, "Fourier-like thermal relaxation of nanoscale explosive hot spots," *J. Phys. Chem. C* **125**, 20570–20582 (2021).
- ⁹³Y. Cao, T. Yu, W. Lai, Y. Liu, and B. Wang, "Analysis of intermolecular interactions in homologous molecular crystals of energetic materials," *Energy Mater. Front.* **1**, 95–102 (2020).
- ⁹⁴Z.-X. Zhang, Y.-T. Si, T. Yu, W.-P. Lai, Y.-D. Ma, M.-C. Liu, Y.-Z. Liu, and B.-Z. Wang, "Extra contribution to the crystal stability of insensitive explosive TATB: The cooperativity of intermolecular interactions," *Def. Technol.* **25**, 88–98 (2023).
- ⁹⁵M. Cawkwell, T. D. Sewell, L. Zheng, and D. L. Thompson, "Shock-induced shear bands in an energetic molecular crystal: Application of shock-front absorbing boundary conditions to molecular dynamics simulations," *Phys. Rev. B* **78**, 014107 (2008).
- ⁹⁶M. P. Kroonblawd and L. E. Fried, "High explosive ignition through chemically activated nanoscale shear bands," *Phys. Rev. Lett.* **124**, 206002 (2020).
- ⁹⁷M. P. Kroonblawd and T. D. Sewell, "Anisotropic relaxation of idealized hot spots in crystalline 1,3,5-triamino-2,4,6-trinitrobenzene (TATB)," *J. Phys. Chem. C* **120**, 17214–17223 (2016).
- ⁹⁸B. W. Hamilton, M. P. Kroonblawd, C. Li, and A. Strachan, "A hotspot's better half: Non-equilibrium intra-molecular strain in shock physics," *J. Phys. Chem. Lett.* **12**, 2756–2762 (2021).
- ⁹⁹G. Chen, "Non-Fourier phonon heat conduction at the microscale and nanoscale," *Nat. Rev. Phys.* **3**, 555–569 (2021).
- ¹⁰⁰A. I. Zhmakin, *Non-Fourier Heat Conduction* (Springer International Publishing, 2023).
- ¹⁰¹G. Xie, D. Ding, and G. Zhang, "Phonon coherence and its effect on thermal conductivity of nanostructures," *Adv. Phys. X* **3**, 1480417 (2018).
- ¹⁰²C. A. Polanco, A. van Roekeghem, B. Brisuda, L. Saminadayar, O. Bourgeois, and N. Mingo, "The phonon quantum of thermal conductance: Are simulations and measurements estimating the same quantity?," *Sci. Adv.* **9**, eadi7439 (2023).

- ¹⁰³K. Schwab, E. A. Henriksen, J. M. Worlock, and M. L. Roukes, "Measurement of the quantum of thermal conductance," *Nature* **404**, 974–977 (2000).
- ¹⁰⁴W. Zhang, Y. Guo, S. Y. Xiong, and H. L. Yi, "Phonon ballistic transport and Anderson localization in $\text{Si}_{1-x}\text{Ge}_x$ alloyed nanowires," *Phys. Rev. B* **108**, 125436 (2023).
- ¹⁰⁵P. E. Hopkins, "Thermal transport across solid interfaces with nanoscale imperfections: Effects of roughness, disorder, dislocations, and bonding on thermal boundary conductance," *Int. Sch. Res. Not.* **2013**, 682586.
- ¹⁰⁶Z. Tong, M. Liu, and H. Bao, "A numerical investigation on the heat conduction in high filler loading particulate composites," *Int. J. Heat Mass Transfer* **100**, 355–361 (2016).
- ¹⁰⁷R. Costescu, D. Cahill, F. Fabreguette, Z. Sechrist, and S. George, "Ultra-low thermal conductivity in $\text{W}/\text{Al}_2\text{O}_3$ nanolaminates," *Science* **303**, 989–990 (2004).
- ¹⁰⁸J. Ravichandran, A. K. Yadav, R. Cheaito, P. B. Rossen, A. Soukiassian, S. Suresha, J. C. Duda, B. M. Foley, C.-H. Lee, Y. Zhu *et al.*, "Crossover from incoherent to coherent phonon scattering in epitaxial oxide superlattices," *Nat. Mater.* **13**, 168–172 (2014).
- ¹⁰⁹N. Zen, T. A. Puurintinen, T. J. Isotalo, S. Chaudhuri, and I. J. Maasilta, "Engineering thermal conductance using a two-dimensional phononic crystal," *Nat. Commun.* **5**, 3435 (2014).
- ¹¹⁰M. I. Hussein, C.-N. Tsai, and H. Honavar, "Thermal conductivity reduction in a nanophononic metamaterial versus a nanophononic crystal: A review and comparative analysis," *Adv. Funct. Mater.* **30**, 1906718 (2020).
- ¹¹¹J. Chen, G. Zhang, and B. Li, "Phonon coherent resonance and its effect on thermal transport in core-shell nanowires," *J. Chem. Phys.* **135**, 104508 (2011).
- ¹¹²F. Yousefi, O. Farzadian, and M. Shafee, "Spontaneous heat current and ultra-high thermal rectification in asymmetric graphene: A molecular dynamics simulation," *Nanotechnology* **36**, 135401 (2025).
- ¹¹³H. Wang, S. Hu, K. Takahashi, X. Zhang, H. Takamatsu, and J. Chen, "Experimental study of thermal rectification in suspended monolayer graphene," *Nat. Commun.* **8**, 15843 (2017).
- ¹¹⁴R. Shrestha, Y. Luan, S. Shin, T. Zhang, X. Luo, J. S. Lundh, W. Gong, M. R. Bockstaller, S. Choi, T. Luo *et al.*, "High-contrast and reversible polymer thermal regulator by structural phase transition," *Sci. Adv.* **5**, eaax3777 (2019).
- ¹¹⁵R. Shrestha, Y. Luan, X. Luo, S. Shin, T. Zhang, P. Smith, W. Gong, M. Bockstaller, T. Luo, R. Chen *et al.*, "Dual-mode solid-state thermal rectification," *Nat. Commun.* **11**, 4346 (2020).
- ¹¹⁶Y. Zhang, T. Xia, and D. Huston, "Radar technology: Radio frequency, interferometric, millimeter wave and terahertz sensors for assessing and monitoring civil infrastructures," in *Sensor Technologies for Civil Infrastructures* (Elsevier, 2022), pp. 169–209.
- ¹¹⁷G. Cheng, X. Wang, Z. Wang, and Y. He, "Heat transfer and storage characteristics of composite phase change materials with high oriented thermal conductivity based on polymer/graphite nanosheets networks," *Int. J. Heat Mass Transfer* **183**, 122127 (2022).
- ¹¹⁸L. Wang and B. Li, "Thermal logic gates: Computation with phonons," *Phys. Rev. Lett.* **99**, 177208 (2007).
- ¹¹⁹A. Hamed, M. Elzouka, and S. Ndaoo, "Thermal calculator," *Int. J. Heat Mass Transfer* **134**, 359–365 (2019).
- ¹²⁰T. Tighe, J. Worlock, and M. Roukes, "Direct thermal conductance measurements on suspended monocrystalline nanostructures," *Appl. Phys. Lett.* **70**, 2687–2689 (1997).
- ¹²¹L. G. Rego and G. Kirczenow, "Quantized thermal conductance of dielectric quantum wires," *Phys. Rev. Lett.* **81**, 232 (1998).
- ¹²²H. Ma and Z. Tian, "Significantly high thermal rectification in an asymmetric polymer molecule driven by diffusive versus ballistic transport," *Nano Lett.* **18**, 43–48 (2018).
- ¹²³Y. Zhang, B. Li, P. Sun, Y. Hou, J. Hong, M. Shi, L. Zeng, and Q. Liu, "Thermal p-n junctions: A macroscopic thermal diode based on heterogeneous materials," *Chem. Eng. J.* **522**, 167537 (2025).
- ¹²⁴M. Zou, H. Geng, R. Ma, W. Chen, L. Sheng, and D. Xing, "Nonreciprocal ballistic transport in asymmetric bands," *Phys. Rev. B* **109**, 155302 (2024).
- ¹²⁵C. W. Chang, D. Okawa, A. Majumdar, and A. Zettl, "Solid-state thermal rectifier," *Science* **314**, 1121–1124 (2006).
- ¹²⁶N. Li, J. Ren, L. Wang, G. Zhang, P. Hägggi, and B. Li, "Colloquium: Phononics: Manipulating heat flow with electronic analogs and beyond," *Rev. Mod. Phys.* **84**, 1045–1066 (2012).
- ¹²⁷Y. Wang, S. Chen, and X. Ruan, "Tunable thermal rectification in graphene nanoribbons through defect engineering: A molecular dynamics study," *Appl. Phys. Lett.* **100**, 163101 (2012).
- ¹²⁸Y. Wang, A. Vallabhaneni, J. Hu, B. Qiu, Y. P. Chen, and X. Ruan, "Phonon lateral confinement enables thermal rectification in asymmetric single-material nanostructures," *Nano Lett.* **14**, 592–596 (2014).
- ¹²⁹M. Peyrard, "The design of a thermal rectifier," *Europhys. Lett.* **76**, 49 (2006).
- ¹³⁰C. Dames, "Solid-state thermal rectification with existing bulk materials," *J. Heat Transfer* **131**, 061301 (2009).
- ¹³¹B. Li, J. Lan, and L. Wang, "Interface thermal resistance between dissimilar anharmonic lattices," *Phys. Rev. Lett.* **95**, 104302 (2005).
- ¹³²J. Jiang, J. Wang, and B. Li, "Topology-induced thermal rectification in carbon nanodevice," *Europhys. Lett.* **89**, 46005 (2010).
- ¹³³J. Lee, V. Varshney, A. K. Roy, J. B. Ferguson, and B. L. Farmer, "Thermal rectification in three-dimensional asymmetric nanostructure," *Nano Lett.* **12**, 3491–3496 (2012).
- ¹³⁴N. Yang, G. Zhang, and B. Li, "Carbon nanocone: A promising thermal rectifier," *Appl. Phys. Lett.* **93**, 243111 (2008).
- ¹³⁵J. Hu, X. Ruan, and Y. P. Chen, "Thermal conductivity and thermal rectification in graphene nanoribbons: A molecular dynamics study," *Nano Lett.* **9**, 2730–2735 (2009).
- ¹³⁶H. Tian, D. Xie, Y. Yang, T.-L. Ren, G. Zhang, Y.-F. Wang, C.-J. Zhou, P.-G. Peng, L.-G. Wang, and L.-T. Liu, "A novel solid-state thermal rectifier based on reduced graphene oxide," *Sci. Rep.* **2**, 523 (2012).
- ¹³⁷N. Wu, Y. Liu, S. Wang, and Z. Xing, "Thermal rectification across an asymmetric layer carbon nanotube van der Waals heterostructure," *ACS Appl. Mater. Interfaces* **16**, 9155–9168 (2024).
- ¹³⁸A. Nese, Y. Li, S. Averick, Y. Kwak, D. Konkolewicz, S. S. Sheiko, and K. Matyjaszewski, "Synthesis of amphiphilic poly(*N*-vinylpyrrolidone)-B-poly(vinyl acetate) molecular bottlebrushes," *ACS Macro Lett.* **1**, 227–231 (2012).
- ¹³⁹S. C. Radzinski, J. C. Foster, and J. B. Matson, "Synthesis of bottlebrush polymers via transfer-to and grafting-through approaches using a raft chain transfer agent with a romp-active Z-group," *Polym. Chem.* **6**, 5643–5652 (2015).
- ¹⁴⁰L. Maurer, S. Mei, and I. Knezevic, "Rayleigh waves, surface disorder, and phonon localization in nanostructures," *Phys. Rev. B* **94**, 045312 (2016).
- ¹⁴¹M. Kaviany, *Heat Transfer Physics* (Cambridge University Press, Cambridge, 2014).
- ¹⁴²A. Cantarero and F. X. Àlvarez, *Nanoscale Thermoelectrics* (Springer Nature, Berlin, 2014), Chap. 1, pp. 1–39.
- ¹⁴³A. Chernatynskiy and S. R. Phillpot, "Phonon-mediated thermal transport: Confronting theory and microscopic simulation with experiment," *Curr. Opin. Solid State Mater. Sci.* **17**, 1–9 (2013).
- ¹⁴⁴L. Chen, N. Kumari, S. Chen, and Y. Hou, "Thermal conductivity of multilayer dielectric films from molecular dynamics simulations," *RSC Adv.* **7**, 26194–26201 (2017).
- ¹⁴⁵V. V. Kuryliuk and O. A. Korotchenkov, "Atomistic simulation of the thermal conductivity in amorphous SiO_2 matrix/Ge nanocrystal composites," *Phys. E Low-Dimensional Syst. Nanostruct.* **88**, 228–236 (2017).
- ¹⁴⁶N. Zhan, B. Chen, C. Li, and P. K. Shen, "Molecular dynamics simulations of the thermal conductivity of graphene for application in wearable devices," *Nanotechnology* **30**, 025705 (2019).
- ¹⁴⁷K. Shimamura, S. Hattori, K-i Nomura, A. Koura, and F. Shimojo, "Thermal conductivity calculation using homogeneous non-equilibrium molecular dynamics simulation with allegro," *Int. J. Heat Mass Transfer* **234**, 126106 (2024).
- ¹⁴⁸H. Bao, X. Ruan, and M. Kaviany, "Theory of the broadening of vibrational spectra induced by lowered symmetry in yttria nanostructures," *Phys. Rev. B* **78**, 125417 (2008).
- ¹⁴⁹Y. Zhang, "First-principles debye-callaway approach to lattice thermal conductivity," *J. Materomics* **2**, 237–247 (2016).
- ¹⁵⁰Z. Li, Y. Xia, and C. Wolverton, "First-principles calculations of lattice thermal conductivity in Ti_3VSe_4 : Uncertainties from different approaches of force constants," *Phys. Rev. B* **108**, 184307 (2023).

- ¹⁵¹X. Wang, J. Yang, Y. Wu, and H. Sun, "First-principles analysis of lattice thermal conductivity in monolayer Mn₂C," *J. Phys. Chem. C* **128**, 7216–7222 (2024).
- ¹⁵²N. Mingo and L. Yang, "Phonon transport in nanowires coated with an amorphous material: An atomistic Green's function approach," *Phys. Rev. B* **68**, 245406 (2003).
- ¹⁵³T. Yamamoto and K. Watanabe, "Nonequilibrium Green's function approach to phonon transport in defective carbon nanotubes," *Phys. Rev. Lett.* **96**, 255503 (2006).
- ¹⁵⁴Z. Huang, T. S. Fisher, and J. Y. Murthy, "Simulation of phonon transmission through graphene and graphene nanoribbons with a Green's function method," *J. Appl. Phys.* **108**, 094319 (2010).
- ¹⁵⁵J.-S. Wang, B. K. Agarwalla, H. Li, and J. Thingna, "Nonequilibrium Green's function method for quantum thermal transport," *Front. Phys.* **9**, 673–697 (2014).
- ¹⁵⁶R. Cheaito, C. A. Polanco, S. Addamane, J. Zhang, A. W. Ghosh, G. Balakrishnan, and P. E. Hopkins, "Interplay between total thickness and period thickness in the phonon thermal conductivity of superlattices from the nanoscale to the microscale: Coherent versus incoherent phonon transport," *Phys. Rev. B* **97**, 085306 (2018).
- ¹⁵⁷L. Medrano Sandonas, R. Gutierrez, A. Pecchia, A. Croy, and G. Cuniberti, "Quantum phonon transport in nanomaterials: Combining atomistic with non-equilibrium Green's function techniques," *Entropy* **21**, 735 (2019).
- ¹⁵⁸C. A. Polanco, "Nonequilibrium Green's functions (NEGF) in vibrational energy transport: A topical review," *Nanoscale Microscale Thermophys. Eng.* **25**, 1–24 (2021).
- ¹⁵⁹A. Giri and P. E. Hopkins, "A review of experimental and computational advances in thermal boundary conductance and nanoscale thermal transport across solid interfaces," *Adv. Funct. Mater.* **30**, 1903857 (2019).
- ¹⁶⁰J. R. Harter, T. S. Palmer, and P. A. Greaney, "Predicting mesoscale spectral thermal conductivity using advanced deterministic phonon transport techniques," *Adv. Heat Transfer* **52**, 335–488 (2020).
- ¹⁶¹Z. M. Zhang, Z. M. Zhang, and Luby, *Nano/Microscale Heat Transfer* (McGraw-Hill Companies, Inc., New York, 2007).
- ¹⁶²P. M. Norris, L. S. Larkin, N. Q. Le, C. A. Polanco, J. L. Smoyer, and J. Zhang, "Progress in measuring, modeling, and manipulating thermal boundary conductance," *Adv. Heat Transfer* **53**, 327–404 (2021).
- ¹⁶³R. Bahru, M. F. M. A. Zamri, A. H. Shamsuddin, N. Shaari, and M. A. Mohamed, "A review of thermal interface material fabrication method toward enhancing heat dissipation," *Int. J. Energy Res.* **45**, 3548–3568 (2021).
- ¹⁶⁴Y. Zhang, J. Ma, N. Wei, J. Yang, and Q.-X. Pei, "Recent progress in the development of thermal interface materials: A review," *Phys. Chem. Chem. Phys.* **23**, 753–776 (2021).
- ¹⁶⁵J. S. Lewis, T. Perrier, Z. Barani, F. Kargar, and A. A. Balandin, "Thermal interface materials with graphene fillers: Review of the state of the art and outlook for future applications," *Nanotechnology* **32**, 142003 (2021).
- ¹⁶⁶C. Monachon, L. Weber, and C. Dames, "Thermal boundary conductance: A materials science perspective," *Annu. Rev. Mater. Res.* **46**, 433–463 (2016).
- ¹⁶⁷E. T. Swartz and R. O. Pohl, "Thermal boundary resistance," *Rev. Mod. Phys.* **61**, 605–668 (1989).
- ¹⁶⁸C. Stamper, D. Cortie, S. M. K. Nazrul-Islam, M. R. Rahman, D. Yu, G. Yang, A. Al-Mamun, X. Wang, and Z. Yue, "Phonon engineering in thermal materials with nano-carbon dopants," *Appl. Phys. Rev.* **11**, 021336 (2024).
- ¹⁶⁹R. M. Costescu, M. A. Wall, and D. G. Cahill, "Thermal conductance of epitaxial interfaces," *Phys. Rev. B* **67**, 054302 (2003).
- ¹⁷⁰R. Hanus, R. Gurunathan, L. Lindsay, M. T. Agne, J. Shi, S. Graham, and G. Jeffrey Snyder, "Thermal transport in defective and disordered materials," *Appl. Phys. Rev.* **8**, 031311 (2021).
- ¹⁷¹R. Gurunathan, R. Hanus, S. Graham, A. Garg, and G. J. Snyder, "Thermal resistance at twist boundary and a semicoherent heterointerface," *Phys. Rev. B* **103**, 144302 (2021).
- ¹⁷²K. Gordiz and A. Henry, "Phonon transport at interfaces: Determining the correct modes of vibration," *J. Appl. Phys.* **119**, 015101 (2016).
- ¹⁷³A. Giri and P. E. Hopkins, "Role of interfacial mode coupling of optical phonons on thermal boundary conductance," *Sci. Rep.* **7**, 11011 (2017).
- ¹⁷⁴P. Schelling, S. Phillpot, and P. Kebinski, "Kapitza conductance and phonon scattering at grain boundaries by simulation," *J. Appl. Phys.* **95**, 6082–6091 (2004).
- ¹⁷⁵P. Zhang, P. Yuan, X. Jiang, S. Zhai, J. Zeng, Y. Xian, H. Qin, and D. Yang, "A theoretical review on interfacial thermal transport at the nanoscale," *Small* **14**, 1702769 (2018).
- ¹⁷⁶Y. Chu, J. Shi, K. Miao, Y. Zhong, P. Sarangapani, T. S. Fisher, G. Klimeck, X. Ruan, and T. Kubis, "Thermal boundary resistance predictions with non-equilibrium Green's function and molecular dynamics simulations," *Appl. Phys. Lett.* **115**, 231601 (2019).
- ¹⁷⁷S. Plimpton, "Fast parallel algorithms for short-range molecular dynamics," *J. Comput. Phys.* **117**, 1–19 (1995).
- ¹⁷⁸S. Steiger, M. Povolotskyi, H.-H. Park, T. Kubis, and G. Klimeck, "Nemo5: A parallel multiscale nanoelectronics modeling tool," *IEEE Trans. Nanotechnol.* **10**, 1464–1474 (2011).
- ¹⁷⁹D. Zhao, X. Qian, X. Gu, S. A. Jajja, and R. Yang, "Measurement techniques for thermal conductivity and interfacial thermal conductance of bulk and thin film materials," *J. Electron. Packag.* **138**, 040802 (2016).
- ¹⁸⁰A. J. Schmidt, X. Chen, and G. Chen, "Pulse accumulation, radial heat conduction, and anisotropic thermal conductivity in pump-probe transient thermoreflectance," *Rev. Sci. Instrum.* **79**, 114902 (2008).
- ¹⁸¹X. Qian, P. Jiang, and R. Yang, "Anisotropic thermal conductivity of 4H and 6H silicon carbide measured using time-domain thermoreflectance," *Mater. Today Phys.* **3**, 70–75 (2017).
- ¹⁸²Z. Guo, A. Verma, X. Wu, F. Sun, A. Hickman, T. Masui, A. Kuramata, M. Higashiwaki, D. Jena, and T. Luo, "Anisotropic thermal conductivity in single crystal β -gallium oxide," *Appl. Phys. Lett.* **106**, 111909 (2015).
- ¹⁸³P. Jiang, X. Qian, and R. Yang, "Time-domain thermoreflectance (TDTR) measurements of anisotropic thermal conductivity using a variable spot size approach," *Rev. Sci. Instrum.* **88**, 074901 (2017).
- ¹⁸⁴A. J. Schmidt, R. Cheaito, and M. Chiesa, "A frequency-domain thermoreflectance method for the characterization of thermal properties," *Rev. Sci. Instrum.* **80**, 094901 (2009).
- ¹⁸⁵E. Ziade, "Wide bandwidth frequency-domain thermoreflectance: Volumetric heat capacity, anisotropic thermal conductivity, and thickness measurements," *Rev. Sci. Instrum.* **91**, 124901 (2020).
- ¹⁸⁶P. Schoderböck, H. Klocker, L. S. Sigl, and G. Seeber, "Evaluation of the thermal diffusivity of thin specimens from laser flash data," *Int. J. Thermophys.* **30**, 599–607 (2009).
- ¹⁸⁷M. Li, J. S. Kang, and Y. Hu, "Anisotropic thermal conductivity measurement using a new asymmetric-beam time-domain thermoreflectance (AB-TDTR) method," *Rev. Sci. Instrum.* **89**, 084901 (2018).
- ¹⁸⁸L. A. Pérez, K. Xu, M. R. Wagner, B. Dörfling, A. Perevedentsev, A. R. Goñi, M. Campoy-Quiles, M. I. Alonso, and J. S. Reparaz, "Anisotropic thermoreflectance thermometry: A contactless frequency-domain thermoreflectance approach to study anisotropic thermal transport," *Rev. Sci. Instrum.* **93**, 034902 (2022).
- ¹⁸⁹P. Jiang, X. Qian, and R. Yang, "A new elliptical-beam method based on time-domain thermoreflectance (TDTR) to measure the in-plane anisotropic thermal conductivity and its comparison with the beam-offset method," *Rev. Sci. Instrum.* **89**, 094902 (2018).
- ¹⁹⁰P. Jiang, X. Qian, X. Li, and R. Yang, "Three-dimensional anisotropic thermal conductivity tensor of single crystalline β -Ga₂O₃," *Appl. Phys. Lett.* **113**, 232105 (2018).
- ¹⁹¹P. Jiang, D. Wang, Z. Xiang, R. Yang, and H. Ban, "A new spatial-domain thermoreflectance method to measure a broad range of anisotropic in-plane thermal conductivity," *Int. J. Heat Mass Transfer* **191**, 122849 (2022).
- ¹⁹²J. P. Feser and D. G. Cahill, "Probing anisotropic heat transport using time-domain thermoreflectance with offset laser spots," *Rev. Sci. Instrum.* **83**, 104901 (2012).
- ¹⁹³J. P. Feser, J. Liu, and D. G. Cahill, "Pump-probe measurements of the thermal conductivity tensor for materials lacking in-plane symmetry," *Rev. Sci. Instrum.* **85**, 104903 (2014).
- ¹⁹⁴L. Tang and C. Dames, "Anisotropic thermal conductivity tensor measurements using beam-offset frequency domain thermoreflectance (BO-FDTR) for materials lacking in-plane symmetry," *Int. J. Heat Mass Transfer* **164**, 120600 (2021).
- ¹⁹⁵D. Rodin and S. K. Yee, "Simultaneous measurement of in-plane and through-plane thermal conductivity using beam-offset frequency domain thermoreflectance," *Rev. Sci. Instrum.* **88**, 014902 (2017).

- ¹⁹⁶M. Rahman, M. Shahzadeh, P. Braeuninger-Weimer, S. Hofmann, O. Hellwig, and S. Pisana, "Measuring the thermal properties of anisotropic materials using beam-offset frequency domain thermoreflectance," *J. Appl. Phys.* **123**, 245110 (2018).
- ¹⁹⁷X. Qian, Z. Ding, J. Shin, A. J. Schmidt, and G. Chen, "Accurate measurement of in-plane thermal conductivity of layered materials without metal film transducer using frequency domain thermoreflectance," *Rev. Sci. Instrum.* **91**, 064903 (2020).
- ¹⁹⁸G. Yang and B.-Y. Cao, "Three-sensor 2ω method with multi-directional layout: A general methodology for measuring thermal conductivity of solid materials," *Int. J. Heat Mass Transfer* **219**, 124878 (2024).
- ¹⁹⁹L. Shi, D. Li, C. Yu, W. Jang, D. Kim, Z. Yao, P. Kim, and A. Majumdar, "Measuring thermal and thermoelectric properties of one-dimensional nanostructures using a microfabricated device," *J. Heat Transfer* **125**, 881–888 (2003).
- ²⁰⁰K. Kurabayashi, M. Asheghi, M. Touzelbaev, and K. E. Goodson, "Measurement of the thermal conductivity anisotropy in polyimide films," *J. Microelectromech. Syst.* **8**, 180–191 (1999).
- ²⁰¹T. Borca-Tasciuc, A. Kumar, and G. Chen, "Data reduction in 3ω method for thin-film thermal conductivity determination," *Rev. Sci. Instrum.* **72**, 2139–2147 (2001).
- ²⁰²M. Slomski, N. Blumenschein, P. P. Paskov, J. F. Muth, and T. Paskova, "Anisotropic thermal conductivity of β -Ga₂O₃ at elevated temperatures: Effect of Sn and Fe dopants," *J. Appl. Phys.* **121**, 235104 (2017).
- ²⁰³G.-P. Su, X.-H. Zheng, L. Qiu, D.-W. Tang, and J. Zhu, "Measurement of thermal conductivity of anisotropic SiC crystal," *Int. J. Thermophys.* **34**, 2334–2342 (2013).
- ²⁰⁴S. Yamaguchi, T. Shiga, S. Ishioka, T. Saito, T. Kodama, and J. Shiomi, "Anisotropic thermal conductivity measurement of organic thin film with bidirectional 3ω method," *Rev. Sci. Instrum.* **92**, 034902 (2021).
- ²⁰⁵C. Forsythe, M. P. Gordon, and J. J. Urban, "3 ω techniques for measurement of volumetric heat capacity and anisotropic thermal conductivity of a solution processable, hybrid organic/inorganic film, Te-PEDOT: PSS," *J. Appl. Phys.* **131**, 105109 (2022).
- ²⁰⁶L. Peri, D. Prete, V. Demontis, E. Degoli, A. Ruini, R. Magri, and F. Rossella, "Measuring thermal conductivity of nanostructures with the 3ω method: The need for finite element modeling," *Nanotechnology* **34**, 435403 (2023).
- ²⁰⁷V. Mishra, C. L. Hardin, J. E. Garay, and C. Dames, "A 3-omega method to measure an arbitrary anisotropic thermal conductivity tensor," *Rev. Sci. Instrum.* **86**, 054902 (2015).
- ²⁰⁸S. Kommandur and S. Yee, "A suspended 3-omega technique to measure the anisotropic thermal conductivity of semiconducting polymers," *Rev. Sci. Instrum.* **89**, 114905 (2018).
- ²⁰⁹A. T. Ramu and J. E. Bowers, "A "2-omega" technique for measuring anisotropy of thermal conductivity," *Rev. Sci. Instrum.* **83**, 124903 (2012).
- ²¹⁰A. T. Ramu and J. E. Bowers, "Analysis of the "3-omega" method for substrates and thick films of anisotropic thermal conductivity," *J. Appl. Phys.* **112**, 043516 (2012).
- ²¹¹M. Handweg, R. Mitdank, Z. Galazka, and S. Fischer, "Temperature-dependent thermal conductivity in mg-doped and undoped β -Ga₂O₃ bulk-crystals," *Semicond. Sci. Technol.* **30**, 024006 (2015).
- ²¹²F. Mazzelli, J. Paterson, F. Leroy, and O. Bourgeois, "A combined $2\omega/3\omega$ method for the measurement of the in-plane thermal conductivity of thin films in multilayer stacks: Application to a silicon-on-insulator wafer," *J. Appl. Phys.* **137**, 015106 (2025).
- ²¹³R. G. Bhardwaj and N. Khare, "3- $\omega\omega$ technique for thermal conductivity measurement—Contemporary and advancement in its methodology," *Int. J. Thermophys.* **43**, 1–32 (2022).
- ²¹⁴A. Palacios, L. Cong, M. Navarro, Y. Ding, and C. Barreneche, "Thermal conductivity measurement techniques for characterizing thermal energy storage materials—a review," *Renewable Sustainable Energy Rev.* **108**, 32–52 (2019).
- ²¹⁵N. Nandihalli, "A short account of thermoelectric film characterization techniques," *Mater. Today Phys.* **36**, 101173 (2023).
- ²¹⁶H. Song, J. Liu, B. Liu, J. Wu, H.-M. Cheng, and F. Kang, "Two-dimensional materials for thermal management applications," *Joule* **2**, 442–463 (2018).
- ²¹⁷T. M. Tritt, *Thermal Conductivity: Theory, Properties, and Applications* (Springer Science & Business Media, 2005).
- ²¹⁸F. Völklein, H. Reith, and A. Meier, "Measuring methods for the investigation of in-plane and cross-plane thermal conductivity of thin films," *Phys. Status Solidi (a)* **210**, 106–118 (2013).
- ²¹⁹O. Corbino, "Thermal oscillations in lamps of thin fibers with alternating current flowing through them and the resulting effect on the rectifier as a result of the presence of even-numbered harmonics," *Phys. Z.* **11**, 413–417 (1910).
- ²²⁰O. Corbino, "Periodic resistance changes of fine metal threads which are brought together by alternating streams as well as deduction of their thermo characteristics at high temperatures," *Phys. Z.* **12**, 292–295 (1911).
- ²²¹S.-M. Lee and D. G. Cahill, "Heat transport in thin dielectric films," *J. Appl. Phys.* **81**, 2590–2595 (1997).
- ²²²S.-M. Lee, D. G. Cahill, and R. Venkatasubramanian, "Thermal conductivity of Si-Ge superlattices," *Appl. Phys. Lett.* **70**, 2957–2959 (1997).
- ²²³Q. Kong, L. Qiu, Y. D. Lim, C. W. Tan, K. Liang, C. Lu, and B. K. Tay, "Thermal conductivity characterization of three dimensional carbon nanotube network using freestanding sensor-based 3 ω technique," *Surf. Coat. Technol.* **345**, 105–112 (2018).
- ²²⁴T. Y. Choi, D. Poulikakos, J. Tharian, and U. Sennhauser, "Measurement of thermal conductivity of individual multiwalled carbon nanotubes by the 3- ω method," *Appl. Phys. Lett.* **87**, 013108 (2005).
- ²²⁵D. Chernodubov and A. Inyushkin, "Automatic thermal conductivity measurements with 3-omega technique," *Rev. Sci. Instrum.* **90**, 024904 (2019).
- ²²⁶D. Kim, D. Kim, S. Cho, S. Kim, S. Lee, and J. Kim, "Measurement of thermal conductivity of TiO₂ thin films using 3 ω method," *Int. J. Thermophys.* **25**, 281–289 (2004).
- ²²⁷D. G. Cahill, M. Katiyar, and J. Abelson, "Heat transport in micron thick a-Si:H films," *Phil. Mag. B* **71**, 677–682 (1995).
- ²²⁸F. Warkusz, "The size effect and the temperature coefficient of resistance in thin films," *J. Phys. D: Appl. Phys.* **11**, 689 (1978).
- ²²⁹M. Bauer, C. Bauer, M. Fish, R. Matthews, G. Garner, A. Litchenberger, and P. Norris, "Thin-film aerogel thermal conductivity measurements via 3 ω ," *J. Non-Cryst. Solids* **357**, 2960–2965 (2011).
- ²³⁰S. Santoso, and H. W. Beaty, eds., *Standard Handbook for Electrical Engineers*, 17th ed. (McGraw-Hill Education, New York, 2018).
- ²³¹J. Y. Duquesne, D. Fournier, and C. Fréty, "Analytical solutions of the heat diffusion equation for 3 ω method geometry," *J. Appl. Phys.* **108**, 086104 (2010).
- ²³²Wolfram Research, Inc., *Mathematica, Version 14.2* (Wolfram Research, Inc., Champaign, IL, 2024).
- ²³³N.-W. Park, W.-Y. Lee, J.-A. Kim, K. Song, H. Lim, W.-D. Kim, S.-G. Yoon, and S.-K. Lee, "Reduced temperature-dependent thermal conductivity of magnetite thin films by controlling film thickness," *Nanoscale Res. Lett.* **9**(1), 8 (2014).
- ²³⁴J. Callaway, "Model for lattice thermal conductivity at low temperatures," *Phys. Rev.* **113**, 1046–1051 (1959).
- ²³⁵G. A. Slack, "Nonmetallic crystals with high thermal conductivity," *J. Phys. Chem. Solids* **34**, 321–335 (1973).
- ²³⁶G. Qin, A. Huang, Y. Liu, H. Wang, Z. Qin, X. Jiang, J. Zhao, J. Hu, and M. Hu, "High-throughput computational evaluation of lattice thermal conductivity using an optimized slack model," *Mater. Adv.* **3**, 6826–6830 (2022).
- ²³⁷W. Jang, Z. Chen, W. Bao, C. N. Lau, and C. Dames, "Thickness-dependent thermal conductivity of encased graphene and ultrathin graphite," *Nano Lett.* **10**, 3909–3913 (2010).
- ²³⁸J. Wang, C. Ren, S. Ma, R. Xu, Y. Liu, and Y. Zhang, "Direct measurement of in-plane thermal conductivity of microscale suspended thin films using a novel 3 ω method," *Int. J. Heat Mass Transfer* **219**, 124870 (2024).
- ²³⁹H. Chen, H. Sun, L. Chen, Y. Chen, J. Chen, X. Qiu, and J. Wang, "Simultaneous measurement of thermal conductivity and thermal diffusivity of individual microwires by using a cross-wire geometry," *Rev. Sci. Instrum.* **93**, 024901 (2022).
- ²⁴⁰J. Wang, M. Gu, X. Zhang, and G. Wu, "Measurements of thermal effusivity of a fine wire and contact resistance of a junction using a T type probe," *Rev. Sci. Instrum.* **80**, 076107 (2009).
- ²⁴¹C. Dames and G. Chen, "1 ω , 2 ω , and 3 ω methods for measurements of thermal properties," *Rev. Sci. Instrum.* **76**, 124902 (2005).
- ²⁴²J. H. Kim, A. Feldman, and D. Novotny, "Application of the three omega thermal conductivity measurement method to a film on a substrate of finite thickness," *J. Appl. Phys.* **86**, 3959–3963 (1999).

- ²⁴³M. Bogner, A. Hofer, G. Benstetter, H. Gruber, and R. Y. Fu, "Differential 3ω method for measuring thermal conductivity of AlN and Si_3N_4 thin films," *Thin Solid Films* **591**, 267–270 (2015).
- ²⁴⁴A. Zhou, W. Wang, B. Yang, J. Li, and Q. Zhao, "Thermal conductivity study of micrometer-thick thermoelectric films by using three-omega methods," *Appl. Therm. Eng.* **98**, 683–689 (2016).
- ²⁴⁵A. Griffin, Jr., F. Brotzen, and P. Loos, "Effect of thickness on the transverse thermal conductivity of thin dielectric films," *J. Appl. Phys.* **75**, 3761–3764 (1994).
- ²⁴⁶J. C. Lambropoulos, M. Jolly, C. Amsden, S. Gilman, M. Sinicropi, D. Diakomihalis, and S. Jacobs, "Thermal conductivity of dielectric thin films," *J. Appl. Phys.* **66**, 4230–4242 (1989).
- ²⁴⁷S. Lefevre and S. Volz, "3 ω -scanning thermal microscope," *Rev. Sci. Instrum.* **76**, 033701 (2005).
- ²⁴⁸G. Pernot, A. Metjari, H. Chaynes, M. Weber, M. Isaiev, and D. Lacroix, "Frequency domain analysis of 3 ω -scanning thermal microscope probe—Application to tip/surface thermal interface measurements in vacuum environment," *J. Appl. Phys.* **129**, 055105 (2021).
- ²⁴⁹N. Harnack, S. Rodehutskors, and B. Gotsmann, "Scanning thermal microscopy method for self-heating in nonlinear devices and application to filamentary resistive random-access memory," *ACS Nano* **19**, 5342–5352 (2025).
- ²⁵⁰I. Moon, Y. H. Jeong, and S. Kwun, "The 3 ω technique for measuring dynamic specific heat and thermal conductivity of a liquid or solid," *Rev. Sci. Instrum.* **67**, 29–35 (1996).
- ²⁵¹J. Kimling, S. Martens, and K. Nielsch, "Thermal conductivity measurements using 1 ω and 3 ω methods revisited for voltage-driven setups," *Rev. Sci. Instrum.* **82**, 074903 (2011).
- ²⁵²P. B. Kaul, K. A. Day, and A. R. Abramson, "Application of the three omega method for the thermal conductivity measurement of polyaniline," *J. Appl. Phys.* **101**, 083507 (2007).
- ²⁵³A. A. Guermoudi, P. Y. Cresson, A. Ouldabbes, G. Boussatour, and T. Lasri, "Thermal conductivity and interfacial effect of polyimide C thin film using the 3-omega method," *J. Therm. Anal. Calorim.* **145**, 1–12 (2021).
- ²⁵⁴G. Boussatour, P.-Y. Cresson, B. Genestie, N. Joly, J.-F. Brun, and T. Lasri, "Measurement of the thermal conductivity of flexible biosourced polymers using the 3-omega method," *Polym. Test.* **70**, 503–510 (2018).
- ²⁵⁵A. Moridi, L. Zhang, W. Liu, S. Duvall, A. Brawley, Z. Jiang, S. Yang, and C. Li, "Characterisation of high thermal conductivity thin-film substrate systems and their interface thermal resistance," *Rev. Sci. Instrum.* **334**, 233–242 (2018).
- ²⁵⁶J. P. Feser, E. M. Chan, A. Majumdar, R. A. Segalman, and J. J. Urban, "Ultralow thermal conductivity in polycrystalline CdSe thin films with controlled grain size," *Nano Lett.* **13**, 2122–2127 (2013).
- ²⁵⁷S. Roy-Panzer, T. Kodama, S. Lingamneni, M. A. Panzer, M. Asheghi, and K. E. Goodson, "Thermal characterization and analysis of microliter liquid volumes using the three-omega method," *Rev. Sci. Instrum.* **86**, 024901 (2015).
- ²⁵⁸Y. K. Koh, S. L. Singer, W. Kim, J. M. Zide, H. Lu, D. G. Cahill, A. Majumdar, and A. C. Gossard, "Comparison of the 3 ω method and time-domain thermoreflectance for measurements of the cross-plane thermal conductivity of epitaxial semiconductors," *J. Appl. Phys.* **105**, 054303 (2009).
- ²⁵⁹Y. Jin, S. Nola, K. P. Pipe, and M. Shtein, "Improving thermoelectric efficiency in organic-metal nanocomposites via extra-low thermal boundary conductance," *J. Appl. Phys.* **114**, 194303 (2013).
- ²⁶⁰W. Parker, R. Jenkins, C. Butler, and G. Abbott, "Flash method of determining thermal diffusivity, heat capacity, and thermal conductivity," *J. Appl. Phys.* **32**, 1679–1684 (1961).
- ²⁶¹V. Khuu, M. Osterman, A. Bar-Cohen, and M. Pecht, "Considerations in the use of the laser flash method for thermal measurements of thermal interface materials," *IEEE Trans. Compon. Packag. Manuf. Technol.* **1**, 1015–1028 (2011).
- ²⁶²A. F. Lele, K. E. N'Tsoukpoe, T. Osterland, F. Kuznik, and W. K. Ruck, "Thermal conductivity measurement of thermochemical storage materials," *Appl. Therm. Eng.* **89**, 916–926 (2015).
- ²⁶³M. Li and M. Akoshima, "Appropriate metallic coating for thermal diffusivity measurement of nonopaque materials with laser flash method and its effect," *Int. J. Heat Mass Transfer* **148**, 119017 (2020).
- ²⁶⁴R. An, J. Zhao, J. Yang, S. Zhai, L. Dai, Q. Wang, J. Li, W. Hu, G. Sun, Y. Fan *et al.*, "Accurate and wide-range measurement of thermal conductivity of semiconductor materials by laser-excited raman spectroscopy," *J. Appl. Phys.* **134**, 015103 (2023).
- ²⁶⁵H. Weingrill, W. Hohenauer, K. Resch-Fauster, and C. Zauner, "Analyzing thermal conductivity of polyethylene-based compounds filled with copper," *Macromol. Mater. Eng.* **304**, 1800644 (2019).
- ²⁶⁶M. Ruoho, K. Valset, T. Finstad, and I. Tittonen, "Measurement of thin film thermal conductivity using the laser flash method," *Nanotechnology* **26**, 195706 (2015).
- ²⁶⁷D. M. Rowe, *CRC Handbook of Thermoelectrics* (CRC Press, 2018).
- ²⁶⁸B. Hay, J. Filtz, J. Hameury, and L. Rongione, "Uncertainty of thermal diffusivity measurements by laser flash method," *Int. J. Thermophys.* **26**, 1883–1898 (2005).
- ²⁶⁹L. Vozár and W. Hohenauer, "Uncertainty of thermal diffusivity measurements using the laser flash method," *Int. J. Thermophys.* **26**, 1899–1915 (2005).
- ²⁷⁰Y. Lee, D. Y. Ku, Y.-H. Park, M.-Y. Ahn, and S. Cho, "Sample holder design for effective thermal conductivity measurement of pebble-bed using laser flash method," *Fusion Eng. Des.* **124**, 995–998 (2017).
- ²⁷¹S. Min, J. Blumm, and A. Lindemann, "A new laser flash system for measurement of the thermophysical properties," *Thermochim. Acta* **455**, 46–49 (2007).
- ²⁷²Y. Takahashi and M. Murabayashi, "Measurement of thermal properties of nuclear materials by laser flash method," *J. Nucl. Sci. Technol.* **12**, 133–144 (1975).
- ²⁷³ASTM. "Standard test method for thermal diffusivity by the flash method," Paper No. ASTM E1461 (2013).
- ²⁷⁴F. De Ponte, *Present and Future Research on Guarded Hot Plate and Heat Flow Meter Apparatus* (ASTM International, 1985).
- ²⁷⁵A. Philipp, J. F. Eichinger, R. C. Aydin, A. Georgiadis, C. J. Cyron, and M. Retsch, "The accuracy of laser flash analysis explored by finite element method and numerical fitting," *J. Heat Mass Transfer* **56**, 811–823 (2020).
- ²⁷⁶A. Rosencwaig, "Thermal-wave imaging," *Science* **218**, 223–228 (1982).
- ²⁷⁷A. Rosencwaig and A. Gershoff, "Theory of the photoacoustic effect with solids," *J. Appl. Phys.* **47**, 64–69 (1976).
- ²⁷⁸C. A. Paddock and G. L. Eesley, "Transient thermoreflectance from thin metal films," *J. Appl. Phys.* **60**, 285–290 (1986).
- ²⁷⁹A. J. Schmidt, R. Cheaito, and M. Chiesa, "Characterization of thin metal films via frequency-domain thermoreflectance," *J. Appl. Phys.* **107**, 024908 (2010).
- ²⁸⁰S. Huxtable, D. G. Cahill, V. Fauconnier, J. O. White, and J.-C. Zhao, "Thermal conductivity imaging at micrometre-scale resolution for combinatorial studies of materials," *Nat. Mater.* **3**, 298–301 (2004).
- ²⁸¹A. Schmidt, "Pump-probe thermoreflectance," *Annu. Rev. Heat Transfer* **16**, 159–181 (2013).
- ²⁸²A. Schmidt, M. Chiesa, X. Chen, and G. Chen, "An optical pump-probe technique for measuring the thermal conductivity of liquids," *Rev. Sci. Instrum.* **79**, 064902 (2008).
- ²⁸³E. Ziade, M. Goni, T. Sato, P. Czubarow, and A. J. Schmidt, "Thermal conductance of nanoscale Langmuir-Blodgett films," *Appl. Phys. Lett.* **107**, 221603 (2015).
- ²⁸⁴Z. Zhang, Z. Chang, X. Fan, J. Zhou, X. Wang, G. Li, X. Zhang, J. Zhu, and D. Tang, "Pressure dependent thermoreflectance spectroscopy induced by interband transitions in metallic nano-film," *iScience* **24**, 102990 (2021).
- ²⁸⁵L. Larkin, J. Smoyer, and P. Norris, "Laser repetition rate in time-domain thermoreflectance techniques," *Int. J. Heat Mass Transfer* **109**, 786–790 (2017).
- ²⁸⁶K. Kang, Y. K. Koh, C. Chiriacescu, X. Zheng, and D. G. Cahill, "Two-tint pump-probe measurements using a femtosecond laser oscillator and sharp-edged optical filters," *Rev. Sci. Instrum.* **79**, 114901 (2008).
- ²⁸⁷J. Zhu, D. Tang, W. Wang, J. Liu, K. W. Holub, and R. Yang, "Ultrafast thermoreflectance techniques for measuring thermal conductivity and interface thermal conductance of thin films," *J. Appl. Phys.* **108**, 094315 (2010).
- ²⁸⁸C. Wei, X. Zheng, D. G. Cahill, and J.-C. Zhao, "Invited article: Micro-resolution spatially resolved measurement of heat capacity using dual-frequency time-domain thermoreflectance," *Rev. Sci. Instrum.* **84**, 071301 (2013).
- ²⁸⁹Y. Wang, J. Y. Park, Y. K. Koh, and D. G. Cahill, "Thermoreflectance of metal transducers for time-domain thermoreflectance," *J. Appl. Phys.* **108**, 043507 (2010).

- ²⁹⁰P. Jiang, X. Qian, and R. Yang, "Tutorial: Time-domain thermoreflectance (TDTR) for thermal property characterization of bulk and thin film materials," *J. Appl. Phys.* **124**, 161103 (2018).
- ²⁹¹D. G. Cahill, "Analysis of heat flow in layered structures for time-domain thermoreflectance," *Rev. Sci. Instrum.* **75**, 5119–5122 (2004).
- ²⁹²R. Cheaito, C. S. Gorham, A. Misra, K. Hattar, and P. E. Hopkins, "Thermal conductivity measurements via time-domain thermoreflectance for the characterization of radiation induced damage," *J. Mater. Res.* **30**, 1403–1412 (2015).
- ²⁹³P. E. Hopkins, J. C. Duda, S. P. Clark, C. P. Hains, T. J. Rotter, L. M. Phinney, and G. Balakrishnan, "Effect of dislocation density on thermal boundary conductance across GaSb/GaAs interfaces," *Appl. Phys. Lett.* **98**, 161913 (2011).
- ²⁹⁴T. L. Boughey, L. Yates, C.-F. Lo, W. Johnson, S. Graham, and B. A. Cola, "Thermal boundary resistance in GaN films measured by time domain thermoreflectance with robust Monte Carlo uncertainty estimation," *Nanoscale Microscale Thermophys. Eng.* **20**, 22–32 (2016).
- ²⁹⁵J. Liu, J. Zhu, M. Tian, X. Gu, A. Schmidt, and R. Yang, "Simultaneous measurement of thermal conductivity and heat capacity of bulk and thin film materials using frequency-dependent transient thermoreflectance method," *Rev. Sci. Instrum.* **84**, 034902 (2013).
- ²⁹⁶B. Sun, X. Gu, Q. Zeng, X. Huang, Y. Yan, Z. Liu, R. Yang, and Y. K. Koh, "Temperature dependence of anisotropic thermal conductivity tensor of bulk black phosphorus," *Adv. Mater.* **29**, 1603297 (2017).
- ²⁹⁷P. Jiang, X. Qian, X. Gu, and R. Yang, "Probing anisotropic thermal conductivity of transition metal dichalcogenides MX₂ (M = Mo, W and X = S, Se) using time-domain thermoreflectance," *Adv. Mater.* **29**, 1701068 (2017).
- ²⁹⁸Y. K. Koh and D. G. Cahill, "Frequency dependence of the thermal conductivity of semiconductor alloys," *Phys. Rev. B* **76**, 075207 (2007).
- ²⁹⁹R. Wilson and D. G. Cahill, "Anisotropic failure of fourier theory in time-domain thermoreflectance experiments," *Nat. Commun.* **5**, 5075 (2014).
- ³⁰⁰R. Wilson, J. P. Feser, G. T. Hohensee, and D. G. Cahill, "Two-channel model for nonequilibrium thermal transport in pump-probe experiments," *Phys. Rev. B* **88**, 144305 (2013).
- ³⁰¹F. Yang and C. Dames, "Heating-frequency-dependent thermal conductivity: An analytical solution from diffusive to ballistic regime and its relevance to phonon scattering measurements," *Phys. Rev. B* **91**, 165311 (2015).
- ³⁰²X. Zheng, D. G. Cahill, and J.-C. Zhao, "Thermal conductivity imaging of thermal barrier coatings," *Adv. Eng. Mater.* **7**, 622–626 (2005).
- ³⁰³D. J. Kirsch, J. Martin, R. Warzoha, M. McLean, D. Windover, and I. Takeuchi, "An instrumentation guide to measuring thermal conductivity using frequency domain thermoreflectance (FDTR)," *Rev. Sci. Instrum.* **95**, 103006 (2024).
- ³⁰⁴W. Capinski, H. Maris, T. Ruf, M. Cardona, K. Ploog, and D. Katzer, "Thermal-conductivity measurements of GaAs/AlAs superlattices using a picosecond optical pump-and-probe technique," *Phys. Rev. B* **59**, 8105 (1999).
- ³⁰⁵S. Sandell, E. Chávez-Ángel, A. El Sachat, J. He, C. M. Sotomayor Torres, and J. Maire, "Thermoreflectance techniques and Raman thermometry for thermal property characterization of nanostructures," *J. Appl. Phys.* **128**, 131101 (2020).
- ³⁰⁶T. Favaloro, J.-H. Bahk, and A. Shakouri, "Characterization of the temperature dependence of the thermoreflectance coefficient for conductive thin films," *Rev. Sci. Instrum.* **86**, 024903 (2015).
- ³⁰⁷G. A. Antonelli, B. Perrin, B. C. Daly, and D. G. Cahill, "Characterization of mechanical and thermal properties using ultrafast optical metrology," *MRS Bull.* **31**, 607–613 (2006).
- ³⁰⁸J. A. Malen, K. Baheti, T. Tong, Y. Zhao, J. A. Hudgings, and A. Majumdar, "Optical measurement of thermal conductivity using fiber aligned frequency domain thermoreflectance," *J. Heat Transfer* **133**, 081601 (2011).
- ³⁰⁹K. Regner, S. Majumdar, and J. A. Malen, "Instrumentation of broadband frequency domain thermoreflectance for measuring thermal conductivity accumulation functions," *Rev. Sci. Instrum.* **84**, 064901 (2013).
- ³¹⁰M. Goni, M. Patelka, S. Ikeda, T. Sato, and A. J. Schmidt, "Frequency domain thermoreflectance technique for measuring the thermal conductivity of individual micro-particles," *Rev. Sci. Instrum.* **89**, 074901 (2018).
- ³¹¹A. Chatterjee, D. Dzicsek, P. Song, J. Liu, A. Wieck, M. Pawlak *et al.*, "Effect of amplitude measurements on the precision of thermal parameters' determination in gaas using frequency-resolved thermoreflectance," *J. Appl. Phys.* **135**, 225101 (2024).
- ³¹²J. Yang, C. Maragliano, and A. J. Schmidt, "Thermal property microscopy with frequency domain thermoreflectance," *Rev. Sci. Instrum.* **84**, 104904 (2013).
- ³¹³Y. Cao, V. Fatemi, S. Fang, K. Watanabe, T. Taniguchi, E. Kaxiras, and P. Jarillo-Herrero, "Unconventional superconductivity in magic-angle graphene superlattices," *Nature* **556**, 43–50 (2018).
- ³¹⁴F. Bonaccorso, L. Colombo, G. Yu, M. Stoller, V. Tozzini, A. C. Ferrari, R. S. Ruoff, and V. Pellegrini, "Graphene, related two-dimensional crystals, and hybrid systems for energy conversion and storage," *Science* **347**, 1246501 (2015).
- ³¹⁵Y. Wang, N. Xu, D. Li, and J. Zhu, "Thermal properties of two dimensional layered materials," *Adv. Funct. Mater.* **27**, 1604134 (2017).
- ³¹⁶F. Wu, H. Tian, Y. Shen, Z.-Q. Zhu, Y. Liu, T. Hirtz, R. Wu, G. Gou, Y. Qiao, Y. Yang *et al.*, "High thermal conductivity 2D materials: From theory and engineering to applications," *Adv. Mater. Inter.* **9**, 2200409 (2022).
- ³¹⁷Y. Fu, J. Hansson, Y. Liu, S. Chen, A. Zehri, M. K. Samani, N. Wang, Y. Ni, Y. Zhang, Z.-B. Zhang *et al.*, "Graphene related materials for thermal management," *2D Mater.* **7**, 012001 (2020).
- ³¹⁸H. Liu, H. Brahma, C. Boix-Constant, H. S. van der Zant, P. G. Steeneken, and G. J. Verbiest, "Optomechanical methodology for characterizing the thermal properties of 2D materials," *APL Mater.* **12**, 021126 (2024).
- ³¹⁹Q. Guo, Z. Di, M. G. Lagally, and Y. Mei, "Strain engineering and mechanical assembly of silicon/germanium nanomembranes," *Mater. Sci. Eng. R.* **128**, 1–31 (2018).
- ³²⁰C. Tan, X. Cao, X.-J. Wu, Q. He, J. Yang, X. Zhang, J. Chen, W. Zhao, S. Han, G.-H. Nam *et al.*, "Recent advances in ultrathin two-dimensional nanomaterials," *Chem. Rev.* **117**, 6225–6331 (2017).
- ³²¹A. Sheraz, N. Mahmood, M. M. Çiçek, İ. Ergün, H. R. Rasouli, E. Durgun, and T. S. Kasirga, "High elasticity and strength of ultra-thin metallic transition metal dichalcogenides," *Nanoscale Adv.* **3**, 3894–3899 (2021).
- ³²²G. Fiori, F. Bonaccorso, G. Iannaccone, T. Palacios, D. Neumaier, A. Seabaugh, S. K. Banerjee, and L. Colombo, "Electronics based on two-dimensional materials," *Nat. Nanotechnol.* **9**, 768–779 (2014).
- ³²³A. K. Katiyar, A. T. Hoang, D. Xu, J. Hong, B. J. Kim, S. Ji, and J.-H. Ahn, "2D materials in flexible electronics: Recent advances and future perspectives," *Chem. Rev.* **124**, 318–419 (2024).
- ³²⁴M. Ku, J. Kim, J. Won, W. Kang, Y. Park, J. Park, J. Lee, J. Cheon, H. Lee, and J.-U. P. Smart, "Soft contact lens for wireless immunosensing of cortisol," *Sci. Adv.* **6**, eabb2891 (2020).
- ³²⁵J. Kim, M. Kim, M.-S. Lee, K. Kim, S. Ji, Y.-T. Kim, J. Park, K. Na, K.-H. Bae, H. Kyun Kim *et al.*, "Wearable smart sensor systems integrated on soft contact lenses for wireless ocular diagnostics," *Nat. Commun.* **8**, 14997 (2017).
- ³²⁶Y.-T. Kwon, Y.-S. Kim, S. Kwon, M. Mahmood, H.-R. Lim, S.-W. Park, S.-O. Kang, J. J. Choi, R. Herbert, Y. C. Jang *et al.*, "All-printed nanomembrane wireless bioelectronics using a biocompatible solderable graphene for multimodal human-machine interfaces," *Nat. Commun.* **11**, 3450 (2020).
- ³²⁷M. Kang, H. Jeong, S.-W. Park, J. Hong, H. Lee, Y. Chae, S. Yang, and J.-H. Ahn, "Wireless graphene-based thermal patch for obtaining temperature distribution and performing thermography," *Sci. Adv.* **8**, eabm6693 (2022).
- ³²⁸D. Kireev, K. Sel, B. Ibrahim, N. Kumar, A. Akbari, R. Jafari, and D. Akinwande, "Continuous cuffless monitoring of arterial blood pressure via graphene bioimpedance tattoos," *Nat. Nanotechnol.* **17**, 864–870 (2022).
- ³²⁹B. Senf, W.-H. Yeo, and J.-H. Kim, "Recent advances in portable biosensors for biomarker detection in body fluids," *Biosensors* **10**, 127 (2020).
- ³³⁰M. A. Ali, C. Hu, S. Jahan, B. Yuan, M. S. Saleh, E. Ju, S.-J. Gao, and R. Panat, "Sensing of COVID-19 antibodies in seconds via aerosol jet nanoprinted reduced-graphene-oxide-coated 3D electrodes," *Adv. Mater.* **33**, 2006647 (2021).
- ³³¹Y. Hu, M. Dai, W. Feng, X. Zhang, F. Gao, S. Zhang, B. Tan, J. Zhang, Y. Shuai, Y. Fu *et al.*, "Ultralow power optical synapses based on mos₂ layers by indium-induced surface charge doping for biomimetic eyes," *Adv. Mater.* **33**, 2104960 (2021).
- ³³²J. Chen, Z. Zhou, B. J. Kim, Y. Zhou, Z. Wang, T. Wan, J. Yan, J. Kang, J.-H. Ahn, and Y. Chai, "Optoelectronic graded neurons for bioinspired in-sensor motion perception," *Nat. Nanotechnol.* **18**, 882–888 (2023).

- ³³³L. P. Mawlong and J.-H. Ahn, "3D-structured photodetectors based on 2D transition-metal dichalcogenide," *Small Struct.* **3**, 2100149 (2022).
- ³³⁴P. V. Pham, S. C. Bodepudi, K. Shehzad, Y. Liu, Y. Xu, B. Yu, and X. Duan, "2D heterostructures for ubiquitous electronics and optoelectronics: Principles, opportunities, and challenges," *Chem. Rev.* **122**, 6514–6613 (2022).
- ³³⁵A. Bhattacharjee, H. Jiang, L. H. Li, S. Huang, Y. I. Chen, and Q. Cai, "Thermal transport property of boron nitride nanosheets," *Appl. Phys. Rev.* **11**, 041322 (2024).
- ³³⁶L. Zhang, Y. Tang, A. R. Khan, M. M. Hasan, P. Wang, H. Yan, T. Yildirim, J. F. Torres, G. P. Neupane, Y. Zhang *et al.*, "2D materials and heterostructures at extreme pressure," *Adv. Sci.* **7**, 2002697 (2020).
- ³³⁷N. Mingo and D. Broido, "Carbon nanotube ballistic thermal conductance and its limits," *Phys. Rev. Lett.* **95**, 096105 (2005).
- ³³⁸C. Jeong, S. Datta, and M. Lundstrom, "Full dispersion versus Debye model evaluation of lattice thermal conductivity with a Landauer approach," *J. Appl. Phys.* **109**, 073718 (2011).
- ³³⁹M.-H. Bae, Z. Li, Z. Aksamija, P. N. Martin, F. Xiong, Z.-Y. Ong, I. Knezevic, and E. Pop, "Ballistic to diffusive crossover of heat flow in graphene ribbons," *Nat. Commun.* **4**, 1734 (2013).
- ³⁴⁰W. Cai, A. L. Moore, Y. Zhu, X. Li, S. Chen, L. Shi, and R. S. Ruoff, "Thermal transport in suspended and supported monolayer graphene grown by chemical vapor deposition," *Nano Lett.* **10**, 1645–1651 (2010).
- ³⁴¹S. Chen, A. L. Moore, W. Cai, J. W. Suk, J. An, C. Mishra, C. Amos, C. W. Magnuson, J. Kang, L. Shi, and R. S. Ruoff, "Raman measurements of thermal transport in suspended monolayer graphene of variable sizes in vacuum and gaseous environments," *ACS Nano* **5**, 321–328 (2011).
- ³⁴²R. Yan, J. R. Simpson, S. Bertolazzi, J. Brivio, M. Watson, X. Wu, A. Kis, T. Luo, A. R. Hight Walker, and H. G. Xing, "Thermal conductivity of monolayer molybdenum disulfide obtained from temperature-dependent Raman spectroscopy," *ACS Nano* **8**, 986–993 (2014).
- ³⁴³T. Beechem, L. Yates, and S. Graham, "Invited Review Article: Error and uncertainty in Raman thermal conductivity measurements," *Rev. Sci. Instrum.* **86**, 041101 (2015).
- ³⁴⁴E. Yalon, B. Aslan, K. K. H. Smith, C. J. McClellan, S. V. Suryavanshi, F. Xiong, A. Sood, C. M. Neumann, X. Xu, K. E. Goodson, T. F. Heinz, and E. Pop, "Temperature-dependent thermal boundary conductance of monolayer MoS₂ by Raman thermometry," *ACS Appl. Mater. Interfaces* **9**, 43013–43020 (2017).
- ³⁴⁵Y. Yu, T. Minhaj, L. Huang, Y. Yu, and L. Cao, "In-plane and interfacial thermal conduction of two-dimensional transition-metal dichalcogenides," *Phys. Rev. Appl.* **13**, 034059 (2020).
- ³⁴⁶J. Liu, P. Li, and H. Zheng, "Review on techniques for thermal characterization of graphene and related 2D materials," *Nanomaterials* **11**, 2787 (2021).
- ³⁴⁷L. Zhang, Z. Lu, Y. Song, L. Zhao, B. Bhatia, K. R. Bagnall, and E. N. Wang, "Thermal expansion coefficient of monolayer molybdenum disulfide using micro-Raman spectroscopy," *Nano Lett.* **19**, 4745–4751 (2019).
- ³⁴⁸S. Jin, Z. He, Q. Ding, H. Cai, H. Zhang, Q. Zeng, G. Li, C. Zhao, N. Ni, and B. Wang, "Improved measurement of local thermal conductivities of coatings by the steady-state Raman spectroscopy method: A case study in TRISO particles," *J. Eur. Ceram. Soc.* **44**, 1412–1420 (2024).
- ³⁴⁹W. Hayes and R. Loudon, *Scattering of Light by Crystals* (Wiley, New York, 1978).
- ³⁵⁰R. Loudon, "The Raman effect in crystals," *Adv. Phys.* **50**, 813–864 (2001).
- ³⁵¹M. Cardona, "Resonance phenomena," in *Light Scattering in Solids II: Basic Concepts and Instrumentation* (Springer, Berlin, Heidelberg, 1982), pp. 19–178.
- ³⁵²S. D. McGrane, D. S. Moore, P. M. Goodwin, and D. M. Dattelbaum, "Quantitative tradeoffs between spatial, temporal, and thermometric resolution of nonresonant Raman thermometry for dynamic experiments," *Appl. Spectrosc.* **68**, 1279–1288 (2014).
- ³⁵³D. Tuschel, "Raman thermometry: Understanding the mathematics to better design Raman measurements," *Spectroscopy* **34**, 8–13 (2019).
- ³⁵⁴J. J. Gallardo, J. Navas, D. Zorrilla, R. Alcántara, D. Valor, C. Fernández-Lorenzo, and J. Martín-Calleja, "Micro-raman spectroscopy for the determination of local temperature increases in TiO₂ thin films due to the effect of radiation," *Appl. Spectrosc.* **70**, 1128–1136 (2016).
- ³⁵⁵Y.-J. Yu, M. Y. Han, S. Berciaud, A. B. Georgescu, T. F. Heinz, L. E. Brus, K. S. Kim, and P. Kim, "High-resolution spatial mapping of the temperature distribution of a Joule self-heated graphene nanoribbon," *Appl. Phys. Lett.* **99**, 183105 (2011).
- ³⁵⁶T. Yoshino, M. Matsumoto, Y. Ozeki, and K. Itoh, "Energy-dependent temperature dynamics in femtosecond laser microprocessing clarified by raman temperature measurement," in *Advanced Fabrication Technologies for Micro/Nano Optics and Photonics V* (SPIE, 2012), Vol. 8249, pp. 275–281.
- ³⁵⁷B. C. Pein, Y. Sun, and D. D. Dlott, "Unidirectional vibrational energy flow in nitrobenzene," *J. Phys. Chem. A* **117**, 6066–6072 (2013).
- ³⁵⁸D. S. Reig, S. Varghese, R. Farris, A. Block, J. D. Mehew, O. Hellman, P. Wozniak, M. Sledzinska, A. E. Sachat, E. Chavez-Angel, S. O. Valenzuela, N. F. van Hulst, P. Ordejon, Z. Zanolli, C. M. S. Torres, M. J. Verstraete, and K.-J. Tielrooij, "Unraveling heat transport and dissipation in suspended MoSe₂ from bulk to monolayer," *Adv. Mater.* **34**, 2108352 (2022).
- ³⁵⁹J. S. Lundh, T. Zhang, Y. Zhang, Z. Xia, M. Wetherington, Y. Lei, E. Kahn, S. Rajan, M. Terrones, and S. Choi, "2D materials for universal thermal imaging of micro-and nanodevices: An application to gallium oxide electronics," *ACS Appl. Electron. Mater.* **2**, 2945–2953 (2020).
- ³⁶⁰S. Sullivan, A. Vallabhaneni, I. Kholmanov, X. Ruan, J. Murthy, and L. Shi, "Optical generation and detection of local nonequilibrium phonons in suspended graphene," *Nano Lett.* **17**, 2049–2056 (2017).
- ³⁶¹A. C. Ferrari and D. M. Basko, "Raman spectroscopy as a versatile tool for studying the properties of graphene," *Nat. Nanotechnol.* **8**, 235–246 (2013).
- ³⁶²S. Xu, T. Wang, D. Hurley, Y. Yue, and X. Wang, "Development of time-domain differential raman for transient thermal probing of materials," *Opt. Express* **23**, 10040–10056 (2015).
- ³⁶³C. Li, S. Xu, Y. Yue, B. Yang, and X. Wang, "Thermal characterization of carbon nanotube fiber by time-domain differential Raman," *Carbon* **103**, 101–108 (2016).
- ³⁶⁴T. Wang, S. Xu, D. H. Hurley, Y. Yue, and X. Wang, "Frequency-resolved raman for transient thermal probing and thermal diffusivity measurement," *Opt. Lett.* **41**, 80–83 (2016).
- ³⁶⁵P. Yuan, H. Tan, R. Wang, T. Wang, and X. Wang, "Very fast hot carrier diffusion in unconstrained MoS₂ on a glass substrate: Discovered by picosecond ET-Raman," *RSC Adv.* **8**, 12767–12778 (2018).
- ³⁶⁶S.-Y. Son, H.-N. Jo, M. Park, G. Y. Jung, D. S. Lee, S. Lee, and H.-I. Joh, "Unusual thermal conductivity of carbon nanosheets with self-emerged graphitic carbon dots," *ACS Appl. Mater. Interfaces* **11**, 13616–13623 (2019).
- ³⁶⁷H. Zobeiri, R. Wang, T. Wang, H. Lin, C. Deng, and X. Wang, "Frequency-domain energy transport state-resolved Raman for measuring the thermal conductivity of suspended nm-thick MoSe₂," *Int. J. Heat Mass Transfer* **133**, 1074–1085 (2019).
- ³⁶⁸H. Zobeiri, N. Hunter, S. Xu, Y. Xie, and X. Wang, "Robust and high-sensitivity thermal probing at the nanoscale based on resonance Raman ratio (R3)," *Int. J. Extrem. Manuf.* **4**, 035201 (2022).
- ³⁶⁹J. Guo, X. Wang, and T. Wang, "Thermal characterization of microscale conductive and nonconductive wires using transient electrothermal technique," *J. Appl. Phys.* **101**, 063537 (2007).
- ³⁷⁰H. Xie, A. Cai, and X. Wang, "Thermal diffusivity and conductivity of multi-walled carbon nanotube arrays," *Phys. Lett. A* **369**, 120–123 (2007).
- ³⁷¹T. Wang, M. Han, R. Wang, P. Yuan, S. Xu, and X. Wang, "Characterization of anisotropic thermal conductivity of suspended nm-thick black phosphorus with frequency-resolved Raman spectroscopy," *J. Appl. Phys.* **123**, 145104 (2018).
- ³⁷²E. Mercado, C. Yuan, Y. Zhou, J. Li, J. H. Edgar, and M. Kuball, "Isotopically enhanced thermal conductivity in few-layer hexagonal boron nitride: Implications for thermal management," *ACS Appl. Nano Mater.* **3**, 12148–12156 (2020).
- ³⁷³R. Wang, T. Wang, H. Zobeiri, D. Li, and X. Wang, "Energy and charge transport in 2D atomic layer materials: Raman-based characterization," *Nanomaterials* **10**, 1807 (2020).
- ³⁷⁴A. P. Gertych, K. Czerniak-Losiewicz, A. Łapińska, M. Świniarski, M. Ojrzyńska, J. Judek, and M. Zdrojek, "Phonon and thermal properties of thin films made from Ws₂ mono-and few-layer flakes," *J. Phys. Chem. C* **125**, 14446–14452 (2021).

- ³⁷⁵C. Rodriguez-Fernandez, A. Nieminen, F. Ahmed, J. Pietila, H. Lipsanen, and H. Caglayan, "Unraveling thermal transport properties of MoTe₂ thin films using the optothermal Raman technique," *ACS Appl. Mater. Interfaces* **15**, 35692–35700 (2023).
- ³⁷⁶J. D. Gupta, P. Jangra, and A. K. Mishra, "Optothermal Raman spectroscopy for thermal transport study," in *Raman Spectroscopy: Advances and Applications* (Springer, 2024), pp. 75–99.
- ³⁷⁷S. P. Langley, "The bolometer and radiant energy," *Proc. Am. Acad. Arts Sci.* **16**, 342–358 (1880).
- ³⁷⁸T. S. Kasirga, *Thermal Conductivity Measurements in Atomically Thin Materials and Devices* (Springer Nature, 2020).
- ³⁷⁹O. Çakiroğlu, N. Mehmood, M. M. Çiçek, A. Aikebaier, H. R. Rasouli, E. Durgun, and T. S. Kasirga, "Thermal conductivity measurements in nanosheets via bolometric effect," *2D Mater.* **7**, 035003 (2020).
- ³⁸⁰F. H. L. Koppens, T. Mueller, P. Avouris, A. C. Ferrari, M. S. Vitiello, and M. Polini, "Photodetectors based on graphene, other two-dimensional materials and hybrid systems," *Nat. Nanotech.* **9**, 780–793 (2014).
- ³⁸¹M. Freitag, T. Low, F. Xia, and P. Avouris, "Photoconductivity of biased graphene," *Nat. Photonics* **7**, 53–59 (2013).
- ³⁸²W. Dickerson, N. Hemsworth, P. Gaskell, E. Ledwojinska, and T. Szkopek, "Bolometric response of free-standing reduced graphene oxide films," *Appl. Phys. Lett.* **107**, 243103 (2015).
- ³⁸³A. Nadtochiy, A. M. Gorb, B. M. Gorelov, O. Polovina, and O. Korotchenkov, *Graphene-Based Polymer Nanocomposites* (Springer, Singapore, 2024).
- ³⁸⁴R. Bhan, R. Saxena, C. Jalwani, and S. Lomash, "Uncooled infrared microbolometer arrays and their characterisation techniques," *Def. Sci. J.* **59**, 580 (2009).
- ³⁸⁵M. E. Itkis, F. Borondics, A. Yu, and R. C. Haddon, "Thermal conductivity measurements of semitransparent single-walled carbon nanotube films by a bolometric technique," *Nano Lett.* **7**, 900–904 (2007).
- ³⁸⁶C. Chiritescu, D. G. Cahill, N. Nguyen, D. Johnson, A. Bodapati, P. Kebbinski, and P. Zschack, "Ultralow thermal conductivity in disordered, layered WSe₂ crystals," *Science* **315**, 351–353 (2007).
- ³⁸⁷M. N. Luckyanova, J. Garg, K. Esfarjani, A. Jandl, M. T. Balsara, A. J. Schmidt, A. J. Minnich, S. Chen, M. S. Dresselhaus, Z. Ren *et al.*, "Coherent phonon heat conduction in superlattices," *Science* **338**, 936–939 (2012).
- ³⁸⁸A. J. Schmidt, K. C. Collins, A. J. Minnich, and G. Chen, "Thermal conductance and phonon transmissivity of metal-graphite interfaces," *J. Appl. Phys.* **107**, 104907 (2010).
- ³⁸⁹R. Prasher, "Thermal boundary resistance and thermal conductivity of multi-walled carbon nanotubes," *Phys. Rev. B* **77**, 075424 (2008).
- ³⁹⁰Z. Chen, W. Jang, W. Bao, C. Lau, and C. Dames, "Thermal contact resistance between graphene and silicon dioxide," *Appl. Phys. Lett.* **95**, 161910 (2009).
- ³⁹¹Y. Zhou, H. Jang, J. M. Woods, Y. Xie, P. Kumaravadivel, G. A. Pan, J. Liu, Y. Liu, D. G. Cahill, and J. J. Cha, "Direct synthesis of large-scale WTe₂ thin films with low thermal conductivity," *Adv. Funct. Mater.* **27**, 1605928 (2017).
- ³⁹²H. Jang, C. R. Ryder, J. D. Wood, M. C. Hersam, and D. G. Cahill, "3D anisotropic thermal conductivity of exfoliated rhenium disulfide," *Adv. Mater.* **29**, 1700650 (2017).
- ³⁹³A. Sood, F. Xiong, S. Chen, R. Cheaito, F. Lian, M. Asheghi, Y. Cui, D. Donadio, K. E. Goodson, and E. Pop, "Quasi-ballistic thermal transport across MoS₂ thin films," *Nano Lett.* **19**, 2434–2442 (2019).
- ³⁹⁴J. Liu, G.-M. Choi, and D. G. Cahill, "Measurement of the anisotropic thermal conductivity of molybdenum disulfide by the time-resolved magneto-optic kerr effect," *J. Appl. Phys.* **116**, 233107 (2014).
- ³⁹⁵C. Muratore, V. Varshney, J. J. Gengler, J. Hu, J. E. Bultman, T. M. Smith, P. J. Shamberger, B. Qiu, X. Ruan, A. K. Roy *et al.*, "Cross-plane thermal properties of transition metal dichalcogenides," *Appl. Phys. Lett.* **102**, 081604 (2013).
- ³⁹⁶D. O. Lindroth and P. Erhart, "Thermal transport in van der Waals solids from first-principles calculations," *Phys. Rev. B* **94**, 115205 (2016).
- ³⁹⁷A. Sood, F. Xiong, S. Chen, H. Wang, D. Selli, J. Zhang, C. J. McClellan, J. Sun, D. Donadio, Y. Cui *et al.*, "An electrochemical thermal transistor," *Nat. Commun.* **9**, 4510 (2018).
- ³⁹⁸S. Kong, T. Wu, M. Yuan, Z. Huang, Q.-L. Meng, Q. Jiang, W. Zhuang, P. Jiang, and X. Bao, "Dramatically enhanced thermoelectric performance of MoS₂ by introducing MoO₂ nanoinclusions," *J. Mater. Chem. A* **5**, 2004–2011 (2017).
- ³⁹⁹E. Chavez-Angel, P. Tsipas, P. Xiao, M. T. Ahmadi, A. H. Daaoub, H. Sadeghi, C. M. Sotomayor Torres, A. Dimoulas, and A. E. Sachat, "Engineering heat transport across epitaxial lattice-mismatched van der Waals heterointerfaces," *Nano Lett.* **23**, 6883–6891 (2023).
- ⁴⁰⁰L. Paulatto, D. Fournier, M. Marangolo, M. Eddrief, P. Atkinson, and M. Calandra, "Thermal conductivity of Bi₂Se₃ from bulk to thin films: Theory and experiment," *Phys. Rev. B* **101**, 205419 (2020).
- ⁴⁰¹Y. K. Koh, M.-H. Bae, D. G. Cahill, and E. Pop, "Heat conduction across monolayer and few-layer graphenes," *Nano Lett.* **10**, 4363–4368 (2010).
- ⁴⁰²A. Sood, C. Sievers, Y. C. Shin, V. Chen, S. Chen, K. K. Smithe, S. Chatterjee, D. Donadio, K. E. Goodson, and E. Pop, "Engineering thermal transport across layered graphene–MoS₂ superlattices," *ACS Nano* **15**, 19503–19512 (2021).
- ⁴⁰³A. El Sachat, P. Xiao, D. Donadio, F. Bonell, M. Sledzinska, A. Marty, C. Vergnaud, H. Boukari, M. Jamet, G. Arregui *et al.*, "Effect of crystallinity and thickness on thermal transport in layered PtSe₂," *npj 2D Mater. Appl.* **6**, 32 (2022).
- ⁴⁰⁴P. Xiao, E. Chavez-Angel, S. Chaitoglou, M. Sledzinska, A. Dimoulas, C. M. Sotomayor Torres, and A. El Sachat, "Anisotropic thermal conductivity of crystalline layered SnSe₂," *Nano Lett.* **21**, 9172–9179 (2021).
- ⁴⁰⁵Y. K. Koh, Y. Cao, D. G. Cahill, and D. Jena, "Heat-transport mechanisms in superlattices," *Adv. Funct. Mater.* **19**, 610–615 (2009).
- ⁴⁰⁶R. Cheaito, J. C. Duda, T. E. Beechem, K. Hattar, J. F. Ihlefeld, D. L. Medlin, M. A. Rodriguez, M. J. Campion, E. S. Piekos, and P. E. Hopkins, "Experimental investigation of size effects on the thermal conductivity of silicon-germanium alloy thin films," *Phys. Rev. Lett.* **109**, 195901 (2012).
- ⁴⁰⁷Y. Chalopin, K. Esfarjani, A. Henry, S. Volz, and G. Chen, "Thermal interface conductance in Si/Ge superlattices by equilibrium molecular dynamics," *Phys. Rev. B* **85**, 195302 (2012).
- ⁴⁰⁸B. Zink and F. Hellman, "Specific heat and thermal conductivity of low-stress amorphous Si–N membranes," *Solid State Commun.* **129**, 199–204 (2004).
- ⁴⁰⁹R. Sultan, A. Avery, G. Stiehl, and B. Zink, "Thermal conductivity of micro-machined low-stress silicon-nitride beams from 77 to 325 K," *J. Appl. Phys.* **105**, 043501 (2009).
- ⁴¹⁰R. Sultan, A. Avery, J. Underwood, S. Mason, D. Bassett, and B. Zink, "Heat transport by long mean free path vibrations in amorphous silicon nitride near room temperature," *Phys. Rev. B* **87**, 214305 (2013).
- ⁴¹¹J. Kim, E. Fleming, Y. Zhou, and L. Shi, "Comparison of four-probe thermal and thermoelectric transport measurements of thin films and nanostructures with microfabricated electro-thermal transducers," *J. Phys. D: Appl. Phys.* **51**, 103002 (2018).
- ⁴¹²I. Jo, M. T. Pettes, E. Ou, W. Wu, and L. Shi, "Basal-plane thermal conductivity of few-layer molybdenum disulfide," *Appl. Phys. Lett.* **104**, 201902 (2014).
- ⁴¹³C. Wang, J. Guo, L. Dong, A. Aiyiti, X. Xu, and B. Li, "Superior thermal conductivity in suspended bilayer hexagonal boron nitride," *Sci. Rep.* **6**, 1–6 (2016).
- ⁴¹⁴S. Lee, F. Yang, J. Suh, S. Yang, Y. Lee, G. Li, H. Sung Choe, A. Suslu, Y. Chen, C. Ko *et al.*, "Anisotropic in-plane thermal conductivity of black phosphorus nanoribbons at temperatures higher than 100 K," *Nat. Commun.* **6**, 1–7 (2015).
- ⁴¹⁵M. T. Pettes, J. Maassen, I. Jo, M. S. Lundstrom, and L. Shi, "Effects of surface band bending and scattering on thermoelectric transport in suspended bismuth telluride nanoplates," *Nano Lett.* **13**, 5316–5322 (2013).
- ⁴¹⁶L. Yang, Y. Tao, Y. Zhu, M. Akter, K. Wang, Z. Pan, Y. Zhao, Q. Zhang, Y.-Q. Xu, R. Chen *et al.*, "Observation of superdiffusive phonon transport in aligned atomic chains," *Nat. Nanotechnol.* **16**, 764–768 (2021).
- ⁴¹⁷H. Wang, W. Chu, and G. Chen, "A brief review on measuring methods of thermal conductivity of organic and hybrid thermoelectric materials," *Adv. Electr. Mater.* **5**, 1900167 (2019).
- ⁴¹⁸M. C. Wingert, Z. C. Chen, E. Dechaumphai, J. Moon, J.-H. Kim, J. Xiang, and R. Chen, "Thermal conductivity of Ge and Ge-Si core-shell nanowires in the phonon confinement regime," *Nano Lett.* **11**, 5507–5513 (2011).
- ⁴¹⁹S. Alaie, D. F. Goettler, K. Abbas, M. F. Su, C. M. Reinke, I. El-Kady, and Z. C. Leseman, "Microfabricated suspended island platform for the measurement of

- in-plane thermal conductivity of thin films and nanostructured materials with consideration of contact resistance," *Rev. Sci. Instrum.* **84**, 105003 (2013).
- ⁴²⁰A. Mavrokefalos, M. T. Pettes, F. Zhou, and L. Shi, "Four-probe measurements of the in-plane thermoelectric properties of nanofilms," *Rev. Sci. Instrum.* **78**, 034901 (2007).
- ⁴²¹Y. Liu, M. Zhang, A. Ji, F. Yang, and X. Wang, "Measuring methods for thermoelectric properties of one-dimensional nanostructural materials," *RSC Adv.* **6**, 48933–48961 (2016).
- ⁴²²A. Weathers, K. Bi, M. T. Pettes, and L. Shi, "Reexamination of thermal transport measurements of a low-thermal conductance nanowire with a suspended micro-device," *Rev. Sci. Instrum.* **84**, 084903 (2013).
- ⁴²³L. Yang, Y. Tao, J. Liu, C. Liu, Q. Zhang, M. Akter, Y. Zhao, T. T. Xu, Y. Xu, Z. Mao *et al.*, "Distinct signatures of electron-phonon coupling observed in the lattice thermal conductivity of NbSe₃ nanowires," *Nano Lett.* **19**, 415–421 (2019).
- ⁴²⁴C. Chen, Y. Shi, Y. S. Zhang, J. Zhu, and Y. Yan, "Size dependence of young's modulus in ZnO nanowires," *Phys. Rev. Lett.* **96**, 075505 (2006).
- ⁴²⁵S. Cuenot, C. Fréaigny, S. Demoustier-Champagne, and B. Nysten, "Surface tension effect on the mechanical properties of nanomaterials measured by atomic force microscopy," *Phys. Rev. B* **69**, 165410 (2004).
- ⁴²⁶J. S. Kang, M. Li, H. Wu, H. Nguyen, and Y. Hu, "Experimental observation of high thermal conductivity in boron arsenide," *Science* **361**, 575–578 (2018).
- ⁴²⁷J. Wang, L. Zhu, J. Chen, B. Li, and J. Thong, "Suppressing thermal conductivity of suspended tri-layer graphene by gold deposition," *Adv. Mater.* **25**, 6884–6888 (2013).
- ⁴²⁸I. Jo, M. T. Pettes, L. Lindsay, E. Ou, A. Weathers, A. L. Moore, Z. Yao, and L. Shi, "Reexamination of basal plane thermal conductivity of suspended graphene samples measured by electro-thermal micro-bridge methods," *AIP Adv.* **5**, 053206 (2015).
- ⁴²⁹M. Yarali, X. Wu, T. Gupta, D. Ghoshal, L. Xie, Z. Zhu, H. Brahmi, J. Bao, S. Chen, T. Luo *et al.*, "Effects of defects on the temperature-dependent thermal conductivity of suspended monolayer molybdenum disulfide grown by chemical vapor deposition," *Adv. Funct. Mater.* **27**, 1704357 (2017).
- ⁴³⁰J. H. Seol, I. Jo, A. L. Moore, L. Lindsay, Z. H. Aitken, M. T. Pettes, X. Li, Z. Yao, R. Huang, D. Broido *et al.*, "Two-dimensional phonon transport in supported graphene," *Science* **328**, 213–216 (2010).
- ⁴³¹M. T. Pettes, I. Jo, Z. Yao, and L. Shi, "Influence of polymeric residue on the thermal conductivity of suspended bilayer graphene," *Nano Lett.* **11**, 1195–1200 (2011).
- ⁴³²L. Lindsay, D. Broido, and N. Mingo, "Flexural phonons and thermal transport in graphene," *Phys. Rev. B* **82**, 115427 (2010).
- ⁴³³S. Ghosh, W. Bao, D. L. Nika, S. Subrina, E. P. Pokatilov, C. N. Lau, and A. A. Balandin, "Dimensional crossover of thermal transport in few-layer graphene," *Nat. Mater.* **9**, 555–558 (2010).
- ⁴³⁴M. Yarali, H. Brahmi, Z. Yan, X. Li, L. Xie, S. Chen, S. Kumar, M. Yoon, K. Xiao, and A. Mavrokefalos, "Effect of metal doping and vacancies on the thermal conductivity of monolayer molybdenum diselenide," *ACS Appl. Mater. Interfaces* **10**, 4921–4928 (2018).
- ⁴³⁵C. Yu, S. Saha, J. Zhou, L. Shi, A. M. Cassell, B. A. Cruden, Q. Ngo, and J. Li, "Thermal contact resistance and thermal conductivity of a carbon nanofiber," *J. Heat Transfer* **128**, 234–239 (2006).
- ⁴³⁶I. Jo, M. T. Pettes, J. Kim, K. Watanabe, T. Taniguchi, Z. Yao, and L. Shi, "Thermal conductivity and phonon transport in suspended few-layer hexagonal boron nitride," *Nano Lett.* **13**, 550–554 (2013).
- ⁴³⁷M. M. Sadeghi, I. Jo, and L. Shi, "Phonon-interface scattering in multilayer graphene on an amorphous support," *Proc. Natl. Acad. Sci. U. S. A.* **110**, 16321–16326 (2013).
- ⁴³⁸A. Pope, B. Zawilski, and T. Tritt, "Description of removable sample mount apparatus for rapid thermal conductivity measurements," *Cryogenics* **41**, 725–731 (2001).
- ⁴³⁹G. Jaffe, S. Mei, C. Boyle, J. Kirch, D. Savage, D. Botez, L. Mawst, I. Knezevic, M. Lagally, and M. Eriksson, "Measurements of the thermal resistivity of InAlAs, InGaAs, and InAlAs/InGaAs superlattices," *ACS Appl. Mater. Interfaces* **11**, 11970–11975 (2019).
- ⁴⁴⁰G. R. Jaffe, V. W. Brar, M. G. Lagally, and M. A. Eriksson, "A simple numerical method for evaluating heat dissipation from curved wires with periodic applied heating," *Appl. Phys. Lett.* **119**, 163501 (2021).
- ⁴⁴¹G. R. Jaffe, K. J. Smith, K. Watanabe, T. Taniguchi, M. G. Lagally, M. A. Eriksson, and V. W. Brar, "Thickness-dependent cross-plane thermal conductivity measurements of exfoliated hexagonal boron nitride," *ACS Appl. Mater. Interfaces* **15**, 12545–12550 (2023).
- ⁴⁴²C. J. Glassbrenner and G. A. Slack, "Thermal conductivity of silicon and germanium from 3 K to the melting point," *Phys. Rev.* **134**, A1058 (1964).
- ⁴⁴³P. Jiang, X. Qian, R. Yang, and L. Lindsay, "Anisotropic thermal transport in bulk hexagonal boron nitride," *Phys. Rev. Mater.* **2**, 064005 (2018).
- ⁴⁴⁴A. Simpson and A. Stuckes, "The thermal conductivity of highly oriented pyrolytic boron nitride," *J. Phys. C: Solid State Phys.* **4**, 1710 (1971).
- ⁴⁴⁵H. Zhang, X. Chen, Y.-D. Jho, and A. J. Minnich, "Temperature-dependent mean free path spectra of thermal phonons along the c-axis of graphite," *Nano Lett.* **16**, 1643–1649 (2016).
- ⁴⁴⁶W. Ouyang, H. Qin, M. Urbakh, and O. Hod, "Controllable thermal conductivity in twisted homogeneous interfaces of graphene and hexagonal boron nitride," *Nano Lett.* **20**, 7513–7518 (2020).
- ⁴⁴⁷A. I. Hochbaum, R. Chen, R. D. Delgado, W. Liang, E. C. Garnett, M. Najarian, A. Majumdar, and P. Yang, "Enhanced thermoelectric performance of rough silicon nanowires," *Nature* **451**, 163–167 (2008).
- ⁴⁴⁸J. M. Ziman, *Electrons and Phonons: The Theory of Transport Phenomena in Solids* (Oxford University Press, 2001).
- ⁴⁴⁹J. Zou, X. Lange, and C. Richardson, "Lattice thermal conductivity of nanoscale AlN/GaN/AlN heterostructures: Effects of partial phonon spatial confinement," *J. Appl. Phys.* **100**, 104309 (2006).
- ⁴⁵⁰P.-C. Hsu, X. Liu, C. Liu, X. Xie, H. R. Lee, A. J. Welch, T. Zhao, and Y. Cui, "Personal thermal management by metallic nanowire-coated textile," *Nano Lett.* **15**, 365–371 (2015).
- ⁴⁵¹J. P. Heremans, M. S. Dresselhaus, L. E. Bell, and D. T. Morelli, "When thermoelectrics reached the nanoscale," *Nat. Nanotechnol.* **8**, 471–473 (2013).
- ⁴⁵²Y. Gao, A. Marconnet, M. Panzer, S. LeBlanc, S. Dogbe, Y. Ezzahri, A. Shakouri, and K. Goodson, "Nanostructured interfaces for thermoelectrics," *J. Electr. Mater.* **39**, 1456–1462 (2010).
- ⁴⁵³Q.-Y. Li, K. Takahashi, H. Ago, X. Zhang, T. Ikuta, T. Nishiyama, and K. Kawahara, "Temperature dependent thermal conductivity of a suspended sub-micron graphene ribbon," *J. Appl. Phys.* **117**, 065102 (2015).
- ⁴⁵⁴Q.-Y. Li, T. Feng, W. Okita, Y. Komori, H. Suzuki, T. Kato, T. Kaneko, T. Ikuta, X. Ruan, and K. Takahashi, "Enhanced thermoelectric performance of as-grown suspended graphene nanoribbons," *ACS Nano* **13**, 9182–9189 (2019).
- ⁴⁵⁵R. Abe, Y. Sekimoto, S. Saini, K. Miyazaki, Q. Li, D. Li, K. Takahashi, T. Yagi, and M. Nakamura, "Round robin study on the thermal conductivity/diffusivity of a gold wire with a diameter of 30 μm tested via five measurement methods," *J. Therm. Sci.* **31**, 1037–1051 (2022).
- ⁴⁵⁶D. L. Nika, A. S. Askerov, and A. A. Balandin, "Anomalous size dependence of the thermal conductivity of graphene ribbons," *Nano Lett.* **12**, 3238–3244 (2012).
- ⁴⁵⁷L. Lu, W. Yi, and D. Zhang, "3 ω method for specific heat and thermal conductivity measurements," *Rev. Sci. Instrum.* **72**, 2996–3003 (2001).
- ⁴⁵⁸Q. Hao, D. Xu, H. Zhao, Y. Xiao, and F. J. Medina, "Thermal studies of nanoporous Si films with pitches on the order of 100 nm—Comparison between different pore-drilling techniques," *Sci. Rep.* **8**, 9056 (2018).
- ⁴⁵⁹Z. L. Wang, D. W. Tang, X. B. Li, X. H. Zheng, W. G. Zhang, L. X. Zheng, Y. T. Zhu, A. Z. Jin, H. F. Yang, and C. Z. Gu, "Length-dependent thermal conductivity of an individual single-wall carbon nanotube," *Appl. Phys. Lett.* **91**, 123119 (2007).
- ⁴⁶⁰F. Zhuge, T. Takahashi, M. Kanai, K. Nagashima, N. Fukata, K. Uchida, and T. Yanagida, "Thermal conductivity of si nanowires with δ -modulated dopant distribution by self-heated 3 ω method and its length dependence," *J. Appl. Phys.* **124**, 065105 (2018).
- ⁴⁶¹S. W. Finefrock, Y. Wang, J. B. Ferguson, J. V. Ward, H. Fang, J. E. Pfluger, D. S. Dudis, X. Ruan, and Y. Wu, "Measurement of thermal conductivity of pbte nanocrystal coated glass fibers by the 3 ω method," *Nano Lett.* **13**, 5006–5012 (2013).
- ⁴⁶²D. Li, Y. Wu, P. Kim, L. Shi, P. Yang, and A. Majumdar, "Thermal conductivity of individual silicon nanowires," *Appl. Phys. Lett.* **83**, 2934–2936 (2003).

- ⁴⁶³R. Chen, A. I. Hochbaum, P. Murphy, J. Moore, P. Yang, and A. Majumdar, "Thermal conductance of thin silicon nanowires," *Phys. Rev. Lett.* **101**, 105501 (2008).
- ⁴⁶⁴A. A. Balandin, "Phonon engineering in graphene and van der waals materials," *MRS Bull.* **39**, 817–823 (2014).
- ⁴⁶⁵J. B. Hertzberg, M. Aksit, O. O. Otelaja, D. A. Stewart, and R. D. Robinson, "Direct measurements of surface scattering in Si nanosheets using a micro-scale phonon spectrometer: Implications for Casimir-limit predicted by Ziman theory," *Nano Lett.* **14**, 403–415 (2014).
- ⁴⁶⁶C. Dames and G. Chen, "Theoretical phonon thermal conductivity of Si/Ge superlattice nanowires," *J. Appl. Phys.* **95**, 682–693 (2004).
- ⁴⁶⁷F. Yang and C. Dames, "Mean free path spectra as a tool to understand thermal conductivity in bulk and nanostructures," *Phys. Rev. B* **87**, 035437 (2013).
- ⁴⁶⁸S. Neogi, J. S. Reparaz, L. F. C. Pereira, B. Graczykowski, M. R. Wagner, M. Sledzinska, A. Shchepetov, M. Prunnila, J. Ahopelto, C. M. Sotomayor-Torres *et al.*, "Tuning thermal transport in ultrathin silicon membranes by surface nanoscale engineering," *ACS Nano* **9**, 3820–3828 (2015).
- ⁴⁶⁹P. Martin, Z. Aksamija, E. Pop, and U. Ravaioli, "Impact of phonon-surface roughness scattering on thermal conductivity of thin Si nanowires," *Phys. Rev. Lett.* **102**, 125503 (2009).
- ⁴⁷⁰Y. He and G. Galli, "Microscopic origin of the reduced thermal conductivity of silicon nanowires," *Phys. Rev. Lett.* **108**, 215901 (2012).
- ⁴⁷¹A. J. Minnich, J. A. Johnson, A. J. Schmidt, K. Esfarnani, M. S. Dresselhaus, K. A. Nelson, and G. Chen, "Thermal conductivity spectroscopy technique to measure phonon mean free paths," *Phys. Rev. Lett.* **107**, 095901 (2011).
- ⁴⁷²S. N. Raja, R. Rhyner, K. Vuttivarakulchai, M. Luisier, and D. Poulikakos, "Length scale of diffusive phonon transport in suspended thin silicon nanowires," *Nano Lett.* **17**, 276–283 (2017).
- ⁴⁷³Y. Zhao, L. Yang, L. Kong, M. H. Nai, D. Liu, J. Wu, Y. Liu, S. Y. Chiam, W. K. Chim, C. T. Lim *et al.*, "Ultralow thermal conductivity of single-crystalline porous silicon nanowires," *Adv. Funct. Mater.* **27**, 1702824 (2017).
- ⁴⁷⁴A. Aiyiti, X. Bai, J. Wu, X. Xu, and B. Li, "Measuring the thermal conductivity and interfacial thermal resistance of suspended MoS_2 using electron beam self-heating technique," *Sci. Bull.* **63**, 452–458 (2018).
- ⁴⁷⁵X. Wei, Y. Wang, Y. Shen, G. Xie, H. Xiao, J. Zhong, and G. Zhang, "Phonon thermal conductivity of monolayer MoS_2 : A comparison with single layer graphene," *Appl. Phys. Lett.* **105**, 103902 (2014).
- ⁴⁷⁶Y. Cai, J. Lan, G. Zhang, and Y.-W. Zhang, "Lattice vibrational modes and phonon thermal conductivity of monolayer MoS_2 ," *Phys. Rev. B* **89**, 035438 (2014).
- ⁴⁷⁷S. Sahoo, A. P. Gaur, M. Ahmadi, M. J.-F. Guinel, and R. S. Katiyar, "Temperature-dependent raman studies and thermal conductivity of few-layer MoS_2 ," *J. Phys. Chem. C* **117**, 9042–9047 (2013).
- ⁴⁷⁸X. Gu, B. Li, and R. Yang, "Layer thickness-dependent phonon properties and thermal conductivity of MoS_2 ," *J. Appl. Phys.* **119**, 085106 (2016).
- ⁴⁷⁹X. Zhang, D. Sun, Y. Li, G.-H. Lee, X. Cui, D. Chenet, Y. You, T. F. Heinz, and J. C. Hone, "Measurement of lateral and interfacial thermal conductivity of single- and bilayer MoS_2 and MoSe_2 using refined optothermal Raman technique," *ACS Appl. Mater. Interfaces* **7**, 25923–25929 (2015).
- ⁴⁸⁰A. Majumdar, "Microscale heat conduction in dielectric thin films," *J. Heat Transfer* **115**, 7–16 (1993).
- ⁴⁸¹A. El Sachat, F. Alzina, C. M. Sotomayor Torres, and E. Chavez-Angel, "Heat transport control and thermal characterization of low-dimensional materials: A review," *Nanomaterials* **11**, 175 (2021).
- ⁴⁸²W. Yi, L. Lu, Z. Dian-Lin, Z. Pan, and S. Xie, "Linear specific heat of carbon nanotubes," *Phys. Rev. B* **59**, R9015 (1999).
- ⁴⁸³B. T. Kelly, *Physics of Graphite* (Applied Science Publishers, London, 1981).
- ⁴⁸⁴A. Majumdar, "Scanning thermal microscopy," *Annu. Rev. Mater. Sci.* **29**, 505–585 (1999).
- ⁴⁸⁵S. Gomès, A. Assy, and P.-O. Chapuis, "Scanning thermal microscopy: A review," *Phys. Status Solidi A* **212**, 477–494 (2015).
- ⁴⁸⁶C. Williams and H. Wickramasinghe, "Scanning thermal profiler," *Microelectron. Eng.* **5**, 509–513 (1986).
- ⁴⁸⁷M. Das, D. P. Ura, P. K. Szewczyk, K. Berniak, J. Knapczyk-Korczak, M. M. Marzec, W. Pichór, and U. Stachewicz, "Thermal energy storage performance of liquid polyethylene glycol in core-shell polycarbonate and reduced graphene oxide fibers," *Adv. Compos. Hybrid Mater.* **7**, 123 (2024).
- ⁴⁸⁸B. Cretin, S. Gomes, N. Trannoy, and P. Vairac, "Scanning thermal microscopy," in *Microscale and Nanoscale Heat Transfer*, Topics in Applied Physics Vol. 107, edited by S. Volz (Springer, 2006), pp. 181–238.
- ⁴⁸⁹C.-C. Teng, C.-C. M. Ma, C.-H. Lu, S.-Y. Yang, S.-H. Lee, M.-C. Hsiao, M.-Y. Yen, K.-C. Chiou, and T.-M. Lee, "Thermal conductivity and structure of non-covalent functionalized graphene/epoxy composites," *Carbon* **49**, 5107–5116 (2011).
- ⁴⁹⁰F. Koönemann, M. Vollmann, T. Wagner, N. Mohd Ghazali, T. Yamaguchi, A. Stemmer, K. Ishibashi, and B. Gotsmann, "Thermal conductivity of a supported multiwalled carbon nanotube," *J. Phys. Chem. C* **123**, 12460–12465 (2019).
- ⁴⁹¹I. Rangelow, T. Gotszalk, P. Grabiec, K. Edinger, and N. Abedinov, "Thermal nano-probe," *Microelectron. Eng.* **57–58**, 737–748 (2001).
- ⁴⁹²Y. Zhang, W. Zhu, F. Hui, M. Lanza, T. Borca-Tasciuc, and M. Muñoz Rojo, "A review on principles and applications of scanning thermal microscopy (STHM)," *Adv. Funct. Mater.* **30**, 1900892 (2020).
- ⁴⁹³F. Menges, H. Riel, A. Stemmer, and B. Gotsmann, "Nanoscale thermometry by scanning thermal microscopy," *Rev. Sci. Instrum.* **87**, 074902 (2016).
- ⁴⁹⁴A. E. Aliev, M. H. Lima, E. M. Silverman, and R. H. Baughman, "Thermal conductivity of multi-walled carbon nanotube sheets: Radiation losses and quenching of phonon modes," *Nanotechnology* **21**, 035709 (2010).
- ⁴⁹⁵M. Fujii, X. Zhang, H. Xie, H. Ago, K. Takahashi, T. Ikuta, H. Abe, and T. Shimizu, "Measuring the thermal conductivity of a single carbon nanotube," *Phys. Rev. Lett.* **95**, 065502 (2005).
- ⁴⁹⁶G. B. M. Fiege, A. Altes, R. Heiderhoff, and L. J. Balk, "Quantitative thermal conductivity measurements with nanometre resolution," *J. Phys. D: Appl. Phys.* **32**, L13 (1999).
- ⁴⁹⁷S. Lefèvre, J.-B. Saulnier, C. Fuentes, and S. Volz, "Probe calibration of the scanning thermal microscope in the AC mode," *Superlattices Microstruct.* **35**, 283–288 (2004).
- ⁴⁹⁸F. Depasse, P. Grossel, and S. Gomes, "Theoretical investigations of dc and ac heat diffusion for submicroscopies and nanoscopies," *J. Phys. D: Appl. Phys.* **36**, 204 (2003).
- ⁴⁹⁹F. Depasse, P. Grossel, and N. Trannoy, "Probe temperature and output voltage calculation for the sthm in AC mode," *Superlattices Microstruct.* **35**, 269–282 (2004).
- ⁵⁰⁰G. Hwang, J. Chung, and O. Kwon, "Enabling low-noise null-point scanning thermal microscopy by the optimization of scanning thermal microscope probe through a rigorous theory of quantitative measurement," *Rev. Sci. Instrum.* **85**, 114901 (2014).
- ⁵⁰¹G. Hwang and O. Kwon, "Measuring the size dependence of thermal conductivity of suspended graphene disks using null-point scanning thermal microscopy," *Nanoscale* **8**, 5280–5290 (2016).
- ⁵⁰²R. Swami, G. Julié, S. Le-Denmat, G. Pernot, D. Singhal, J. Paterson, J. Maire, J. Motte, N. Paillet, H. Guillou *et al.*, "Experimental setup for thermal measurements at the nanoscale using a STHM probe with niobium nitride thermometer," *Rev. Sci. Instrum.* **95**, 054904 (2024).
- ⁵⁰³J. Duvigneau, H. Schonherr, and G. J. Vancso, "Nanoscale thermal AFM of polymers: Transient heat flow effects," *ACS Nano* **4**, 6932–6940 (2010).
- ⁵⁰⁴M. Muñoz Rojo, S. Grauby, J.-M. Rampnoux, O. Caballero-Calero, M. Martín-González, and S. Dilhaise, "Fabrication of Bi_2Te_3 nanowire arrays and thermal conductivity measurement by 3ω -scanning thermal microscopy," *J. Appl. Phys.* **113**, 054308 (2013).
- ⁵⁰⁵K. Luo, Z. Shi, J. Lai, and A. Majumdar, "Nanofabrication of sensors on cantilever probe tips for scanning multiprobe microscopy," *Appl. Phys. Lett.* **68**, 325–327 (1996).
- ⁵⁰⁶K. Kim, W. Jeong, W. Lee, and P. Reddy, "Ultra-high vacuum scanning thermal microscopy for nanometer resolution quantitative thermometry," *ACS Nano* **6**, 4248–4257 (2012).
- ⁵⁰⁷F. Menges, H. Riel, A. Stemmer, and B. Gotsmann, "Quantitative thermometry of nanoscale hot spots," *Nano Lett.* **12**, 596–601 (2012).
- ⁵⁰⁸L. Shi and A. Majumdar, "Thermal transport mechanisms at nanoscale point contacts," *J. Heat Transfer* **124**, 329–337 (2002).
- ⁵⁰⁹S. Gomès, N. Trannoy, and P. Grossel, "Dc thermal microscopy: Study of the thermal exchange between a probe and a sample," *Meas. Sci. Technol.* **10**, 805 (1999).

- ⁵¹⁰U. F. Wischnath, J. Welker, M. Munzel, and A. Kittel, "The near-field scanning thermal microscope," *Rev. Sci. Instrum.* **79**, 073708 (2008).
- ⁵¹¹M. E. McConney, D. D. Kulkarni, H. Jiang, T. J. Bunning, and V. V. Tsukruk, "A new twist on scanning thermal microscopy," *Nano Lett.* **12**, 1218–1223 (2012).
- ⁵¹²P. D. Tovee and O. V. Kolosov, "Mapping nanoscale thermal transfer in-liquid environment—Immersion scanning thermal microscopy," *Nanotechnology* **24**, 465706 (2013).
- ⁵¹³N. Fleurence, S. Demeyer, A. Allard, S. Douri, and B. Hay, "Quantitative measurement of thermal conductivity by STHM technique: Measurements, calibration protocols and uncertainty evaluation," *Nanomaterials* **13**, 2424 (2023).
- ⁵¹⁴J. Martinek, P. Klapetek, and A. C. Campbell, "Methods for topography artifacts compensation in scanning thermal microscopy," *Ultramicroscopy* **155**, 55–61 (2015).
- ⁵¹⁵R. S. Prasher and P. E. Phelan, "Microscopic and macroscopic thermal contact resistances of pressed mechanical contacts," *J. Appl. Phys.* **100**, 063538 (2006).
- ⁵¹⁶D. Zhang, K. Ryu, X. Liu, E. Polikarpov, J. Ly, M. E. Tompson, and C. Zhou, "Transparent, conductive, and flexible carbon nanotube films and their application in organic light-emitting diodes," *Nano Lett.* **6**, 1880–1886 (2006).
- ⁵¹⁷X. Cui, C. Miao, S. Lu, X. Liu, Y. Yang, and J. Sun, "Strain sensors made of MXene, CNTs, and TPU/PSF asymmetric structure films with large tensile recovery and applied in human health monitoring," *ACS Appl. Mater. Interfaces* **15**, 59655–59670 (2023).
- ⁵¹⁸A. Hussain, K. Murashko, A. P. Tsapenko, E.-X. Ding, E. I. Kauppinen, and A. Lähde, "Single-step fabrication of iron single-walled carbon nanotube film from ferrocene as a conductive-electrocatalyst interlayer in lithium-sulfur batteries," *J. Phys. Chem. C* **127**, 23577–23585 (2023).
- ⁵¹⁹L. Zhang, H. Shang, Q. Zou, C. Feng, H. Gu, and F. Ding, "n-type PVP/ SWCNT composite films with improved stability for thermoelectric power generation," *ACS Appl. Mater. Interfaces* **16**, 6025–6032 (2024).
- ⁵²⁰K. Okada, T. Horii, Y. Yamaguchi, K. Son, N. Hosoya, S. Maeda, and T. Fujie, "Ultraconformable capacitive strain sensor utilizing network structure of single-walled carbon nanotubes for wireless body sensing," *ACS Appl. Mater. Interfaces* **16**, 10427–10438 (2024).
- ⁵²¹C. Yu, L. Shi, Z. Yao, D. Li, and A. Majumdar, "Thermal conductance and thermopower of an individual single-wall carbon nanotube," *Nano Lett.* **5**, 1842–1846 (2005).
- ⁵²²S. O. Kanstad and P.-E. Nordal, "Photoacoustic and photothermal spectroscopy—Novel tools for the analysis of particulate matter," *Powder Technol.* **22**, 133–137 (1979).
- ⁵²³X. Wang, H. Hu, and X. Xu, "Photo-acoustic measurement of thermal conductivity of thin films and bulk materials," *J. Heat Transfer* **123**, 138–144 (2001).
- ⁵²⁴X. Wang, Z. Zhong, and J. Xu, "Noncontact thermal characterization of multi-wall carbon nanotubes," *J. Appl. Phys.* **97**, 064302 (2005).
- ⁵²⁵A. Nadtochiy, O. K. Suwal, D.-S. Kim, and O. Korotchenkov, "Revealing CdSe quantum dots plasmonics confined in Au nanotrenches by thermoacoustic spectroscopy," *ACS Appl. Opt. Mater.* **1**, 1272–1280 (2023).
- ⁵²⁶T.-R. Tseng, C.-H. Yang, H.-C. Lu, C.-P. Liu, and B.-M. Cheng, "Analysis of carbon materials with infrared photoacoustic spectroscopy," *Anal. Chem.* **96**, 10732–10737 (2024).
- ⁵²⁷J. Zhou, S. Xu, and J. Liu, "Review of photothermal technique for thermal measurement of micro-/nanomaterials," *Nanomaterials* **12**, 1884 (2022).
- ⁵²⁸Y. Xu, Y. Zhang, E. Suhir, and X. Wang, "Thermal properties of carbon nanotube array used for integrated circuit cooling," *J. Appl. Phys.* **100**, 074302 (2006).
- ⁵²⁹J. Che, T. Cagin, and W. A. Goddard III, "Thermal conductivity of carbon nanotubes," *Nanotechnology* **11**, 65–69 (2000).
- ⁵³⁰M. A. Osman and D. Srivastava, "Temperature dependence of the thermal conductivity of single-wall carbon nanotubes," *Nanotechnology* **12**, 21–24 (2001).
- ⁵³¹J. D. Mehew, M. Y. Timmermans, D. Saleta Reig, S. Sergeant, M. Sledzinska, E. Chávez-Ángel, E. Gallagher, C. M. Sotomayor Torres, C. Huyghebaert, and K.-J. Tielrooij, "Enhanced thermal conductivity of free-standing double-walled carbon nanotube networks," *ACS Appl. Mater. Interfaces* **15**, 51876–51884 (2023).
- ⁵³²J. Hone, M. Llaguno, N. Nemes, A. Johnson, J. Fischer, D. Walters, M. Casavant, J. Schmidt, and R. Smalley, "Electrical and thermal transport properties of magnetically aligned single wall carbon nanotube films," *Appl. Phys. Lett.* **77**, 666–668 (2000).
- ⁵³³Q. Zhang, G. Chen, S. Yoon, J. Ahn, S. Wang, Q. Zhou, Q. Wang, J. Li *et al.*, "Thermal conductivity of multiwalled carbon nanotubes," *Phys. Rev. B* **66**, 165440 (2002).
- ⁵³⁴S. Xie, W. Li, Z. Pan, B. Chang, and L. Sun, "Mechanical and physical properties on carbon nanotube," *J. Phys. Chem. Solids* **61**, 1153–1158 (2000).
- ⁵³⁵Y. Yue, X. Huang, and X. Wang, "Thermal transport in multiwall carbon nanotube buckypapers," *Phys. Lett. A* **374**, 4144–4151 (2010).
- ⁵³⁶T. Wang, X. Wang, Y. Zhang, L. Liu, L. Xu, Y. Liu, L. Zhang, Z. Luo, and K. Cen, "Effect of zirconium (IV) propoxide concentration on the thermophysical properties of hybrid organic-inorganic films," *J. Appl. Phys.* **104**, 013528 (2008).
- ⁵³⁷B. Rémy, A. Degiovanni, and D. Maillet, "Measurement of the in-plane thermal diffusivity of materials by infrared thermography," *Int. J. Thermophys.* **26**, 493–505 (2005).
- ⁵³⁸A. Salazar, E. Apinaniz, A. Mendioroz, R. Celorio *et al.*, "Simultaneous measurement of thermal diffusivity and optical absorption coefficient using photothermal radiometry. II. Multilayered solids," *J. Appl. Phys.* **110**, 033516 (2011).
- ⁵³⁹E. Apinaniz, A. Mendioroz, A. Salazar *et al.*, "Simultaneous measurement of thermal diffusivity and optical absorption coefficient using photothermal radiometry. I. Homogeneous solids," *J. Appl. Phys.* **110**, 033515 (2011).
- ⁵⁴⁰S. Xu and X. Wang, "Across-plane thermal characterization of films based on amplitude-frequency profile in photothermal technique," *AIP Adv.* **4**, 107122 (2014).
- ⁵⁴¹K. D. Cole and W. McGahan, "Theory of multilayers heated by laser absorption," *J. Heat Transfer* **115**, 767–771 (1993).
- ⁵⁴²H. Machlab, W. A. McGahan, J. A. Woollam, and K. Cole, "Thermal characterization of thin films by photothermally induced laser beam deflection," *Thin Solid Films* **224**, 22–27 (1993).
- ⁵⁴³J. Guo, X. Wang, D. B. Geohegan, and G. Eres, "Thermal characterization of multi-wall carbon nanotube bundles based on pulsed laser-assisted thermal relaxation," *Funct. Mater. Lett.* **01**, 71–76 (2008).
- ⁵⁴⁴J. Guo, X. Wang, D. B. Geohegan, G. Eres, and C. Vincent, "Development of pulsed laser-assisted thermal relaxation technique for thermal characterization of microscale wires," *J. Appl. Phys.* **103**, 113505 (2008).
- ⁵⁴⁵X. Feng, G. Liu, S. Xu, H. Lin, and X. Wang, "3-dimensional anisotropic thermal transport in microscale poly (3-hexylthiophene) thin films," *Polymer* **54**, 1887–1895 (2013).
- ⁵⁴⁶N. Taketoshi, T. Baba, and A. Ono, "Development of a thermal diffusivity measurement system for metal thin films using a picosecond thermoreflectance technique," *Meas. Sci. Technol.* **12**, 2064 (2001).
- ⁵⁴⁷T. Baba, "Analysis of one-dimensional heat diffusion after light pulse heating by the response function method," *Jpn. J. Appl. Phys.* **48**, 05EB04 (2009).
- ⁵⁴⁸T. Baba, N. Taketoshi, and T. Yagi, "Development of ultrafast laser flash methods for measuring thermophysical properties of thin films and boundary thermal resistances," *Jpn. J. Appl. Phys.* **50**, 11RA01 (2011).
- ⁵⁴⁹C.-W. Nan, R. Birringer, D. R. Clarke, and H. Gleiter, "Effective thermal conductivity of particulate composites with interfacial thermal resistance," *J. Appl. Phys.* **81**, 6692–6699 (1997).
- ⁵⁵⁰J. Loureiro, N. Neves, R. Barros, T. Mateus, R. Santos, S. Filonovich, S. Reparaz, C. M. Sotomayor-Torres, F. Wyczisk, L. Divay *et al.*, "Transparent aluminium zinc oxide thin films with enhanced thermoelectric properties," *J. Mater. Chem. A* **2**, 6649–6655 (2014).
- ⁵⁵¹J. Alvarez-Quintana, E. Martínez, E. Pérez-Tijerina, S. Pérez-García, and J. Rodríguez-Viejo, "Temperature dependent thermal conductivity of polycrystalline ZnO films," *J. Appl. Phys.* **107**, 063713 (2010).
- ⁵⁵²N. Vogel-Schäuble, T. Jaeger, Y. E. Romanyuk, S. Populoh, C. Mix, G. Jakob, and A. Weidenkaff, "Thermal conductivity of thermoelectric Al-substituted ZnO thin films," *Phys. Stat. Solidi: Rapid Res. Lett.* **7**, 364–367 (2013).
- ⁵⁵³S. Saini, P. Mele, H. Honda, D. J. Henry, P. E. Hopkins, L. Molina-Luna, K. Matsumoto, K. Miyazaki, and A. Ichinose, "Enhanced thermoelectric performance of Al-doped ZnO thin films on amorphous substrate," *Jpn. J. Appl. Phys.* **53**, 060306 (2014).
- ⁵⁵⁴Y. Xu, M. Goto, R. Kato, Y. Tanaka, and Y. Kagawa, "Thermal conductivity of ZnO thin film produced by reactive sputtering," *J. Appl. Phys.* **111**, 084320 (2012).

- ⁵⁵⁵Z. X. Huang, Z. A. Tang, J. Yu, and S. Bai, "Thermal conductivity of nanoscale polycrystalline ZnO thin films," *Physica B* **406**, 818–823 (2011).
- ⁵⁵⁶J. Wang, M. Shen, Z. Liu, and W. Wang, "MXene materials for advanced thermal management and thermal energy utilization," *Nano Energy* **97**, 107177 (2022).
- ⁵⁵⁷Y. Liu, Y. Wu, and X. Wang, "Thermal transports in the MXenes family: Opportunities and challenges," *Nano Res.* **17**, 7700–7716 (2024).
- ⁵⁵⁸Y. Liu, W. Zou, N. Zhao, and J. Xu, "Electrically insulating PbO/MXene film with superior thermal conductivity, mechanical properties, thermal stability, and flame retardancy," *Nat. Commun.* **14**, 5342 (2023).
- ⁵⁵⁹F. Zhang, Y. Feng, and W. Feng, "Three-dimensional interconnected networks for thermally conductive polymer composites: Design, preparation, properties, and mechanisms," *Mat. Sci. Eng. R* **142**, 100580 (2020).
- ⁵⁶⁰S. Shen, A. Henry, J. Tong, R. Zheng, and G. Chen, "Polyethylene nanofibres with very high thermal conductivities," *Nat. Nanotechnol.* **5**, 251–255 (2010).
- ⁵⁶¹A. Wang, S. Li, X. Zhang, and H. Bao, "Roles of electrons on the thermal transport of 2D metallic MXenes," *Phys. Rev. Mater.* **6**, 014009 (2022).
- ⁵⁶²H. Mianehrow, G. L. Re, F. Carosio, A. Fina, P. T. Larsson, P. Chen, and L. A. Berglund, "Strong reinforcement effects in 2D cellulose nanofibril-graphene oxide (CNF-GO) nanocomposites due to GO-induced CNF ordering," *J. Mater. Chem. A* **8**, 17608–17620 (2020).
- ⁵⁶³R. Kang, Z. Zhang, L. Guo, J. Cui, Y. Chen, X. Hou, B. Wang, C.-T. Lin, N. Jiang, and J. Yu, "Enhanced thermal conductivity of epoxy composites filled with 2D transition metal carbides (MXenes) with ultralow loading," *Sci. Rep.* **9**, 9135 (2019).
- ⁵⁶⁴Q. Chen, Z. Ma, Z. Wang, L. Liu, M. Zhu, W. Lei, and P. Song, "Scalable, robust, low-cost, and highly thermally conductive anisotropic nanocomposite films for safe and efficient thermal management," *Adv. Funct. Mater.* **32**, 2110782 (2022).
- ⁵⁶⁵G. Xin, H. Sun, T. Hu, H. R. Fard, X. Sun, N. Koratkar, T. Borca-Tasciuc, and J. Lian, "Large-area freestanding graphene paper for superior thermal management," *Adv. Mater.* **26**, 4521–4526 (2014).
- ⁵⁶⁶Z. Cheng, Y. R. Koh, H. Ahmad, R. Hu, J. Shi, M. E. Liao, Y. Wang, T. Bai, R. Li, E. Lee *et al.*, "Thermal conductance across harmonic-matched epitaxial Al-sapphire heterointerfaces," *Commun. Phys.* **3**, 115 (2020).
- ⁵⁶⁷Z. Cheng, F. Mu, L. Yates, T. Suga, and S. Graham, "Interfacial thermal conductance across room-temperature-bonded GaN/diamond interfaces for GaN-on-diamond devices," *ACS Appl. Mater. Interfaces* **12**, 8376–8384 (2020).
- ⁵⁶⁸J. T. Gaskins, G. Kotsonis, A. Giri, S. Ju, A. Rohskopf, Y. Wang, T. Bai, E. Sachet, C. T. Shelton, Z. Liu *et al.*, "Thermal boundary conductance across heteroepitaxial ZnO/GaN interfaces: Assessment of the phonon gas model," *Nano Lett.* **18**, 7469–7477 (2018).
- ⁵⁶⁹M. G. Muraleedharan, K. Gordiz, A. Rohskopf, S. T. Wyant, Z. Cheng, S. Graham, and A. Henry, "Understanding phonon transport properties using classical molecular dynamics simulations," *arXiv:2011.01070* (2020).
- ⁵⁷⁰B. Liu, J. A. Baimova, C. D. Reddy, A. W.-K. Law, S. V. Dmitriev, H. Wu, and K. Zhou, "Interfacial thermal conductance of a silicene/graphene bilayer heterostructure and the effect of hydrogenation," *ACS Appl. Mater. Interfaces* **6**, 18180–18188 (2014).
- ⁵⁷¹B. Liu, F. Meng, C. D. Reddy, J. A. Baimova, N. Srikanth, S. V. Dmitriev, and K. Zhou, "Thermal transport in a graphene-MoS₂ bilayer heterostructure: A molecular dynamics study," *RSC Adv.* **5**, 29193–29200 (2015).
- ⁵⁷²T. Feng, H. Zhou, Z. Cheng, L. S. Larkin, and M. R. Neupane, "A critical review of thermal boundary conductance across wide and ultrawide bandgap semiconductor interfaces," *ACS Appl. Mater. Interfaces* **15**, 29655–29673 (2023).
- ⁵⁷³Y. Yue, J. Zhang, Y. Xie, W. Chen, and X. Wang, "Energy coupling across low-dimensional contact interfaces at the atomic scale," *Int. J. Heat Mass Transfer* **110**, 827–844 (2017).
- ⁵⁷⁴S. T. Huxtable, D. G. Cahill, S. Shenogin, L. Xue, R. Ozisik, P. Barone, M. Usrey, M. S. Strano, G. Siddons, M. Shim *et al.*, "Interfacial heat flow in carbon nanotube suspensions," *Nat. Mater.* **2**, 731–734 (2003).
- ⁵⁷⁵C.-W. Nan, G. Liu, Y. Lin, and M. Li, "Interface effect on thermal conductivity of carbon nanotube composites," *Appl. Phys. Lett.* **85**, 3549–3551 (2004).
- ⁵⁷⁶R. S. Prasher, X. Hu, Y. Chalopin, N. Mingo, K. Lofgreen, S. Volz, F. Cleri, and P. Kebinski, "Turning carbon nanotubes from exceptional heat conductors into insulators," *Phys. Rev. Lett.* **102**, 105901 (2009).
- ⁵⁷⁷Y. Chalopin, S. Volz, and N. Mingo, "Upper bound to the thermal conductivity of carbon nanotube pellets," *J. Appl. Phys.* **105**, 084301 (2009).
- ⁵⁷⁸D. Xu, R. Hanus, Y. Xiao, S. Wang, G. J. Snyder, and Q. Hao, "Thermal boundary resistance correlated with strain energy in individual Si film-wafer twist boundaries," *Mater. Today Phys.* **6**, 53–59 (2018).
- ⁵⁷⁹J. Hickman and Y. Mishin, "Thermal conductivity and its relation to atomic structure for symmetrical tilt grain boundaries in silicon," *Phys. Rev. Mater.* **4**, 033405 (2020).
- ⁵⁸⁰J. Cho, Z. Li, E. Bozorg-Grayeli, T. Kodama, D. Francis, F. Ejekam, F. Faili, M. Asheghi, and K. E. Goodson, "Improved thermal interfaces of GaN-diamond composite substrates for hemt applications," *IEEE Trans. Compon. Packag. Manuf. Technol.* **3**, 79–85 (2013).
- ⁵⁸¹D. G. Cahill, A. Bullen, and L. Seung-Min, "Interface thermal conductance and the thermal conductivity of multilayer thin films," *High Temp. High Press.* **32**, 135–142 (2000).
- ⁵⁸²T. Borca-Tasciuc, W. Liu, J. Liu, T. Zeng, D. W. Song, C. D. Moore, G. Chen, K. L. Wang, M. S. Goorsky, T. Radetic *et al.*, "Thermal conductivity of symmetrically strained Si/Ge superlattices," *Superlattices Microstruct.* **28**, 199–206 (2000).
- ⁵⁸³T. Yamane, N. Nagai, S.-i Katayama, and M. Todoki, "Measurement of thermal conductivity of silicon dioxide thin films using a 3ω method," *J. Appl. Phys.* **91**, 9772–9776 (2002).
- ⁵⁸⁴S. Rausch, D. Rauh, C. Deibel, S. Vidi, and H. Ebert, "Thin-film thermal-conductivity measurement on semi-conducting polymer material using the 3ω technique," *Int. J. Thermophys.* **34**, 820–830 (2013).
- ⁵⁸⁵E. Pop, D. A. Mann, K. E. Goodson, and H. Dai, "Electrical and thermal transport in metallic single-wall carbon nanotubes on insulating substrates," *J. Appl. Phys.* **101**, 093710 (2007).
- ⁵⁸⁶J. C. Duda, J. L. Smoyer, P. M. Norris, and P. E. Hopkins, "Extension of the diffuse mismatch model for thermal boundary conductance between isotropic and anisotropic materials," *Appl. Phys. Lett.* **95**, 031912 (2009).
- ⁵⁸⁷D. G. Cahill, "Thermal-conductivity measurement by time-domain thermoreflectance," *MRS Bull.* **43**, 782–789 (2018).
- ⁵⁸⁸S. Sadasivam, N. Ye, J. P. Feser, J. Charles, K. Miao, T. Kubis, and T. S. Fisher, "Thermal transport across metal silicide-silicon interfaces: First-principles calculations and Green's function transport simulations," *Phys. Rev. B* **95**, 085310 (2017).
- ⁵⁸⁹P. E. Hopkins, T. Beechem, J. C. Duda, K. Hattar, J. F. Ihlefeld, M. A. Rodriguez, and E. S. Piekos, "Influence of anisotropy on thermal boundary conductance at solid interfaces," *Phys. Rev. B* **84**, 125408 (2011).
- ⁵⁹⁰R. Stoner and H. Maris, "Kapitza conductance and heat flow between solids at temperatures from 50 to 300 K," *Phys. Rev. B* **48**, 16373 (1993).
- ⁵⁹¹P. E. Hopkins, R. Salaway, R. Stevens, and P. Norris, "Temperature-dependent thermal boundary conductance at Al/Al₂O₃ and Pt/Al₂O₃ interfaces," *Int. J. Thermophys.* **28**, 947–957 (2007).
- ⁵⁹²Z. Lu, Y. Wang, and X. Ruan, "Metal/dielectric thermal interfacial transport considering cross-interface electron-phonon coupling: Theory, two-temperature molecular dynamics, and thermal circuit," *Phys. Rev. B* **93**, 064302 (2016).
- ⁵⁹³H.-K. Lyeo and D. G. Cahill, "Thermal conductance of interfaces between highly dissimilar materials," *Phys. Rev. B* **73**, 144301 (2006).
- ⁵⁹⁴G. Mahan, "Kapitza thermal resistance between a metal and a nonmetal," *Phys. Rev. B* **79**, 075408 (2009).
- ⁵⁹⁵D. Grimm, R. B. Wilson, B. Teshome, S. Gorantla, M. H. Rümmeli, T. Bublat, E. Zallo, G. Li, D. G. Cahill, and O. G. Schmidt, "Thermal conductivity of mechanically joined semiconducting/metal nanomembrane superlattices," *Nano Lett.* **14**, 2387–2393 (2014).
- ⁵⁹⁶A. Sood, R. Cheaito, T. Bai, H. Kwon, Y. Wang, C. Li, L. Yates, T. Bouger, S. Graham, M. Asheghi *et al.*, "Direct visualization of thermal conductivity suppression due to enhanced phonon scattering near individual grain boundaries," *Nano Lett.* **18**, 3466–3472 (2018).
- ⁵⁹⁷E. López-Honorato, C. Chiriteescu, P. Xiao, D. G. Cahill, G. Marsh, and T. Abram, "Thermal conductivity mapping of pyrolytic carbon and silicon carbide coatings on simulated fuel particles by time-domain thermoreflectance," *J. Nucl. Mater.* **378**, 35–39 (2008).
- ⁵⁹⁸J.-C. Zhao, X. Zheng, and D. G. Cahill, "Thermal conductivity mapping of the Ni-Al system and the Beta-NiAl phase in the Ni-Al-Cr system," *Scr. Mater.* **66**, 935–938 (2012).

- ⁵⁹⁹E. K. Pek, J. Brethauer, and D. G. Cahill, "High spatial resolution thermal conductivity mapping of SiC/SiC composites," *J. Nucl. Mater.* **542**, 152519 (2020).
- ⁶⁰⁰X. Ji, S. Matsuo, N. R. Sottos, and D. G. Cahill, "Anisotropic thermal and electrical conductivities of individual polyacrylonitrile-based carbon fibers," *Carbon* **197**, 1–9 (2022).
- ⁶⁰¹D. B. Brown, W. Shen, X. Li, K. Xiao, D. B. Geohegan, and S. Kumar, "Spatial mapping of thermal boundary conductance at metal–molybdenum diselenide interfaces," *ACS Appl. Mater. Interfaces* **11**, 14418–14426 (2019).
- ⁶⁰²Z. Cheng, F. Mu, X. Ji, T. You, W. Xu, T. Suga, X. Ou, D. G. Cahill, and S. Graham, "Thermal visualization of buried interfaces enabled by ratio signal and steady-state heating of time-domain thermoreflectance," *ACS Appl. Mater. Interfaces* **13**, 31843–31851 (2021).
- ⁶⁰³W. Hodges, A. Jarzembski, A. McDonald, E. Ziade, and G. W. Pickrell, "Sensing depths in frequency domain thermoreflectance," *J. Appl. Phys.* **131**, 245103 (2022).
- ⁶⁰⁴B. Treweek, V. Akcelik, W. Hodges, A. Jarzembski, M. Bahr, M. Jordan, A. McDonald, L. Yates, T. Walsh, and G. Pickrell, "Inversion for thermal properties with frequency domain thermoreflectance," *ACS Appl. Mater. Interfaces* **16**, 4117–4125 (2024).
- ⁶⁰⁵R. J. Stevens, L. V. Zhigilei, and P. M. Norris, "Effects of temperature and disorder on thermal boundary conductance at solid-solid interfaces: Nonequilibrium molecular dynamics simulations," *Int. J. Heat Mass Transfer* **50**, 3977–3989 (2007).
- ⁶⁰⁶C. Caddeo, C. Melis, A. Ronchi, C. Giannetti, G. Ferrini, R. Rurali, L. Colombo, and F. Banfi, "Thermal boundary resistance from transient nanocalorimetry: A multiscale modeling approach," *Phys. Rev. B* **95**, 085306 (2017).
- ⁶⁰⁷M. Li, J. Liu, W. Yu, Y. Zhang, and H. Zhou, "Atomistic molecular dynamic simulations of the thermal transport across h-BN/cellulose nanocrystal interface," *Int. J. Heat Mass Transfer* **171**, 121043 (2021).
- ⁶⁰⁸K. Gordiz and A. Henry, "A formalism for calculating the modal contributions to thermal interface conductance," *New J. Phys.* **17**, 103002 (2015).
- ⁶⁰⁹P. K. Schelling, S. R. Phillpot, and P. Kebinski, "Phonon wave-packet dynamics at semiconductor interfaces by molecular-dynamics simulation," *Appl. Phys. Lett.* **80**, 2484–2486 (2002).
- ⁶¹⁰J. Shi, J. Lee, Y. Dong, A. Roy, T. S. Fisher, and X. Ruan, "Dominant phonon polarization conversion across dimensionally mismatched interfaces: Carbon-nanotube-graphene junction," *Phys. Rev. B* **97**, 134309 (2018).
- ⁶¹¹Z. Tian, K. Esfarjani, and G. Chen, "Enhancing phonon transmission across a Si/Ge interface by atomic roughness: First-principles study with the Green's function method," *Phys. Rev. B* **86**, 235304 (2012).
- ⁶¹²J. Shi, X. Yang, T. S. Fisher, and X. Ruan, "Dramatic increase in the thermal boundary conductance and radiation limit from a nonequilibrium Landauer approach," *arXiv:1812.07910* (2018).
- ⁶¹³J. Shi, "Atomistic simulations of thermal transport across interfaces," Ph.D. thesis (Purdue University, 2018).
- ⁶¹⁴A. Giri, J.-P. Niemelä, T. Tynell, J. T. Gaskins, B. F. Donovan, M. Karppinen, and P. E. Hopkins, "Heat-transport mechanisms in molecular building blocks of inorganic/organic hybrid superlattices," *Phys. Rev. B* **93**, 115310 (2016).
- ⁶¹⁵R. J. Stevens, A. N. Smith, and P. M. Norris, "Measurement of thermal boundary conductance of a series of metal-dielectric interfaces by the transient thermoreflectance technique," *J. Heat Transfer* **127**, 315–322 (2005).
- ⁶¹⁶P. E. Hopkins, "Multiple phonon processes contributing to inelastic scattering during thermal boundary conductance at solid interfaces," *J. Appl. Phys.* **106**, 013528 (2009).
- ⁶¹⁷M. A. Panzer, H. M. Duong, J. Okawa, J. Shiomi, B. L. Wardle, S. Maruyama, and K. E. Goodson, "Temperature-dependent phonon conduction and nanotube engagement in metalized single wall carbon nanotube films," *Nano Lett.* **10**, 2395–2400 (2010).
- ⁶¹⁸K. Sääskilahti, J. Oksanen, J. Tulkki, and S. Volz, "Role of anharmonic phonon scattering in the spectrally decomposed thermal conductance at planar interfaces," *Phys. Rev. B* **90**, 134312 (2014).
- ⁶¹⁹X. Wu and T. Luo, "The importance of anharmonicity in thermal transport across solid-solid interfaces," *J. Appl. Phys.* **115**, 014901 (2014).
- ⁶²⁰P. E. Hopkins and P. M. Norris, "Relative contributions of inelastic and elastic diffuse phonon scattering to thermal boundary conductance across solid interfaces," *J. Heat Transfer* **131**, 022402 (2009).
- ⁶²¹S. Shin, M. Kaviani, T. Desai, and R. Bonner, "Roles of atomic restructuring in interfacial phonon transport," *Phys. Rev. B* **82**, 081302 (2010).
- ⁶²²P. E. Hopkins, J. C. Duda, and P. M. Norris, "Anharmonic phonon interactions at interfaces and contributions to thermal boundary conductance," *J. Heat Transfer* **133**, 062401 (2011).
- ⁶²³J. Dai and Z. Tian, "Rigorous formalism of anharmonic atomistic Green's function for three-dimensional interfaces," *Phys. Rev. B* **101**, 041301 (2020).
- ⁶²⁴C. A. Polanco, R. Rastgarkafshgarkolaei, J. Zhang, N. Q. Le, P. M. Norris, and A. W. Ghosh, "Design rules for interfacial thermal conductance: Building better bridges," *Phys. Rev. B* **95**, 195303 (2017).
- ⁶²⁵H. Rafii-Tabar, *Computational Physics of Carbon Nanotubes* (Cambridge University Press, 2008).
- ⁶²⁶J. C. Duda, T. S. English, E. S. Piekos, W. A. Soffa, L. V. Zhigilei, and P. E. Hopkins, "Implications of cross-species interactions on the temperature dependence of Kapitza conductance," *Phys. Rev. B* **84**, 193301 (2011).
- ⁶²⁷K. T. Butler, D. W. Davies, H. Cartwright, O. Isayev, and A. Walsh, "Machine learning for molecular and materials science," *Nature* **559**, 547–555 (2018).
- ⁶²⁸T. Wang, C. Zhang, H. Snoussi, and G. Zhang, "Machine learning approaches for thermoelectric materials research," *Adv. Funct. Mater.* **30**, 1906041 (2020).
- ⁶²⁹R. Jaafreh, Y. S. Kang, and K. Hamad, "Lattice thermal conductivity: An accelerated discovery guided by machine learning," *ACS Appl. Mater. Interfaces* **13**, 57204–57213 (2021).
- ⁶³⁰Y. Luo, M. Li, H. Yuan, H. Liu, and Y. Fang, "Predicting lattice thermal conductivity via machine learning: A mini review," *npj Comput. Mater.* **9**, 4 (2023).
- ⁶³¹S. Ju, T. Shiga, L. Feng, Z. Hou, K. Tsuda, and J. Shiomi, "Designing nanostructures for phonon transport via bayesian optimization," *Phys. Rev. X* **7**, 021024 (2017).
- ⁶³²A. Karamati, S. Xu, H. Lin, M. Rahbar, and X. Wang, "Thermophysical properties of 1D materials: Transient characterization down to atomic level," *JUSTC* **53**, 1001 (2023).
- ⁶³³J. Hansson, T. M. Nilsson, L. Ye, and J. Liu, "Novel nanostructured thermal interface materials: A review," *Int. Mater. Rev.* **63**, 22–45 (2018).
- ⁶³⁴Y. Yao, J. Sun, X. Zeng, R. Sun, J.-B. Xu, and C.-P. Wong, "Construction of 3D skeleton for polymer composites achieving a high thermal conductivity," *Small* **14**, 1704044 (2018).
- ⁶³⁵Y. Cui, M. Li, and Y. Hu, "Emerging interface materials for electronics thermal management: Experiments, modeling, and new opportunities," *J. Mater. Chem. C* **8**, 10568–10586 (2020).
- ⁶³⁶X. Guo, S. Cheng, W. Cai, Y. Zhang, and X-a Zhang, "A review of carbon-based thermal interface materials: Mechanism, thermal measurements and thermal properties," *Mater. Des.* **209**, 109936 (2021).